COBALT NANOPARTICLES FOR FISCHER-TROPSCH SYNTHESIS: FROM COLLOIDAL TO WELL-DEFINED SUPPORTED NANOCATALYSTS

Jorge Alonso Delgado Delgado

Dipòsit Legal: T 976-2015

UNIVERSITAT ROVIRA I VIRGILI
COBALT NANOPARTICLES FOR FISCHER-TROPSCH SYNTHESIS: FROM COLLOIDAL TO WELL-DEFINED SUPPORTED NANOCATALYSTS
Jorge Alonso Delgado Delgado
Dipòsit Legal: T 976-2015

The present work deals with the design of novel cobalt nanocatalysts for the Fischer-Tropsch Synthesis (FTS). Cobalt nanoparticles (CoNPs) stabilized by polymers were synthesized via chemical reduction method or thermal decomposition of organometallic precursors. Once isolated, these CoNPs were fully characterized and tested in the Aqueous phase Fischer-Tropsch Synthesis. For comparison purposes, some of the prepared nanoparticles were also immobilized on TiO_2 and tested in FTS using fixed bed reactors. It was concluded that the catalytic performance for both colloidal and supported catalytic systems were highly dependent on parameters such as the synthetic methodology, the polymeric stabilizer and the particle size.

UNIVERSITAT ROVIRA I VIRGILI
SAPIENTIAE LIBERI LIBERTATI SAPIENTES

DOCTORAL THESIS

Jorge Alonso Delgado Delgado

UNIVERSITAT ROVIRA I VIRGILI

2014

Cobalt Nanoparticles for Fischer-Tropsch Synthesis: From Colloidal to Well-defined Supported Nanocatalysts

Jorge Alonso Delgado Delgado

DOCTORAL THESIS

Departament de Química Física i Inorgànica
Tarragona, 2014

Jorge Alonso Delgado Delgado

Cobalt nanoparticles for Fischer-Tropsch Synthesis: from colloidal to well-defined supported nanocatalysts

DOCTORAL THESIS

Supervised by

Dr. Cyril Godard and Prof. Carmen Claver

Departamento de Química Física i Inorgánica

Centre Tecnològic de la Química de Catalunya

2014

Tarragona

UNIVERSITAT ROVIRA I VIRGILI

UNIVERSITAT ROVIRA I VIRGILI
DEPARTAMENT DE QUÍMICA FÍSICA I INORGÀNICA
Campus Sescelades
Marcel·lí Domingo, s/n
43007 Tarragona
Tel. +34 977 55 81 37
Fax +34 977 55 95 63
www.quimica.urv.es

I STATE that the present study, entitled "**Cobalt nanoparticles for Fischer-Tropsch Synthesis: from colloidal to well-defined supported nanocatalysts** ", presented by Jorge Alonso Delgado Delgado for the award of the degree of Doctor, has been carried out under my supervision at the Department of Quimica Fisica i Inorganica of this university, and that it fulfils all the requirements to be eligible for the International Doctorate Award.

Tarragona, October 2014

Doctoral Thesis Supervisor/s

Dr. Cyril Godard

Prof. Carmen Claver

The work performed in the present doctoral thesis has been possible thanks to the funding of Total S.A. and to a mobility grant (AEE2013-24) from the Universitat Rovira i Virgili.

UNIVERSITAT ROVIRA I VIRGILI

To my family

Agradecimientos

La realización del trabajo que a continuación se presenta, fue posible solo gracias a la suma de esfuerzos de un sinnúmero de personas, entidades y naciones cada uno de ellos participando de una u otra manera, directa o indirectamente.

En primer lugar quisiera agradecer a mis padres, María de Jesús y Jorge Alonso por darme el ser. Gracias a ellos por el soporte incondicional a la distancia, por esperar mi regreso siempre con los brazos abiertos, incluso, por desearme siempre lo mejor incluso implicando el retorno indeterminado a casa. Agradezco también a mis hermanos Noel, Yenifer y Jeraldin también por el apoyo incondicional y por "encontrarme" en aquellas temporadas en que la comunicación con la familia se hacía menos frecuente. A todos los familiares que en la distancia han estado pendientes de mí, Nelly, Belén, Yuldor, José, Hans (tio) y Julieth mis sinceros agradecimientos.

Quiero agradecer a mi país Colombia por la formación brindada durante mis primeros años como químico, a España por recibirme con las manos abiertas y por su hospitalidad durante los últimos cuatro años y a Francia por recibirme también durante mi estancia doctoral.

En el plano académico, quisiera dar mi profundo agradecimiento a Carmen Claver y a Cyril Godard, por la oportunidad de trabajar en el OMICH y por su dirección durante estos años. A Carmen quisiera agradecer especialmente por enseñarme los diversos aspectos de la labor científica. Además de una enciclopedia de química organometálica siempre serás para mí un ejemplo de persona íntegra y de trabajador incansable. A Cyril, muchísimas gracias por la paciencia, y por las incontables horas dedicadas en pro de mi formación como científico. En días como los que corren hoy en día, no es fácil encontrar un par de personas tan comprometidas en la formación como lo han sido Carmen y Cyril, por esa razón muchísimas gracias. Como no agradecer a Sergio Castillón por sus invaluables reflexiones orgánicas y por las inmejorables veladas con el los grupos de orgánica e inorgánica al son de Niche.

Quisiera agradecer a Total S. A. por la financiación de este trabajo y especialmente a Daniel Curulla-Ferre por la confianza depositada en mi durante estos años de trabajo coordinado. Muchas gracias a él por las invaluables reuniones y siempre fructíferos intercambios de mails.

Quisiera también agradecer a todos y cada uno de los miembros del OMICH, Verónica, Angélica, Tatiana, Oriol, Jessi, Eli, Alberto, Fran y Antón porque de cada

uno de ellos he aprendido algo, y porque todos participaron de una u otra forma en la realización de esta tesis. Quisiera agradecer especialmente a Jessi y a Eli, porque fueron ellas quieres me dieron la mano cuando recién llegue al grupo, y fue en gran parte gracias a ellas que al final del Master me sentí tan a gusto que facilitó la continuidad con el doctorado. Muchas gracias a Raquel, por su infinita cordialidad y a Silvia y demás secretarias del departamento por su colaboración con la inevitable parte burocrática de cada proceso.

En este punto como no agradecer a toda la gente querida del CTQ(cinc anys). A Jordi Colavida, por pinchar la música en el laboratorio siempre con los éxitos del momento (y por chinchar la vida). A Dolores Gonzales, una química excelente, gracias por su disposición incondicional para ayudarme siempre que le necesitaba, y por nuestras conversaciones de química y de la vida (tal vez menos frecuentes al final de este camino llamado tesis). A Mónica Viciano, gracias por su elocuencia, siempre lograste sacarme una sonrisa☺… y se lo difícil que a veces esto puede llegar a ser. A Bianquis, Stefano, Isabel, Ivonne, muchas gracias por el buen rollo siempre. Finalmente, a todo el "CTQ(cinc anys) team" quisiera dar mis profundo agradecimiento por aguantar mis silencios ininterrumpidos y mi difícil carácter durante estos años. Mi especial agradecimiento a Montse por su participación directa durante inicio de mi tesis, muchísimas gracias por su paciencia. Finalmente quisiera agradecer a Laura por brindarme su ayuda en la interminable labor que representa el análisis de datos de FT. Thank you very much Justyna Stapinska for all the synthetic work that you carried out, and for your smile☺, my best wishes in your starting project. Como no agradecer a Olga Sánchez, por el trabajo hombro a hombro con el proyecto de hidrogenación. Muchas gracias por la paciencia y por la siempre buena actitud, estoy seguro que grandes cosas te esperan.

También agradezco a otros miembros del CTQ(cinq anys), Josep María, Patricia, Isabel, Pablo, Claude, Bernabé y Fernando por su asistencia en algún aspecto de la tesis así como por los buenos momentos compartidos.

I'd like to give my sincere thanks to Andrei Khodakov for the opportunity to work in their laboratories at the Ecole Centrale and the UCCS in Lille. To Vitaly Ordomsky, thank you very much for the supervision and the rain of ideas you always gave me each time we talked about chemistry. Thanks also to all the nice people I meet in such rainy, cold albeit beautiful place, Diego, David, Guido, Marco, Luca, Lu, Belen, Maria, Paola, Abel and Takayuki because without their company the experience in France would not have been so wonderful.

En el plano personal quisiera agradecer a mis dos amigos aquí en Tarragona, Judith y Sebastián. A Judith, gracias por brindarme su amistad incondicional sin reparos,

por las desahogadas y los siempre directos consejos. Al Sebas, por su pleno apoyo desde el comienzo de mi tesis, muchísimas gracias por nuestras tan constructivas conversaciones sobre la vida, siempre las recordare.

En el plano extra-académico como no agradecer a Magda y a la Isla del Mojito donde he pasado tantos buenos momentos los últimos años. Gracias a Ileana y a Brian por enseñarme no a bailar salsa sino a disfrutar de ella. A ellos, Magda, Ramón, Claudia, Elena, Yurani, Arturo, Andry y Daylin, muchas gracias por los incontables buenos momentos en la isla. Cuando llegue el día en que ya no esté en Tarragona seguramente los extrañaré mucho.

También quisiera agradecer a aquellas amistades consolidadas durante este periodo. A Daniel y Javier, gracias por las arepadas los sábados y los combates de Battlefield. Javier, muchísimas gracias por su amistad sincera durante los últimos años. A Diana Rojas, muchísimas gracias por el grato reencuentro, sabes que eres una amiga muy importante y me alegra muchísimo el haber recuperado nuestra amistad, esta vez para siempre. Como no agradecer de manera especial a Daniel Rojas Montaño, amigo del alma y autor de la portada de esta tesis. También agradezco a Carolina, por la colaboración en el proceso de fotografía.

Finalmente quisiera dar el más especial de mis agradecimientos a Yanine Arrieta quien me ha dado su apoyo incondicional durante este último año y medio de tesis. Gracias por todos los buenos momentos compartidos, gracias a ella mi experiencia en el doctorado fue aún más memorable. Sólo puedo esperar que lo compartido en Europa sea apenas una pequeña parte de lo que nos depare el futuro.

Si fuese solo un poco más minucioso en incluir todas y cada una de las personas a quien debo un agradecimiento, o si detallase solo un poco más su modo de participación, mis agradecimientos podrían extenderse tanto como la tesis misma. Por esta razón, quiero agradecer de manera general a todos aquellos quienes encontrándose con estas líneas saben de su participación pero que por descuido mío no fueron incluidos en los anteriores parágrafos.

Table of Contents

Glossary of Terms and Abbreviations

[BMI]	1-*n*-butyl-3-methylimidazolium
[DMI]	1-*n*-decyl-3-methylimidazolium
[FAP]	trifluoro-tris-(pentafluoroethane) phosphate
[NTf_2]	*N*-bis(trifluoromethanesulfonyl)-imidate
AFTS	Aqueous phase Fischer-Tropsch Synthesis
ASF	Anderson Schulz–Flory
bct	Body centered tetragonal
Cn	Carbon number
CNFs	Carbon nanofibers
CNTs	Carbon nanotubes
CoNPs	Cobalt nanoparticles
DDAB	di-dodecyl-di-methylammonium bromide
DFT	Density functional theory
DFT	density functional theory
DOPO	Dioctylphosphine oxide
fcc	Face centered cubic
FID	Flame ionization detector
FT	Fischer-Tropsch
FTIR	Fourier-transformed infrared spectroscopy
FTS	Fischer-Tropsch Synthesis
hcp	Hexagonal compact packing
HR-TEM	High-resolution transmission electron microscopy
ICP	Induced coupled plasma
IS	Internal standard
MCC	microcrystalline cellulose
MFC	Mass flow controller
M-NPs	Metal nanoparticles

MSD	Mass spectroscopy detector
NPs	Nanoparticles
O/P	Olefin to paraffin ratio
OAT	2-ethylhexyl)sulfosuccinate
PEG	polyethyleneglycol
PPO	poly(2,6-dimethyl-1,4-phenyleneoxide)
PVP	Polyvinylpyrrolidone
RuNPs	Ruthenium nanoparticles
SB12	dodecyl-*N*,*N*-di-methyl-3-ammonio-1-propanesulfonate
SSITKA	Steady state isotopic transient kinetic analysis
STR	Stirred tank reactor
STY	Site time yield
TCD	Thermal conductivity detector
TEM	Transmission electron microscopy
TGA	Thermo gravimetric analysis
TOF	Turnover frequency
TON	Turnover number
TPR	Thermal programmed reduction
TS	Transition state
XPS	X-ray photoelectron spectroscopy
XRD	X-ray diffraction
WGS	Water-gas shift

Electronic Supplementary Material

- xlsx files of calibration curves used in product analysis
- xlsx file used for the analysis of Fisher-Tropsch catalytic experiments

You learn much more when the things do not work than when they do

Thin, G.

CHAPTER I

General Introduction

Table of Contents

I.1. Brief historical background

The synthesis of fuels instead of traditional extraction-refining processes is a century old concept which has its origins at the beginning of the 20th century.[1] Among the different process developed for this purpose, the Fischer-Tropsch Synthesis (FTS), which consists in the catalytic hydrogenation of carbon monoxide to yield hydrocarbon products, remains nowadays one of the most studied alternatives for the production of fuels.

There are two events which can be considered the first steps towards the development of synthetic fuels technology: the invention of the high-pressure coal liquefaction by Bergius and the experiments on catalytic hydrogenation of carbon monoxide by Sabatier and Senderens.[2] The parallel increasing of Germany´s industrialization and their fuel demand at the end of the 19th century, in conjunction with the lack of petroleum deposits, stimulated the invention of processes that enabled them to synthesize petroleum from their country´s abundant coal supplies.[3] During the first decade of the past century, Friedrich Bergius in Rheinau-Mannheim developed a process in which reacted a coal-oil paste with hydrogen gas at high pressure and temperature (200 atm and 400 ºC) to yield petroleum-like products.[1] Almost in parallel, Sabatier and Senderens synthesized methane from a mixture of CO or CO_2 with hydrogen using cobalt or nickel catalysts at 200ºC and atmospheric pressure.[4] A decade after Bergius began his work Franz Fischer and Hans Tropsch at the Kaiser-Wilhelm Institute invented an indirect process for the synthesis of liquid fuels from coal, the Fischer-Tropsch Synthesis.[1] The process consisted in the reaction of coal with stream to give a mixture of carbon monoxide and hydrogen and the subsequent reaction of the mixture over an alkalized iron catalyst (100-150 bar and 400-450 ºC [5]) to yield finally petroleum-like products. Fischer and his co-workers in the 1920s-30 developed the cobalt catalysts at milder conditions (1bar, 250-300ºC [6]) that were critical to the FT success and in 1934 Ruhrchemie acquired the patent rights to the synthesis. Some years after, in 1936, the first commercial-size FT plant started operation in Braunkhole-Benzin and to the end of the World War II, Germany reached a capacity of 660000 tons of primary products per year

with the operation of nine FT plants using cobalt based catalysts. Under the perception of the limited oil reserves as well as the desire of fuel independence, other countries such as France, England, Japan, US, and South Africa, showed interest in the German´s technology. The US Bureau of Mines had begun small-scale research on FTS in 1927 and coal liquefaction in 1936, but did not seriously work on them until the government expressed considerable concern about the country´s rapidly increasing petroleum consumption in the immediate post-World War II. For the late 1940s and mid-1950s, four synthetic fuel plants were constructed in the US: three FT plants located in Kansas, Texas and Pennsylvania, and a one coal liquefaction plant in Virginia.[7] During the same period, the abundance of low price petroleum after the discovery of the huge crude oil reserves in the Middle East, shifted the interest for FT process resulting in the shutdown of most of the US synthetic fuel plants.[8]

Following the plant shutdowns in the US and until the global energy crises of 1970s, all major synthetic fuel research and development ceased except for the construction in 1955 of the South African Coal, Oil and Gas Corporation´s (SASOL) first FT plant in Sasolburg, South Africa. The plant based on coal and which employed an iron based catalyst, was the materialization of South Africa´s desire for energy independence as a consequence to the embargo caused by its apartheid policy.[1]

The 1970s energy crisis caused by the OAPEC oil embargo (Organization of Arab Petroleum Exporting Countries) revitalized synthetic fuel research and development in the US and Germany and led to joint government-industry programs that quickly disappeared once the crisis had passed. Gulf Oil, Atlantic Richfield, and Exxon in the US, AG, Ruhrkohle AG and Veba Chemie in Germany constructed FT and coal liquefaction pilot plants in the 1970s and early 1980s only to end their operation with the collapse of petroleum process a few years later.[9] A direct correlation between the research in FT and the crude oil price during the 1970s oil crisis is displayed in Figure 1. The simultaneous increase of both indicators, the number of patents and papers and the crude oil price during this period, is clearly displayed.

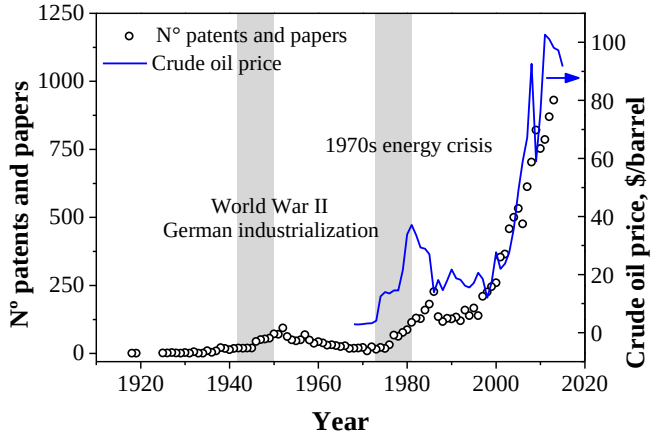

Figure 1. Comparison of the number of patents and papers published on FTS and the crude oil prices in the last century. Data sources: number of patents and papers from SciFinder search, August 2014. Imported Crude Oil Prices consulted in EIA (U.S. Energy Information Administration).

In the mid-1990s, the rising price of oil as well as problems of utilization of stranded gas, diversification of sources of fossil fuels, and environmental concerns, triggered another synthetic fuel revival.[10] The resurgence of the interest of FT synthesis is also evidenced in Figure 1 with the exponential increase of related patents and papers published during the last two decades (also in parallel with oil price increasing).

The abundant reserves of natural gas in many parts of the world have made it attractive to commission new plants based on steam reforming and FT technology, the gas-to-liquid technology (GTL). Based on GTL process, the Mossgas plant in South Africa with a capacity of 220000 bbl/day and the Shell plant in Bintulu, Malaysia with an initial capacity of 120000 bbl/day, came on stream in 1992 and 1993 respectively.[11] More recently in 2006, the Sasol Oryx-GTL plant with a capacity of 34000 bbl/day was inaugurated. The utilization of biomass has emerged in the past decades as the only renewable carbon source to synthesize liquid fuels or chemicals by the BTL process.[10] In 2007, Choren, a bio-energy company built a

300 bbl/day BTL plant that used Shell´s FTS technology to transform biomass into bio-diesel.[12]

To summarize, the synthetic fuel industry from the beginning of the 20th century to 1990 has experienced intermittent periods of intense activity in times of crisis, only to face quick dismissal as unnecessary or uneconomical upon disappearance of the crisis.[1] In the last two decades a global renaissance of FT synthesis is the response for the urgent replacement of the crude oil by other carbon resources such as natural gas, coal and biomass as a key process of the GTL, CTL and BTL technologies.[13]

I.2. Fischer-Tropsch Synthesis

Fischer-Tropsch Synthesis is a heterogeneous catalytic process for the transformation of syngas (a mixture of CO and H_2) into straight chain hydrocarbon products. This reaction occurs at the surface of transition metals in the zero valent state which have the capacity of both adsorb and dissociate carbon monoxide and hydrogen.[14]For the majority of the transition metals, however, the nature of the adsorption (dissociative or molecular) is very sensitive to the surface temperature and surface structure (e.g. the Miller index plane), and the presence of any lower co-ordination sites such as step sites and defects). In contrast, the chemisorption of hydrogen is an activated process yielding monoatomic hydrogen.[15] This process as well as the metal coverage is favored by the increasing of the temperature, different to the case of CO adsorption. Finally, the reaction between the dissociation products, hydrogen, carbon and oxygen, results in the polymerization reaction that yield the FT products.

The main products in FTS are n-alkanes, n-alkenes, methane and water, (Equations **1** and **2**) but depending on the catalyst, the support and promoters, temperatures and pressures, and even the type of reactor used, the FTS also give rise to small amounts of other organic compounds including branched hydrocarbons and oxygenates such as alcohols, aldehydes and carboxylic acids (Equations **3-5**).[13b,16] Several other metal-catalyzed reactions involving hydrogen and carbon monoxide,

but giving quite different products, can also occur. These include methanol synthesis and the water-gas shift reaction (WGS) (Equations **6** and **7**).[16]

Alkanes	$(2n+1)H_2 + nCO \rightarrow C_nH_{(2n+2)} + nH_2O$	**(1)**
Alkenes	$2nH_2 + nCO \rightarrow C_nH_{2n} + nH_2O$	**(2)**
Alcohols	$2nH_2 + nCO \rightarrow C_nH_{(2n+1)}OH + (n-1)H_2O$	**(3)**
Adehydes	$(2n-1)H_2 + nCO \rightarrow C_nH_{2n}O + (n-1)H_2O$	**(4)**
Acids	$nH_2 + nCO \rightarrow C_nH_{2n}O_2$	**(5)**
Methanol	$2H_2 + CO \rightarrow CH_3OH$	**(6)**
WGS	$CO + H_2O \rightarrow CO_2 + H_2$	**(7)**

I.2.1. Thermodynamics

In the Fischer-Tropsch Synthesis, the formation of water can be considered the thermodynamic "driving force" of the reaction. The thermodynamics of the CO hydrogenation reactions for the production of simple compounds (Equations **8-15**) indicate that the most favorable path is that leading to methane and water (Equation **8**). The fact that FTS under typical conditions does not give excessive amounts of methane is the proof that not only thermodynamics but also kinetics defines the product selectivity in this reaction.

The Gibbs free energy values at 220ºC ($\Delta G_{(227ºC)}$) for the series of C2 compounds (Equations **10-13**[16]) suggest that the alkane formation is more favorable than the alkene > alcohol > aldehyde, respectively, which match the abundances by family compounds experimentally observed in typical FTS.[17]

Methane	$3H_2 + CO \rightarrow CH_4 + H_2O$	$\Delta G_{(220ºC)}$= -94 kJ/mol	**(8)**
Methanol	$2H_2 + CO \rightarrow CH_3OH$	$\Delta G_{(220ºC)}$= +27 kJ/mol	**(9)**
Ethane	$5/2H_2 + CO \rightarrow 1/2C_2H_6 + H_2O$	$\Delta G_{(220ºC)}$= -58 kJ/mol	**(10)**
Ethene	$2H_2 + CO \rightarrow 1/2C_2H_4 + 2H_2O$	$\Delta G_{(220ºC)}$= -22 kJ/mol	**(11)**
Ethanol	$2H_2 + CO \rightarrow 1/2C_2H_5OH + 1/2H_2O$	$\Delta G_{(220ºC)}$= -13 kJ/mol	**(12)**
Ethanoic acid	$H_2 + CO \rightarrow 1/2C_2H_4O_2$	$\Delta G_{(220ºC)}$= -10 kJ/mol	**(13)**
Propene	$H_2 + CO \rightarrow 1/2C_2H_4O_2$	$\Delta G_{(220ºC)}$= -31 kJ/mol	**(14)**

WGS $CO + H_2O \rightarrow CO_2 + H_2$ $\Delta G_{(220^oC)}$= -28 kJ/mol **(15)**

It is therefore quite remarkable that the course of the reaction can be efficiently diverted to give either long-chain hydrocarbons or alkenes depending on the reaction conditions (temperature and pressure).[16] Concerning the heat of reaction, the formation of alkanes and alkenes are both strongly exothermic ($\Delta H_{(\approx 220^oC)}$=165–204 kJ/$mol_{CO}$), and the efficient heat removal is therefore crucial to control the reaction temperature and as much avoiding problems related to overheating of the catalyst (resulting in sintering and deactivation) and the production of undesired products such as methane.[17] Finally, according to several reports the formation of carbon clusters and deposition on the catalyst surface is thermodynamically favored under FT conditions.[18]

I.2.2. Mechanism of FTS

The Fischer-Tropsch Synthesis is a polymerization reaction, in which the monomers are being produced in-situ from hydrogen and carbon monoxide at the metal surface. Insights in the mechanism of this reaction were early supported by the identification of surface species at the steady-state during the FT synthesis. A summary of the most relevant observed and postulated surface species is given in Figure 2.[14] Species such as terminal (1), bridged (2) and vicinal (3) adsorbed CO were identified by infra-red spectroscopy (FTIR),[19] surface methylidyne (4), methylene (5) and methyl (6) species using secondary ion mass spectroscopy (SIMS)[20] and electron energy loss spectroscopy (EELS)[21] among other species such as surface oxygen (7), hydroxyl (8), and acyl species (9).

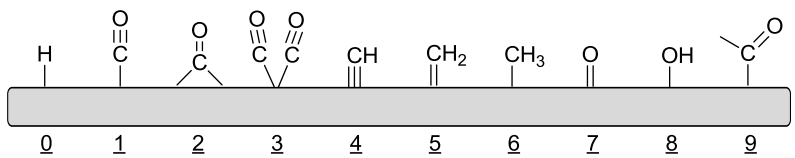

Figure 2. Some experimentally observed and postulated surface species on the catalyst surface during FTS.[14]

Most quantum-chemical calculations indicate that methyl is preferentially located on terminal sites, methylene on bridge sites and methylidyne on triply bridging sites (hollow sites) (Figure 3).[22] The importance of surface methylene and methylidyne species in the FT synthesis was highlighted by van Bameveld and Ponec.[23] They observed the conversion of CH_xCl_{4-x} in the presence of hydrogen to long chain hydrocarbons for x=l or 2, whereas only methane was obtained with methylchloride (x-3). This shows that the presence of surface methylene or methylidyne species may result in chain growth. Based on these surface species, numerous reaction pathways have been proposed to explain the observed product distribution in the FT synthesis,[14] however after many years of discussion, the scientific community has converged in at least two mechanisms: the carbide/alkyl mechanism and the CO insertion chain growth mechanism.[24]

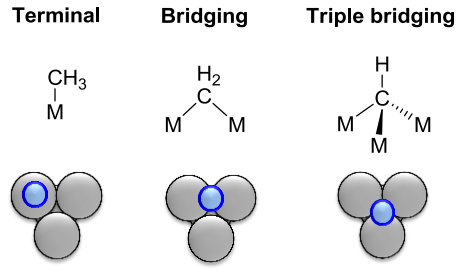

Figure 3. Localization of methyl, methylene and methylidyne grops on metal sites.

As a polymerization reaction, the mechanisms described for FTS are composed by three different reaction sections:

1. Generation of the chain initiator
2. Chain growth or propagation
3. Termination or desorption

In the ***carbide mechanism*** (Figure 4), the chain initiation takes place via dissociative CO chemisorption, by which surface carbon and surface oxygen is generated (Figure 4 a).[14] Surface oxygen is removed from the surface by reaction with adsorbed hydrogen yielding water or with adsorbed carbon monoxide yielding

CO_2 (b).[16] Surface carbon is subsequently hydrogenated yielding in a consecutive reaction CH, CH_2 and CH_3 surface species (c, d, e). The CH_3 surface species is regarded as the chain initiator, and the CH_2 or CH surface species as the monomer in this reaction scheme. Chain growth is thought to take place by successive incorporation of the monomer, CH_2 or CH surface species (f). Finally, product formation takes place by either β-hydrogen abstraction or hydrogen addition yielding 1-alkenes (g) and 1-alkanes (h) as primary products respectively.[14]

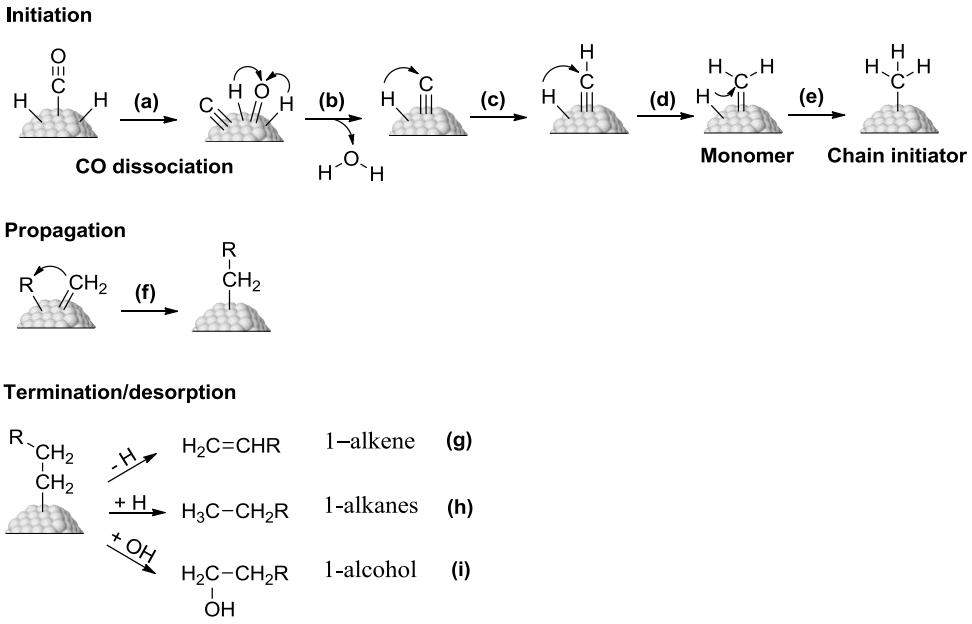

Figure 4. Reaction scheme of the Fischer–Tropsch reaction according to the carbide/alkyl mechanism.

The ***CO insertion mechanism*** is based on the known CO-insertion from coordination chemistry and homogeneous catalysis (Figure 5).[25]

The chain initiator is again a surface methyl species, however the reaction pathway leading to the formation of this species differs from the carbide mechanism at the time of the oxygen elimination from the surface species (Figure 5 a, b, c). For this mechanism, chemisorbed CO is the monomer. Subsequently, the chain growth takes place by CO-insertion in a metal-alkyl bond leading to a surface acyl species

(d). Then, the elimination of oxygen from the surface species leads to the formation of the enlarged alkyl species (e, f). Finally, the formation reaction steps leading to the formation of 1-alkenes (g) and 1-alkanes (h) are the same than the proposed in the carbide mechanism (β-elimination and H addition respectively). Additionally, chain termination involving the surface acyl species may result in the formation of aldehydes (i) and alcohols (j).

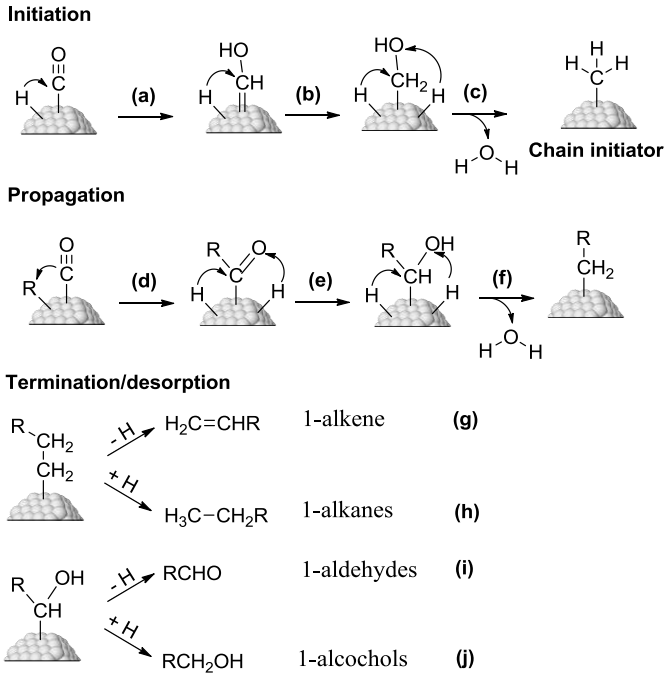

Figure 5. Reaction scheme of the Fischer–Tropsch reaction according to the CO insertion chain growth mechanism.

The development of modern tools such as the computational chemistry as well as advanced characterization techniques like Steady State Isotopic Transient Kinetic Analysis (SSITKA),[24] has made possible the discrimination between the two mechanistic options. As it has been discussed already in a very early theoretical study of this reaction,[26] the key issue concerns the nature of the monomeric single C atom containing "C1" intermediate that is incorporated into the growing hydrocarbon chain. For instance, recently van Santen and co-workers using DFT

calculations gave insights in favor of the carbide mechanism.[24] According to this report, Figure 6 schematically represents the surface energies (based on DFT calculations) for CO adsorption and dissociation followed by C-C bond formation according to the carbide and CO dissociation mechanisms calculated for a reactive site on Ru(1121). For this case, it is evident that the overall barrier for CH-CH coupling (TS1-3, Figure 6) is lower in the carbide mechanism than the overall activation barrier for CHC formation via CO insertion because of the high C-O bond cleavage activation energy (TS3, Figure 6).

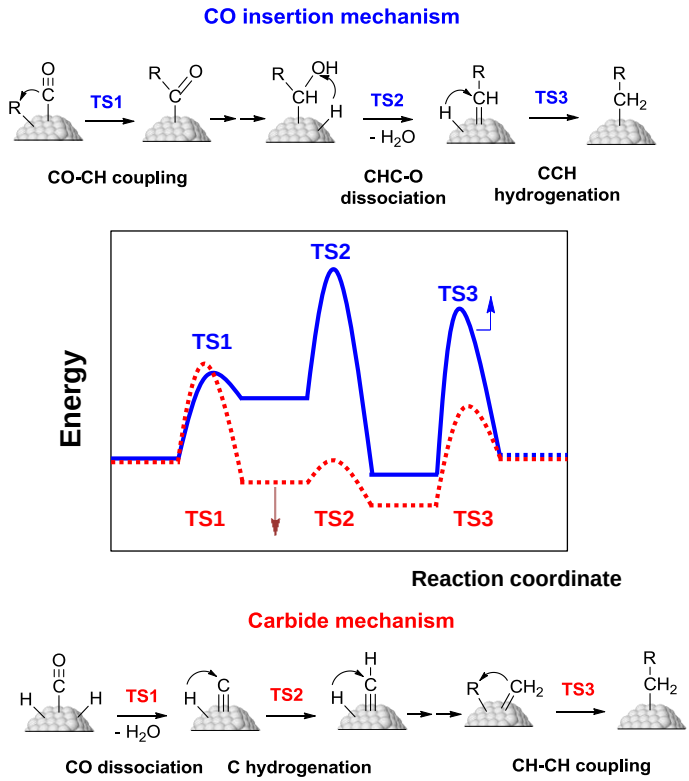

Figure 6. Comparison of activation barriers of elementary reaction steps for C-C coupling according to the carbide and CO insertion mechanism on Ru(1121) surface. Adapted from ref. [24]

Considering this results, the carbide chain growth mechanism will dominate. In addition, the empirical kinetic model has found to be consistent with only the

carbide mechanism for which is satisfied that the apparent rate of CO transformation to CH_x is slow compared to the rate of chain growth (this is the so-called monomer formation kinetics limit in agreement with the relatively large energy barrier for TS1 in Figure 6).[27]

Another argument in favor of the carbide mechanism is that whit this mechanism, the Fischer-Tropsch reaction should be highly structure sensitive, since only specific sites have the overall activation energy to activate and deliver CH_x fast enough for the chain growth reaction to reach a reasonable rate. The structural sensitivity of metallic cobalt particles was demonstrated by de Jong and co-workers, since cobalt particles smaller than 6 nm exhibited lower FT activity. This was atributed to the low stabilization of step-edge sites, which are important for CO activation. In contrast, bigger cobalt particles readily stabilize this sites.[28] However, Burtron and co-workers very recently reported experimental data fitting a kinetic model of FTS product distribution based on the CO insertion mechanism.[29] This model predicted that adsorbed CO is the most abundant species on the metal surface (in agreement with experimental measurements).

To conclude, there are two conflicting mechanistic proposals of the Fischer–Tropsch reaction: the carbide mechanism and the CO insertion mechanism, which involve cleavage of the C–O before incorporation of a CH_x species into the growing hydrocarbon chain (the carbide mechanism) or after incorporation into the growing hydrocarbon chain (the CO insertion mechanism). In spite of the many arguments in favor or against the different mechanistic options, the discussion is still open.

I.2.3. Selectivity of FTS

A wide variety of products of different chain length and different functionality are formed in the Fischer-Tropsch Synthesis. The products from the FTS on Co, Fe, and Ru show the following characteristics:[30]

1. The distribution for hydrocarbon products gives the highest concentration for C_1 and decreases for higher carbon numbers, although around C_3-C_4, often a local maximum is observed.

2. The olefin content decreases asymptotically to zero with increasing carbon number.

The main factors that influence the product selectivity (chain growth) in FTS are the temperature of the reaction, the nature of the metal catalyst, the chemical and structural promoters added to the catalyst, the gas composition and, more specifically, the partial pressures of the gases in contact with the catalyst inside the reactor.[14]

- *Temperature*

Independent of the catalyst used, rising the FT operating temperature shifts the spectra to lower carbon number products. Desorption of growing surface species is one of the main chain termination steps and since desorption is an endothermic process higher temperatures should increase the rate of desorption which would then result in a shift to lower molecular mass products. Putting it in another way, thermodynamically the formation of methane is much more favored than the formation of higher molecular mass products at all FT operating temperatures.[31]

- *Pressure and partial pressure of H_2 and CO*

Most studies show that the product selectivity shifts to heavier products and to more oxygenates with increasing total pressure. Increasing H_2/CO ratios in the reactor results in lighter hydrocarbons and a lower olefin content due to the higher hydrogenation character of the syngas mixture.[32]

- *Space velocity*

The decrease of the methane selectivity and the olefin to paraffin ratio with decreasing space velocity was observed by Iglesia *et al.*[33] and Kuipers *et al.*[34] The occurrence of secondary reactions of olefins explains the effect of the space velocity on the selectivity.

The exponential declination of the molar amount of products of individual carbon number fractions in the Fischer-Tropsch Synthesis has been often related to a polymerization reaction that proceeds via stepwise addition of a carbon monomer.[35] Inspired in the polymerization kinetics, several models have been developed for the explanation of the product distributions for this reaction.[36] As a result in which

different contributors participated, the Anderson-Schulz-Flory model describes the molecular weight distribution of radical polymerization products according to the following formula:[37]

$$W_n = n\alpha^{n-1}(1-\alpha)^2 \quad \textbf{(16)}$$

Where Wn is the weight fraction of a hydrocarbon containing n atoms. The quantity α (alpha value), which characterizes the probability of chain growth (Figure 7a), is usually calculated from the slope of a straight line obtained in the Log(Wn/n) vs. Cn (carbon number) (Figure 7b). Although the Schulz-Flory equation adequately describes the molecular weight distribution of C_{5+} hydrocarbons in the majority of cases, deviations are usually observed in the distribution of gaseous products. For instance, Dry reported that mass-transfer limitations will result in an increase of the thermodynamically favored products (e.g., methane) thus resulting in deviations from the predicted by the Schulz–Flory equation. [38] Other deviations from ASF are sometimes assigned to analytical difficulties,[39] non-steady-state conditions of the reactor system[40] and secondary reactions.[34]

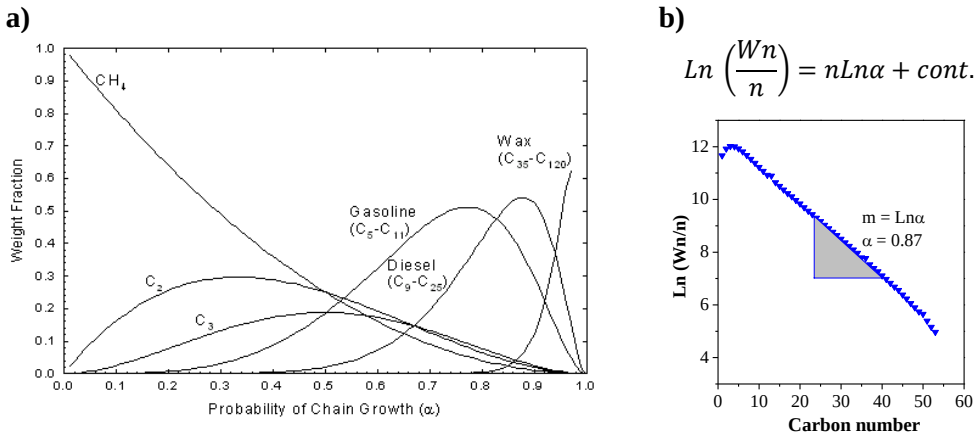

Figure 7. a) Product selectivity as a function of chain growth probability.[41] b) Typical ASF distribution for FT products.[42]

I.2.4. Catalysts for FTS

Although several transition metals are active in FT, only iron, cobalt, nickel and ruthenium have been found to be sufficiently active for application in FT synthesis.[31] The main properties in terms of FT performance, selectivity and price of these metals are displayed in Table 1. While nickel was used in the early German investigations, [1] it produced large amounts of methane at low synthesis pressures while at high pressures, where the methane production was lower, volatile nickel were formed, e.g. nickel carbonyl complexes was lost from the reactors. The high price and low availability of ruthenium rule it out as a viable option. This leaves only cobalt and iron as practical catalysts. The relatively low cost iron catalysts are characterized by their high selectivity to olefins, and appear to be stable when high H_2:CO ratio is used. The main drawback of iron based catalysts is their high WGS activity. As counterpart, cobalt catalysts give the highest yields and longest lifetime and produce predominantly linear alkanes.[17] In addition, they are not inhibited by water, and exhibit low WGS activity, resulting in high productivity at high syngas conversion.[43] Therefore, cobalt catalysts are viable for natural gas based Fischer-Tropsch processes for the production of middle distillates and high-molecular-weight products.[44]

Table 1. Comparison of properties of active metals in FTS.[a]

Metal	Relative price	Products Selectivity
Fe	1	Olefins
Ni	200	Methane
Co	400	Linear alkanes
Ru	25000	Methane at low pressures (P < 100 bar) Wax (high P and low T)[17]

[a] Prices relative to iron ore (November 2014)[45]

I.3. Cobalt based FT catalysts

Industrial cobalt FT catalysts generally require a support.[46] As a result, most of the studies have been dedicated to supported cobalt catalysts, although recently the feasibility to use colloidal cobalt nanoparticles as catalyst in FTS has been proved when they are embedded in a solvent which acts as “phase separator” of

the cobalt active phase.[47] In the next sections some general aspects affecting the catalytic performance of cobalt based FT catalysts will be discussed.

I. 3.1. General aspects of cobalt based catalysts

In the following sections, some general aspects intrinsic of cobalt based catalysts such as the effect of promoters, deactivation pathways, the effect of water and mass transfer limitation will be described.

I.3.1.1 Promoters

A promoter is defined as an additive which enhances the performance of the catalyst through any of the following process:

- Increasing the reducibility of the active phase
- Enhancement of cobalt dispersion
- Inhibition of catalyst deactivation

In the next paragraphs various types of promoters applied in cobalt based FT catalysts will be briefly described.

I.3.1.1.1. Promotion with noble metals

Numerous studies have shown that the introduction of a noble metal (Ru, Rh, Pt, and Pd) has a strong impact on the structure and dispersion of cobalt species, FT reaction rates, and selectivities.[48] The promoting metal is typically introduced via co-impregnation or subsequent impregnation. Introduction of noble metals could result in the following phenomena: much easier reduction of cobalt oxide particles, formation of bimetallic particles and alloys, a lower fraction of barely reducible mixed oxides, enhancement in cobalt dispersion, inhibition of catalyst deactivation, appearance of additional sites of hydrogen activation, and an increase in the intrinsic reactivity of surface sites.[49]

I.3.1.1.2. Promotion with oxides and others

Promotion with oxides has been also used to improve the catalytic performance of FT catalysts.[4] Among the different oxide promoters, ZrO_2, La_2O_3,

MnO, and CeO_2 have been most often employed. Addition of oxide promoters could modify the catalyst texture and porosity, prevent the formation of hardly reducible mixed cobalt oxides, increase the fraction of different cobalt metal crystalline phases, enhance mechanical and attrition resistance of cobalt FT catalysts, and improve the chemical stability of the support. Jacobs *et al.* found that addition of ZrO_2 to silica-supported cobalt catalysts slightly increased cobalt reducibility without effect in the cobalt dispersion. However for Al_2O_3 supported catalysts, the zirconia addition increased the cobalt dispersion and decreased the reducibility of cobalt species.[50] Zhang *et al.* found that the presence of small amounts of Mn improved the dispersion of the cobalt active phase and favored the formation of bridged-type adsorbed CO.[51] A significant promoting effect of Mn was observed on titania-supported catalysts prepared by Morales and Weckhuysen.[52] They reported that the extent of interaction between Mn and the active Co phase as well as the level of Mn dispersion over the TiO_2 surface largely determine the enhancement of the selectivity in the Fischer-Tropsch Synthesis at pressures of 1 bar. According to Figure 8, single cobalt crystallites are formed after the reduction of the cobalt and manganese mixed oxide, and the resulting MnO or Ti_2MnO species may act as spacers of the cobalt crystallites thus improving their dispersion on the support.

Figure 8. Localization of cobalt and manganese species in TiO_2-supported catalysts prepared via deposition-precipitation before and after reduction.[52]

Other oxides have been evaluated as potential promoters of cobalt catalysts in FTS. For instance, Guerrero-Ruiz *et al.* found that cobalt and carbon supported ruthenium catalysts promoted with magnesium, vanadium, and cerium oxides enhanced the specific activity and selectivity for alkenes and long-chain hydrocarbons.[53]

Recently, boron was proposed as a promoter to enhance the stability of nickel catalysts during steam reforming [54] and cobalt catalysts during Fischer-Tropsch Synthesis.[55] For instance, Saeys and co-workers used density functional theory (DFT) to study the effect of boron in a cobalt catalyst. According to this study, boron atoms are thermodynamically stable at step and subsurface sites of a cobalt cluster under FT conditions. The calculations hence suggest that boron promotion can selectively block the deposition, nucleation, and growth of resilient carbon species. To evaluate the theoretical predictions, the authors tested a supported 20 wt % Co catalysts promoted with 0.5 wt % boron under realistic FTS conditions. Boron promotion was found to reduce the deactivation rate 6-fold, without affecting selectivity and activity.

Conversely, other authors reported a negative effect on the catalytic performance of boron doped cobalt catalysts. For instance, for the CO hydrogenation reaction, Jinlin *et al.* reported that the introduction of 0.02-1.5% boron as H_2BO_3 resulted in a decrease of the reducibility and the metal dispersion is a 10 wt% Co/TiO_2 catalyst.[56] As a consequence, the CO conversion and the overall hydrogenation rate decreased by the presence of boron, however addition of small amounts of B (0.1%) resulted in the increase of α, less CH_4 production and the increase in the olefin to paraffin ratio. This last observation could suggest that in FT the detrimental effect of boron is more associated to the presence large excess of B, but in the right amounts it could exert a promotional effect in terms of selectivity.

I.3.1.2. Deactivation of cobalt based catalysts

On most cobalt catalysts, the FT reaction rates slowly evolve with the time on stream. Deactivation of a cobalt catalyst is usually a complex problem where several mechanisms contribute to the loss of activity/selectivity. Some of the main deactivation mechanisms for cobalt based FT catalysts are the following:

- Poisoning: Sulfur and possibly nitrogen contaminants from syngas are reported to affect negatively the catalyst performance. Purification of the feed is thus vital for the process and the levels of sulfur should be kept

below 0.02 mg/m^3. Other species like alkali metals, carbon or metal carbonyls were also hold responsible for catalyst poisoning.[57]

- Sintering: Exothermicity of the reaction makes of the sintering a possible deactivation mechanism. Alumina appears to stabilize cobalt crystallites and make the catalyst more resistant against sintering. In addition, crystallite transformations may increase surface mobility and enhance the possibility of agglomeration.[58]
- Carbon formation: Carbon species accumulates and physically block the surface or even strongly chemisorb on the catalytically active sites.[59]
- Re-oxidation: Corresponds to the irreversible oxidation of small cobalt crystallites (less than 5nm) resulting in the catalyst deactivation. Several studies are proposing water-induced re-oxidation as a deactivation mechanism according to thermodynamic calculations.[60] In contradiction, further reduction during FTS has been proposed as well.[61]
- Metal–support solid state reactions: The formation of hardly reducible cobalt–support species has been claimed by several groups. It was also reported that water may promote this side effect.[62]

Other deactivation mechanisms such as carbidization, surface reconstruction, leaching of active phase and attrition have been proposed for cobalt based FT catalysts.[63]

I.3.1.3. Effect of water on cobalt based catalysts

The effect of water on the performances of various cobalt catalysts for FTS was reviewed by Burtron and co-workers.[64] According to this report, the effect of water on FTS is quite complex and depends on the support and its nature, Co metal loading, its promotion with noble metals, and preparation procedure. Among the reviewed data, the water effect has been reported as either negligible,[65] negative,[66] or positive[65]. For instance, the addition of water revealed a positive effect on unsupported Co_3O_4 catalyst. In general, for silica, water effect is positive in terms of

higher CO conversion [67] whereas for alumina, the effect was negative.[68] Finally, water had exert little or no impact for titania supported catalysts.[69]

The effect of water on supported cobalt catalyst can be viewed as an oxidation process. The extent of oxidation is a function of cobalt crystallite size and the ratio of reactor partial pressures of hydrogen and water (P_{H2O}/P_{H2}). Generally, the negative effect of water is linked to the formation of inactive oxides of cobalt of highly dispersed phases or the formation of irreducible cobalt support compounds[66] resulting also in the sintering of the catalyst.[70]

In contrast, the mechanism responsible for the positive effects of water is reported to facilitate intra-particle transport of syngas and hydrocarbons and affect the kinetics of reaction.[71] For instance, water can lower the barrier of CO dissociation (according to the carbide mechanism, Figure 4) by direct interaction with co-adsorbed CO and inhibits the secondary hydrogenation of olefin products as a result of competitive adsorption of water molecules.

I.3.1.4. Mass transfer limitations

Transport of each species at the interface around the catalyst particle or between gaseous and liquid phases may also limit the activity and selectivity of FT catalysts. Yang and co-workers investigated the mass transfer limitations on fixed-bed for Fischer–Tropsch Synthesis changing synthesis gas superficial velocity, catalyst pellet size, and catalyst amount. They reported that external mass transfer limitation by synthesis gas superficial velocity was important for hydrocarbon chain growth.[72] For the case of the slurry reactors the presence of an additional liquid phase makes the mass transfer phenomena more complex.

For the case of FTS where a bi-component gas mixture is used, the composition of CO and H_2 should not necessarily be proportional in the gas phase and at the metal surface thus resulting in the unbalancing of the H_2:CO which may potentially affect the selectivity in catalysis. The extent to which the performance of a slurry reactor is limited by gas-liquid mass transfer has been subject of discussion. Satterfield and Huff concluded that H_2 mass transfer could definitely limit reactor productivity.[73] Deckwer *et al.* disagreed with this conclusion and showed on the

basis on their own analysis that mass-transfer resistance is small compared to the reaction resistance.[74]

Later, it was established that the significance of mass transfer depends heavily on the bubble size used in the calculation of the interfacial area.[75] Subsequently, T. Bell and co-workers analyzed theoretically the influence of mass transfer on the H_2/CO ratio in the liquid phase of a slurry reactor used for Fischer-Tropsch Synthesis.[76] It was determined that even under circumstances where the gas-liquid mass-transfer resistance is a small fraction of the overall resistance, differences in the solubilities and diffusivities of H_2 and CO can give rise to liquid-phase H_2/CO ratios which differ substantially from that of the gas fed to the reactor. The direction and magnitude of the change in the liquid-phase H_2/CO ratio is dependent on the H_2-CO consumption ratio, the interfacial area for mass transfer from the bubble phase, and the space velocity of the feed gas.

I.3.2. Supported catalysts

The goal of active phase deposition is to spread cobalt onto a support thus providing the precursors of cobalt metal clusters. While unsupported cobalt catalysts have been utilized in a few instances, the activity is generally low and the lifetime short. For this reason nowadays only supported catalysts have found use in commercial operations.[46] In the following paragraphs, some of the main relevant methods of preparation for supported cobalt catalysts will be described and the possible influence of the support in FTS, discussed.

I.3.2.1. Methods for the preparation of supported catalysts

The catalytic performance of FT catalysts usually depends on the preparation method.[4] The preparation of cobalt-supported catalysts involves several important parameters: selection of the appropriate catalyst support, choice of the deposition method of the active phase (and catalyst promoters), and oxidative and reductive treatments.[4] Among the methods reported for cobalt catalysts, some of the most widely used are: impregnation,[77] deposition-precipitation[78] and colloidal-immobilization [79].

- *Impregnation method*

Incipient wetness impregnation is the most common method to prepare cobalt-supported catalysts.[80] Typically, a solution of cobalt salt (cobalt nitrate generally), is added over a dry support, and by capillarity, the cobalt solution is adsorbed inside the pores of the support (Figure 9). Although at first sight, the practical procedure of incipient wetness impregnation is simple, the fundamental phenomena underlying impregnation and drying are extremely complex. Reproducible synthesis of cobalt catalyst requires the careful control of all impregnation parameters: temperature, rate of addition of the impregnating solution, temperature and time of drying, etc.

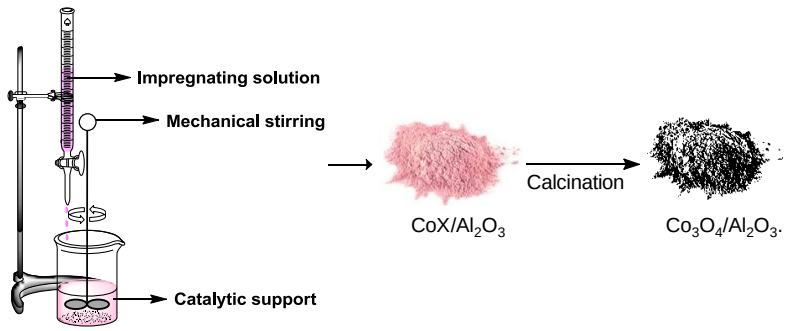

Figure 9. Schematic representation of the preparation of supported cobalt catalyst by impregnation method.[4]

- *Deposition-precipitation method*

Using this technique, a solvated metal precursor is deposited exclusively onto the surface of a suspended support by the slow introduction of a precipitating agent, generally hydroxyl ions (Figure 10). With this method, the nucleation of the metal precursor in the bulk solution is avoided. Concerning the support, a fine and homogeneous phase can be obtained by involving surface OH groups of the support like is the case of silica. During the deposition, adsorption of the metal ions onto the support coincides with nucleation and growth of a surface compound, acting the support as a nucleating agent. Urea is frequently used as the source of hydroxyl ions since its hydrolysis slowly increases the pH of aqueous solutions. De Jong *et al.*,

successfully applied this method in the preparation of highly dispersed Co/SiO_2 catalysts.[78a]

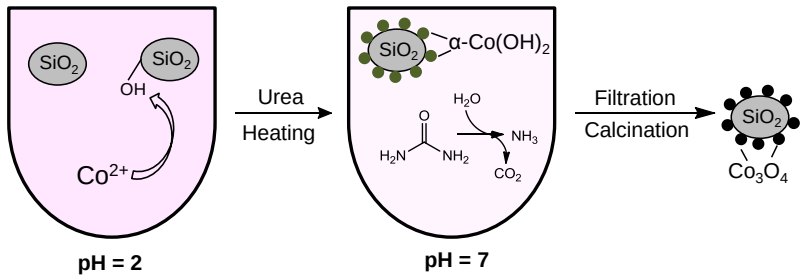

Figure 10. Schematic representation of the preparation of supported cobalt catalyst by deposition-precipitation method

- *Colloidal-immobilization method*

Colloidal synthesis has been widely used as an efficient route to control metal particle size and shape, crystallinity and structure. Metal colloids displayed remarkable catalytic performance in a wide range of reactions.[81] Metal hydroxides are also frequently deposited on solid supports as precursor of the corresponding metals after calcination and reduction processes. The immobilization of colloidal metal nanoparticles or hydroxides exhibits the advantage of the heterogenization of a "semi-homogenous" catalyst still maintaining the well-defined characteristics of the colloidal nanomaterials. This method consists in two basic steps:

1. Preparation of metal or hydroxide NPs.
2. Immobilization of the nanoparticles on the solid support

Various approaches exist for the immobilization of metal or hydroxide colloids depending on the mechanism used to anchor the particles onto the support surface, such as the microemulsion destabilization,[79a-c] direct colloidal deposition and coordination capture method[79d,82].

- *Microemulsion destabilization:* This technique has been widely used for the preparation of cobalt based catalyst for FTS since it enables the control of

metal particle size with a narrow particle size distribution.[79a-c] The method consists of preparing two microemulsions: the first microemulsion contains the cobalt salt encapsulated in droplets, and the second microemulsion includes the reducing agent or base ($NaBH_4$, N_2H_4, NH_3 etc.). Then the two microemulsions are mixed together, resulting in the reduction of the cobalt salt or formation of the hydroxide inside the micelles.[83] Subsequently a selected support is added over the formed NPs and after the addition of a solvent (e.g. acetone) the microemulsion is destabilized thus depositing the metal particles on the support (Figure 11).

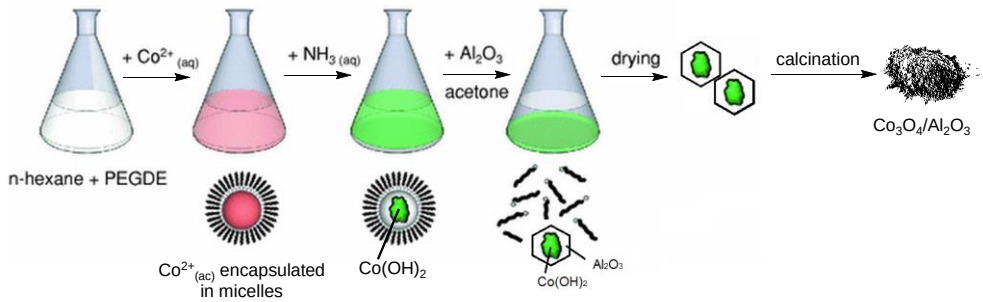

Figure 11. Schematic representation of the preparation of supported cobalt catalyst by microemulsion-destabilization.[84]

Other supports can be used with this methodology. For instance, Prieto reported the preparation of a series of zeolite supported cobalt catalysts (10%Co/ITQ-2) by combining a reverse micellar synthesis with a the ITQ-2 zeolite. The catalysts displayed rather uniform Co particle size distributions in the 5–11 nm range.[79b] More recently, other authors have prepared carbon nanotubes supported CoNPs for FTS using this approach.[79a,79c]

- *Direct colloidal deposition:* This method consist in the direct addition of the solid support on a suspension of cobalt nanoparticles in a poorly dispersing solvent (Figure 12). The lack of interaction between the cobalt nanoparticles and the solvent in conjunction with the thermodynamically favored deposition of the particles on the support by the reduction of the metal

surface area, are the driving forces of this impregnation. Campbell and Sellers reported that when a particle adheres to a support without any change in the particle´s surface area, the system's total energy decreases.[85]

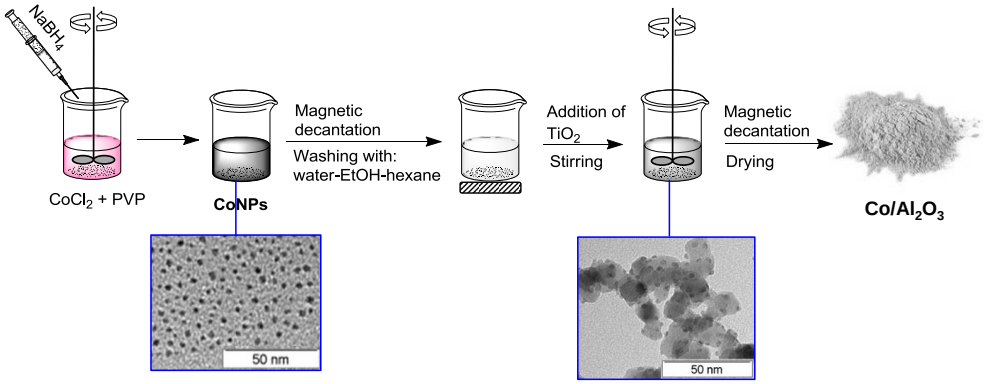

Figure 12. Schematic representation of the preparation of supported cobalt catalysts by colloidal-immobilization method.

- *Coordination capture method*: This method involves the capture of colloidal metal particles onto the surface of functionalized solids by ligand coordination (Figure 13). This method, however, suffers from the need for a series of complicated steps to prepare the functionalized support and has been mainly applied for the anchoring of noble metal nanoparticles such as Pt, Pd, Rh, Ir and Ru on Al_2O_3, MgO and PS.[79d,82]

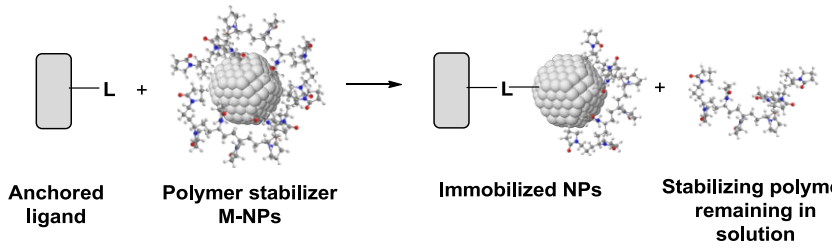

Figure 13. Schematic representation of the preparation of supported cobalt catalyst by coordination capture method.

In a different approach, Wang *et al.* prepared cobalt nanoparticles supported by faujasite zeolites.[86] Cobalt particles of *ca.* 20 nm were obtained after treatment of cobalt exchanged zeolite (Co^{2+}-faujaiste zeolites) with sodium borohydride solution.

Finally, it should be mentioned that other methods of preparation for cobalt catalysts such as co-precipitation method,[87] sol-gel method,[88] egg-shell method,[89] chemical vapor deposition[90] and plasma methods[91] have been reported.

I.3.2.2. Influence of the support on cobalt based catalysts in FTS.

The main role of the catalyst support is to disperse cobalt and produce stable metal particles after reduction. The performance of cobalt based catalysts are largely influenced by the properties of the support (external) and the derived metal/support interactions (internal).[92] Externally, the solid support dissipate the heat released by the FT reaction and thus reduce a temperature gradient in fixed bed reactors.[68b] Also, the texture of the support modifies the diffusion of reagents and products inside the catalyst grains thus affecting the diffusion and capillary condensation of the reaction products in the catalyst pores. Therefore, narrow pores are more likely to be filled by liquid reaction products than wider ones.[4]

Internally, the metal/support interactions can affect the reducibility of the catalyst and the dispersion. The support was also reported to affect the structure and electronic properties of small cobalt metal particles. For instance, Ishihara *et al.* suggested that electron-donor supports could enrich in electron density the cobalt active phase thus resulting in the easy cleavage of the C−O bond of adsorbed carbon monoxide.[93] It is important to consider that depending on the support nature, it could react with cobalt species forming cobalt−support mixed compounds.

A large number of reports have focused on the effect of support in FTS.[85,94] Reuel and Bartholomew studied the catalytic activity of cobalt-based catalysts as a function of support and described the following order: Co/TiO_2 > Co/Al_2O_3 > Co/SiO_2 > 100% Co > Co/MgO.[94g] In contrast, negligible influence of the support on the selectivity to methane and C_{5+} were reported by Iglesia *et al.* at pressures

greater than 5 bar and high conversions. [94d] According to the authors, the slight differences observed in terms of C_{5+} are the reflect of transport-enhanced secondary reactions and not modifications of intrinsic chain growth kinetics due to the differences in dispersion between the different supports.

For silica supported catalysts, it is well known that interaction between support and cobalt is relatively weak. This usually leads to better cobalt reducibility in comparison to Al_2O_3 supports.[88,95] At the same time, cobalt dispersion is much lower in silica-supported catalysts than in alumina-supported ones, as a consequence of the lower interaction between cobalt and support.

Cobalt reducibility is one of the most important problems of alumina-supported cobalt FT catalysts. As counterpart of silica based catalysts, it is well known that cobalt oxide precursors strongly interact with Al_2O_3 support. As a result of this strong interaction, better cobalt dispersions and relatively smaller cobalt crystallites are obtained in alumina supports in comparison to silica.[94c] Nevertheless, chemical reaction of small cobalt particles (<10 nm) with the support may result in diffusion of cobalt active phase into alumina and formation of cobalt aluminate spinels, which are hardly reduced under typical activation procedures.[96]

For TiO_2 supported catalysts, several studies have pointed out the superior catalytic performance of Co/TiO_2 catalyst compared to other oxidic supports.[92,94g] For instance, Ki-Won Jun and co-workers investigated the catalytic performance of $Co/\gamma\text{-}Al_2O_3$, Co/SiO_2 and Co/TiO_2 catalysts in a slurry-phase FTS. They observed that although Co/SiO_2 catalyst exhibited higher CO conversion than the others, the intrinsic activity is much higher on Co/TiO_2. This was explained by the large pore size of this support and the low deactivation of large cobalt particles by re-oxidation mechanism on TiO_2.

A drawback of oxide supports is their reactivity with cobalt, leading the formation of mixed oxides which are not active in FT synthesis. Carbon-based materials are an alternative to overcome these difficulties. Nevertheless, they are less stable than inorganic oxides and can gasify in the presence of hydrogen.[97]

In the last years, carbon nanofibers (CNFs), carbon nanotubes (CNTs)[28,79c,98] and very recently silicon carbide[99] have been tested in FTS.

Recently, Xiog et al studied the effect on FTS of cobalt catalysts supported on different carbon based supports: CNFs, CNTs-inside (cobalt crystallites inside the fibers) and CNTs-outside (cobalt crystallites at the external surface of the fibers). It was observed that the Co/CNT-in exhibited the highest FTS activity. This was ascribed to a higher reducibility and an optimal dispersion for this catalyst, resulting from the interaction between cobalt and surface groups of carbon. The pore-confined Co/CNT-in catalyst was found to reduce easily and showed a higher reducibility in comparison to the Co/CNT-out catalyst. The enhancement in reducibility was ascribed to a pore confinement effect. Simultaneously, Co/CNT-in showed a higher FTS catalytic activity and this is proposed to result from the higher reducibility and dispersion.[100]

In conclusion, the performances of cobalt based catalysts are largely influenced by the support since it can affect the dispersion and reducibility of the active phase as a consequence of the interactions between cobalt and the support.

I.3.3. Unsupported catalysts: cobalt nanocatalysts

Nowadays, nanoscience affords accurate control of size, shape and structure of materials at the nanometric scale.[101] The ability to tune nanoparticles and compare series of materials prepared in a like manner provides a valuable way to get information about how catalytic systems work at a molecular and atomic level.[102] Nano-materials based catalysts have already afforded a number of insights into the fundamental chemistry that underlies the Fischer-Tropsch process.[13a] Specifically, they have been used to show the importance of the cobalt particle size owing to the difficulty of reducing very small nanoparticles;[103] the importance of oxide pore size in controlling growth and diffusion[95b] and the likely role of hydrogen spill-over in the precious metal promotion that is widely used in commercial catalysts.[104]

I.3.3.1. Synthetic methods for the preparation of CoNPs

The methods used for the synthesis of M-NPs are commonly classified as “top-down” and “bottom-up” approaches.[81] The top-down approach is subject to drastic limitations for dimensions smaller than 100 nm. This size restriction and the

high cost of this approach make the bottom-up approach the most promising strategy. The bottom-up approach consists in the synthesis of M-NPs starting from metallic molecules by "stabilization procedures".[105] In the line of the bottom-up approach, three main methodologies have been used for the synthesis of cobalt nanoparticles: chemical reduction, thermal decomposition and the organometallic approach.

- *Chemical reduction*

This synthetic method is the most commonly used and consists in the direct reduction of a cobalt salt using a suitable reducing agent in a solvated media (Figure 14).[81] Due to the relatively negative reduction potential of cobalt(II) (E_0=-0.28 V), the use of strong reducing agents such as sodium borohydride, basic hydrazine, strong hydrides such as $Li(C_2H_5)_3BH$ or boiling alcohols are generally required to obtain the reduced metal colloid. Recently the use of a "noble metal-assisted" methodology allowed the synthesis of bimetallic Co-Pt NPs by simultaneous H_2 reduction of $Co(acac)_2$ and K_2PtCl_4 in water under mild conditions.[47c]

This methodology has the advantage of the generally easy implementation and the compatibility with a large variety of solvents and stabilizing agents. The disadvantage could rely on the involvement of "spectator-compounds" such as counterions which could coordinate the metal surface thus affecting the catalytic properties of the NPs.

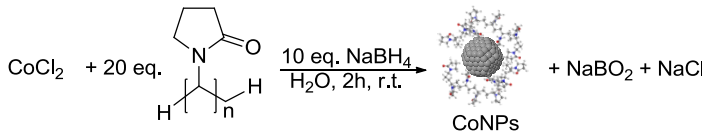

Figure 14. Synthesis of CoNPs by chemical reduction of cobalt chloride using $NaBH_4$.

- *Thermal decomposition*

Several cobalt complexes (generally carbonyl based) in solution can be thermally decomposed to their respective zerovalent element (Figure 15). The coalescence of single cobalt atoms will end in the formation of metal clusters. The

size and shape of the resulted cobalt cluster has been demonstrated to be a function of the stabilizer and the synthesis conditions (temperature, solvent, cobalt concentration, etc.).[47a,106] The main advantages of this method is that gram scale production of NPs can be achieved and the absence of additional compounds for the synthesis.

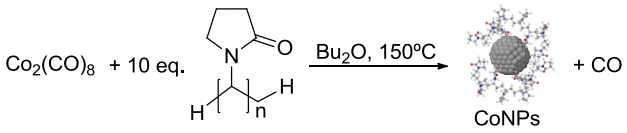

Figure 15. Synthesis of CoNPs by thermal decomposition of $Co_2(CO)_8$.

- *Organometallic approach*

The organometallic approach to synthesize CoNPs through ligand displacement was developed by Chaudret and co-workers.[107] Organometallic precursors can be decomposed by ligand displacement using H_2 as a reducing gas. For instance, $[Co(\eta^3\text{-}C_8H_{13})(\eta^4\text{-}C_8H_{12})]$,[108] and $Co[N(SiMe_3)_2]_2$[109] complexes have been successfully utilized for the synthesis of CoNPs by H_2 reduction via hydrogenolysis (Figure 16). The advantage of this methodology is the possibility to obtain CoNPs with clean surfaces by decomposition of organometallic precursors, usually low valence state organometallic complexes, under mild conditions. The disadvantage is the high cost and difficult synthesis of the metallic precursor and organic ligands.

There exist other methodologies of synthesis of CoNPs such as microwave irradiation, photocatalytic decomposition among others.[110]

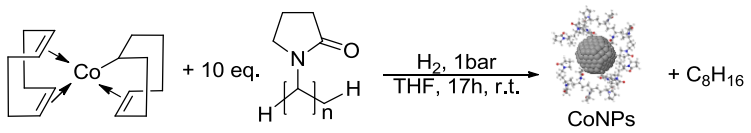

Figure 16. Synthesis of CoNPs through the organometallic approach by hydrogenolysis of $[Co(\eta^3\text{-}C_8H_{13})(\eta^4\text{-}C_8H_{12})]$.

I.3.3.2. Stabilizers used for the synthesis of CoNPs

Generally, M-NPs are unstable with respect to agglomeration towards the bulk since at short interparticle distances and in the absence of any repulsive effect, the van der Waals forces will attract two M-NPs to each other favoring their agglomeration.[111] Hence, it is necessary to use stabilizing agents to provide stable M-NPs in solution. Nanoparticles stabilization is usually discussed in terms of two general categories: (i) steric stabilization and (ii) electrostatic stabilization.

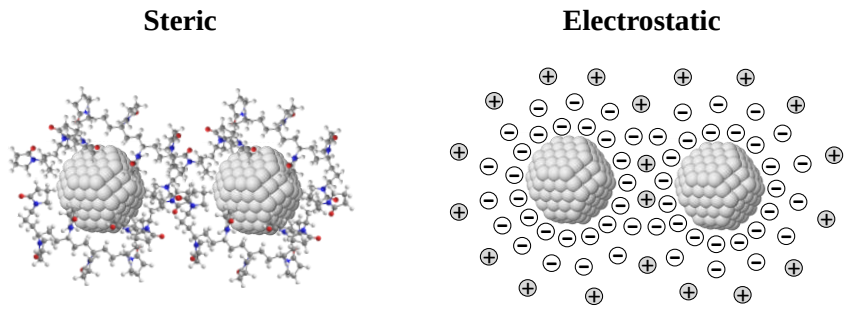

Figure 17. Stabilization strategies of nanoparticles through: (a) steric repulsion and (b) electrostatic repulsion.[112]

In the case of steric stabilization, organic molecules which present coordinating groups in its molecular structure can prevent M-NPs aggregation by providing a protective layer.[81] In contrast with the electrostatic stabilization, which is mainly used in aqueous media, the steric stabilization can be used in organic or in aqueous phase.

Electrostatic stabilization of M-NPs can be performed by ionic compounds such as halides, carboxylates, or polyoxoanions, in solution (generally aqueous).[113] The presence of these compounds and their related counter-ions surrounding the metallic surface will generate an electrical double-layer around the M-NPs which results in a Coulombic repulsion between the M-NPs. If the electric potential associated with the double layer is high enough, then the electrostatic repulsion will prevent particle aggregation. Finally, the electrostatic and steric stabilization can be combined to maintain M-NPs stable in solution. This type of stabilization is

generally provided by ionic surfactants, which contain a polar group able to generate an electronic double layer and a lipophilic side chain able to provide steric repulsion.[81]

According to the respective stabilization category three main groups of stabilizing agents have been applied for the synthesis of CoNPs: polymers, ionic liquids and surfactants:[114]

- *Polymers*

The stabilization of CoNPs by polymers, and in particular polyvinylpyrrolidone (PVP), has been largely described since this stabilizing agent is non-toxic and soluble in many polar solvents.[115] Some structures of polymers used as stabilizing agents in the synthesis of CoNPs are displayed in Figure 18.

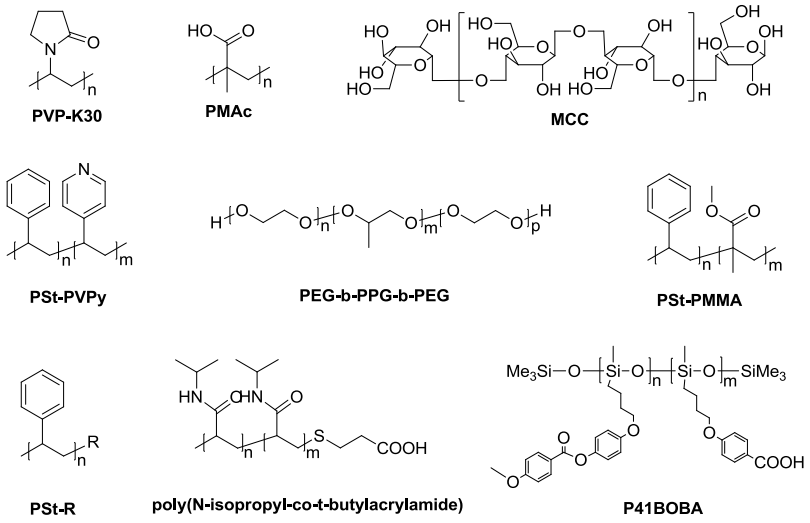

Figure 18. Polymers used as stabilizing agents in the synthesis of CoNPs.[114]

Metin *et al.* reported the synthesis of CoNPs of 7.2 ± 2.1 nm stabilized by PVP K-30 by $NaBH_4$ reduction of $CoCl_2.6H_2O$ in methanol solution.[116] Kou and co-workers reported the synthesis of water-soluble Co-NPs (*ca.* 3-5 nm) stabilized by PVPK-30 using $Co(OAc)_2$ as cobalt precursor, $NaBH_4$ as reducing agent in water,[47c,117] or polyethyleneglycol (PEG200)[118] as solvent. The same author also prepared CoNPs of *ca.*15-30 nm by thermal decomposition of $Co_2(CO)_8$ using a

modified C_8-PVP as stabilizer in toluene or squalane.[47d] The synthesis of CoNPs of 5.3‑6.3 nm stabilized by microcrystalline cellulose (MCC) matrix was carried out by reduction of $Co(AcO)_2$ and $CoSO_4$ using NaH_2PO_2 as reducing agents.[119] Co-NPs were also synthesized by thermal decomposition of $Co_2(CO)_8$ in the presence of end-functional polystyrene bearing either amine (PSt-NH_2), carboxylic acids (PSt-COOH) or phosphine oxide (PSt-Dioctylphosphine oxide, DOPO) ligating moieties.[120] The resulting PSt-CoNPs displayed a wide range of mean diameters (between 18 and 43 nm) and showed organization of dipolar colloids into extended nanoparticle chains. The formation CoNPs of 13 nm stabilized by block copolymer poly-(ethylene glycol)-block-poly(propylene glycol)-block-poly-(ethylene glycol) (PEG-b-PPG-b-PEG), a biocompatible amphiphilic polymer, was carried out by solvothermal treatment of ethylene glycol solution of $CoCl_2$.[121] These Co-NPs could be dispersed in polar and nonpolar solvents. Chaudret and co-workers reported the synthesis of Co-NPs by decomposition of $[Co(C_8H_{13})(C_8H_{12})]$ under 3 bar H_2 at 60 ºC. They obtained CoNPs of 1.5‑2.0 nm and 4.0 nm using as stabilizers PVP K-30 and poly(2,6-dimethyl-1,4-phenyleneoxide) (PPO), respectively.[108]

- *Ionic liquids*

Dupont and co-workers have reported the synthesis of CoNPs by thermal decomposition of $Co_2(CO)_8$ dissolved in different imidazolium cations (1-*n*-butyl-3-methylimidazolium [BMI], 1-*n*-decyl-3-methylimidazolium [DMI]) and anions (hexafluorophosphate [PF_6], *N*-bis(trifluoromethanesulfonyl)-imidate [NTf_2], tetrafluoroborate [BF_4] and trifluoro-tris-(pentafluoroethane) phosphate [FAP]) as stabilizing agents (Figure 19).[47a,106b] The authors observed that using [DMI][NTf_2] as stabilizing agent, CoNPs with a binomial size distribution were formed (79 $\pm$ 17 nm and 11$\pm$3 nm, respectively).[47a] Using [DMI][FAP], CoNPs of 53$\pm$ 22 nm were obtained after 5 min and longer reaction times (*ca.* 300 min) produced CoNPs of 5.5 $\pm$ 1.1 nm. Interestingly, smaller CoNPs with irregular shape were obtained using [DMI][BF_4] and [BMI] based ILs associated with NTf_2, FAP, and BF_4 ions.[106b]

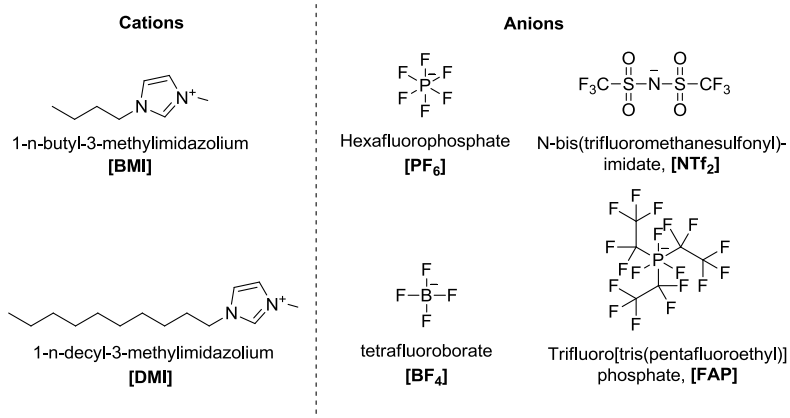

Figure 19. Structures of ions from ionic liquids used in the synthesis of CoNPs.

Very recently the same author reported the synthesis of bimetallic Co/Pt-NPs of 4.4±1.9 nm by reaction of $Co(Cp)_2$ and $Pd_2(dba)_3$ complexes in $[BMI][PF_6]$ at 150 °C under hydrogen (10 bar) for 24 h. They proposed that these bimetallic NPs displayed a core–shell like structures in which mainly Pt composes the external shell and its concentration decreases in the inner-shells ($CoPt_3$@Pt-like structure).[47b] Other authors such as Vollmer et al synthesized CoNPs of 5.1, 8.1 and 14 nm by decomposition of the $Co_2(CO)_8$ in presence of $[BMI][BF_4]$ using microwave irradiation, photocatalytic treatment and thermal treatment at 100 ºC respectively.[110]

- *Surfactants*

Water soluble CoNPs of 4 and 7.5-9.0 nm were synthesized by $NaBH_4$ reduction of $CoCl_2$ at room temperature in presence of the surfactants, di-dodecyl-di-methylammonium bromide (DDAB)[122] and of dodecyl-*N*,*N*-di-methyl-3-ammonio-1-propanesulfonate (SB12).[123] CoNPs of 6.4 nm with a polydispersity of 21% were formed by $NaBH_4$ reduction at room temperature of $[Co(OAT)_2]$ (OAT = (2-ethylhexyl)sulfosuccinate). The sodium (2-ehtylhexyl)sulfosuccinate formed during the reaction is a surfactant that acts as stabilizing agent.[124] The structures of surfactants used in the synthesis of CoNPs are displayed in Figure 20.

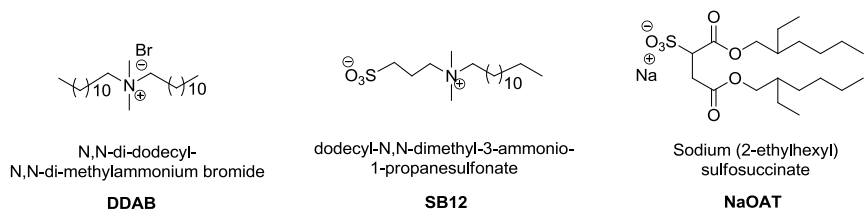

N,N-di-dodecyl-N,N-di-methylammonium bromide
DDAB

dodecyl-N,N-dimethyl-3-ammonio-1-propanesulfonate
SB12

Sodium (2-ethylhexyl) sulfosuccinate
NaOAT

Figure 20. Surfactants used as stabilizing agents in the synthesis of Co-NPs.[114]

I.3.3.3. FTS catalyzed by colloidal NPs

Currently, the control of the selectivity is one of the main goals in FT investigation.[125] In this context, the use of unsupported nanoparticles is of high interest as they mimic metal surface activation and catalysis at the nanoscale, and can shed some light on the role of the support during catalysis.[126]

I.3.3.3.1. FTS catalyzed by colloidal CoNPs

Up to date, the research in the field of FTS catalysed by colloidal CoNPs has been mostly developed in the groups of Kou and Dupont.[47b,47c,127] The first study concerning the application of colloidal CoNPs in the FTS was reported by Kou and co-workers and dealt about the one-pot synthesis of 2-alkyl dioxolanes under FT conditions.[117] According to this report, colloidal NPs of Ru, Fe, Ni, and Co resulted active in the production of a mixture of 2-alkyl-dioxolanes and hydrocarbons when FTS was carried out using ethylenglycol as solvent. From these metals, RuNPs resulted to be the most active and selective catalyst towards the oxygenated products (1.5 $mol_{CO}mol_{Ru}^{-1}h^{-1}$ and 67 wt% oxy-sel.). Although the CoNPs were less active than Ru, higher hydrocarbon selectivities were obtained for the former metal (0.07 $mol_{CO}mol_{Co}^{-1}h^{-1}$ and 69 wt% HC-sel.). Figure 21 summarises the methodology of synthesis of the Co and RuNPs and their corresponding product selectivities observed in catalysis.

Insights into the mechanistic aspect of the reaction were obtained by means of experiments consisting in the addition of aldehydes or alkenes to the reaction media. With these experiments it was proposed that the hydroformylation of the olefin with syngas could be involved in the production of dioxolanes. In relation to

this finding, the same author previously demonstrated the hydroformylation of 1-hexene catalyzed by cobalt nanoparticles also synthesized by a similar synthetic route.[128]

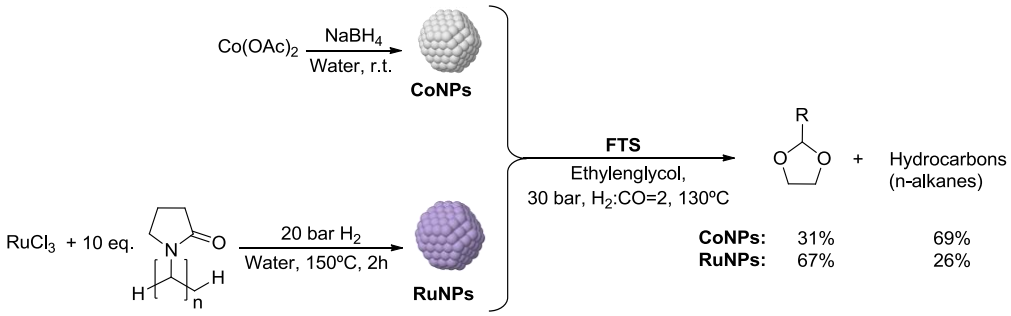

Figure 21. Preparation of Co and RuNPs for the synthesis of 2-alyl dioxolanes and hydrocarbons from ethylenglycol and syngas.

In a posterior study, Kou reported an activity of 0.12 $mol_{CO}mol_{Co}^{-1}h^{-1}$ at 170ºC in the aqueous phase Fischer-Tropsch Synthesis (AFTS) using CoNPs synthesized by the same chemical reduction using sodium borohydride in water.[118] In this case, PVP-K30 was used as stabilizer during the synthesis of the CoNPs, however no additional information regarding size of the NPs nor the product selectivity in catalysis was given. Recently, Kou and co-workers reported the use of cobalt/platinum alloy nanoparticles stabilized by PVP as catalysts of the AFTS (Figure 22).[47c]

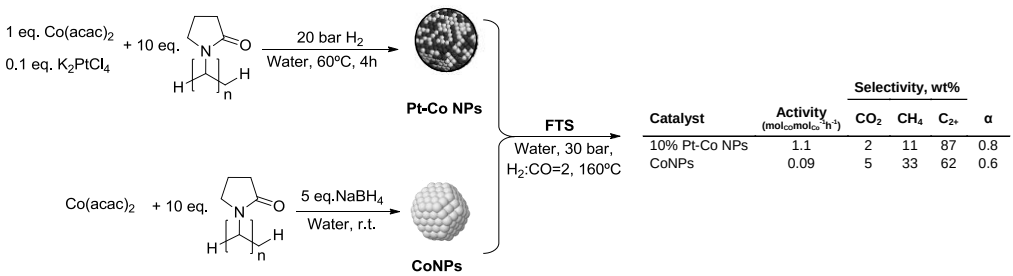

Figure 22. Synthesis of bimetallic Pt-Co and monometallic CoNPs and their catalytic performances in the AFTS.

According to this report, TOF up to 1.1 $mol_{CO}mol_{Co}^{-1}h^{-1}$ with a growth factor (α) of 0.8 was obtained at 160ºC, in contrast to the lower values observed for the monometallic NPs (0.09 and 0.6 respectively). Based on DFT calculations, the authors proposed that the outstanding activity in the former case was rationalized by the formation of stained Co layers on Pt or Pt-Co alloy NPs. As a result, these structures would improve the overall energetics and kinetics by forming favourable transition states (TSs) due to the lattice expansion of the supported Co layers.

More recently, Wang and Kou, tested in the AFTS Co nanoparticles prepared by chemical reduction of cobalt salts using two different reducing agents, $LiBEt_3H$ and $NaBH_4$ (Figure 23).[129] In fact both NPs were completely different from the synthetic point of view since not only different reducing agents but also different stabilizing agents and solvents where used for the synthesis ($NaBH_4$/PVP/water vs. $LiBEt_3H$/THF/SB3-12). Better catalytic performances in terms of activity and selectivity were obtained for the NPs synthesized with $LiBEt_3H$ (0.27 vs. 0.1 $mol_{CO}mol_{Co}^{-1}h^{-1}$). Analysis of the fresh and used catalysts by XRD, TEM and ICP demonstrated relevant differences in size, structure and composition of the initial catalyst, suggesting the reconstruction of the NPs during the reaction.

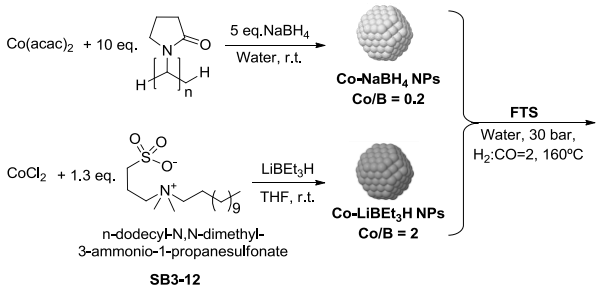

Catalyst	Activity ($mol_{CO}mol_{Co}^{-1}h^{-1}$)	Selectivity, wt% CO_2	CH_4	C_{2+}	α
Co-$NaBH_4$	0.10	7	40	53	0.6
Co-$LiBEt_3H$	0.27	8	29	63	0.7

Figure 23. Synthesis of CoNPs using $NaBH_4$ or $LiBEt_3H$ as reducing agent, and their catalytic performances in the AFTS.

The differences in activity were interpreted in terms of the B-doping occurred during the synthesis of the NPs, which is intrinsic to the use of boron based reducing agents. According to the authors, the higher activity observed for Co-$LiBEt_3H$ catalyst resulted from the lower boron content (Co/B atom ratio, 2 vs. 0.2)

considering that the presence of boron reduces the activity and reducibility of the catalyst.

The application of other colloidal Co nanocatalysts in FTS have been reported in non aqueous solvents such as ionic liquids,[47a,47b,106b] squalane,[47d] and polyethyleneglycol,[118] nevertheless in most the cases, low activity and/or agglomeration issues were described.

Dupont and co-workers have reported the synthesis of cobalt nanocubes and nanospheres by thermal decomposition of $Co_2(CO)_8$ in ionic liquids and evaluated their catalytic activity in FTS. The size, shape and structure of the nanomaterials varied as a function of the ionic liquid used for the synthesis of the catalysts; cobalt nanocubes (54 ± 22 nm, Co ε-phase) or nanospheres (7.7 ± 1.2, Co-fcc) were obtained when [DMI][NTf_2][47a] or [BMI][NTf_2][106b] were used as solvent respectively. In catalysis, a higuer TOF was observed with the spheric CoNPs in comparison to the nanocubes (0.26 vs. $1.17x10^{-5}$ $mol_{CO}mol_{Suf\text{-}Co}^{-1}h^{-1}$).

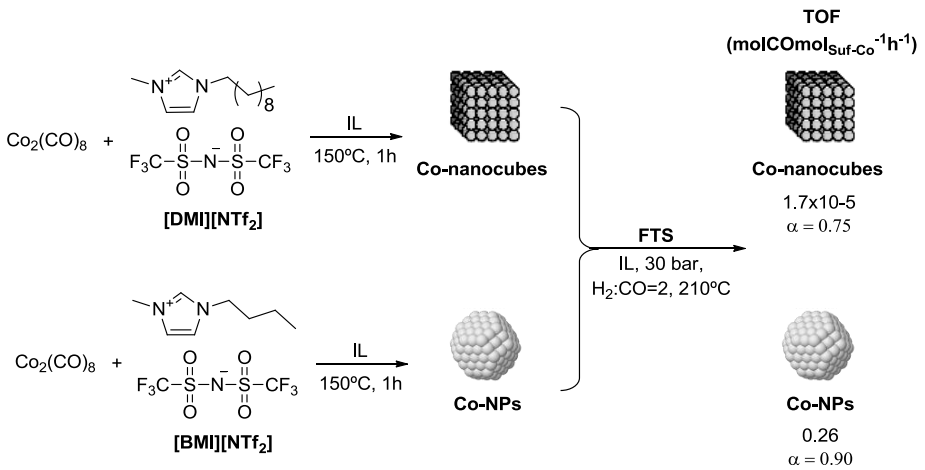

Figure 24. Synthesis of cobalt nanocubes and NPs by thermal decomposition of $Co_2(CO)_8$ in IL and, and their catalytic performances in the AFTS.

Interestingly, the hydrocarbons formed in the FTS using cobalt nanocubes prepared in [DMI][NTf_2] showed a monomodal hydrocarbon distribution centered at C12, which is quite different from the bimodal distribution (centered at C12 and

C21) obtained with cobalt nanoparticles prepared in [BMI][NTf_2]. The authors speculated that these differences were related not only to the different particle-size distribution, but also to the presence of different active sites, that is, the Co-fcc phase in [BMI][NTf_2] and ε-phase in [DMI][NTf_2]. A summary up to date of reports concerning colloidal cobalt nanoparticles applied in the FTS is displayed in Table 2.

Table 2. Catalytic activity and/or surface-specific activity (TOF) of colloidal Co nanocatalysts reported in literature for the liquid phase FT synthesis.

Catalyst synthesis	Size/shape of CoNPs	FT conditions	Activity ($mol_{CO}mol_{Co}^{-1}h^{-1}$)	α	Ref.
a) $CoCl_2$, SB3-12, $LiBEt_3H$, THF, rt. b) $Co(OAc)_2$, PVP, $NaBH_4$, water, rt.	a) 8.3 ± 2.0 b) 14 ± 6 nm	30 bar ($CO:H_2$:Ar = 32:64:4), 24-48h, water, **130-170 ºC**	a) 0.27 b) 0.10 at 170ºC	0.70-0.62	[129]
$Co(acac)_2 2H_2O$, 0.1 K_2PtCl_4 , PVP, H_2, water, 60ºC, 4h	2.9-3.5 nm	30 bar (H_2:CO, 2:1), 12-36h, water PVP sln (PVP:Co, 5:1), **130-170 ºC**	(1.1 at 160 ºC, TOF)	0.8	[47c]
$Co(OAc)_2$, PVP, $NaBH_4$, water, rt.	5 nm	30 bar (H_2:CO, 2:1), 12-36h, water PVP sln (PVP:Co, 5:1), **130-170 ºC**	0.08 (130 ºC) 0.09 (150 ºC) 0.12 (170 ºC)		[118]
$Co(OAc)_2$, PVP, $NaBH_4$, PEG 200, rt.		30 bar (H_2:CO, 2:1), 12-36h, PEG 200, **150 ºC**	0.030		[118]
$Co(OAc)_2$, PVP, $NaBH_4$, water, rt.		45 bar (H_2:CO, 2:1), 6-12h, ethyleneglycol, **130 ºC**	0.070		[117]
$Co_2(CO)_8$, C_8-PVP, toluene, 110ºC.		30 bar (H_2:CO, 2:.1), 12-36h, squalane, **150-200 ºC**	0.2 (150 ºC) 0.7 (185 ºC) 1.3 (200 ºC)		[47d]
$Co(Cp)_2$, $Pd_2(dba)_3$, H_2, heating, [BMI][PF_6]					[47b]
$Co_2(CO)_8$, [DMI][NTf_2], 150ºC, 1h.	53 ±22 nm, nanocubes (Co-ε phase)	20 bar (H_2:CO, 2:.1), [DMI][NTf_2], 20h, **210 ºC**	($1.17x10^{-5}$, TOF)	0.75	[47a]
$Co_2(CO)_8$, [BMI][NTf_2], 150ºC, 1h.	7.7 ± 1.2 nm, spherical (Co-fcc)	20 bar (H_2:CO, 2:.1), [BMI][NTf_2], 20h, **210 ºC**	0.021	0.90	[106b]

Very recently, Dupont and co-workers reported the synthesis of bimetallic Co/Pt NPs in [BMI][PF_6] and its application in the FTS.[47b] The nanoparticles were synthesized by an organometallic approach using [bis(cylopentadienyl)cobalt(II)] and [tris(dibenzylideneacetone) bisplatinum(0)] as metal precursors and hydrogen as reducing agent. The authors proposed for these bimetallic NPs a core–shell like structure in which mainly Pt composes the external shell and its concentration decreases in the inner shells ($CoPt_3$@Pt-like structure). The isolated bimetallic NPs resulted active catalysts for the Fischer–Tropsch Synthesis, with selectivity for naphtha products.

The synthesis of CoNPs by thermal decomposition of $Co_2(CO)_8$ was also reported by Kou and co-workers but using a modified lipophilic C_8-PVP stabilizing agent and squalane as solvent.[47d] The resulting CoNPs showed a size of 3.54 ± 1.63 nm and a FT activity of 0.022 $mol_{CO}mol_{Co}^{-1}h^{-1}$.

I.3.3.3.2. FTS catalyzed by colloidal Ru and FeNPs

- *RuNPs*

The first report of the aqueous phase FT synthesis (AFTS) concerned the use of PVP stabilized ruthenium NPs as catalysts.[130] RuNPs were synthesized in water by hydrogenation of $RuCl_3$ in presence of PVP-K30 as stabilizing agent. The particle size of the RuNPs was modulated between 1.6 and 4.5 nm through the seeded growth method, and the series tested in the AFTS (Figure 25). Surprisingly, the Ru nanocatalysts with 2.0 nm diameter exhibited the highest activity of the series; however, no explanation of this unusual behaviour was given. The structure sensitivity of PVP stabilized RuNPs in the AFTS has been also reported by Claver[127] and Hensen.[131]

In more recent publications, several parameters such as the nature of the reducing agent, the PVP:Ru molar ratio, the effect of ionic additives,[132] the temperature,[133] and the effect of the stabilizer[134] have been studied for the ruthenium catalytic system. Concerning the reducing agent, more active RuNPs were obtained when H_2 was used in comparison with those prepared using $NaBH_4$. It

was proposed that cleaner surfaces free of ions or deposits (which could potentially block active sites) are obtained with the former methodology.[132]

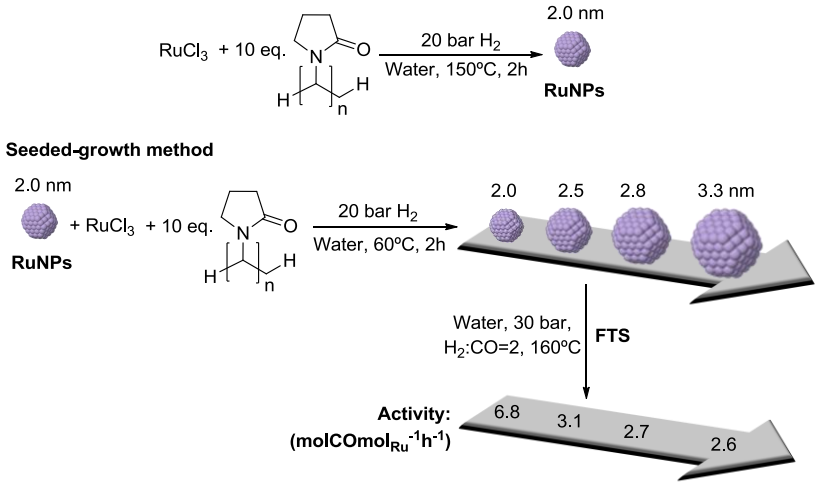

Figure 25. Synthesis of variable size RuNPs through the seeded growth method, and their catalytic performances in the AFTS.

Hensen and co-workers studied the effect of the reaction temperature on the selectivity in the AFTS catalyzed by RuNPs. According to this report, an unprecedented oxygenate selectivity was observed at low temperature (up to 70% at 125ºC).[133b] The authors proposed that at these temperatures, the termination through the CO insertion FT mechanism (See section I.2.2.) becomes important due to the higher CO coverage (favored also at low temperatures), thus resulting in a higher oxygenate selectivity, particularly aldehydes. Burtron and co-workers recently corroborated these observations obtaining high oxygenate selectivity in the AFTS catalyzed by RuNPs when operated at low temperature.[135]

The nature of the polymeric stabilizers also influences the catalytic behavior of NPs during the AFTS. Recently, the catalytic performance in the AFTS of lignin stabilized RuNPs was investigated in our group.[127] It was observed that PVP stabilized RuNPs were more active and selective towards hydrocarbons compared to those stabilized by lignins, indicating that the nature of the stabilizing polymer does

affect the catalytic performance in AFTS and strongly influenced the production of CO_2 by WGS reaction.

Hensen and co-workers tested RuNPs (supported on carbon nanotubes) stabilized with trimethyl(tetradecyl)ammonium bromide (TTAB), polyvinylpyrrolidone (PVP), and sodium 3-mercapto-1-propanesulfonate (SMPS) in the AFTS (Figure 13). The activity in the FT reaction increased in the order: Ru-SMPS≪Ru-PVP<Ru-TTAB<Ru.[134] It was proposed that the activity in catalysis was inversely proportional to the interaction strength between the metal surface and the ligand. Therefore, a stabilizing agent with an excessive affinity to the metal surface could block active sites thus reducing the catalyst activity.

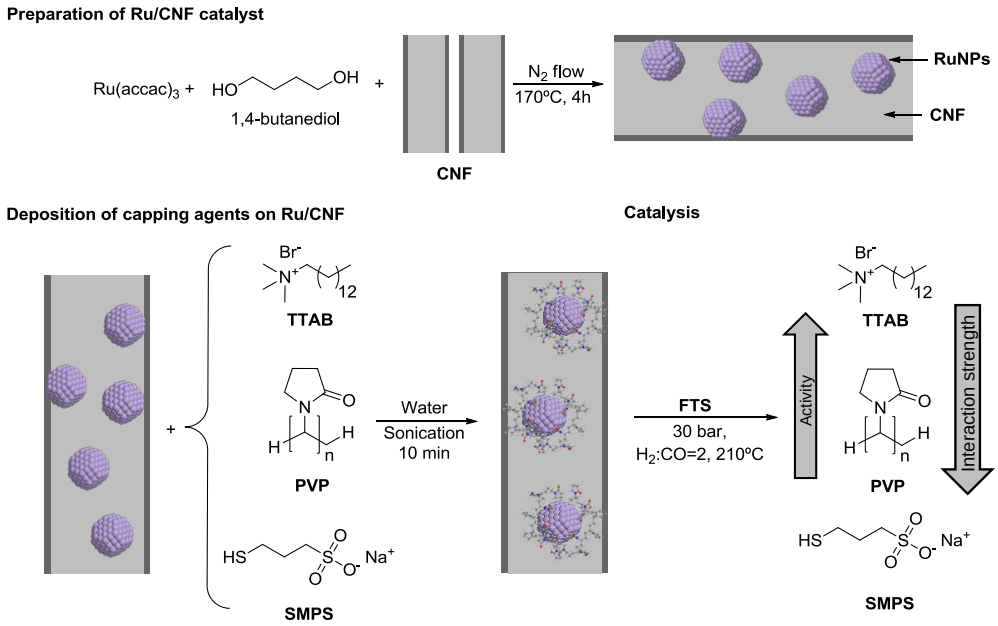

Figure 26. Synthesis of Ru/CNF catalyst with deposited stabilizing agents, and their catalytic performances in the AFTS.

- *FeNPs*

Although iron is much cheaper and environmentally friendly than ruthenium and cobalt, FeNPs are not stable in water.[136] In addition, considering that under typical FT conditions, iron is transformed into iron carbide, oxidation of this carbide

by water to form Fe_3O_4 may occur at low water partial pressures.[18] Under these considerations, solvents with the proper reduction ability to stabilize metallic state of iron nanoparticles (or iron carbide) have been applied such as ethylenglycol[117] and polyethylenglycol.[118] Kou and co-workers reported the use of FeNPs dispersed in polyethylene glycol (PEG200) in the Fischer-Tropsch Synthesis under mild conditions (150 °C, 2.0 MPa H_2, 1.0 MPa CO) with an activity as high as 1.5 $mol_{CO}mol_{Fe}^{-1}h^{-1}$. The hydrocarbon products were insoluble in PEG, making them easily separable from the reaction mixture as depicted in Figure 27.

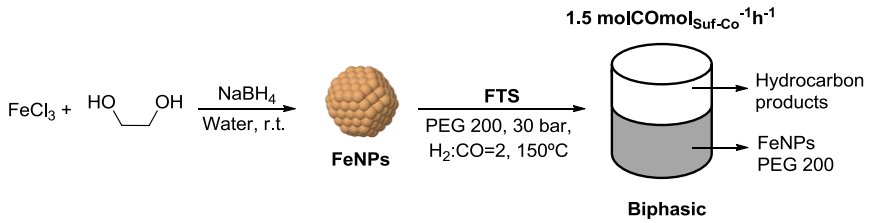

Figure 27. Synthesis of FeNPs in ethylene glycol, and their catalytic performances in the FTS in PEG 200.

In a previous report, the same author also used iron nanoparticle for the one-step synthesis of 2-alkyl-dioxolanes from ethylene glycol and syngas.[117] The catalyst exhibited high activity and selectivity towards dioxolanes (0.58 $mol_{CO}mol_{Fe}^{-1}h^{-1}$ and 68 wt% sel.).

In this context the work described in the following chapters deals with the study of cobalt nanoparticles prepared by colloidal methods as nanocatalysts of the Fischer-Tropsch Synthesis. We investigated the correlation between the size, structure, and composition of the CoNPs with the observed performance in catalysis.

I.4. References

[1] Stranges, A. N. In *Stud. Surf. Sci. Catal.*; Davis, B. H., Occelli, M. L., Eds.; Elsevier: 2007; Vol. 163, p 1-27.
[2] Casci, J. L.; Lok, C. M.; Shannon, M. D. *Catal. Today* **2009**, *145*, 38-44.
[3] Stranges, A. N. *Energia* **2001**, *12*, 1-2.
[4] Khodakov, A. Y.; Chu, W.; Fongarland, P. *Chem. Rev.* **2007**, *107*, 1692-1744.
[5] Davis, B. H. *Catal. Today* **2002**, *71*, 249-300.

[6] Fischer, F.; Tropsch, H. *Brennstoff-Chem* **1923**, *4*, 276.
[7] Stranges, A. N. *Ann. Sci.* **1997**, *54*, 29-68.
[8] Dry, M. E. *Endeavour* **1984**, *8*, 2-4.
[9] Stranges, A. N. *J. Chem. Educ.* **1983**, *60*, 617.
[10] Jahangiri, H.; Bennett, J.; Mahjoubi, P.; Wilson, K.; Gu, S. *Catal. Sci. Technol.* **2014**, *4*, 2210-2229.
[11] Dry, M. E. *Catal. Today* **2002**, *71*, 227-241.
[12] Rapier, R.; http://robertrapier.wordpress.com/2008/05/03/visit-to-new-choren-btl-plant-3/, Ed. 2008.
[13] (a) Zhang, Q.; Deng, W.; Wang, Y. *J. Eng. Chem.* **2013**, *22*, 27-38.(b) Zhang, Q.; Kang, J.; Wang, Y. *ChemCatChem* **2010**, *2*, 1030-1058.
[14] Claeys, M.; van Steen, E. In *Stud. Surf. Sci. Catal.*; André, S., Mark, D., Eds.; Elsevier: 2004; Vol. 152, p 601-680.
[15] Reuel, R. C.; Bartholomew, C. H. *J. Catal.* **1984**, *85*, 63-77.
[16] Maitlis, P. M. In *Greener Fischer-Tropsch Processes for Fuels and Feedstocks*; Wiley-VCH Verlag GmbH & Co. KGaA: 2013, p 237-265.
[17] Van Der Laan; and, G. P.; Beenackers, A. A. C. M. *Catal. Rev.* **1999**, *41*, 255-318.
[18] van Steen, E.; Claeys, M. *Chem. Eng. Technol.* **2008**, *31*, 655-666.
[19] Lahtinen, J.; Vaari, J.; Kauraala, K.; Soares, E. A.; Van Hove, M. A. *Surf. Sci.* **2000**, *448*, 269-278.
[20] Kaminsky, M. P.; Winograd, N.; Geoffroy, G. L.; Vannice, M. A. *J. Am. Chem. Soc.* **1986**, *108*, 1315-1316.
[21] Erley, W.; McBreen, P. H.; Ibach, H. *J. Catal.* **1983**, *84*, 229-234.
[22] Zheng, C.; Apeloig, Y.; Hoffmann, R. *J. Am. Chem. Soc.* **1988**, *110*, 749-774.
[23] van Barneveld, W. A. A.; Ponec, V. *J. Catal.* **1984**, *88*, 382-387.
[24] van Santen, R. A.; Markvoort, A. J.; Filot, I. A. W.; Ghouri, M. M.; Hensen, E. J. M. *Phys. Chem. Chem. Phys.* **2013**, *15*, 17038-17063.
[25] Pichler, H.; Schulz, H. *Chem. Ing. Tech.* **1970**, *42*, 1162-1174.
[26] Daudel, R.; Pullman, A.; Salem, L.; Veillard, A. *Quantum Theory of Chemical Reactions: Vol. III: Chemisorption, Catalysis, Biochemical Reactions*; Springer, 1982.
[27] (a) Das, T. K.; Zhan, X.; Li, J.; Jacobs, G.; Dry, M. E.; Davis, B. H. In *Stud. Surf. Sci. Catal.*; Davis, B. H., Occelli, M. L., Eds.; Elsevier: 2007; Vol. 163, p 289-314.(b) Lapidus, A. L. *Solid Fuel Chem.* **2013**, *47*, 315-328.
[28] Bezemer, G. L.; Bitter, J. H.; Kuipers, H. P. C. E.; Oosterbeek, H.; Holewijn, J. E.; Xu, X.; Kapteijn, F.; van Dillen, A. J.; de Jong, K. P. *J. Am. Chem. Soc.* **2006**, *128*, 3956-3964.
[29] Todic, B.; Ma, W.; Jacobs, G.; Davis, B. H.; Bukur, D. B. *Catal. Today* **2014**, *228*, 32-39.
[30] Wojciechowski, B. W. *Catal. Rev.* **1988**, *30*, 629-702.
[31] Dry, M. E. In *Stud. Surf. Sci. Catal.*; André, S., Mark, D., Eds.; Elsevier: 2004; Vol. 152, p 196-257.
[32] Donnelly, T. J.; Satterfield, C. N. *App. Catal.* **1989**, *52*, 93-114.
[33] Iglesia, E.; Reyes, S. C.; Madon, R. J. *J. Catal.* **1991**, *129*, 238-256.
[34] Kuipers, E. W.; Scheper, C.; Wilson, J. H.; Vinkenburg, I. H.; Oosterbeek, H. *J. Catal.* **1996**, *158*, 288-300.
[35] Herrington, E. F. G. *Chem. Ind.* **1946**, *65*, 346.
[36] (a) Friedel, R. A.; Anderson, R. B. *J. Am. Chem. Soc.* **1950**, *72*, 2307-2307.(b) Henrici-Olivé, G.; Olivé, S. *Angew. Chem. Int. Ed.* **1976**, *15*, 136-141.(c) Krylova, A. Y. *Solid Fuel Chemistry* **2014**, *48*, 22-35.
[37] Sachtler, W. M. H.; Ichikawa, M. *J. Phys. Chem.* **1986**, *90*, 4752-4758.

[38] Dry, M. E. *J. Mol. Catal.* **1982**, *17*, 133-144.
[39] Puskas, I.; Hurlbut, R. S.; Pauls, R. E. *J. Catal.* **1993**, *139*, 591-601.
[40] Huff, G. A.; Satterfield, C. N. *Ind. Eng. Chem. Process Des. Dev.* **1985**, *24*, 986-995.
[41] Spath, P. L.; Dayton, D. C. *Preliminary screening-technicaland economic assessment of synthesis gas to fuels and chemicals with emphasis on the potential for biomas-dervied syngas*, National Renewable Energy Laboratory, 2003.
[42] Lee, S.; Speight, J. G.; Loyalka, S. K. *Handbook of Alternative Fuel Technologies*; Taylor & Francis, 2007.
[43] Rofer-DePoorter, C. K. *Chem. Rev.* **1981**, *81*, 447-474.
[44] Sie, S. T.; Senden, M. M. G.; Van Wechem, H. M. H. *Catal. Today* **1991**, *8*, 371-394.
[45] Infomine; http://www.infomine.com/investment/metal-prices/, Ed. 2014.
[46] Davis, B. H. In *Greener Fischer-Tropsch Processes for Fuels and Feedstocks*; Wiley-VCH Verlag GmbH & Co. KGaA: 2013, p 193-207.
[47] (a) Scariot, M.; Silva, D. O.; Scholten, J. D.; Machado, G.; Teixeira, S. R.; Novak, M. A.; Ebeling, G.; Dupont, J. *Angew. Chem. Int. Ed.* **2008**, *47*, 9075-9078.(b) Silva, D. O.; Luza, L.; Gual, A.; Baptista, D. L.; Bernardi, F.; Zapata, M. J. M.; Morais, J.; Dupont, J. *Nanoscale* **2014**, *6*, 9085-9092.(c) Wang, H.; Zhou, W.; Liu, J.-X.; Si, R.; Sun, G.; Zhong, M.-Q.; Su, H.-Y.; Zhao, H.-B.; Rodriguez, J. A.; Pennycook, S. J.; Idrobo, J.-C.; Li, W.-X.; Kou, Y.; Ma, D. *J. Am. Chem. Soc.* **2013**, *135*, 4149-4158.(d) Yan, N.; Zhang, J.-g.; Tong, Y.; Yao, S.; Xiao, C.; Li, Z.; Kou, Y. *Chem. Commun.* **2009**, 4423-4425.
[48] Jacobs, G.; Ma, W.; Davis, B. *Catalysts* **2014**, *4*, 49-76.
[49] Khodakov, A. Y.; Chu, W.; Fongarland, P. *Chem. Rev.* **2007**, *107*, 1692-1744.
[50] Jacobs, G.; Das, T. K.; Zhang, Y.; Li, J.; Racoillet, G.; Davis, B. H. *App. Catal. A-Gen* **2002**, *233*, 263-281.
[51] Zhang, J.-L.; Ren, J.; Chen, J.-G.; Sun, Y.-H. *Acta Phys.-Chim. Sin.* **2002**, *18*, 260.
[52] Morales, F.; Grandjean, D.; de Groot, F. M. F.; Stephan, O.; Weckhuysen, B. M. *Phys. Chem. Chem. Phys.* **2005**, *7*, 568-572.
[53] Guerrero-Ruiz, A.; Sepu´lveda-Escribano, A.; Rodri´guez-Ramos, I. *Appl. Catal. A-Gen* **1994**, *120*, 71-83.
[54] (a) Xu, J.; Chen, L.; Tan, K. F.; Borgna, A.; Saeys, M. *J. Catal.* **2009**, *261*, 158-165.(b) Xu, J.; Saeys, M. *J. Catal.* **2006**, *242*, 217-226.
[55] (a) Saeys, M.; Tan, K. F.; Chang, J.; Borgna, A. *Ind. Eng. Chem. Res.* **2010**, *49*, 11098-11100.(b) Tan, K. F.; Chang, J.; Borgna, A.; Saeys, M. *J. Catal.* **2011**, *280*, 50-59.
[56] Li, J.; Coville, N. J. *App. Catal. A-Gen* **1999**, *181*, 201-208.
[57] Madikizela-Mnqanqeni, N. N.; Coville, N. J. *App. Catal. A-Gen* **2008**, *340*, 7-15.
[58] Saib, A. M.; Moodley, D. J.; Ciobîcă, I. M.; Hauman, M. M.; Sigwebela, B. H.; Weststrate, C. J.; Niemantsverdriet, J. W.; van de Loosdrecht, J. *Catal. Today* **2010**, *154*, 271-282.
[59] Moodley, D. J.; van de Loosdrecht, J.; Saib, A. M.; Overett, M. J.; Datye, A. K.; Niemantsverdriet, J. W. *App. Catal. A-Gen* **2009**, *354*, 102-110.
[60] (a) Jacobs, G.; Zhang, Y.; Das, T. K.; Li, J.; Patterson, P. M.; Davis, B. H. In *Stud. Surf. Sci. Catal.*; J.J. Spivey, G. W. R., Davis, B. H., Eds.; Elsevier: 2001; Vol. 139, p 415-422.(b) van Steen, E.; Claeys, M.; Dry, M. E.; van de Loosdrecht, J.; Viljoen, E. L.; Visagie, J. L. *J. Phys. Chem. B* **2005**, *109*, 3575-3577.
[61] Rønning, M.; Tsakoumis, N. E.; Voronov, A.; Johnsen, R. E.; Norby, P.; van Beek, W.; Borg, Ø.; Rytter, E.; Holmen, A. *Catal. Today* **2010**, *155*, 289-295.

[62] Tavasoli, A.; Malek Abbaslou, R. M.; Dalai, A. K. *App. Catal. A-Gen* **2008**, *346*, 58-64.
[63] Tsakoumis, N. E.; Rønning, M.; Borg, Ø.; Rytter, E.; Holmen, A. *Catal. Today* **2010**, *154*, 162-182.
[64] Dalai, A. K.; Davis, B. H. *Appl. Catal. A-Gen.* **2008**, *348*, 1-15.
[65] Huber, G. W.; Guymon, C. G.; Conrad, T. L.; Stephenson, B. C.; Bartholomew, C. H. In *Stud. Surf. Sci. Catal.*; J.J. Spivey, G. W. R., Davis, B. H., Eds.; Elsevier: 2001; Vol. 139, p 423-430.
[66] van de Loosdrecht, J.; Balzhinimaev, B.; Dalmon, J. A.; Niemantsverdriet, J. W.; Tsybulya, S. V.; Saib, A. M.; van Berge, P. J.; Visagie, J. L. *Catal. Today* **2007**, *123*, 293-302.
[67] (a) Das, T. K.; Conner, W. A.; Li, J.; Jacobs, G.; Dry, M. E.; Davis, B. H. *Energ. Fuels* **2005**, *19*, 1430-1439.(b) Li, J.; Jacobs, G.; Das, T.; Zhang, Y.; Davis, B. *App. Catal. A-Gen* **2002**, *236*, 67-76.
[68] (a) Li, J.; Zhan, X.; Zhang, Y.; Jacobs, G.; Das, T.; Davis, B. H. *App. Catal. A-Gen* **2002**, *228*, 203-212.(b) Storsæter, S.; Borg, Ø.; Blekkan, E. A.; Tøtdal, B.; Holmen, A. *Catal. Today* **2005**, *100*, 343-347.
[69] Storsæter, S.; Borg, Ø.; Blekkan, E. A.; Holmen, A. *J. Catal.* **2005**, *231*, 405-419.
[70] Sadeqzadeh, M.; Chambrey, S.; Piché, S.; Fongarland, P.; Luck, F.; Curulla-Ferré, D.; Schweich, D.; Bousquet, J.; Khodakov, A. Y. *Catal. Today* **2013**, *215*, 52-59.
[71] Iglesia, E. *App. Catal. A-Gen* **1997**, *161*, 59-78.
[72] Yang, J. H.; Kim, H.-J.; Chun, D. H.; Lee, H.-T.; Hong, J.-C.; Jung, H.; Yang, J.-I. *Fuel Process. Technol.* **2010**, *91*, 285-289.
[73] Satterfield, C. N.; Huff Jr, G. A. *Chem. Eng. Sci.* **1980**, *35*, 195-202.
[74] Deckwer, W. D.; Serpemen, Y.; Ralek, M.; Schmidt, B. *Chem. Eng. Sci.* **1981**, *36*, 773-774.
[75] Quicker, G.; Deckwer, W. D. *Chem. Eng. Sci.* **1981**, *36*, 1577-1579.
[76] Stern, D.; T. Bell, A.; Heinemann, H. *Chem. Eng. Sci.* **1983**, *38*, 597-605.
[77] (a) Zhang, J.; Chen, J.; Ren, J.; Sun, Y. *App. Catal. A-Gen* **2003**, *243*, 121-133.(b) Zhang, Y.; Hanayama, K.; Tsubaki, N. *Catal. Commun.* **2006**, *7*, 251-254.
[78] (a) de Jong, K. P. In *Stud. Surf. Sci. Catal.*; G. Poncelet, P. A. J. P. G., Delmon, B., Eds.; Elsevier: 1991; Vol. 63, p 19-36.(b) Lok, C. M. In *Stud. Surf. Sci. Catal.*; Xinhe, B., Yide, X., Eds.; Elsevier: 2004; Vol. 147, p 283-288.
[79] (a) Nakhaei Pour, A.; Housaindokht, M. *Catal. Lett.* **2013**, *143*, 1328-1338.(b) Prieto, G.; Martínez, A.; Concepción, P.; Moreno-Tost, R. *J. Catal.* **2009**, *266*, 129-144.(c) Trépanier, M.; Dalai, A. K.; Abatzoglou, N. *App. Catal. A-Gen* **2010**, *374*, 79-86.(d) Wang, Y.; Liu, H.; Jiang, Y. *J. Chem. Soc., Chem. Commun.* **1989**, 1878-1879.
[80] Dry, M. E. In *Stud. Surf. Sci. Catal.*; André, S., Mark, D., Eds.; Elsevier: 2004; Vol. 152, p 533-600.
[81] Roucoux, A.; Schulz, J.; Patin, H. *Chem. Rev.* **2002**, *102*, 3757-3778.
[82] Yu, W.; Liu, M.; Liu, H.; An, X.; Liu, Z.; Ma, X. *J. Mol. Catal. A: Chem.* **1999**, *142*, 201-211.
[83] Fletcher, P. D. I.; Howe, A. M.; Robinson, B. H. *J. Chem. Soc., Faraday Trans. 1* **1987**, *83*, 985-1006.
[84] Fischer, N.; Minnermann, M.; Baeumer, M.; van Steen, E.; Claeys, M. *Catal. Lett.* **2012**, *142*, 830-837.
[85] Campbell, C. T.; Sellers, J. R. V. *Faraday Discuss.* **2013**, *162*, 9-30.
[86] Wang, Y.; Wu, H.; Zhang, Q.; Tang, Q. *Micropor. Mesopor. Mat.* **2005**, *86*, 38-49.
[87] Khassin, A. A.; Yurieva, T. M.; Kaichev, V. V.; Bukhtiyarov, V. I.; Budneva, A. A.; Paukshtis, E. A.; Parmon, V. N. *J. Mol. Catal. A: Chem.* **2001**, *175*, 189-204.

[88] Okabe, K.; Li, X.; Wei, M.; Arakawa, H. *Catal. Today* **2004**, *89*, 431-438.
[89] Iglesia, E.; Soled, S. L.; Baumgartner, J. E.; Reyes, S. C. *J. Catal.* **1995**, *153*, 108-122.
[90] Suvanto, s.; Pakkanen, T. A. *J. Mol. Catal. A: Chem.* **1997**, *125*, 91-96.
[91] Zhang, Y.; Chu, W.; Cao, W.; Luo, C.; Wen, X.; Zhou, K. *Plasma Chem. Plasma Process.* **2000**, *20*, 137-144.
[92] Oh, J.-H.; Bae, J.; Park, S.-J.; Khanna, P. K.; Jun, K.-W. *Catal. Lett.* **2009**, *130*, 403-409.
[93] Ishihara, T.; Eguchi, K.; Arai, H. *J. Mol. Catal.* **1992**, *72*, 253-261.
[94] (a) Bae, J. W.; Kim, S.-M.; Kang, S.-H.; Chary, K. V. R.; Lee, Y.-J.; Kim, H.-J.; Jun, K.-W. *J. Mol. Catal. A: Chem.* **2009**, *311*, 7-16.(b) Borg, Ø.; Dietzel, P. D. C.; Spjelkavik, A. I.; Tveten, E. Z.; Walmsley, J. C.; Diplas, S.; Eri, S.; Holmen, A.; Rytter, E. *J. Catal.* **2008**, *259*, 161-164.(c) Borg, Ø.; Eri, S.; Blekkan, E. A.; Storsæter, S.; Wigum, H.; Rytter, E.; Holmen, A. *J. Catal.* **2007**, *248*, 89-100.(d) Iglesia, E.; Soled, S. L.; Fiato, R. A. *J. Catal.* **1992**, *137*, 212-224.(e) Jacobs, G.; Das, T. K.; Li, J.; Luo, M.; Patterson, P. M.; Davis, B. H. In *Stud. Surf. Sci. Catal.*; Davis, B. H., Occelli, M. L., Eds.; Elsevier: 2007; Vol. 163, p 217-253.(f) Ma, W.; Jacobs, G.; Sparks, D. E.; Gnanamani, M. K.; Pendyala, V. R. R.; Yen, C. H.; Klettlinger, J. L. S.; Tomsik, T. M.; Davis, B. H. *Fuel* **2011**, *90*, 756-765.(g) Reuel, R. C.; Bartholomew, C. H. *J. Catal.* **1984**, *85*, 78-88.
[95] (a) Girardon, J.-S.; Lermontov, A. S.; Gengembre, L.; Chernavskii, P. A.; Griboval-Constant, A.; Khodakov, A. Y. *J. Catal.* **2005**, *230*, 339-352.(b) Khodakov, A. Y.; Bechara, R.; Griboval-Constant, A. *App. Catal. A-Gen* **2003**, *254*, 273-288.
[96] Chin, R. L.; Hercules, D. M. *J. Phys. Chem.* **1982**, *86*, 360-367.
[97] Moreno-Castilla, C.; Carrasco-Marin, F. *J. Chem. Soc., Faraday Trans.* **1995**, *91*, 3519-3524.
[98] Bezemer, G. L.; Radstake, P. B.; Koot, V.; van Dillen, A. J.; Geus, J. W.; de Jong, K. P. *J. Catal.* **2006**, *237*, 291-302.
[99] Liu, Y.; Ersen, O.; Meny, C.; Luck, F.; Pham-Huu, C. *ChemSusChem* **2014**, *7*, 1218-1239.
[100] Xiong, H.; Motchelaho, M. A. M.; Moyo, M.; Jewell, L. L.; Coville, N. J. *Catal. Today* **2013**, *214*, 50-60.
[101] Odom, T. W.; Pileni, M.-P. *Acc. Chem. Res.* **2008**, *41*, 1565-1565.
[102] Beaumont, S. K. *Phys. Chem. Chem. Phys.* **2014**, *16*, 5034-5043.
[103] den Breejen, J. P.; Radstake, P. B.; Bezemer, G. L.; Bitter, J. H.; Frøseth, V.; Holmen, A.; Jong, K. P. d. *J. Am. Chem. Soc.* **2009**, *131*, 7197-7203.
[104] Shannon, M. D.; Lok, C. M.; Casci, J. L. *J. Catal.* **2007**, *249*, 41-51.
[105] Balzani, V. *Small* **2005**, *1*, 278-283.
[106] (a) Puntes, V. F.; Zanchet, D.; Erdonmez, C. K.; Alivisatos, A. P. *J. Am. Chem. Soc.* **2002**, *124*, 12874-12880.(b) Silva, D. O.; Scholten, J. D.; Gelesky, M. A.; Teixeira, S. R.; Dos Santos, A. C. B.; Souza-Aguiar, E. F.; Dupont, J. *ChemSusChem* **2008**, *1*, 291-294.
[107] Chaudret, B.; Philippot, K. *Oil Gas Sci. Technol.* **2007**, *62*, 799-817.
[108] Osuna, J.; de Caro, D.; Amiens, C.; Chaudret, B.; Snoeck, E.; Respaud, M.; Broto, J.-M.; Fert, A. *J. Phys. Chem.* **1996**, *100*, 14571-14574.
[109] Zadoina, L.; Soulantica, K.; Ferrere, S.; Lonetti, B.; Respaud, M.; Mingotaud, A. F.; Falqui, A.; Genovese, A.; Chaudret, B.; Mauzac, M. *J. Mater. Chem.* **2011**, *21*, 6988-6994.
[110] Vollmer, C.; Redel, E.; Abu-Shandi, K.; Thomann, R.; Manyar, H.; Hardacre, C.; Janiak, C. *Chem-Eur. J* **2010**, *16*, 3849-3858.

[111] Gates, B. D.; Xu, Q.; Stewart, M.; Ryan, D.; Willson, C. G.; Whitesides, G. M. *Chem. Rev.* **2005**, *105*, 1171-1196.
[112] Aguey-Zinsou, K.-F.; Ares-Fernandez, J.-R. *Energy Environ. Sci.* **2010**, *3*, 526-543.
[113] Aiken Iii, J. D.; Finke, R. G. *J. Mol. Catal. A: Chem.* **1999**, *145*, 1-44.
[114] Gual, A.; Godard, C.; Castillón, S.; Curulla-Ferré, D.; Claver, C. *Catal. Today* **2012**, *183*, 154-171.
[115] He, B.; Ha, Y.; Liu, H.; Wang, K.; Liew, K. Y. *J. Colloid Interface Sci.* **2007**, *308*, 105-111.
[116] Metin, Ö.; Özkar, S. *Energ. Fuels* **2009**, *23*, 3517-3526.
[117] Fan, X.-B.; Yan, N.; Tao, Z.-Y.; Evans, D.; Xiao, C.-X.; Kou, Y. *ChemSusChem* **2009**, *2*, 941-943.
[118] Fan, X.-B.; Tao, Z.-Y.; Xiao, C.-X.; Liu, F.; Kou, Y. *Green Chem.* **2010**, *12*, 795-797.
[119] Pirkkalainen, K.; Leppänen, K.; Vainio, U.; Webb, M. A.; Elbra, T.; Kohout, T.; Nykänen, A.; Ruokolainen, J.; Kotelnikova, N.; Serimaa, R. *Eur. Phys. J. D.* **2008**, *49*, 333-342.
[120] Bull, M. M.; Chung, W. J.; Anderson, S. R.; Kim, S.-j.; Shim, I.-B.; Paik, H.-j.; Pyun, J. *J. Mater. Chem.* **2010**, *20*, 6023-6025.
[121] Qiao, R.; Zhang, X. L.; Qiu, R.; Li, Y.; Kang, Y. S. *J. Phys Chem. C.* **2007**, *111*, 2426-2429.
[122] Ago, H.; Komatsu, T.; Ohshima, S.; Kuriki, Y.; Yumura, M. *Appl. Phys. Lett.* **2000**, *77*, 79-81.
[123] Subramanian, N. D.; Balaji, G.; Kumar, C. S. S. R.; Spivey, J. J. *Catal. Today* **2009**, *147*, 100-106.
[124] Petit, C.; Taleb, A.; Pileni, M.-P. *Adv. Mater.* **1998**, *10*, 259-261.
[125] Sousa-Aguiar, E. F.; Noronha, F. B.; Faro, J. A. *Catal. Sci. Technol.* **2011**, *1*, 698-713.
[126] Astruc, D.; Lu, F.; Aranzaes, J. R. *Angew. Chem. Int. Ed.* **2005**, *44*, 7852-7872.
[127] Gual, A.; Delgado, J. A.; Godard, C.; Castillón, S.; Curulla-Ferré, D.; Claver, C. *Top. Catal.* **2013**, *56*, 1208-1219.
[128] Cai, Z.; Wang, H.; Xiao, C.; Zhong, M.; Ma, D.; Kou, Y. *J. Mol. Catal. A: Chem.* **2010**, *330*, 94-98.
[129] Wang, H.; Kou, Y. *Chin. J. Catal.* **2013**, *34*, 1914-1925.
[130] Xiao, C.-x.; Cai, Z.-p.; Wang, T.; Kou, Y.; Yan, N. *Angew. Chem. Int. Ed.* **2008**, *47*, 746-749.
[131] Quek, X.-Y.; Pestman, R.; van Santen, R. A.; Hensen, E. J. M. *Catal. Sci. Technol.* **2014**.
[132] (a) Liu, L.; Sun, G.; Wang, C.; Yang, J.; Xiao, C.; Wang, H.; Ma, D.; Kou, Y. *Catal. Today* **2012**, *183*, 136-142.(b) Wang, C.; Zhao, H.; Wang, H.; Liu, L.; Xiao, C.; Ma, D. *Catal. Today* **2012**, *183*, 143-153.
[133] (a) Pendyala, V.; Jacobs, G.; Luo, M.; Davis, B. *Catal. Lett.* **2013**, *143*, 395-400.(b) Quek, X.-Y.; Guan , Y.; van Santen, R. A.; Hensen, E. J. M. *ChemCatChem* **2011**, *3*, 1735-1738.
[134] Quek, X.-Y.; Pestman, R.; van Santen, R. A.; Hensen, E. J. M. *ChemCatChem* **2013**, *5*, 3148-3155.
[135] Pendyala, V.; Shafer, W.; Davis, B. *Catal. Lett.* **2013**, *143*, 895-901.
[136] Chen, W.; Fan, Z.; Pan, X.; Bao, X. *J. Am. Chem. Soc.* **2008**, *130*, 9414-9419.

CHAPTER II

Objectives

The aim of this thesis is to study the catalytic performance of cobalt nanoparticles prepared by colloidal methods in the Fischer-Tropsch Synthesis. The principal objective is to gain understanding on the effect of catalyst modification and reaction conditions in order to design more efficient cobalt FT catalysts. The effect of the NPs size, solvent and stabilizing polymer, were particularly looked at.

The specific objectives classified by chapters can be summarized as follows:

Chapter IV.

- Evaluation of the catalytic performance of in-situ prepared NPs and isolated NPs in the aqueous phase Fischer-Tropsch Synthesis (AFTS).
- Study of the pH effect of the aqueous media in the activity and selectivity of the CoNPs.

Chapter V.

- Evaluation of the effect of the addition of co-solvents such as hydrocarbons and alcohols in the AFTS catalyzed by colloidal cobalt nanoparticles.
- Study the effect of the composition of heptane/water mixtures used as solvent in the AFTS.
- Optimization of the hydrocarbon co-solvent in the AFTS from a series of linear alkanes.
- Evaluation of the FTS using linear alcohols as reaction solvent.
- Study the effect of the composition of ethanol/water mixtures used as solvent in the AFTS.

Chapter VI.

- Study of particle size effects in the Fischer-Tropsch Synthesis catalyzed by cobalt nanoparticles.
- Comparison between colloidal and supported catalysts to elucidate the possible influence of the support on catalysis.

Chapter VII.

- Study of the effect of the polymeric stabilizer on the catalytic performance of cobalt nanoparticles in the FTS.
- Comparison between the colloidal and supported catalysts to elucidate the possible influence of the stabilizing polymer in both catalysis systems and the possible interaction with the support.

CHAPTER III

Experimental Set-up and Chromatographic Analysis

Table of Contents

III.1. Experimental set-up for catalytic tests using unsupported, colloidal catalysts

III.1.1. Description of the Stirred Tank Reactor (STR)

The experimental set-up used for the Fischer-Tropsch catalytic experiments using unsupported colloidal nanoparticles as catalysts is schematized in Figure 1.

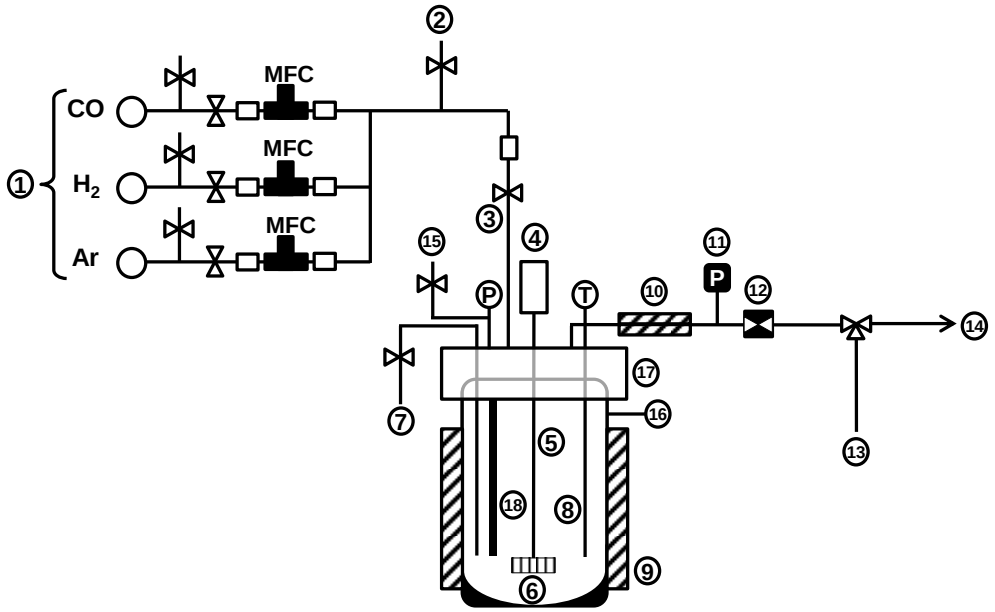

Figure 1. Schematic representation of the experimental set-up. (1) CO, H_2 and Ar mass flow controllers;(2) Independent gas supply; (3) Gas entry; (4) Stirrer; (5) Shaft; (6) Impeller; (7) Liquid sampler; (8) Thermocouple; (9) Heater; (10) Thermostated line; (11) Pressure transducer; (12) Electronic pressure valve; (13) Line to GC; (14) Vent; (15) Evacuation valve; (16) Autoclave´s vessel; (17) Autoclave´s head; (18) Baffle bar.

As displayed in Figure 1, the set-up includes a 100 ml stirred tank reactor (STR, EZE Seal 100ML, Autoclave Engineers) connected online to a GC-TCD/MSD (Agilent 7890 MSD 5975). The autoclave was supplied by H_2 (99.999 %), CO (99.997 %) and Ar (99.999 %) by using mass flow controllers (1) (MFCs: Bronkhorst F-201CV) connected independently to the corresponding bottle. Argon was used for the autoclave's purge cycles. An additional gas supply (2) was located

between the mass flow controllers (MFCs) and the reactor vessel, for the cases when independent gas supply were necessary (gas blending of stock gas mixture, gas solubility measurements, etc). The gases entered to the autoclave through (3). The stirring system was comprised by a Magnedrive® (MAG075) (4) which allowed the stirring control from 0-1300 rpm, a shaft (5) and impeller (6) provided with the Dispersimax™ technology. According to the specifications, this system allowed the gas to be drawn down the superior hollow shaft (Figure 2b) and promote a positive flow through the hole in the impeller for dispersion, thus offering an effect of re-circulating the gas again down the shaft. A liquid sampler (7) was also available. The temperature was controlled within the autoclave by communication of the internal thermocouple (type K) (8) and the external heater (9). To avoid condensation of reaction products during experiments, the tubing that connected the autoclave to the pressure valve was thermostated to the reaction temperature (10) using a wire resistance. During the catalytic experiments the pressure was maintained to the set value through a micrometric electronic pressure valve (12) communicated to a pressure transducer (11). The autoclave was connected online to a GC through (13) for gas analysis, but normally during reactions the overpressure inside the autoclave was released through (14) for extraction in the fumehood. Finally, the autoclave contained an evacuation valve (15) directly attached to the reactor vessel which allows the manual release of gases.

All the connections of this set-up used stainless steel tubing of 1/8 o.d. The MFCs, the stirring and pressure systems as well as the temperature system were controlled by three analogous control units commercialized by PID Eng&Tech. These units were also connected to a PC through an Ethernet cable and were managed from the control software, Process@ (PID Eng&Tech, Iberfluid). This software allowed the continuous acquisition of the different reaction parameters (temperature, pressure, stirring rate, MFCs flow) during the experiments.

A picture of the experimental set-up described above and the internal view of the autoclave is displayed in Figure 2a and b respectively.

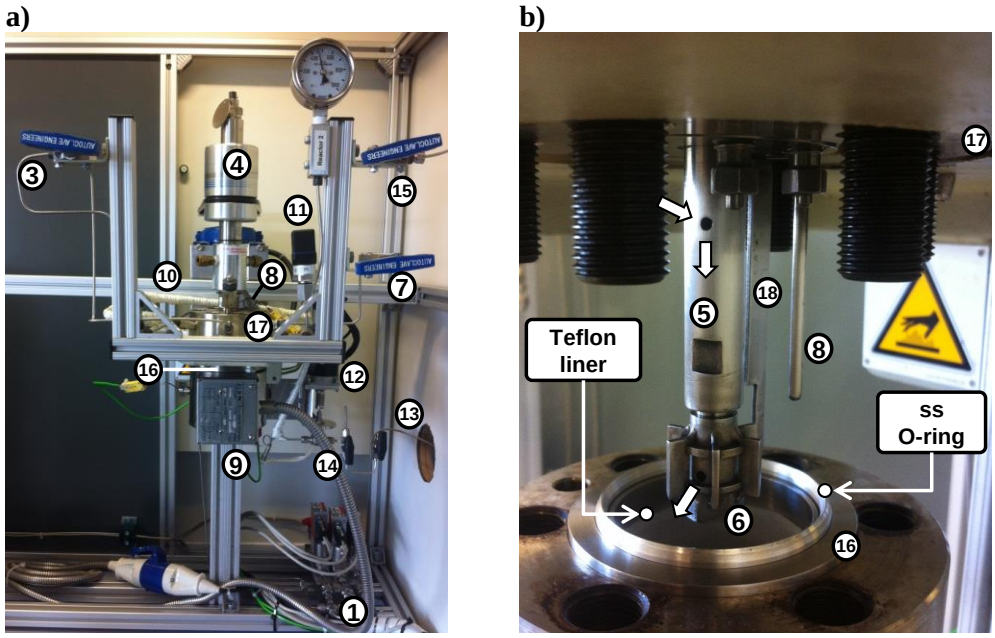

Figure 2. (a) Photograph of the experimental set-up used in the Fischer-Tropsch catalytic experiments. (b) Internal view of the autoclave. In arrows indicated the Dispersimax system. Numbers referred to Figure 1.

III.1.2. Fischer-Tropsch catalytic experiments

Detail of the procedures involved in the performing of a FT experiment will be described according to the following sections:

- Charge of catalytic mixture
- Purge and charge of gases
- FT experiment
- Finish of the experiment and analysis of the gas and liquid phases

Charge of catalytic mixture

Fischer-Tropsch reactions using the colloidal catalysts were carried out in a 100 ml stainless steel autoclave operated in batch mode. A suitable amount of isolated CoNPs (*ca.* 0.60 mg corresponding to *ca.* 1 mmol of Co) were re-dispersed in 66 ml of water, and placed inside a Teflon liner in the autoclave. Then, the

autoclave´s vessel (16) is attached to the head (17) by adjusting the hexagonal screws (always in crossed order) using a dynamometric ratchet calibrated at 20 Nm.

Purge and charge of gases

Since the internal pressure of the autoclave is controlled automatically by the Process@ software, before of the autoclave pressurization, the pressure set value should be set at a superior value of the total working pressure (30 bar for typical catalysis). Then a pressure of 40 bar is set to avoid undesired releases while the autoclave is charged with gases, as depicted in Figure 3 by arrows. It is noteworthy that the check box of "Manual" (indicated by arrows in the zoom) must be always unchecked in concordance with the automatic pressure mode, otherwise the autoclave will behave as a completely closed system without regulating the pressure to the set value.

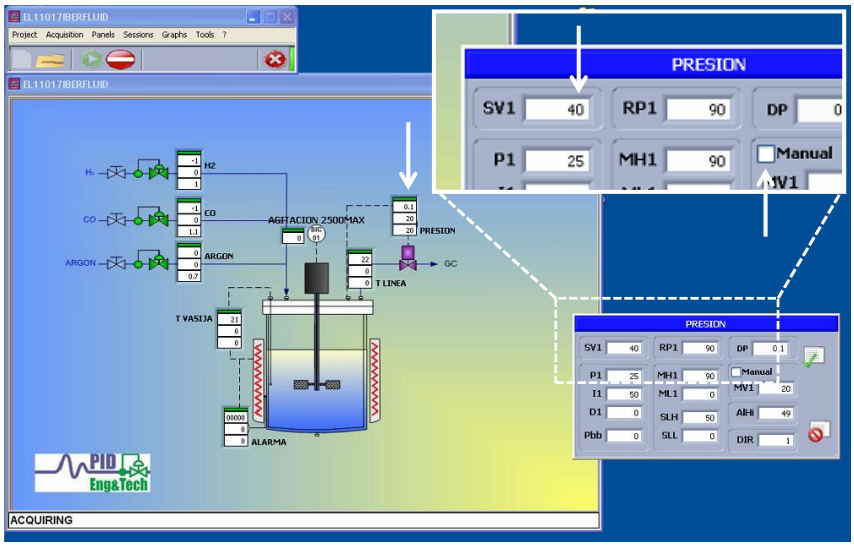

Figure 3. View of the Process@ software for the setting of pressure in automatic mode.

Next, the autoclave purge is performed by closing the evacuation valve (15) and opening the gas entry (3), then the Ar-MFC is fully opened (200 µl/min). During the purges the autoclave is stirred at 1000 rpm to enhance the exchange of gases with the solvent. When the system reached 10 bar, the gas entry (3) is closed and the evacuation valve (15) opened to evacuate to a minimal pressure of 1 bar, then the

purge and evacuation cycle is repeated two times more to ensure complete purging of the system with Ar. During the gas release of the last purge cycle the Ar-MFC valve is closed and the evacuation valve (15) is closed too when the Ar pressure drop to 1.5 bar.

Subsequently, the CO-MFC valve is opened and the flow rate set at 500 µl/min till the pressure increased to 11.5 bar, then the corresponding MFC valve is closed. Later, the H_2-MFC valve is opened and the flow rate set at 1500 µl/min till the pressure increased to 31.5 bar (thus resulting in a H_2:CO ratio of 2), then the corresponding MFC valve is closed. Finally, the gas entry valve (3) is closed and the system leaved some minutes to check the stability of the pressure. The variation of the pressure during the purge and charging process is easily followed with the acquired pressure values (in blue color) as depicted in Figure 4. In this plot, the periods of Ar, CO and H_2 flow are indicated by gray, orange and pink color respectively. In Figure 4 is appreciated the three initial purge cycles with Ar followed by the CO and H_2 charge and finally the stabilization time prior to catalysis.

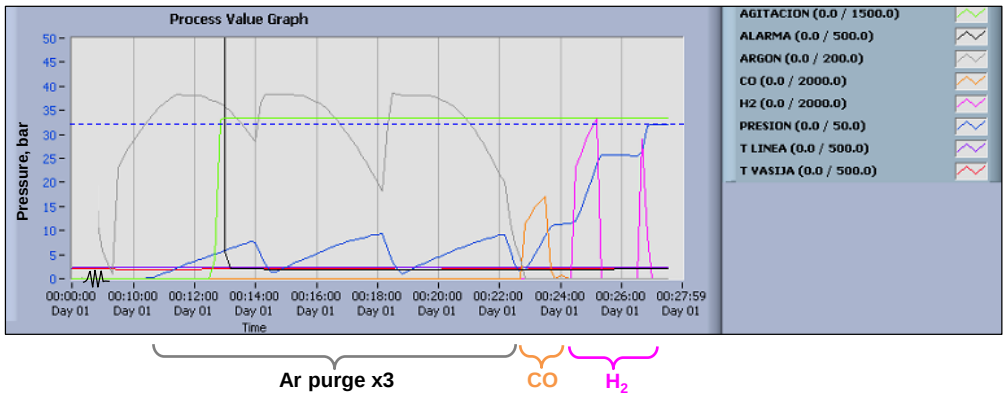

Figure 4. View of the Process Value Graph of a typical purge and charge experiment as displayed in the ExperimentViewer software.

FT experiment

Once the autoclave is charged with the syngas mixture and the pressure (31.5 bar) is stable for several minutes, the catalytic experiment can start. For this

purpose, several parameters are modified simultaneously to the reaction conditions, using a session table. A session table consists in a series of consecutive events named "Sessions" executed automatically by the Process@. Each "Session" overwrites the values of the control parameters set in previous Session. As displayed in a typical Session table used in catalysis (Figure 5), Session 1 set the different temperature values for the reactor (T VASIJA=180ºC), the thermostated line (T LINEA=180ºC) the heater (ALARMA=273ºC), pressure (PRESION=31.5bar) and stirring rate (AGITACION=1000rpm). Session 2, only prolongs during 13h the values set in the previous. Session 3, turns off the heating of the autoclave (ALARMA=0ºC, T VASIJA=180ºC) and one hour after, Session 4 turn off the thermostated line (T LINEA=180ºC). Finally, Session 5 turn off the stirring (AGITACION=0).

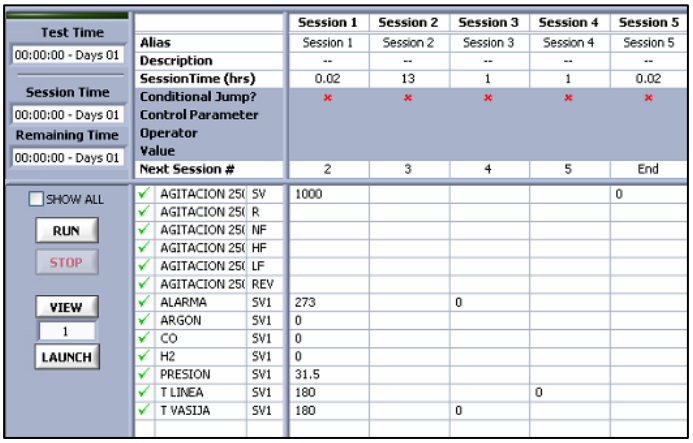

			Session 1	Session 2	Session 3	Session 4	Session 5
	Alias		Session 1	Session 2	Session 3	Session 4	Session 5
	Description		--	--	--	--	--
	SessionTime (hrs)		0.02	13	1	1	0.02
	Conditional Jump?		×	×	×	×	×
	Control Parameter						
	Operator						
	Value						
	Next Session #		2	3	4	5	End
✓	AGITACION 25(	SV	1000				0
✓	AGITACION 25(	R					
✓	AGITACION 25(	NF					
✓	AGITACION 25(	HF					
✓	AGITACION 25(	LF					
✓	AGITACION 25(	REV					
✓	ALARMA	SV1	273		0		
✓	ARGON	SV1	0				
✓	CO	SV1	0				
✓	H2	SV1	0				
✓	PRESION	SV1	31.5				
✓	T LINEA	SV1	180			0	
✓	T VASIJA	SV1	180		0		

Figure 5. Session table used for the control of parameters of a typical catalytic experiment. Conditions: 0.99 mmol Co, 31.5 bar (H_2:CO:Ar = 2:1:0.15), 180 ºC, 12h.

A typical view of the evolution of the different parameters (pressure and temperatures) during a catalytic experiment is displayed in Figure 6. According to this, the system requires *ca*. 1 h to reach the desired temperatures (in red color, T VASIJA), for that reason the heating time was set to 13 h, thus resulting in an effective time of catalysis of 12 h approximately. Also is appreciated the oscillation of the heater temperature (in black color, T ALARMA, also indicated by arrows), in

order to adjust the set temperature in the autoclave. It is also noteworthy that the pressure drop at the end of the reaction is of *ca.* 2-3 bar in general for the experiments carried out using water as solvent.

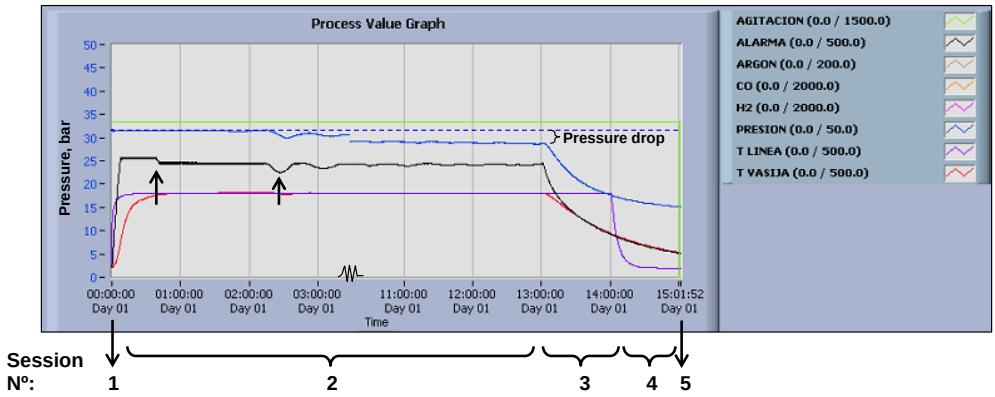

Figure 6. View of the Process Value Graph of a typical catalytic experiment as displayed in the ExperimentViewer software. Conditions: 31.5 bar (H_2:CO:Ar = 2:1:0.15), 180 ºC, 12h.

End of the experiment and analysis of the gas and liquid phases

As commented above, after the completion of the reaction, the heating is automatically turned off and the system is cooled by the effect of the ambient. Once the internal temperature of the autoclave reaches 40 ºC or less the gas phase can be injected to the GC-TCD. The values of pressure and temperature of the reactor just before the gas analysis are registered for the posterior calculations of the moles of gas using the ideal gas law.

For analysis of the gas phase, firstly the three way valve located after the electronic pressure valve must direct the gas flow to the GC. Subsequently, the pressure is set to a value inferior to the present value. For instance, the experiments in water usually resulted in a pressure of *ca.* 18 bar, at room temperature after catalysis. Then the pressure is set to 10 bar, in consequence the 8 bar of excess are released by the electronic pressure valve to the GC. Generally, the tubing which communicates the autoclave with the GC is purged a few seconds before the injection. The bridge which communicates the autoclave is depicted in Figure 7.

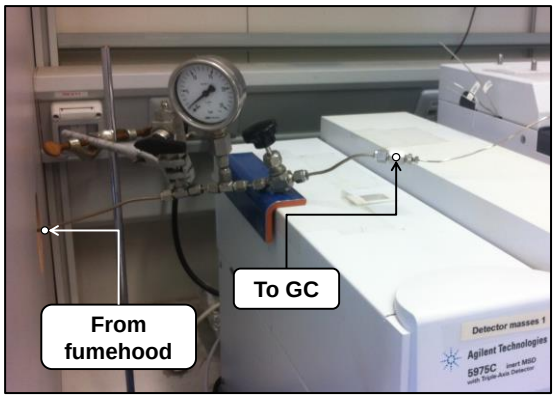

Figure 7. Valve array located outside the fumehood used for gas injection to the GC-TCD.

Following this procedure, the gas phase is analyzed twice to confirm the analysis, for instance at 12 and 6 bar. If significant differences are encountered, a third injection is carried out.

After analysis of the gas phase, the autoclave is finally evacuated using (16) and opened. The catalytic mixture (*ca.*66 ml) is transferred to a Erlenmeyer where the metal nanoparticles are magnetically decanted to the bottom, and the supernatant is transferred to a separatory funnel. Separately, 10 ml of dichloromethane (for experiments in water) or cyclohexane (for experiments in alcohols) are mixed with 5 µl of bicyclohexyl. The organic solution is passed through the shaft to collect the reaction products as quantitatively as possible. Additional washing of the shaft and the autoclave vessel with water are performed, and all the washings (organic and aqueous) are passed through the Erlenmeyer with the NPs and the supernatant added to the funnel. The separatory funnel is shake vigorously and the mixture is leaved to separate during several minutes. For the cases when alcohols and cyclohexane were mixed, it was necessary the addition of NaCl to induce destabilization of the emulsion and phase separation. Finally, the organic phase is collected with the reaction products and analyzed immediately by GC-MSD.

III.1.3. Chromatographic analysis

III.1.3.1.Analysis of the gas phase

The components of the gas phase (CO, H_2, O_2, N_2, Ar, CO_2, and C_1-C_8 hydrocarbons) were analyzed by GC-TCD on an Agilent 7890A GC using a system including several isolation valves and three columns: Hayesep Q (3ft x 1/8 in), HP-Molsieve (30m x 0.320 mm x 12 µm) and HP-Plot/Q (30m x 0.320 mm x 20 µm) using helium as carrier gas. HP-Molsieve column was used for the separation of permanent gases, CO, H_2, O_2, N_2, Ar, and methane. The combination of an HP-PLOT Q column and isolation valves was used for the separation of CO_2 from the other gases. Higher hydrocarbons (C_2-C_8) were also separated with the HP-PLOT Q. The chromatographic method consisted basically in an initial isotherm at 50 ºC during 5 min followed by a ramp of 20 ºC/min up to 260 ºC, and finally a hold time of 10 min. Helium was used as carrier gas to allow the analysis of H_2.

The quantification of all gas components (CO, H_2, O_2, N_2, Ar, CO_2, and C_1-C_8 hydrocarbons) was carried out using calibration curves for each component prepared by gas blending of a commercial standard (Calibration mixture, Abello Linde, Nº 312896). For the case of CO and H_2, a wide calibration covering the whole range of molar percentages was performed by blending of the same gases used in synthesis. Gas blending was carried out directly in the reactor vessel by diluting the corresponding gases (calibration mixture diluted with H_2) and analyzed by GC-TCD over identical conditions that a typical catalysis. In all the cases, Ar purge was performed before gas blending, leaving a 5 mol%.

Table 1, summarizes the composition of the calibration mixture used for the analysis of the gas phase. The chromatogram of this mixture acquired using the standard method of gas analysis and injected directly to the GC, is displayed in Figure 8 with the corresponding peaks identity. As can be appreciated in Figure 8, the hydrogen peak is negative due to the lower thermal conductivity of this component in relation to the carrier gas, helium. For those cases in which not complete resolution of the peaks could be obtained (e.g. C4, C5), the medium point was used to separate the peak integration.

Table 1. Composition of calibration mixture used for the analysis of the gas phase.

E	Compound	Mass %[a]	mol %
1	Methane	4.698	3.031
2	Ethane	10.070	3.467
3	Ethene	0.905	0.334
4	Propane	4.991	1.172
5	Propene	0.939	0.231
6	Isobutane	10.470	1.865
7	Butene	9.980	1.841
8	tras-2-butene	5.000	0.923
9	Butane	4.960	0.915
10	Pentene	2.004	0.288
11	Pentane	1.043	0.150
12	CO	4.933	1.823
13	CO_2	5.433	1.278
14	Nitrogen	19.800	6.833
15	Hydrogen	14.770	75.851

[a] Values provided by the standard supplier, Abello Linde Nº 312896 (27/09/2010) Lot. Nº: 7155

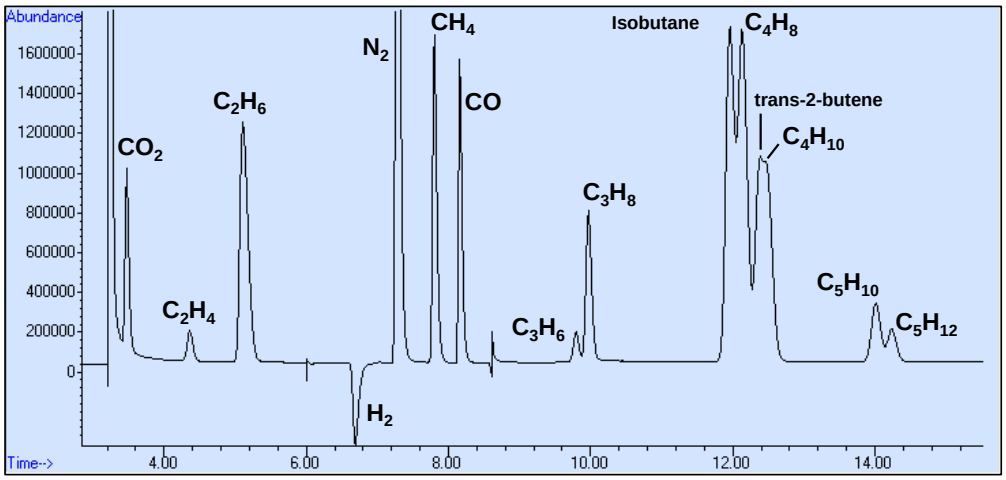

Figure 8. Chromatogram of the calibration mixture using the standard method of gas analysis.

Figure 9a displays the amplification of the ethane and ethane peaks region of the chromatograms obtained after dilution of the calibration mixture by factors of 2.5, 7, 12, 31 and 157 respectively.

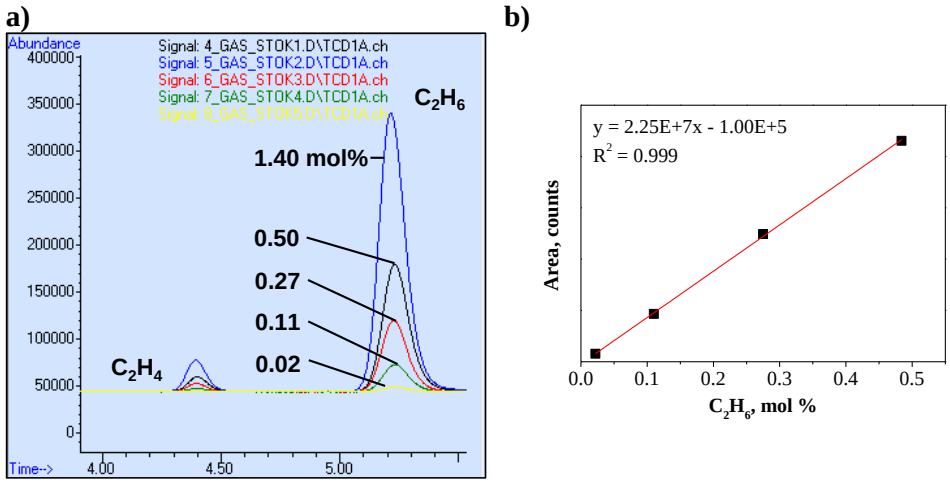

Figure 9. (a) Chromatograms obtained after dilution of the calibration mixture. Amplification of the ethane and ethane peaks. (b) Calibration curve for the percentage range of 0.02-0.50 mol% obtained for ethane.

Calibration curves for each component were prepared by plotting the area of the component (A_i) vs. the corresponding molar percentage (X_i), Equation (1).

$$A_i = mX_i + b \qquad \begin{matrix} A_i: \text{area of the component } i \\ X_i: \text{molar percentage of } i \end{matrix} \qquad \textbf{(1)}$$

Straight lines with R^2 values over 0.99 were obtained in all the cases, as exemplified in Figure 9b for the case of ethane (R^2 = 0.999). The same approach was applied to H_2 and CO, but covering a wider range of molar percentages, as can be appreciated in Figure 10a and b respectively. According to the corresponding calibration curves (Figure 11), linearity between the component percentage and the detector response were obtained for H_2 in the range of 20-85 mol% (R^2 = 993), and for CO in the range of 5-60 mol% (R^2 = 0.995). As was mentioned before, the response of H_2 is negative due to the lower thermal conductivity of this gas in comparison to helium which is the carrier gas.

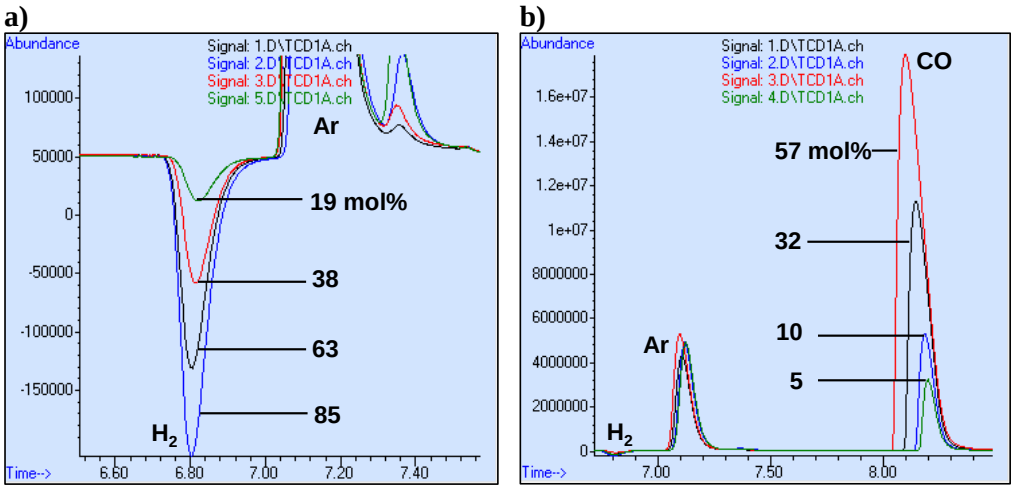

Figure 10. Chromatograms obtained at variable percentages of (a) H_2 and (b) CO.

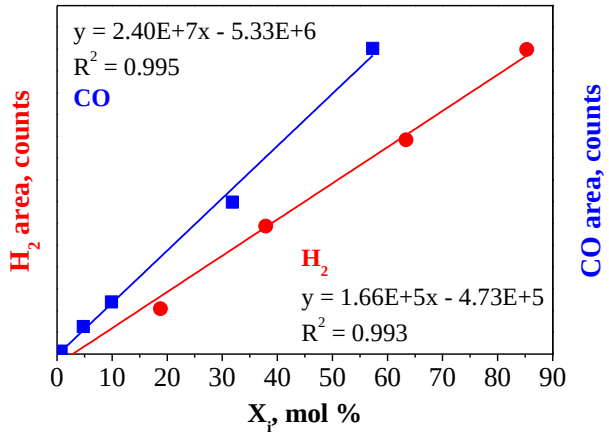

Figure 11. Calibration curves for H_2 and CO.

Quantification of the components contained in the gas phase (after catalytic experiments) was carried out by extrapolation of the obtained areas in the corresponding calibration curve. For the case of C_6, C_7 and C_8 hydrocarbons which were not present in the calibration mixture, the trend in the response factors of the preceding hydrocarbons (C_3-C_5) as a function of the carbon number were used to estimate the calibration curves for these components.

The chromatogram of the gas phase analysis of a typical Fischer-Tropsch experiment carried out in water (Conditions: 0.99 mmol Co, 31.5 bar (H_2:CO:Ar = 2:1:0.15), 180 ºC, 12h) is displayed in Figure 12. Under these conditions, compounds such as of CO_2, CH_4, and the series of n-alkanes and n-alkenes from C_2-C_8 were obtained. It can be also appreciated the presence of an important peak at 7.10 min corresponding to Ar, as well as unreacted H_2, CO and small amounts of N_2.

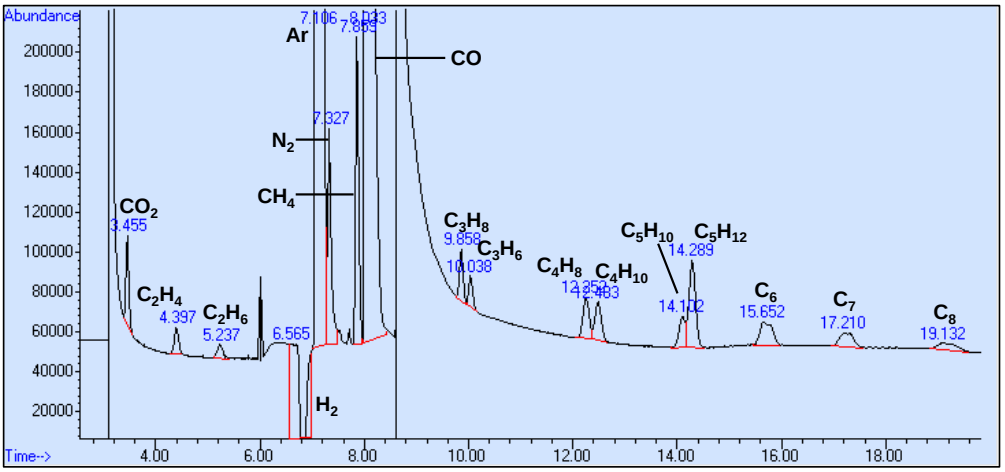

Figure 12. Chromatogram of the gas phase of a typical Fischer-Tropsch experiment carried out in water. Conditions: 0.99 mmol Co, 31.5 bar (H_2:CO:Ar = 2:1:0.15), 180 ºC, 12h)

The sequence of operations employed for the calculation of the catalyst activity and the products selectivity are described with the following equations:

$$A_i = mX_i + b \qquad X_i = \frac{(A_i - b)}{m}$$

A_i *:* Area of the product *i*
X_i *:* Molar percentage of *i*

(2)

$$\sum_{i}^{n} X_i \approx 100$$

i=0 to n: represent all the FT products

(3)

$$n_{Tot} = \frac{pv}{RT}$$

$$n_i = X_i * \frac{n_{Tot}}{100}$$

n_{Tot}: total mol of gases in gas phase.
p: final pressure after catalysis.
v: gas volume (36.2 ml)
R: 0.082 atm L $K^{-1}mol^{-1}$
T: temperature of reactor (rt)
n_i: mol of product i **(4)**

$$n_i^{CO} = n_i * C_n$$

C_n: carbon number of product i.
n_i^{CO}: mol of CO by mol of product i **(5)**

$$n_{Tot}^{CO} = \sum_i^n n_i^{CO}$$

n_{Tot}^{CO}:total mol of CO converted to products of catalysis. **(6)**

$$Co\_TY = \frac{n_{Tot}^{CO}}{n_{Co} * t}$$

Co_TY: cobalt time-yield (activity) in $mol_{CO}mol_{Co}h^{-1}$
n_{Co}: mol of cobalt (generally 0.93 mmol)
t: reaction time (12 h) **(7)**

$$W_i = n_i * MW_i$$

W_i: weight of product i
MW_i: molecular weight of product i **(8)**

$$S_i = \frac{W_i}{\sum_i^n W_i} * 100$$

$$S_{i-k} = \frac{\sum_i^k W_i}{\sum_i^n W_i} * 100$$

S_i: selectivity of product i (in wt%)
S_{i-k}: selectivity of fraction of products i-k **(9)**

Equation (2) represents the calculation of the molar percentage (X_i) using the linear equation of the corresponding calibration curve. Subsequently, the total moles of gas present in the gas phase (n_{Tot}) are calculated using the ideal gas law at the analysis conditions, Equation (4); while the moles of a product i (n_i) are calculated from computing the total moles and the molar percentage of such a product i. Later, the moles of product i are converted to the equivalent moles of CO according Equation (5), considering the number of carbons (C_n) of the hydrocarbon chain.

The cobalt time-yield or activity (*Co_TY*), which is defined as the moles of CO converted per moles of catalysts, per unit of time, are calculated using Equation (7) and (6). The calculation of the activity in those catalysis that contained product in both the gas and the liquid phase, included the contributions of the liquid products in terms to moles of CO to the total moles of CO (n_{Tot}) according to Equation (6).

Finally the selectivities reported in the present work are calculated as a weight basis (wt %), for that reason, the weight of a product *i* is calculated by computing the moles (n_i) by its corresponding molar weight (MW_i), Equation (8). Then, the selectivity of a product *i* or a fraction of products *i-k* is calculated using the expressions described in Equation (9).

The whole quantification of the different parameters of the catalytic experiments (activity, selectivities, alpha, etc) was carried out automatically using an excel file which required the manual entry of the summary of GC analysis (the areas) as well as the conditions of the autoclave after the reaction (pressure and temperature) which will be the conditions of the CG analysis. A copy of this excel file and the files of the different calibration curves (calibration mixture and H_2/CO) is provided in the Electronic Supplementary Material which accompany this work.

III.1.3.1.Analysis of the liquid phase

The products and the internal standard (bicyclohexyl) contained in the organic phase (either, dichloromethane or cyclohexane) after the extraction procedure were analyzed by GC-MS. These analyses were performed on a 7890A GC/9575C MSD system (Agilent) using a HP-Innowax capillary column (30m x 0.250 mm x 0.15 μm), and helium as carrier gas. The chromatographic method consisted basically in an initial isotherm at 34 ºC during 10 min, followed by a ramp of 10 ºC/min up to 260 ºC, and a final hold time of 10 min. The identification of products was performed using the mass spectra and by comparison with standards. The quantification was carried out using the corresponding calibration curve for each compound.

Stock solutions for each family of compounds (alkanes, alkenes, aldehydes and alcohols) were prepared by mixing standards for each compound and diluted in dichloromethane (for alkenes, aldehydes and alcohols) or purchased for the case of the series of linear alkanes (Aldrich, C_7-C_{30} Saturated Alkanes, 1000 μg/mL each component in hexane). In most of the cases, the analytical standards were purchased from Aldrich.

The chromatograms of the stock solutions for the four families of compounds (alkanes, alkenes, aldehydes and alcohols) are displayed in Figure 13. As can be observed, in most of the cases the peak of the IS (bicyclohexyl) that appears at *ca.*12.5 min does not interfere with other compounds under this chromatographic method.

Calibration curves for each compound were obtained using dilution of the stock solution of the corresponding family of compounds in dichloromethane. In all the cases bicyclohexyl was present as internal standard in a concentration of 2.59 mM.

Due to the chromatographic complexity of the reaction products of the Fischer-Tropsch synthesis, a methodology of ion extraction was implemented for each family of compounds in order to simplify the analysis and to maximize the sensibility of detection according to the properties of the MS detector. The ion extraction was particularly helpful for the identification of trace amounts of products obtained for catalytic systems with low activity or low selectivity towards liquid products (for instance, using water as solvent).

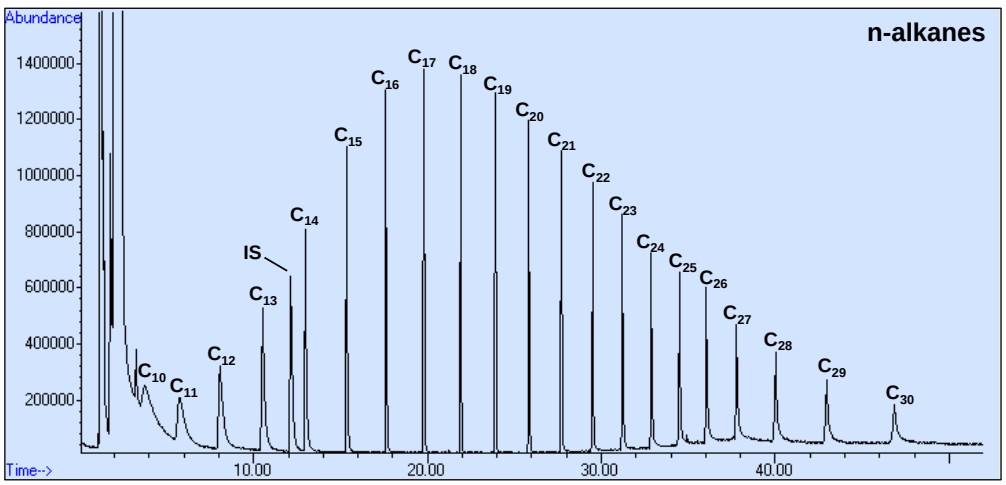

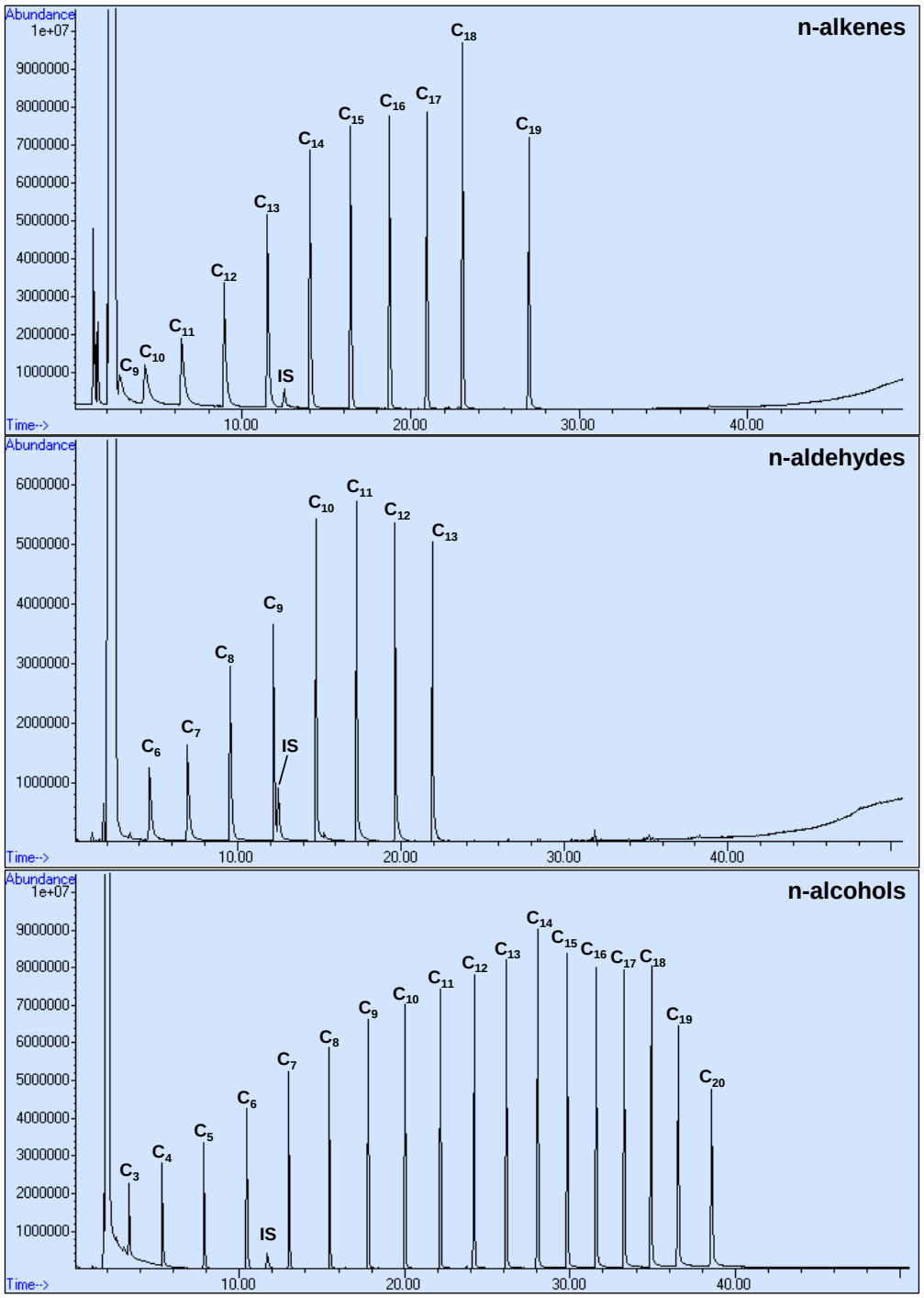

Figure 13. Chromatograms of the stock solutions of linear n-alkanes, n-alkenes, n-aldehydes and n-alcohols.

Figure 14 displays the ion extracted chromatograms obtained after dilution of the corresponding stock solutions for each family of compounds, amplifying the region of the closer peaks to the IS (bicyclohexyl). The ions used for the analysis of n-alkanes, n-alkenes, n-aldehydes and n-alcohols (57, 55, 41 and 56 respectively) were selected according to their high abundance in the mass spectra of the respective family of compounds (in order to obtain the maximal sensibility) and trying to be as selective as possible avoiding the interference with ions of compounds from other families. It is noteworthy that for the case of the n-alkanes, and n-alcohols, the selected ions were so selective that no signal of the IS was appreciated in the chromatograms. The ion selected for the analysis of the IS was 82.

n-alkanes (ion 57)

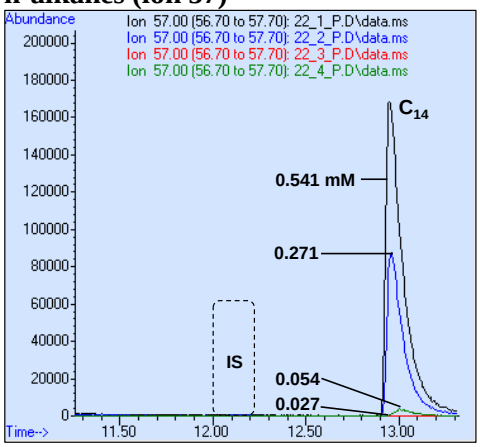

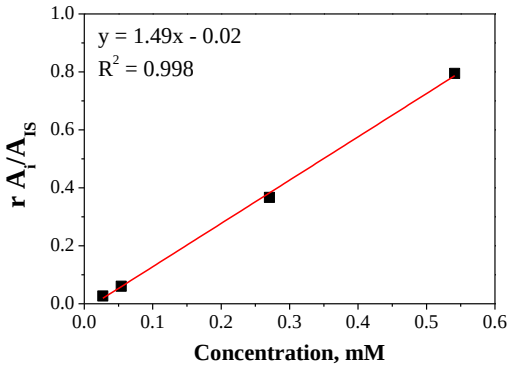

n-alkenes (ion 55)

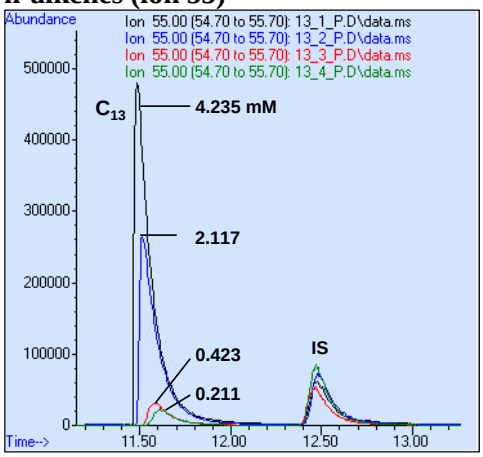

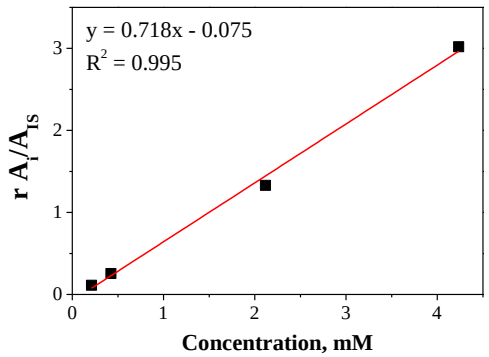

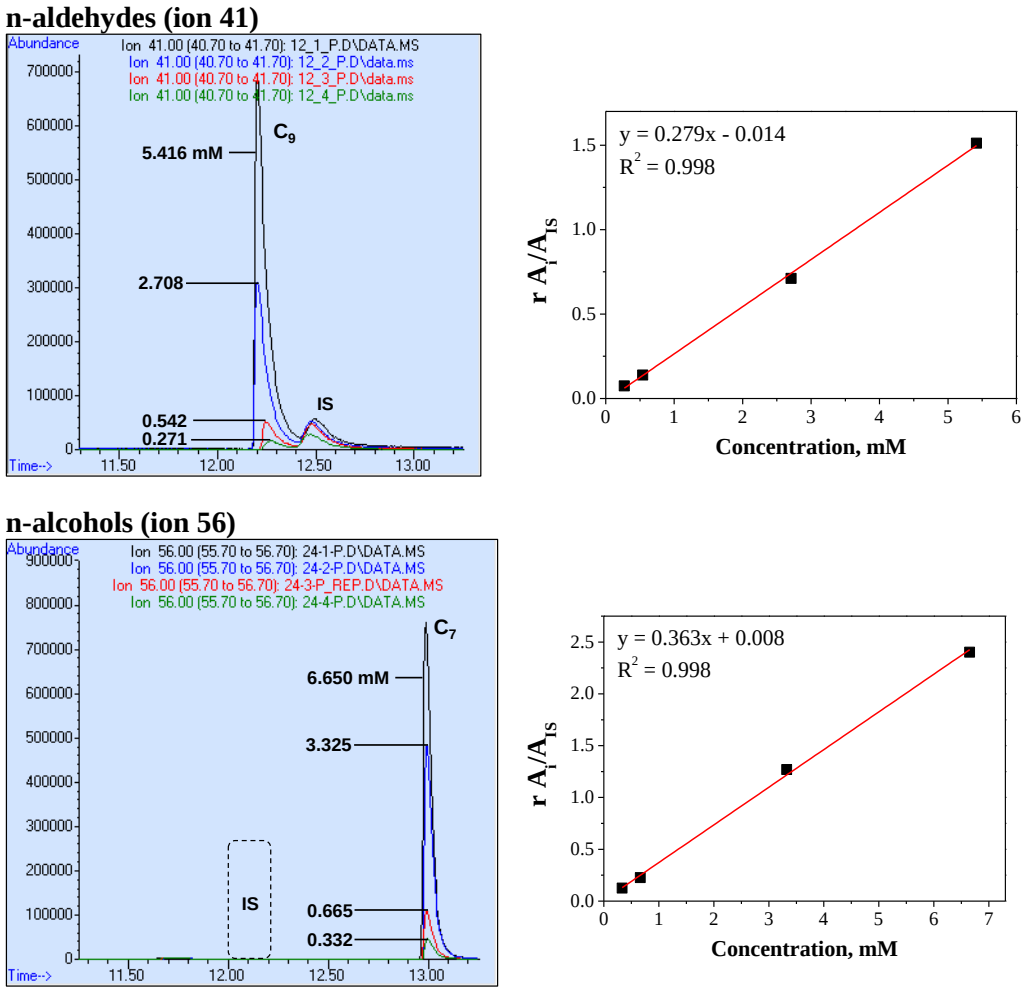

Figure 14. Chromatograms for each family of compounds obtained after dilution of the corresponding stock solutions, amplifying the region of the peaks closer to the IS and calibration curves for compounds indicated in the corresponding chromatograms.

Calibration curves for each once of the analyzed compounds were prepared by plotting the relation of areas (rA_i) between the component (A_i) and the IS (A_{IS}) vs. the molar concentration (C_i), Equation (10). Good linearity with R^2 values over 0.99 were obtained, as exemplified in Figure 14 for the case of n-tetradecane (R^2 = 0.998), n-tridecene (R^2 = 0.995), n-nonaldehyde (R^2 = 0.998) and n-heptanol (R^2 = 0.998).

$$rA_i = \frac{A_i}{A_{IS}} \qquad rA_i = mC_i + b \qquad \textbf{(10)}$$

rA_i : relation of areas
A_i : area of the component i
A_{IS} : area of the component i
C_i : molar concentration of i in mM

a)

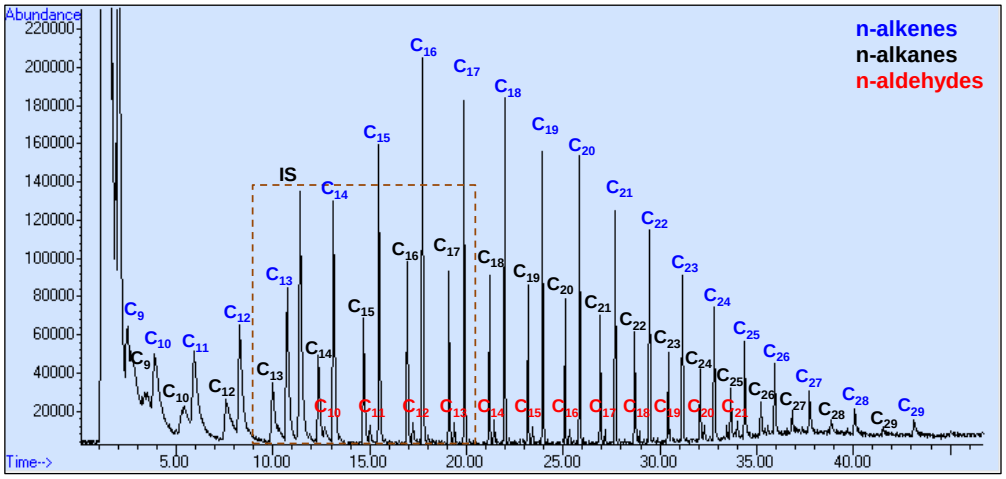

b)

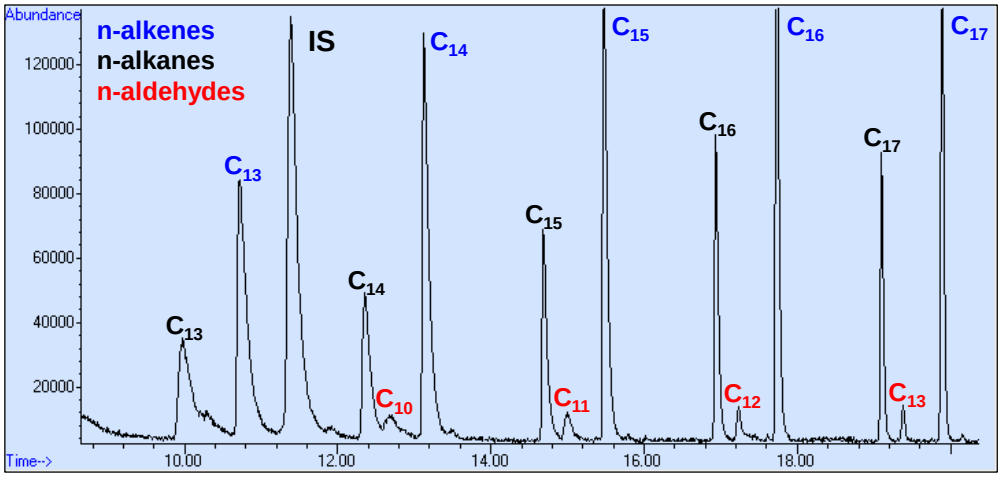

Figure 15. (a) Chromatogram of the liquid phase analysis of a typical Fischer-Tropsch experiment carried out in 50% heptane/water mixture. (b) Amplification of the dotted region in a. Conditions: 0.99 mmol Co, 31.5 bar (H_2:CO:Ar = 2:1:0.15), 180 ºC, 12h)

The compendium of all the calibration curves for each family of compounds is provided in the Electronic Supplementary Information. The chromatogram of the liquid phase analysis of a typical Fischer-Tropsch experiment carried out in a mixture of 50% heptane/water (Conditions: 0.93 mmol Co, 31.5 bar (H_2:CO:Ar = 2:1:0.15), 180 ºC, 12h) is displayed in Figure 15. Under these conditions, a series of linear n-alkanes, n-alkenes and n-aldehydes were obtained in the range of C_{10}-C_{30}.

The sequence of operations employed for the calculation of the moles of CO transformed to liquid products follows an analogous approach to the used whit the components of the gas phase. The used equations are described below:

$$rA_i = mC_i + b \qquad C_i = \frac{(rA_i - b)}{m}$$

rA_i : relation of areas
A_i : area of the component *i*
A_{IS} : area of the component *i*
C_i : molar concentration of *i* in mM **(11)**

$$n_i = C_i * v_l$$

n_i: moles of product *i*
v_l: volume of extraction solvent (10 ml) **(12)**

$$n_i^{CO} = n_i * C_n$$

n_i^{CO}: mol of CO by mol of product *i*
C_n: carbon number of product *i*. **(13)**

Equation (11) represents the calculation of the molar concentration (C_i) using the linear equation of the corresponding calibration curve. Subsequently, the moles of product are obtained by multiplying this concentration by the volume of the extraction solvent, Equation (12). The moles of CO converted to a product *i* are calculated using Equation (13) by considering the number of carbons contained in the hydrocarbon chain of that product. Finally, the moles of CO converted to liquid products are introduced in Equation (7) for the calculation of the cobalt time-yield (activity) and in Equation (9) for the calculation of the selectivity.

The distribution of the hydrocarbon products was analyzed using the Anderson–Schulz–Flory (ASF) equation, Equation (14). The alpha value (α) represents the chain growth probability.

$$Ln\left(\frac{W_i}{C_n}\right) = C_n Ln\alpha + cont. \quad \textbf{(14)}$$

W_i: weight of product *i*
C_n: carbon number of product *i*.
A_i : area of the component *i*
X_i : molar percentage of *i* in mol%
α: chain growth probability

$y = mx + b$ (for linear function) **(15)**

$m = Ln\alpha$

$\alpha = e^m$

According to Equation (14), the chain growth probability (α) of a FT experiment was calculated by plotting the natural logarithm of the relation between the weight fraction of a product *i* and the corresponding carbon number (C_n) vs. the carbon number (C_n). A typical ASF distribution of the products obtained in a catalysis carried out in water is displayed in Figure 16. Finally, the alpha value is extracted from the slope of the linear regression of this plot according to Equation (15), as depicted also in Figure 16.

a) **b)**

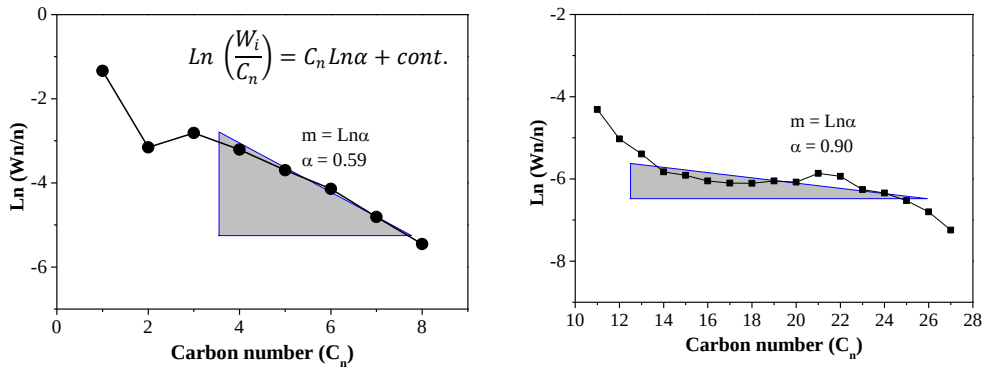

Figure 16. ASF distributions of the products obtained in a typical FT experiment carried out in (a) water and (b) 50% heptane/water mixture. Conditions: 0.99 mmol Co, 31.5 bar (H_2:CO:Ar = 2:1:0.15), 180 ºC, 12h.

III.2. Numerical and experimental modelization of the two-phase mixing in a small scale stirred vessel

The group of Dr. Vernet at the Mechanical Enginery Department in the Universitat Rovira i Virgili developed a project which consisted in the experimental and numerical Modelization of the two phase mixing in the stirred tank reactor used in this thesis. We acknowledge with thanks the work performed by Dr. Vernet´s group since the data obtained in his laboratories is valuable for the understanding of the current setup.

The main objective of this project was the prediction using numerical simulations, of the mass transfer rate of gas components within the liquid phase in the STR. To reach this objective experiments have been conducted in a transparent model of the reactor equipped with the stirrer used in the normal operation of the reactor. The visualization of the air-water two-phase flow in the model at different rotation rates of the stirrer allowed the determination of the size and number of the air bubbles, as well as the flow regime. This experimental information has been used in the numerical simulations to predict the mass transfer rates of gas components from the gas phase to the liquid phase. In particular simulations of the distribution of the liquid and gas phases at the operating conditions of the reactor were carried out and bubbles with the experimentally measured diameter were numerically tracked to determine the particle Reynolds number, which is an important parameter, together with the Schmidt number, to determine the mass transfer rates. The mass transfer rates of the gas components to the liquid phase were estimated using conventional mass transfer correlations.

As conclusions of the experimental modeling, it was experimentally determined that the amount of bubbles inside the reactor increases with the rotation rate (Ω), while the bubble size decreases. Typical bubble diameters range from 0.2 mm to 0.7 mm. Experimentally, three flow regimes have been observed. At low rotation rates bubbles are not observed and the liquid phase and the gas phase are separated by a well-defined interphase which is deformed vertically by rotation. At larger rotation rates gas bubbles are observed within the liquid phase. An emulsion

is formed for rotation rates between 1000 and 1400 rpm for the unbaffled configuration, while bubbly flow is observed for the baffled configuration in the whole range of rotation rates studied (up to 1721 rpm). In general at the same rotation rate the number of bubbles is smaller in the baffled configuration than in the unbaffled configuration.

Some experiments were conducted for three phase flows (air-water-heptane) and the flow behavior was analyzed. Different compositions of the liquid mixture and rotation rates were studied. The three-phase system shows different behaviors depending on the composition and rotation rate. At Ω=606 rpm, for the pure fluids (heptane or water) no air bubbles are observed in the liquid phases. At this rotation rate and for a 15/85 water/heptane mixture water drops can be seen within the heptane. A liquid-liquid emulsion is formed for 50/50 and 85/15 water/heptane mixtures. At Ω=1371 rpm and pure composition of the liquid phase air bubbles are observed. The mean diameter of the air bubbles depends on the composition, ranging from 1.114±0.052 mm for pure heptane to 0.479±0.017 mm for pure water. In the case of mixtures it is not clear if air bubbles are distributed within the liquid phases since the visualization cannot differentiate between air bubbles or water drops.

Numerical simulations with the multiple reference frame technique were conducted. The simulations predicted correctly the shape of the interphase observed experimentally. Bubbles with the experimentally measured diameter were tracked numerically to determine the particle Reynolds number. Mass transfer rates of hydrogen and carbon monoxide were estimated with conventional mass transfer correlations for particles using the computed particle Reynolds number.

For the reactor with the baffle the emulsion is not observed in the range of rotation rates considered. In this case predictions indicate that the mass transfer rates of hydrogen and carbon monoxide from the gas phase to the liquid phase increase with the rotation rate. For example the increase of the rotation rate from 1000 rpm to 2500 rpm increases the mass transfer coefficient of H_2 or CO by a factor of 3.3. Curiously, for the unbaffled configuration there is a reduction, of about 65%, of the mass transfer rates from the bubble regime at 1000 rpm to the emulsion at 1400 rpm.

Further increase of the rotation rate from 1500 rpm to 2500 rpm resulted in the in the increase of the mass transfer rate by a factor of 2.7.

Finally, is important to consider that the direct quantitative extrapolation of these conclusions to the real operating conditions of the reactor has to be made with care. It is noteworthy that the simulations have been performed with the physical properties of the fluids used in the real operation of the actual reactor but the sizes and amount of bubbles are obtained from experiments performed with air and water

Details of the procedures and results obtained in this work are also available as an appendix in format of a full report written by Vernet´s Group.

CHAPTER IV

Aqueous Phase Fischer-Tropsch Synthesis Catalyzed by Co Nanoparticles: Effect of NPs Preparation and pH on Catalyst Activity and Selectivity

Table of Contents

IV.1. Abstract

Small and well dispersed cobalt nanoparticles were synthesized in water using $NaBH_4$ as the reducing agent and PVP as stabilizer. Cobalt nanoparticles from 1.7 to 3.1 nm were obtained varying the PVP:Co ratio from 80 to 10. These NPs were fully characterized using various techniques (TEM, HRTEM, XRD, XPS, TGA) and their catalytic performances evaluated in the aqueous phase Fischer-Tropsch Synthesis (AFTS). The pH of the catalytic mixture was shown to affect both the activity and selectivity of the AFTS reaction since side reactions such as WGS and formation of carbonates and formates were favored at basic pH. The modification of the syngas composition under such conditions favors the methane production and the formation formates from CO_2.

Keywords: Fischer-Tropsch, cobalt nanoparticles, aqueous phase, pH effect.

IV.2. Introduction

The increasing worldwide energy demand has made major companies to consider alternative feedstocks such as natural gas, coal and biomass to replace fossil fuels.[1] In this context, the Fischer-Tropsch Synthesis (FTS) has been considered a key process of the biomass-to-liquid (BTL), gas-to-liquid (GTL) and solid-to-liquid technologies (STL)[2] since through this catalytic reaction, syngas can be transformed into high quality synthetic fuels (Scheme 1).[3] FTS is catalyzed by several transition metals including Ru, Co and Fe. However, Co-catalysts are more attractive from an industrial point of view due to their higher hydrocarbon productivity, good stability and commercial availability.[1]

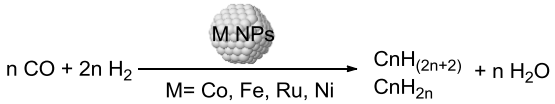

Scheme 1. Fischer-Tropsch synthesis catalyzed by metal nanoparticles

Metal supported and unsupported catalysts have been widely investigated over the last 80 years or more.[4] Alumina, silica, titania, magnesia, carbon, and zeolites among others as well as the microporous version of these materials have been extensively studied as supports for these metal catalysts.[5] With the aim to enhance the productivity of the process, many efforts have been dedicated to the preparation of ultrafine particle catalysts and the study of their interactions with the supports.[6] Currently, the control of the selectivity is one of the main goals in FT investigation.[7] In this context, the use of unsupported nanoparticles is of high interest as they mimic metal surface activation and catalysis at the nanoscale, and shed some light on the effect of the support on catalysis.[8] The first report of the aqueous phase FT synthesis (AFTS) was reported using ruthenium nanoclusters stabilized with poly(N-vinyl-2-pyrrolidone) (PVP) as catalysts.[9] The effect of the RuNPs size was investigated, and the highest activity was achieved for nanoparticles of 2.0 ± 0.2 nm. In more recent publications, several parameters such as the nature of the reducing agent, the PVP:Ru molar ratio, the effect of ionic additives,[10] the temperature,[11] and the effect of the stabilizer[12] have been studied with this ruthenium catalytic system. Recently, the effect of the polymer stabilizer was also studied in our group in the AFTS catalysed by RuNPs.[13] It was observed that PVP stabilized RuNPs were more active and selective towards hydrocarbons compared to those stabilized by lignins, indicating that the nature of the stabilizing polymer does affect the catalytic performance in AFTS, influencing strongly the production of CO_2 by Water Gas Shift (WGS) reaction.

One of the earliest studies on colloidal cobalt nanocatalysts applied in the AFTS was published by Kou and co-workers who reported activity of $0.12 mol_{CO} mol_{Co}^{-1} h^{-1}$ at 170ºC. In this study, the CoNPs were synthesized by chemical reduction using sodium borohydride as reducing agent in water.[14] More recently, the same author compared Co nanoparticles reduced by $LiBEt_3H$ and $NaBH_4$, in the aqueous-phase Fischer-Tropsch synthesis.[15] Higher catalytic performance was observed for the former case, and comparing the particle size distribution of the catalysts before and after reaction, it was suggested that catalyst reconstruction occurs during the reaction. In addition the authors proposed that B-

doping could affect the catalytic performance of these NPs. They also reported the use of cobalt/platinum alloy nanoparticles stabilized by PVP as catalysts of the AFTS.[16] According to this report, activity up to 1.1 $mol_{CO}mol_{Suf\text{-}Co}^{-1}h^{-1}$ with a growth factor (α) of 0.8 was obtained at 160ºC. This outstanding activity was rationalized by the formation of Co overlayer structures on Pt NPs or Pt-Co alloy NPs. Finally, the synthesis of CoNPs by thermal decomposition of $Co_2(CO)_8$ was also reported using a modified lipophilic C_8-PVP stabilizing agent and squalane as solvent.[17] The resulting CoNPs showed a size of 3.54 ± 1.63 nm and a FT activity of 0.022 $mol_{CO}mol_{Co}^{-1}h^{-1}$.

Other colloidal Co nanocatalysts for FTS were reported in ionic liquids[18] and squalane[17] although in these cases, low activity and agglomeration issues were described. Dupont and co-workers reported the synthesis of Co nanocubes of 54 ± 22 nm by thermal decomposition of $Co_2(CO)_8$ in [DMI][NTf_2] as solvent. The obtained Co nanocubes were evaluated in the FT synthesis with an average TOF of $1.17x10^{-5}$ $mol_{CO}mol_{Suf\text{-}Co}^{-1}h^{-1}$.[18a] In a second report, the same authors used a distinct ionic liquid, namely [BMI][NTf_2], and obtained spherical nanoparticles of 7.7 ± 1.2 nm which were active in the FT synthesis (average TOF of 0.26 $mol_{CO}mol_{Suf\text{-}Co}^{-1}h^{-1}$).[18b] Very recently, Dupont and co-workers reported the synthesis of bimetallic Co/Pt NPs in [BMI][PF_6] and its application in the FTS.[19] The nanoparticles were synthesized via an organometallic approach using [bis(cylopentadienyl)cobalt(II)] and [tris(dibenzylideneacetone) bisplatinum(0)] as metal precursors and hydrogen as reducing agent. The authors proposed for these bimetallic NPs a core–shell like structure in which mainly Pt composes the external shell. The isolated bimetallic NPs resulted active catalysts for the Fischer–Tropsch synthesis and selective for naphtha products.

In the present work, we describe the synthesis and characterization of colloidal CoNPs stabilized with poly(N-vinyl-2-pyrrolidone) and their evaluation as nanocatalysts in the aqueous phase FT synthesis. Some parameters such as the PVP:Co ratio, the pH and the possible effect of the size of the nanocatalysts are discussed.

IV.3. Results and Discussion

IV.3.1. Synthesis and characterization of CoNPs

CoNPs were synthesized by chemical reduction of cobalt chloride in the presence of polyvinylpyrrolidone (PVP) as stabilizer and sodium borohydride as reducing agent (Scheme 2). Four sets of CoNPs, **Co1-4** were obtained by the variation of the PVP:Co ratio (10, 20, 40 and 80, respectively).

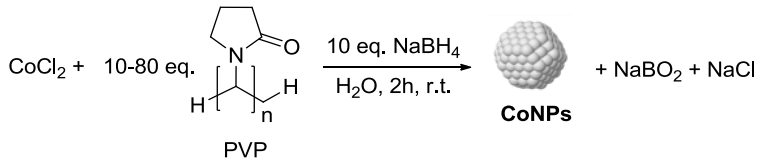

Scheme 2. Synthesis of CoNPs **Co1-4** by chemical reduction method.

The TEM micrographs and size histograms of **Co1-4** displayed in Figure 1 showed the formation of spherical cobalt nanoparticles with diameters in the range 1.7-3.1 nm. The variations in particle size as a function of the PVP:Co ratio are summarized in Table 1.

When a PVP:Co ratio of 10 was used (PVP:Co ratio based on mol of monomer units per mol of Co), the NPs **Co1** with a mean size of 3.13 ± 1.58 nm were obtained. The broad size distribution was attributed to the poor stabilization of the NPs due to the low PVP concentration during their synthesis. For the **Co2-4** NPs, when the PVP:Co ratio was increased to 20, 40 and 80, smaller NPs with sharper distributions were obtained (Figure 1 and Table 1).

The variation of the stabilizer amount is a method widely applied for the synthesis of size controlled metal nanoparticles.[20] For instance, Lu *et al*. reported the tuning of the size of the spherical cobalt nanoparticles between 2–7.5 nm by varying the concentration of the polymer stabilizer (end-functionalized poly(methacrylic acid).[21] The decreasing size of the cobalt nanoparticles agrees with a slower growth relative to nucleation when higher concentration of PVP are used.[22]

Table 1. Mean diameters of **Co1-4** synthesized by chemical reduction method.[a]

Entry	NPs	PVP:Co	D(nm)
1	**Co1**	10	3.13 ± 1.58
2	**Co2**	20	2.64 ± 0.92
3	**Co3**	40	2.11 ± 0.41
4	**Co4**	80	1.71 ± 0.73

[a] Conditions: 0.93 mmol of $CoCl_2.6H_2O$; PVP K-30; 9.31mmol $NaBH_4$; water; quantitative yield.

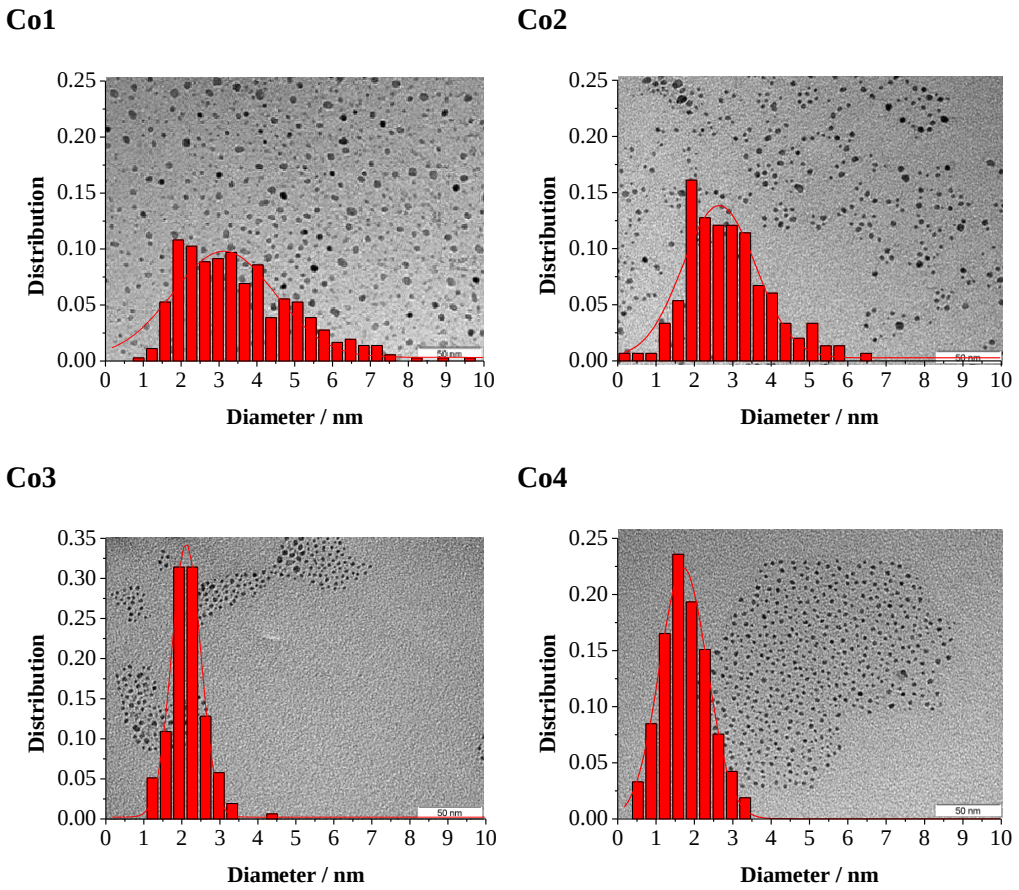

Figure 1. Size histograms and TEM micrographs of **Co1-4.**

The fine structure of the CoNPs **Co2** was also studied by high-resolution transmission electron microscopy (HR-TEM). The HR-TEM micrograph of **Co2** is displayed in Figure 2 and the inset corresponds to the selected area electron (SAED)

diffraction pattern. In the micrograph, single particles of *ca*. 2.6 nm size were observed, in agreement with the size previously obtained by TEM (2.64 ± 0.92 nm). Analysis of the diffraction pattern revealed the presence of crystalline CoO-fcc and Co_3O_4-fcc. However, no crystalline metallic cobalt phase was identified. The diffuse rings present in the diffraction pattern of the **Co2** suggest an amorphous structure, in agreement with previously reported synthesis of amorphous CoNPs through similar colloidal methods.[23]

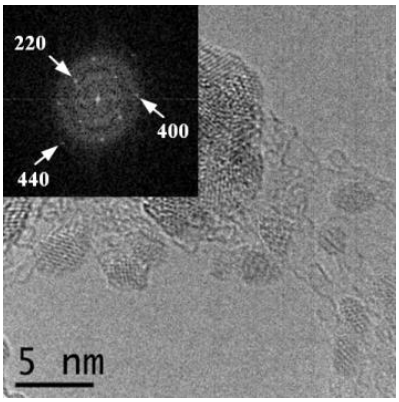

Figure 2. HRTEM image of **Co2** NPs and electron diffraction pattern.

Analysis of the XRD patterns obtained for **Co1-4** revealed in all cases the presence of at least three broad bands centred at 34º, 45º and 60º (Figure 3), which could not be unambiguously attributed to a specific metallic or oxide phase. Similar XRD patterns have been reported in the literature for CoNPs synthesized by chemical reduction using $NaBH_4$ as reducing agent.[23c,24] For instance, Torres *et al*. reported the synthesis of CoNPs of *ca*. 1 nm exhibiting XRD patterns with broad bands and attributed this effect to the small size of the CoNPs.[24] However, Pileni and co-workers attributed the broadness of XRD patterns of 7 nm CoNPs (also synthesized by chemical reduction) to their amorphous structure.[23c] Therefore, in view of these reports, the broad bands observed here could arise from the amorphous structure and/or due to the small size of the CoNPs.

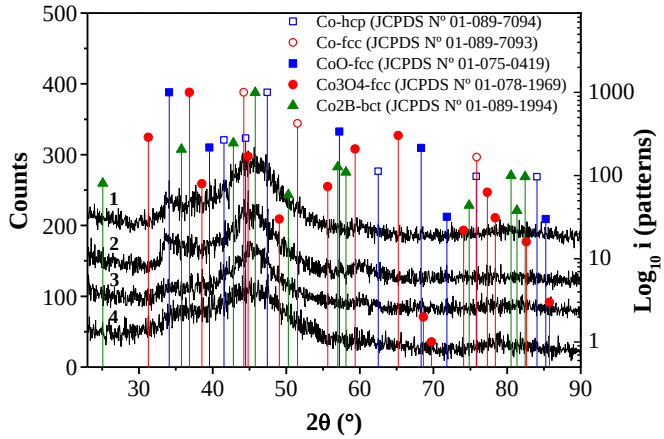

Figure 3. XRD patterns of cobalt nanocatalysts prepared under different PVP:Co ratios: (1) **Co1**, PVP:Co = 10; (2) **Co2**, PVP:Co = 20; (3) **Co3**, PVP:Co = 40 and (4) **Co4**, PVP:Co = 80.

Other authors ascribed a similar broad band centered at 45º to the amorphous structure of Co_2B also synthesized from chemical reduction of cobalt salts using sodium borohydride as reducing agent.[23b,25] The chemistry of the reaction between aqueous cobalt and sodium borohydride is quite complex, partly because metals such as Co catalyze the BH_4^- hydrolysis (Scheme 3).[26] For this reason the addition of a borohydride excess is usually required to completely reduce the metal salt.

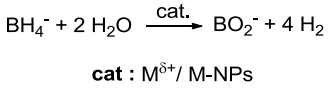

Scheme 3. Borohydride hydrolysis catalyzed by metal ions or metal nanoparticles.[27]

Glavee *et al.* reported that in aqueous solutions, the reduction of Co^{2+} with $NaBH_4$ yields Co_2B as the primary product if the two reagents are rapidly mixed and the product is handled under anaerobic conditions, while the Co_2B is converted to

metallic Co particles and boron oxide under aerobic conditions (Scheme 4a and b respectively).[27-28]

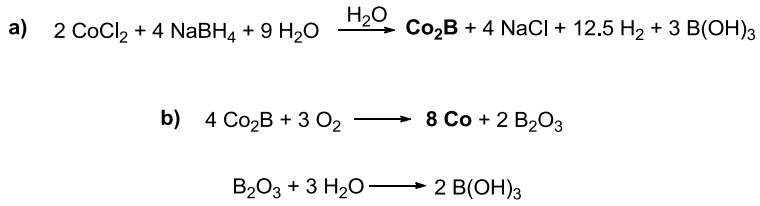

Scheme 4. Formation of (a) Co_2B or (b) CoNPs depending on the handling atmosphere during the synthesis.[27]

The same authors reported an experimental procedure to determine the nature of this type of materials through the thermal treatment of the NPs under inert atmosphere followed by the analysis of the crystalline structure of the resulting species since this treatment forces the crystallization of the NPs.[28a]

To clarify any ambiguity about the nature of the materials obtained in this work, the procedure described by Glavee *et al*. was applied on **Co2**. For this purpose, **Co2** was brought to 500 ºC within 2-5 min under argon flow and kept at this temperature for 2 h, after which the solid was allowed to rapidly cool to ambient temperature (5-10 min). The diffraction pattern of the thermal treated sample exhibited only fcc and hcp cobalt crystalline phases together with a defined pattern of $B(OH)_3$ (Figure 4). It was therefore concluded that **Co1-4** correspond to a mixture of cobalt, cobalt oxide and $B(OH)_3$ amorphous phases.

Surface analysis of the CoNPs synthesized in this study was performed by X-ray photoelectron spectroscopy (XPS). The full XPS spectra of **Co1-4** revealed the presence of Na, Co, O, N, C and B, according to the peaks observed at their characteristic binding energies (1071.6; 781.5; 530.9; 399.2; 284.5 and 191.1 eV respectively). The Co 2p XPS spectrum of the series **Co1-4** exhibits two sets of peaks at *ca.* 777-794 and 795-806 eV readily assigned to Co $2p_{3/2}$ and Co $2p_{1/2}$, respectively. Each region was readily deconvoluted in three bands corresponding to

metallic cobalt, Co^{2+} (CoO) and a prominent shake-up satellite located at around 785 or 801 eV (Figure 5).[29]

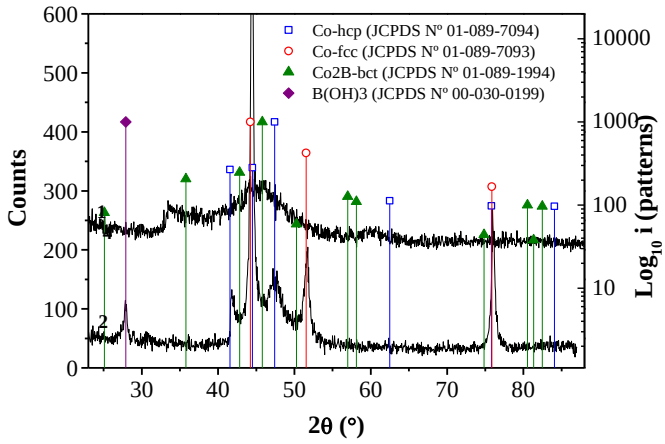

Figure 4. XRD patterns of **Co2** before (1) and after (2) thermal treatment at 500 ºC for 2h under argon.

The fractions of Co^0 and Co^{2+} resulting from the deconvolution of the Co $2p_{3/2}$ spin orbit peaks are displayed in Table 2. According to these data, the content of Co^0 increases from 23 to 38% when the PVP:Co ratio was increased from 10 to 80. This observation agrees with previous reports which suggested that NPs synthesized at higher PVP:metal ratios are less susceptible to water or oxygen oxidation due to the protective effect of a larger polymer shell.[20a]

Furthermore, the B 1s XPS spectra of the series **Co1-4** were similar and exhibited the presence of two bands at 187.97 and 191.6. These bands were assigned to elemental boron and borates respectively according to reported data (BO_2^- BE= 191.8 eV[30]).[31]

Quantification of the content of cobalt and boron in **Co1-4** was performed by ICP (Table 3). The Co/B atom ratio for the series of CoNPs was in the range between 2.5-2.9. Curiously, Kou and co-workers reported Co/B values of *ca.* 0.2 for CoNPs of 14 ± 6 nm synthesized using $NaBH_4$ as reducing agent in water. Such low values suggest a considerably higher boron content in comparison to the observed in

Co1-4, which can be attributed, according to Glavee's report, to the anaerobic conditions used by Kou *et al.* for the synthesis of the CoNPs.[15]

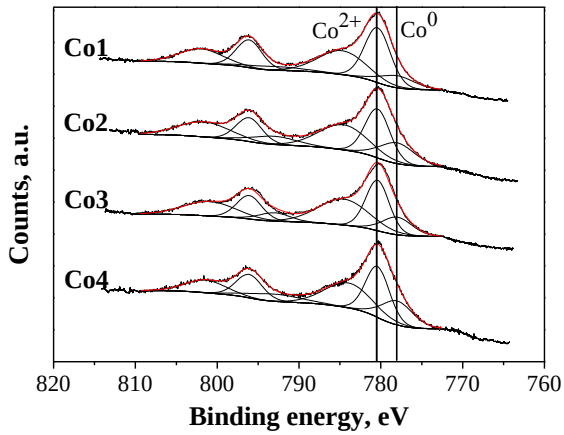

Figure 5. Co 2p XPS spectra of **Co1-4** NPs.

Table 2. Percentage of Co species in colloidal NPs from XPS spectra decomposition.[a]

Entry	NPs	PVP:Co	Co^0	Co^{2+}
1	**Co1**	10	23	77
2	**Co2**	20	37	63
3	**Co3**	40	31	69
4	**Co4**	80	38	62

[a] Percentages corresponding to the Co $2p_{3/2}$ spin orbit peaks. [b] **Co2** NPs after FTS using water as solvent

Recently, Demirci and Miele reviewed the cobalt based catalysts for the hydrolysis of $NaBH_4$ and NH_3BH_3.[32] They discussed the different catalytic active phase of cobalt reported in previous literature and proposed a structure based on a core of cobalt covered by cobalt oxides and an outer shell of polyborates, $Co@B_\alpha O_\beta (OH)_\gamma$.[33]

Raman spectroscopy is frequently used for the characterization of cobalt oxide species present in cobalt or cobalt supported catalysts for FT.[29] The Raman spectra of the series **Co1-4** were all similar and displayed shifts at 196, 450, 492,

586 and 666 cm^{-1} that were assigned to cobalt oxide species (CoO) based on literature data.[34] This observation confirmed the high valent state of cobalt in these NPs. Interestingly, no signals for polymer could be detected.

Table 3. ICP data of **Co1-4** catalysts

Entry	NPs	PVP:Co	Co/B (atom ratio)[a]
1	**Co1**	10	2.62
2	**Co2**	20	2.79
3	**Co3**	40	2.52
4	**Co4**	80	2.90

Next, the presence of PVP at the surface of these CoNPs was investigated by FTIR spectroscopy. For the whole series of CoNPs, no band corresponding to either free or bound PVP could be detected. Apparently, the successive washing of the NPs by water could remove completely the PVP from the metal surface. This was confirmed by thermogravimetric analysis, which did not exhibit any weight loss in the range of temperatures corresponding to PVP decomposition (see Supporting Information, Figure S7). It was therefore concluded that no PVP is present at the surface of the isolated CoNPs **Co1-Co4**.

To summarize, CoNPs of sizes between 1.7 to 3.1 nm were synthesized using various PVP:Co ratios. These CoNPs contained both an amorphous structure of metallic cobalt and a crystalline cobalt oxide phase. No PVP was detected at the NPs surface by IR and TGA, independently of the PVP:Co ratio. Analysis of the composition of the CoNPs also revealed the presence of boron from the reducing agent.

IV.3.2. Fischer-Tropsch catalytic experiments

IV.3.2.1. Effect of the PVP:Co ratio using *in-situ* formed and isolated CoNPs

First, the CoNPs **Co1-4** were used following a reported procedure for RuNPs catalysed AFTS, which includes the *in-situ* synthesis of these nanocatalysts within the autoclave and the use of the synthetic mixture directly in catalysis using a H_2:CO= 2.[9,13] The results are summarized in Figure 6.

With all catalysts, FT activities of *ca*. 0.03 $mol_{CO}mol_{Co}^{-1}h^{-1}$ were measured, indicating that the PVP/Co ratio used during the synthesis of the NPs had little influence on their activity (Figure 6a). In terms of selectivity, high CO_2 selectivity (up to 68%) was observed, with similar values for CH_4 (up to 20%) and C_{2+} (up to 30%). It should be mentioned that the hydrocarbons produced under these conditions were in the C_{2-12} range with typical chain growth probability (α) values around 0.5 and olefin to paraffin ratios (O/P) of 0.6. No clear trends could be deduced for product selectivity as a function of the PVP:Co ratio.

Interestingly, at the end of the reactions, analysis of the gas phase revealed an increase in the ratio H_2:CO > 3. Such a variation of the syngas composition during catalysis suggested that an additional process was occurring with these catalytic systems and explained the low O/P ratio observed in the hydrocarbon products (0.6), in agreement with a hydrogen rich gas mixture.

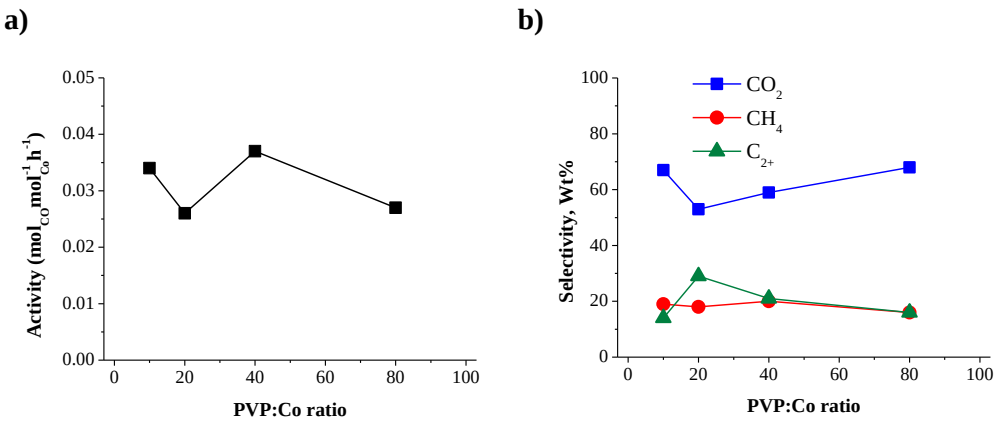

Figure 6. (a) Activity in $mol_{CO}.mol_{Co}^{-1}.h^{-1}$ and (b) product selectivity in wt% of **Co1-4** *in-situ* CoNPs. Conditions: 0.949 mmol Co, 30 bar H_2/CO/Ar (2:1:0,15); 66 ml water, 1000 rpm, 180 ºC, 12h

For the following experiments, the **Co1-4** NPs were isolated and re-dispersed in water prior to FT catalysis. The activity and product selectivity in FT for this series of CoNPs are displayed in Figure 7. Using **Co1** as catalyst (PVP:Co ratio of 10) activity of 0.016 $mol_{CO}mol_{Co}^{-1}h^{-1}$ was obtained. However, for the CoNPs synthesized in the presence of higher PVP:Co ratios (**Co2-4**), the activity increased

up to 0.025 $mol_{CO}mol_{Co}^{-1}h^{-1}$, similarly to those obtained with the *in-situ* formed CoNPs (Figure 6).

In terms of product selectivity, however, the FT products C_{2+} were mainly formed under these conditions, with constant selectivity of *ca.* 50% for the series (Figure 7b). No clear difference was observed in CH_4 selectivity, although a slight increase at higher PVP:Co ratio was observed (from 18 to 25%). In contrast, the CO_2 selectivity was *ca.* 20% and remained unchanged across the series. When compared to the values obtained with *in-situ* formed NPs (Figure 6), a decrease in CO_2 selectivity and increase in C_{2+} products were detected and associated to the isolation of the NPs prior to catalysis. Additionally, the alpha value obtained in general for the series of NPs was in the range of 0.61-0.67 with O/P ratios of 0.9. It is noteworthy that under these conditions, analysis of the gas phase at the end of the reactions showed that the final H_2:CO ratio was this time *ca*. 2.

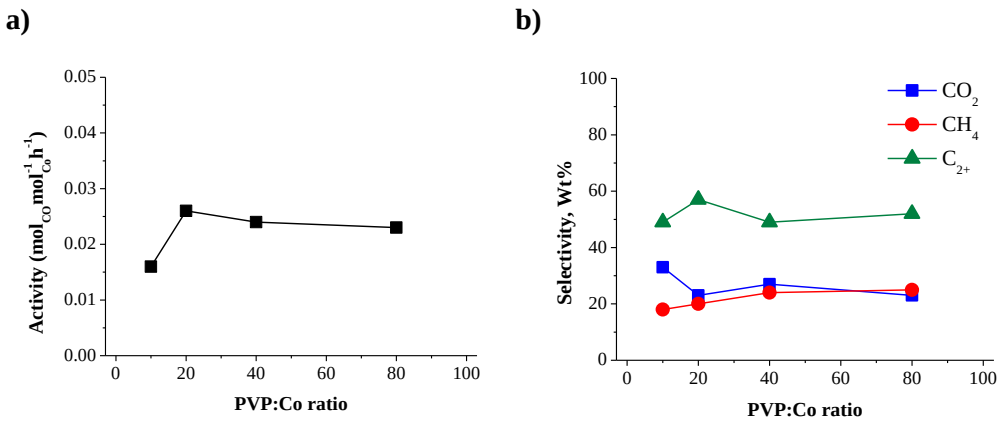

Figure 7. (a) Activity in $molCO.molCo^{-1}.h^{-1}$ and (b) product selectivity in wt% of **Co1-4** isolated CoNPs**.** Conditions: 0.949 mmol Co, 30 bar H_2/CO/Ar (2:1:0,15); 66 ml water, 1000 rpm, 180 ºC, 12h

When compared to the results reported by Kou and co-workers, similar activities and product distributions were observed, although significant differences were evidenced in terms of selectivity: CH_4 (40 vs. 25%), CO_2 (7 vs. 25%) and O/P ratio (0.6 vs. 0.9). Such variations were attributed to the differences in CoNPs size, structure (CoB_x or metallic cobalt phase) and composition (boron content).

The variations in size of the nanocatalysts before and after catalysis were monitored by TEM microscopy. However, no drastic changes in the size of **Co1-4** were observed after catalysis, suggesting that these catalysts are stable under these conditions. Furthermore, XRD analysis of the used catalysts also demonstrated no significant variations in their diffraction pattern compared with those of the fresh catalysts (Supporting Information, Figure S4). In contrast, Kou and co-workers reported a decreased of the CoNPs size from 14 ± 6 nm to 3.1 ± 1 nm after AFTS.

To conclude, large differences were observed in the product selectivity and final H_2:CO ratio comparing the *in-situ* formed CoNPs and the isolated CoNPs. Since the two series of NPs exhibit the same size, it was concluded that the presence of excess PVP and the products from $NaBH_4$ hydrolysis in solution during catalysis must be responsible for such variations

IV.3.2.2. Effect of the addition of PVP

First, we hypothesized that the large amounts of PVP remaining in solution from the synthesis when *in-situ* NPs were used as catalysts could be responsible for the selectivity variations described previously in this paper (Figure 6 *vs*. Figure 7). To corroborate this hypothesis, a series of solutions containing various concentrations of PVP were added over the isolated NPs **Co2** prior to catalysis. The amounts of PVP were adjusted to obtain PVP:Co ratio of 10, 20, 40 or 80 and the catalytic results compared with those obtained with isolated **Co2** without added PVP (Figure 8).

As shown in Figure 8, both the activity and selectivity remained constant when these PVP solutions were added. However, when a concentrated PVP solution corresponding to PVP:Co ratio of 80 was added, a decrease in activity was observed to *ca*. 0.02, together with an increase of CO_2 selectivity up to 46% and a decrease in C_{2+} selectivity down to 37%. This latter result could be explained by the increase of the viscosity of the reaction mixture at high concentration of PVP that would lower the diffusion of gases and result in a decrease in catalytic activity. A similar observation was reported for AFTS catalyzed by RuNPs.[10a]

It was therefore concluded that the presence of additional PVP during catalysis does not affect significantly the performance of the cobalt nanoparticles and could not explain the variations previously observed between in situ and isolated catalysts.

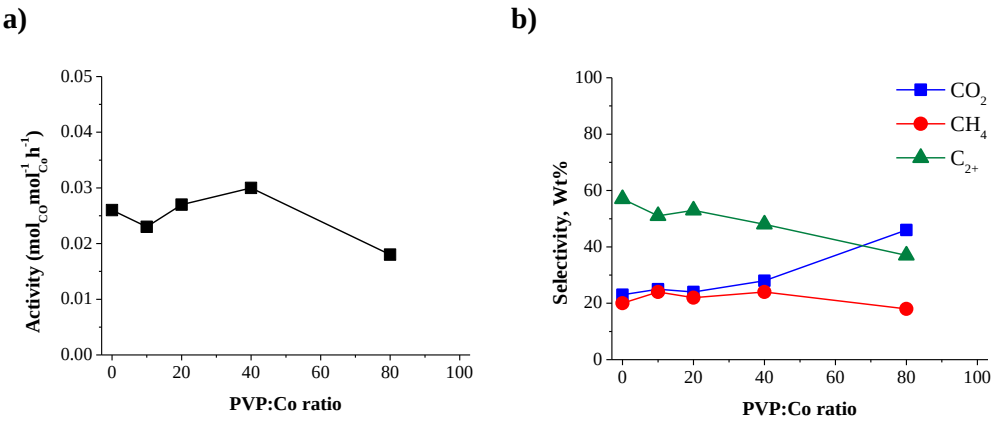

Figure 8. (a) Activity in molCO.molCo-1.h-1 and (b) product selectivity in wt% of isolated **Co1-4** NPs with addition of extra PVP. Conditions: 0.949 mmol Co, 30 bar H_2/CO/Ar (2:1:0,15); 66 ml water, 1000 rpm, 180 ºC, 12h.

IV.3.2.3. Effect of the pH

During the syntheses of the CoNPs **Co1-4** by chemical reduction using $NaBH_4$, an increase of the pH of the solution from 7 to 10 was observed. The amount of base present in solution after synthesis of the CoNPs was quantified by potentiometric titration of the remaining solution after magnetic decantation of the CoNPs. It was determined that 8 equivalents of base per mol of Co used in synthesis were produced (Supporting Information, Figure S6). Therefore, it was thought that the variation of pH of the catalytic medium could be responsible for the differences in the catalytic performance of *in-situ* formed CoNPs and isolated CoNPs. A series of experiments at different pHs were therefore carried out using *in-situ* formed NPs, but adjusting the pH to values comprised between 2.6 and 13 *via* the addition of aqueous solutions of HCl or NaOH.

The Figure 9a and 9b represent the activity and product selectivity obtained as a function of the pH using **Co2** as catalyst. The activity exhibited a volcano shape

behavior with maxima at pH around 12.6. It is noteworthy that this high activity at pH=12.6 (0.195 $mol_{CO}mol_{Co}^{-1}h^{-1}$) is *ca*. six times higher than the typical values obtained for these CoNPs (at pH=10).

The C_{2+} selectivity remained constant from pH=2.6 until 8.6 (50%), but at more basic pH, this selectivity decreased to 9% (Figure 9b). The CH_4 selectivity remained almost constant (*ca*. 30%) for pH values between 2 and 12, but exhibited an exponential increase for pH > 12. The CO_2 selectivity initially increased from 12 to 38% when the pH increases from 2 to 12.

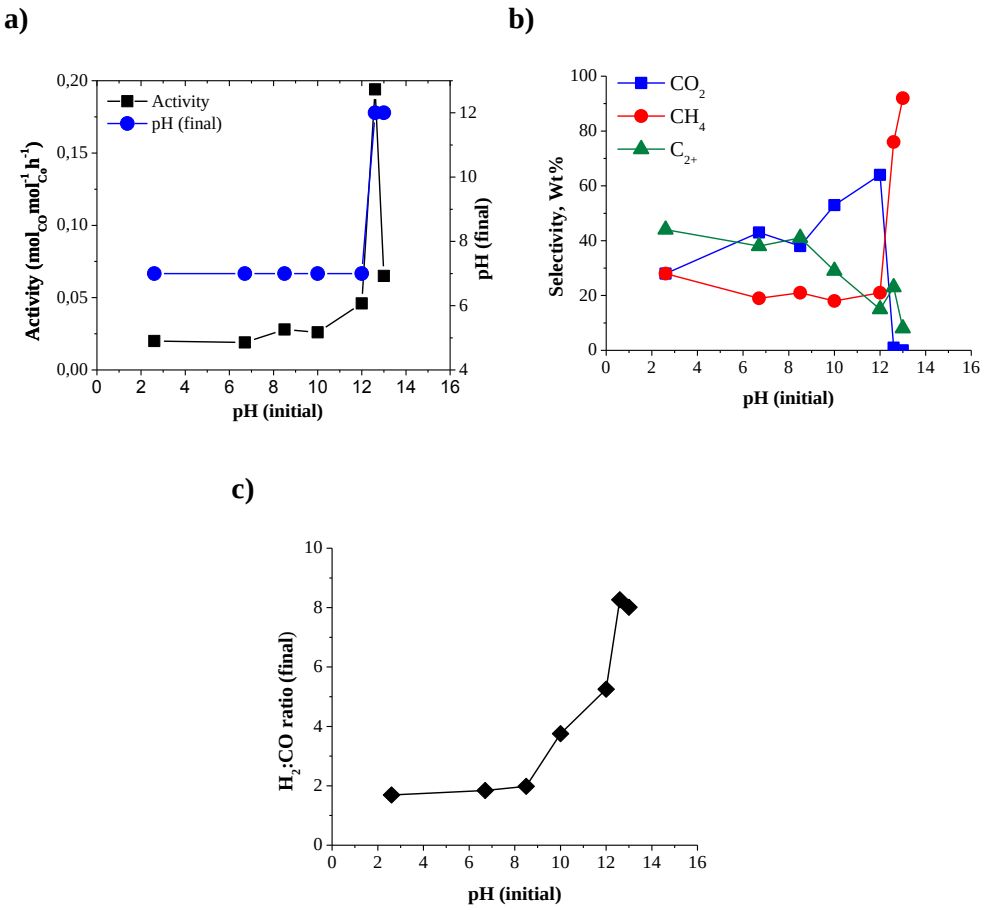

Figure 9. (a) Activity in $mol_{CO}.mol_{Co}^{-1}.h^{-1}$ and (b) product selectivity in wt% and (c) H_2:CO ratio after catalysis of *in-situ* **Co2** tested at different pHs**.** Conditions: 0.949 mmol Co, 30 bar H_2/CO/Ar (2:1:0,15); 66 ml water, 1000 rpm, 180 ºC, 12h.

Surprisingly, at higher pH values, complete suppression of the CO_2 was observed. Figure 9c displays the final H_2:CO ratio measured after 12h of catalysis as a function of the pH. Curiously, the final H_2:CO ratio was observed to be independent of the pH for values <8 (*ca.* 2) but increased exponentially at higher pHs and reached a maximum of *ca*. 8 at pH 12.

Interestingly, when a control experiment involving PVP (in the absence of Co catalyst) in water at pH=12 under FT conditions (180 °C, 30 bar syngas) during 12h, the H_2:CO ratio increased up to 3.4 at the end of the experiment and GC-analysis of the liquid phase showed the presence of large amounts of PVP decomposition products such as 1-ethylpyrrolidin-2-one and acetaldehyde (Scheme 5a). In contrast, when this experiment was repeated at pH=6, the syngas composition remained constant at *ca*. 2 (Scheme 5b).

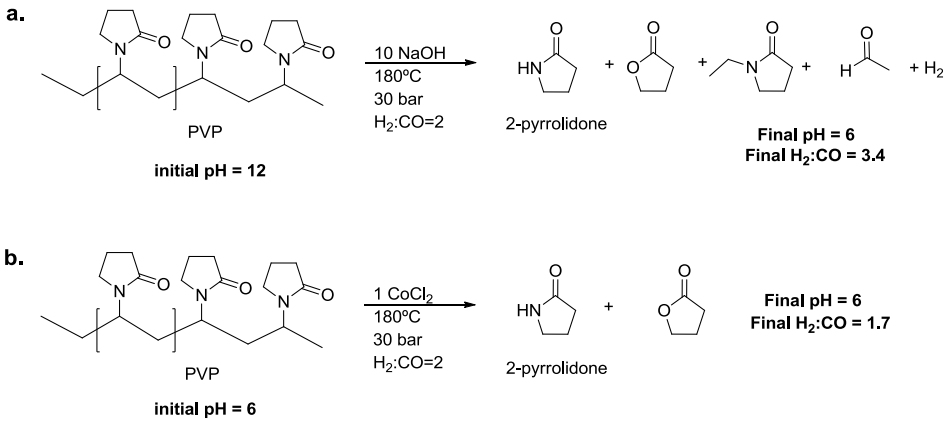

Scheme 5. PVP decomposition products detected in the organic phase during control experiments.

In this case, traces of 2-pyrrolidone and butyrolactone were also observed due to the decomposition of PVP under the reaction conditions.

It was therefore concluded that under catalytic conditions, the basic medium promotes the increase in H_2:CO ratio via decomposition of the PVP present in solution and that the Co nanocatalysts are not involved in this variation of syngas

composition. The decomposition of polymers such as cellulose has been reported to release H_2 during its hydrothermal gasification in presence of sodium hydroxide.[35]

The higher methane selectivity at basic pH, and consequently lower C_{2+}production, could thus be rationalized by the increase of the H_2:CO ratio during catalysis.[36] To investigate the possible effect of the presence of base in the reaction media without the interference of undesired side reactions, a series of experiments were carried out at different pH using previously isolated **Co2**.

Figure 10a and b describe the activity and the product selectivity obtained using **Co2** nanocatalyst as a function of the initial pH. Since the effect of acidic pH resulted negligible in the catalytic performance of this catalyst, only basic pHs were tested in this section (7-13.3). According to Figure 10a, the activity resulted constant from pH 7 to 12.6. For higher pHs, an exponential increase up to pH 13.2 was observed (0.186 $mol_{CO}mol_{Co}^{-1}h^{-1}$, corresponding to an addition of 11.8 eq. of NaOH *vs* Co), although increasing the pH to 13.3 resulted in a loss of activity (0.100 $mol_{CO}mol_{Co}^{-1}h^{-1}$). In terms of hydrocarbon selectivity, the C_{2+} selectivity decreased from 57 to 10% while the pH increased from 7 to 13.3. In contrast, the increase of pH from 7 to 13.1 resulted in the increase of the CO_2 selectivity from 23 to 68%. Curiously, for slightly higher pH (13.2 and 13.3), the CO_2 formation was completely suppressed. The methane selectivity remained constant within the range of pH 7 - 13.1, but suddenly increased up to 90% for higher pHs. Analysis of the gas phase after catalysis demonstrated that the H_2:CO ratio remained constant during catalysis in the range between pH 7 and 12.6, but increased up to 12 at pH 13.3 (Figure 10c).

To summarize, the increase in pH caused an increase in H_2:CO ratio during catalysis. An increase in CO_2 selectivity was also observed up to pH= 13.1 but was totally suppressed at higher pH while an increase in CH_4 selectivity was also observed. The higher WGS activity under basic conditions was previously reported in the literature[37] and could explain the initial increase in H_2 and CO_2 concentration. However, the suppression of CO_2 selectivity suggested that this product was transformed under very basic conditions.[38] The increase in CH_4 selectivity was related to the increase in H_2:CO ratio during the reaction, which was reported to favor the methane formation.[36]

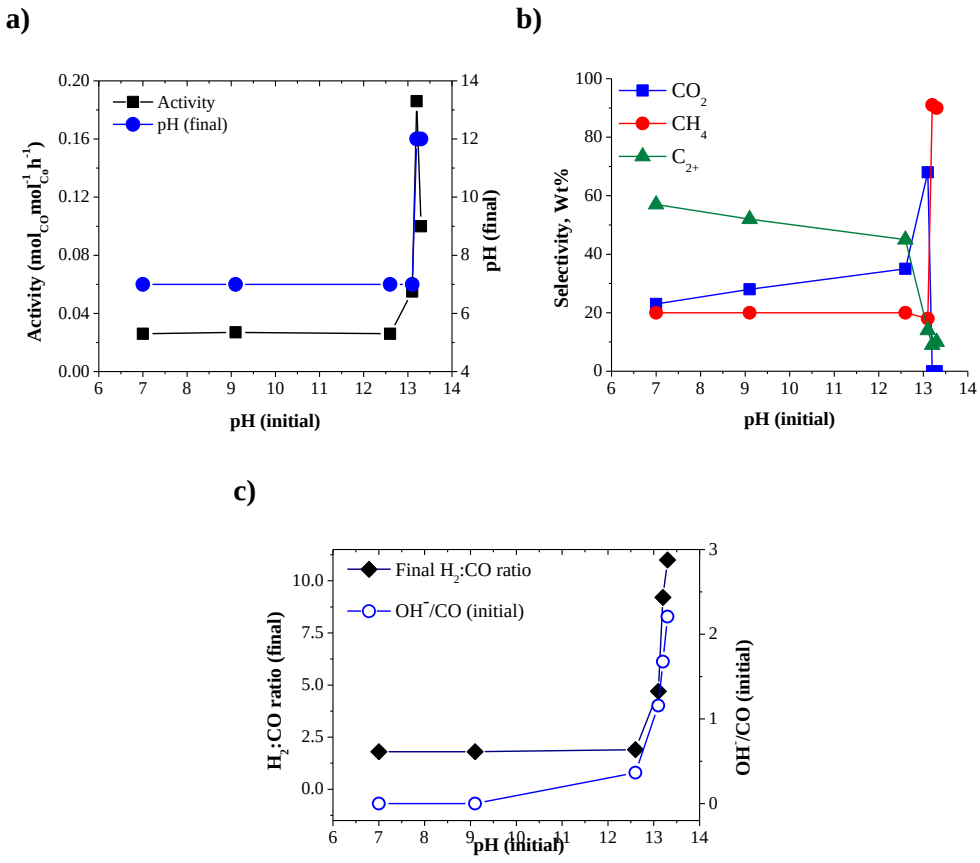

Figure 10. (a) Activity in $mol_{CO}.mol_{Co}^{-1}.h^{-1}$, **(b)** product selectivity in wt% and **(c)** H_2:CO ratio after catalysis of isolated **Co2** tested at different pHs. Conditions: 0.949 mmol Co, 30 bar H_2/CO/Ar (2:1:0,15); 66 ml water, 1000 rpm, 180 ºC, 12h

Analysis of the liquid phase after catalysis under basic conditions by ^{13}C NMR revealed the presence of formate HCO_2^- but carbonate species were not detected. This observation suggested the possibility of hydrogenation of the carbonate species into formate under FT conditions. To investigate the potential role of the CoNPs as catalysts for this transformation, the direct hydrogenation of HCO_3^- to formate was tested in presence of the CoNPs under basic FT conditions (15 mol% CoNPs; 5.40 mmol $NaHCO_3$ 10.80 mmol NaOH) and full conversion of HCO_3^- to HCO_2^- was observed according to ^{13}C NMR analysis of the resulting solution. To the best of our knowledge, this is the first example of carbonate hydrogenation to

formate catalyzed by CoNPs. This catalytic transformation has been mainly documented through homogenous organometallic catalysis[39] but there are some reports employing heterogeneous catalysts based on Pd.[40] In this study, the molecular / heterogenous nature of the catalyst was not investigated.

It is well known that the addition of sodium has a severe effect on FT performances and usually causes significant decrease of the catalytic activity, although no strong effect on the selectivity was reported.[41] Since the base used for these studies was NaOH, the possible influence of sodium on the colloidal catalyst **Co2** was evaluated through the use of a non-alkaline base and a catalytic experiment was performed under typical FT conditions at pH 11.3 using NH_4OH as the base. Using this base, similar results to those with NaOH were obtained and it was concluded that the presence of Na^+ in these experiments did not affect the catalytic performances of the CoNPs.

It was therefore concluded that the CO_2 produced by WGS reacted with hydroxyl groups under basic conditions to form carbonate which is in turn reduced to formate through hydrogenation catalysed by the CoNPs, as summarized in Scheme 6. Reaction (a) corresponds to the WGS reaction. Path (b) corresponds to the reaction between CO and hydroxide to yield sodium formate.[42] In (c) the CO_2 formed from WGS reacts with hydroxide to form carbonate species HCO_3^- or CO_3^-.[43] Finally (d) the carbonate species are hydrogenated into formate in the presence of the CoNPs.

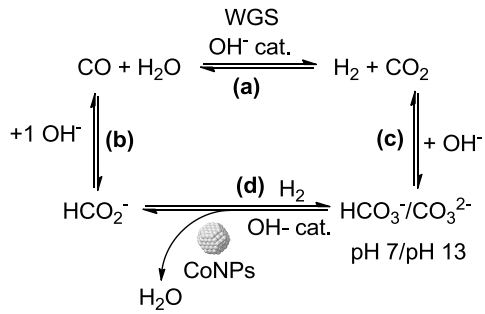

Scheme 6. Possible reaction pathways involved in the Co-catalyzed aqueous FTS performed under basic conditions.

IV.4. Conclusions

Small and well defined cobalt nanoparticles were synthesized in water using PVP as stabilizer and $NaBH_4$ as reducing agent. Small variations in the particle size between 1.7 and 3.1 nm were observed when the PVP:Co ratio varied from 10 to 80.

Surface analysis of the CoNPs by XPS indicated that the oxidation degree of the CoNPs depends on the PVP:Co ratio with a higher content in metallic cobalt when high PVP:Co ratios are used during the synthesis. Analysis by FTIR and TGA demonstrated that after work-up, no PVP remained at the surface of the CoNPs.

Relevant differences in activity and product selectivity were observed when *in-situ* or isolated CoNPs were tested in the AFTS. In this study, we showed that the pH increased during the NPs synthesis, which consequently affected the catalytic performance of the CoNPs. Indeed, at basic pH, the WGS activity was enhanced thus producing high amounts of H_2 and CO_2. The increase in H_2 partial pressure resulted in higher selectivity for methane while CO_2 reacts with hydroxide to form carbonate which is subsequently hydrogenated in the presence of CoNPs to form the corresponding formate. To the best of our knowledge, this is the first example of carbonate hydrogenation to formate catalyzed by CoNPs. This result opens the possibility to employ cobalt nanoparticles in the catalytic reduction of CO_2, a reaction of interest in current scientific research.

IV.5. Experimental Section

Synthesis of cobalt nanoparticles by chemical reduction method (Co1-4)

As a standard procedure, the cobalt salt was dissolved in H_2O containing the polymer (PVP-K30). Then, a solution of $NaBH_4$ (10 eq. $NaBH_4$/ eq. metal) in H_2O was added at room temperature during 5 minutes. The solution was maintained under a vigorous mechanical stirring for 2 h. Then, 100 µl of the colloidal solution was centrifuged, washed with water and re-dispersed by sonication. Three drops of the obtained colloidal solution were deposited on a Cu-formvar or holey carbon grids for TEM or HR-TEM analysis. Additional spectroscopic and crystallographic characterization of the CoNPs was performed using isolated NPs. For this purpose

the freshly prepared CoNPs were initially precipitated by a strong magnetic field (using a neodymium magnet) and the supernatant was decanted. Then, the decanted NPs were washed with 3 x 10ml of water, 3 x 10ml of absolute ethanol and 3 x 10 ml of hexane. The resulted CoNPs were finally dried overnight under vacuum and kept in the dry box prior to the respective analysis.

- **Co1:** was synthesized according to the general procedure using $CoCl_2 6H_2O$ (0.226 g, 0.931 mmol) in presence of PVP-K30 (1.033 g, PVP:Co=10, based in monomers per cobalt) dissolved in 50 ml of deionized water ([Co] = 0.018 M). $NaBH_4$ (0.358 g, 9.369 mmol) was dissolved in 16.6 ml ([$NaBH_4$] = 0.550 M).

  TEM: D = 3.13 ± 1.58 nm.

  XRD: 45, 35 and 60º

  XPS: Co^0, 23%; Co^{2+}, 77%.

  TGA: Temperature ºC/Δ wt. % (attribution); 72/-3.5 (solvent), 246/-3.7 (polymer), 360/-0.13 (polymer), 900end/+1.16

  ICP: Co, 74.8 wt%, B, 5.7 wt%; Co/B atom ratio, 2.62

  FTIR: 3478, 1620, 1430 cm^{-1}.

  RAMAN: 653, 585, 491, 447 cm^{-1}.

- **Co2:** was synthesized according to the general procedure using $CoCl_2 6H_2O$ (0.226 g, 0.931 mmol) in presence of PVP-K30 (2.066 g, PVP:Co=20) dissolved in 50 ml of deionized water ([Co] = 0.018 M). $NaBH_4$ (0.358 g, 9.369 mmol) was dissolved in 16.6 ml ([$NaBH_4$] = 0.550 M).

  TEM: D = 2.64 ± 0.92 nm.

  HR-TEM: *ca.* 2.6 nm; detection of CoO-fcc and Co_3O_4-fcc.

  XRD: 45, 35 and 60º

  XPS: Co^0, 37%; Co^{2+}, 63%.

  TGA: Temperature ºC/Δ wt. % (attribution); 70/-3.5 (solvent), 244/-3.7 (polymer), 900end/+0.92.

  ICP: Co, 82.4 wt%, B, 5.9 wt%; Co/B atom ratio, 2.79

  FTIR: 3477, 1644, 1425 cm^{-1}.

  RAMAN: 666, 586, 492, 450, 196 cm^{-1}.

- **Co3:** was synthesized according to the general procedure using $CoCl_2 6H_2O$ (0.226 g, 0.931 mmol) in presence of PVP-K30 (4.132 g, PVP:Co=40) dissolved in 50 ml of deionized water ([Co] = 0.018 M). $NaBH_4$ (0.358 g, 9.369 mmol) was dissolved in 16.6 ml ([$NaBH_4$] = 0.550 M).

  TEM: D = 2.11 ± 0.41 nm.

  XRD: 45, 34 and 60º

  XPS: Co^0, 31%; Co^{2+}, 69%.

  TGA: Temperature ºC/Δ wt. % (attribution); 81/-3.3 (solvent), 238/-2.9 (polymer), 900end/+0.9.

  ICP: Co, 79.0 wt%, B, 6.3 wt%; Co/B atom ratio, 2.52

  FTIR: 3465, 1644, 1425 cm^{-1}.

  RAMAN: 665, 593, 502, 454, 173 cm^{-1}.

- **Co4:** was synthesized according to the general procedure using $CoCl_2 6H_2O$ (0.226 g, 0.931 mmol) in presence of PVP-K30 (8.264 g, PVP:Co=80) dissolved in 50 ml of deionized water ([Co] = 0.018 M). $NaBH_4$ (0.358 g, 9.369 mmol) was dissolved in 16.6 ml ([$NaBH_4$] = 0.550 M).

  TEM: D = 1.71 ± 0.73 nm.

  XRD: 45, 34 and 60º

  XPS: Co^0, 38%; Co^{2+}, 62%.

  TGA: Temperature ºC/Δ wt. % (attribution); 72/-0.9 (solvent), 198/-1.7 (polymer), 446/-0.25 (polymer), 900end/+1.25.

  ICP: Co, 82.7 wt%, B, 5.7 wt%; Co/B atom ratio, 2.9

  FTIR: 3447, 1639, 1421 cm^{-1}.

  RAMAN: 666, 600, 506, 464, 186 cm^{-1}.

Fischer-Tropsch catalytic experiments

The FT experiments were performed according to reported methods.[9,44] For the catalytic experiments, two methodologies were used:

- *For the experiments using "in-situ" prepared nanoparticles.*

In a typical experiment, after the synthesis of the Co-NPs (from 0.93 mmol $CoCl_2$) within the autoclave, the system was purged three times with Ar, and sealed

at a pressure of 1.5 bar. 10 bar CO and 20 bar H_2 were then added providing a final pressure of 31.5 bar (H_2:CO:Ar = 2:1:0.15) and the autoclave was heated at 180 ºC under mechanical stirring at 1000 rpm during 12h. At this point, the autoclave was cooled to room temperature prior to gas analysis. All the components contained in the gas phase (CO, H_2, Ar, CO_2, and C_1-C_8 hydrocarbons) were analyzed by GC-TCD and quantified using calibration curves for each component. The compounds present in the aqueous phase were extracted with dichloromethane (10 ml) containing 1 µl of bicyclohexyl as internal standard. The organic phase containing the hydrocarbon and oxygenated products were analyzed by GC-MS. The identification and quantification of products was performed by comparison with standards using calibration curves for each compound.

- *For the FT experiments using "isolated" nanoparticles:*

Freshly synthesized Co-NPs (0.93 mmol Co, as described above) were magnetically decanted and washed three times with water and then re-dispersed in 66 ml of water. The obtained suspension of CoNPs was finally transferred to the autoclave using a Teflon liner. The autoclave was then purged with Ar and charged with a mixture of Ar (1.5 bar) and syngas (30 bar, H_2:CO= 2:1) and the catalytic experiment carried out following the procedure described above.

IV.6. Acknowledgements

The authors are grateful to Total S.A., the Spanish Ministerio de Economía y Competitividad (CTQ2013-43438-R, and *Ramon y Cajal* fellowship to C. Godard) and the Generalitat de Catalunya (2014SGR670) for financial support.

IV.7. References

[1] Calderone, V. R.; Shiju, N. R.; Curulla-Ferré, D.; Chambrey, S.; Khodakov, A.; Rose, A.; Thiessen, J.; Jess, A.; Rothenberg, G. *Angew. Chem. Int. Ed.* **2013**, *52*, 4397-4401.

[2] Khodakov, A. Y. *Catal. Today* **2009**, *144*, 251-257.

[3] (a) A. Steynberg; Dry., M.; Elsevier, 152: 2006.(b) *Fischer-Tropsch synthesis, catalysts and catalysis*; B.H. Davis; Occelli, M. L., Eds.; Elsevier, 163, 2007.(c) Zhang, Q.; Kang, J.; Wang, Y. *ChemCatChem* **2010**, *2*, 1030-1058.

[4] *The Fischer–Tropsch Synthesis, Academic*; Anderson, R. B., Ed.; Academic Press: London, 1984.

[5] (a) Cheng, K.; Kang, J.; Huang, S.; You, Z.; Zhang, Q.; Ding, J.; Hua, W.; Lou, Y.; Deng, W.; Wang, Y. *ACS Catalysis* **2012**, *2*, 441-449.(b) Hong, J.; Chernavskii, P. A.; Khodakov, A. Y.; Chu, W. *Catal. Today* **2009**, *140*, 135-141.(c) Kang, J. S.; Awate, S. V.; Lee, Y. J.; Kim, S. J.; Park, M. J.; Lee, S. D.; Hong, S.-I.; Moon, D. J. *J Nanosci Nanotech* **2010**, *10*, 3700-3704.(d) Khodakov, A. Y.; Bechara, R.; Griboval-Constant, A. *App. Catal. A-Gen* **2003**, *254*, 273-288.(e) Reuel, R. C.; Bartholomew, C. H. *J. Catal.* **1984**, *85*, 63-77.

[6] (a) Bechara, R.; Balloy, D.; Vanhove, D. *App. Catal. A-Gen* **2001**, *207*, 343-353.(b) Borg, Ø.; Dietzel, P. D. C.; Spjelkavik, A. I.; Tveten, E. Z.; Walmsley, J. C.; Diplas, S.; Eri, S.; Holmen, A.; Rytter, E. *J. Catal.* **2008**, *259*, 161-164.(c) Borg, Ø.; Eri, S.; Blekkan, E. A.; Storsæter, S.; Wigum, H.; Rytter, E.; Holmen, A. *J. Catal.* **2007**, *248*, 89-100.(d) Xiong, H.; Zhang, Y.; Wang, S.; Li, J. *Catal. Commun.* **2005**, *6*, 512-516.

[7] Sousa-Aguiar, E. F.; Noronha, F. B.; Faro, J. A. *Catal. Sci. Technol.* **2011**, *1*, 698-713.

[8] Astruc, D.; Lu, F.; Aranzaes, J. R. *Angew. Chem. Int. Ed.* **2005**, *44*, 7852-7872.

[9] Xiao, C.-x.; Cai, Z.-p.; Wang, T.; Kou, Y.; Yan, N. *Angew. Chem. Int. Ed.* **2008**, *47*, 746-749.

[10] (a) Liu, L.; Sun, G.; Wang, C.; Yang, J.; Xiao, C.; Wang, H.; Ma, D.; Kou, Y. *Catal. Today* **2012**, *183*, 136-142.(b) Wang, C.; Zhao, H.; Wang, H.; Liu, L.; Xiao, C.; Ma, D. *Catal. Today* **2012**, *183*, 143-153.

[11] (a) Pendyala, V.; Jacobs, G.; Luo, M.; Davis, B. *Catal. Lett.* **2013**, *143*, 395-400.(b) Quek, X.-Y.; Guan , Y.; van Santen, R. A.; Hensen, E. J. M. *ChemCatChem* **2011**, *3*, 1735-1738.

[12] Quek, X.-Y.; Pestman, R.; van Santen, R. A.; Hensen, E. J. M. *ChemCatChem* **2013**, *5*, 3148-3155.

[13] Gual, A.; Delgado, J. A.; Godard, C.; Castillón, S.; Curulla-Ferré, D.; Claver, C. *Top. Catal.* **2013**, *56*, 1208-1219.

[14] Fan, X.-B.; Tao, Z.-Y.; Xiao, C.-X.; Liu, F.; Kou, Y. *Green Chem.* **2010**, *12*, 795-797.

[15] Wang, H.; Kou, Y. *Chin. J. Catal.* **2013**, *34*, 1914-1925.

[16] Wang, H.; Zhou, W.; Liu, J.-X.; Si, R.; Sun, G.; Zhong, M.-Q.; Su, H.-Y.; Zhao, H.-B.; Rodriguez, J. A.; Pennycook, S. J.; Idrobo, J.-C.; Li, W.-X.; Kou, Y.; Ma, D. *J. Am. Chem. Soc.* **2013**, *135*, 4149-4158.

[17] Yan, N.; Zhang, J.-g.; Tong, Y.; Yao, S.; Xiao, C.; Li, Z.; Kou, Y. *Chem. Commun.* **2009**, 4423-4425.

[18] (a) Scariot, M.; Silva, D. O.; Scholten, J. D.; Machado, G.; Teixeira, S. R.; Novak, M. A.; Ebeling, G.; Dupont, J. *Angew. Chem. Int. Ed.* **2008**, *47*, 9075-9078.(b) Silva, D. O.; Scholten, J. D.; Gelesky, M. A.; Teixeira, S. R.; Dos Santos, A. C. B.; Souza-Aguiar, E. F.; Dupont, J. *ChemSusChem* **2008**, *1*, 291-294.

[19] Silva, D. O.; Luza, L.; Gual, A.; Baptista, D. L.; Bernardi, F.; Zapata, M. J. M.; Morais, J.; Dupont, J. *Nanoscale* **2014**, *6*, 9085-9092.

[20] (a) Chen, Y.; Liew, K. Y.; Li, J. *Appl. Surf. Sci.* **2009**, *255*, 4039-4044.(b) Chou, K.-S.; Chang, Y.-C.; Chiu, L.-H. *Ind. Eng. Chem. Res.* **2012**, *51*, 4905-4910.(c) Seoudi, R.; Shabaka, A.; El Sayed, Z. A.; Anis, B. *Physica E* **2011**, *44*, 440-447.

[21] Lu, L. T.; Tung, L. D.; Robinson, I.; Ung, D.; Tan, B.; Long, J.; Cooper, A. I.; Fernig, D. G.; Thanh, N. T. K. *J. Mater. Chem.* **2008**, *18*, 2453-2458.

[22] Reetz, M. T. In *Nanoparticles and Catalysis*; Wiley-VCH Verlag GmbH & Co. KGaA: 2008, p 253-277.

[23] (a) Chuan Wu; Chun Hui Pang; Feng Wu; Ying Bai; Chi Chen; Zhong, Y. *Adv. Mat. Res.* **2011**, *391-392*, 1085.(b) Mitov, M.; Popov, A.; Dragieva, I. *J. Appl. Electrochem.* **1999**, *29*, 59-63.(c) Petit, C.; Wang, Z. L.; Pileni, M. P. *J. Phys. Chem. B* **2005**, *109*, 15309-15316.

[24] Garcia-Torres, J.; Vallés, E.; Gómez, E. *J. Nanopart. Res.* **2010**, *12*, 2189-2199.

[25] Patel, N.; Fernandes, R.; Miotello, A. *J. Catal.* **2010**, *271*, 315-324.

[26] Muir, S. S.; Yao, X. *Int. J. Hydrogen Energy* **2011**, *36*, 5983-5997.

[27] Glavee, G. N.; Klabunde, K. J.; Sorensen, C. M.; Hadjapanayis, G. C. *Langmuir* **1992**, *8*, 771-773.

[28] (a) Glavee, G. N.; Klabunde, K. J.; Sorensen, C. M.; Hadjipanayis, G. C. *Langmuir* **1993**, *9*, 162-169.(b) Glavee, G. N.; Klabunde, K. J.; Sorensen, C. M.; Hadjipanayis, G. C. *Inorg. Chem.* **1993**, *32*, 474-477.

[29] Khodakov, A. Y.; Chu, W.; Fongarland, P. *Chem. Rev.* **2007**, *107*, 1692-1744.

[30] Hensley, D. A.; Garofalini, S. H. *Appl. Surf. Sci.* **1994**, *81*, 331-339.

[31] Arzac, G. M.; Rojas, T. C.; Fernández, A. *ChemCatChem* **2011**, *3*, 1305-1313.

[32] Demirci, U. B.; Miele, P. *Phys. Chem. Chem. Phys.* **2014**, *16*, 6872-6885.

[33] Akdim, O.; Demirci, U. B.; Miele, P. *Int. J. Hydrogen Energy* **2011**, *36*, 13669-13675.

[34] Jongsomjit, B.; Sakdamnuson, C.; Goodwin, J. G.; Praserthdam, P. *Catal. Lett.* **2004**, *94*, 209-215.

[35] Onwudili, J. A.; Williams, P. T. *Int. J. Hydrogen Energy* **2009**, *34*, 5645-5656.

[36] Van Der Laan; and, G. P.; Beenackers, A. A. C. M. *Catal. Rev.* **1999**, *41*, 255-318.

[37] (a) Elliott, D. C.; Hallen, R. T.; Sealock, L. J. *Ind. Eng. Chem. Prod. Res. Dev.* **1983**, *22*, 431-435.(b) Elliott, D. C.; Sealock, L. J. *Ind. Eng. Chem. Prod. Res. Dev.* **1983**, *22*, 426-431.

[38] Tepe, J. B., Dodge, B.F. *Trans. Am. Inst. Chem. Eng.* **1943**, *39*, 255-276.

[39] Wang, W.; Wang, S.; Ma, X.; Gong, J. *Chem. Soc. Rev.* **2011**, *40*, 3703-3727.

[40] Wiener, H.; Blum, J.; Feilchenfeld, H.; Sasson, Y.; Zalmanov, N. *J. Catal.* **1988**, *110*, 184-190.

[41] Patanou, E.; Lillebø, A. H.; Yang, J.; Chen, D.; Holmen, A.; Blekkan, E. A. *Ind. Eng. Chem. Res.* **2013**, *53*, 1787-1793.

[42] Boswell, M. C.; Dickson, J. V. *J. Am. Chem. Soc.* **1918**, *40*, 1779-1786.

[43] Yoo, M.; Han, S.-J.; Wee, J.-H. *J. Environ. Manage.* **2013**, *114*, 512-519.

Supporting Information for:

Aqueous phase Fischer-Tropsch synthesis catalyzed by Co nanoparticles: Effect of NPs preparation and pH on catalyst activity and selectivity

Materials and Methods

All syntheses of CoNPs were carried under aerobic conditions using a mechanical stirrer. Milli-Q water was used for all the experiments. Solvents were purchased from Merck and used as received. $CoCl_2 \cdot 6H_2O$, $NaBH_4$ and PVP K-30 and were purchased from Sigma-Aldrich. Hydrogen (5.0) was purchased from Air Liquide and CO (4.7) and argon (5.0) from Carburos Metálicos.

Transmission electron microscopy (TEM) measurements were performed at the "Unitat de Microscopia dels Serveis Cientificotècnics de la Universitat Rovira I Virgili" in Tarragona with Zeiss 10 CA electron microscope operated at 100 kV with resolution of 3 Å. High resolution electron microscopy (HRTEM) measurements were performed at the "Centres Científics i Tecnològics de la UB" in Barcelona with a JEOL 2011(FEG) electron microscope operated at 200 kV with a point resolution of 2 Å.

FTIR spectra were acquired from KBr discs on a Bruker Equinox 55 Spectrometer using Opus software. Raman spectra was acquired by scattering of a 514nm Ar lamp on a Renishaw InVia Raman microscope using a x50LW objective, 60s of exposition time and 100% of laser intensity.

XPS experiments were performed in a PHI 5500 Multitechnique System (from Physical Electronics) with a monochromatic X-ray source (Aluminium Kalfa line of 1486.6 eV energy and 350 W), placed perpendicular to the analyzer axis and calibrated using the 3d5/2 line of Ag with a full width at half maximum (FWHM) of 0.8 eV. The analized area was a circle of 0.8 mm diameter, and the selected resolution for the spectra was 187.5eV of Pass Energy and 0.8 eV/step for the general spectra and 23.5 eV of Pass Energy and 0.1 eV/step for the spectra of the different elements in the depth profile spectra. A low energy electron gun (less than 10 eV) was used in order to discharge the surface when necessary. All Measurements were made in a ultra high vacuum (UHV) chamber pressure between $5x10^{-9}$ and $2x10^{-8}$ torr.

XRD measurements were made using a Siemens D5000 diffractometer (Bragg-Brentano parafocusing geometry and vertical θ-θ goniometer) fitted with a curved graphite diffracted-beam monochromator, incident and diffracted -beam Soller slits, a 0.06º receiving slit and scintillation counter as a detector. The angular 2θ diffraction range was between 25 and 120º. The data were collected with an angular step of 0.05º at 16s per step and sample rotation. A low background Si(510) wafer was used as sample holder. $Cu_{k\alpha}$ radiation was obtained from a copper X-ray tube operated at 40 kV and 30 mA.

GC-TCD analyses were carried out on an Agilent 7890A GC using a system with three columns: Hayesep Q (3ft x 1/8 in), HP-Molesieve (30m x 0.320 mm x 12 µm) and HP-Plot/Q (30m x 0.320 mm x 20 µm) using helium as carrier gas. GC-MS analyses were performed on a 9575C MSD system (Agilent) using a HP-Innowax capillary column (30m x 0.250 mm x 0.15 µm), using helium as carrier gas. Standard reference of gases (CO, CO_2, H_2, N_2) and hydrocarbons (C_1-C_5) was purchased from Avello Linde.

Thermogravimetric analysis (TGA) were performed at the "Centres Científics i Tecnològics de la UB" in Barcelona with a thermobalance (Mettler TGA/SDTA851e) equipped with a gas flow system. A 2-6 mg sample was heated in an alumina crisol in a flow of nitrogen. Then the catalyst was heated under a 50 ml/min of nitrogen flow from 30 ºC to 900 ºC (heat rate: 10 ºC/min).

Product analysis

All the hydrocarbon products were identified by comparison with reference samples.

The components contained in the gas phase (CO, H_2, Ar, CO_2, and C_1-C_8 hydrocarbons) were analysed on a Agilent 7890A GC using a system of three columns: Hayesep Q (3ft x 1/8 in), HP-Molesieve (30m x 0.320 mm x 12 µm) and HP-Plot/Q (30m x 0.320 mm x 20 µm) using helium as carrier gas. The quantification was carried out using calibration curves for each gas. Mixtures at different concentration of gases were prepared by gas blending from a standard reference of gases (Avello Linde).

The compounds present in the aqueous phase were extracted with dichloromethane (10 ml) containing 1 µl of bicyclohexyl as internal standard. The bottom organic phase containing the hydrocarbon and oxygenated products were analyzed immediately by GC-MS on a 9575C MSD system using a using a HP-Innowax capillary column (30m x 0.250 mm x 0.15 µm), and helium as carrier gas.

The identification and quantification of products was performed by comparison with standards using calibration curves for each compound.

Activity and Selectivity Calculations

The activity and selectivity was calculated based on the number of moles of carbon being formed as products according to the following formulas:

$$\text{Activity} = \frac{\text{total mol of C formed as products}}{\text{mol of Co} * \text{reaction time (h)}}$$

$$\text{Selectivity } Cn = \frac{\text{Wt } C_n}{\text{Wt of all products}}\ x\ 100$$

Figure S1. TEM micrographs and size distribution of **Co1-4** NPs: a) **Co1**, PVP:Co = 10, D = 3.13 ± 1.58 nm; b) **Co1**, PVP:Co = 10 after catalysis, D = 3.54 ± 1.41 nm; c) **Co2** , PVP:Co = 20, D = 2.64 ± 0.92 nm; d) **Co2**, PVP:Co = 20 after catalysis, D = 3.28 ± 1.17 nm; e) **Co3**, PVP:Co = 40, D = 2.11 ± 0.41 nm; f) **Co3**, PVP:Co = 40 after catalysis, D = 2.55 ± 0.98 nm; g) **Co4**, PVP:Co = 80, D = 1.71 ± 0.73 nm; h) **Co4**, PVP:Co = 80 after catalysis, D = 2.67 ± 0.81 nm.

a) **Co1**, PVP:Co = 10 before catalysis D = 3.13 ± 1.58 nm.

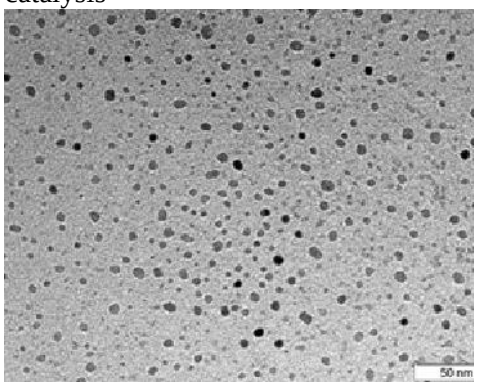

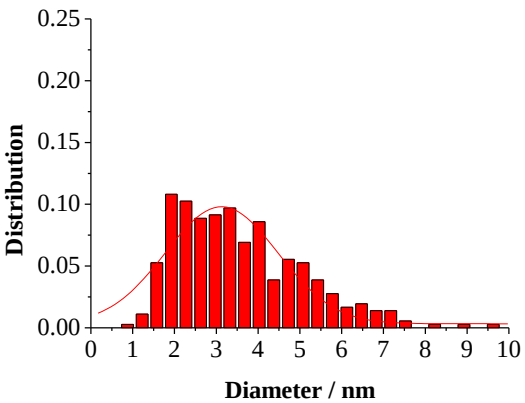

b) **Co1**, PVP:Co = 10 after catalysis D = 3.54 ± 1.41 nm.

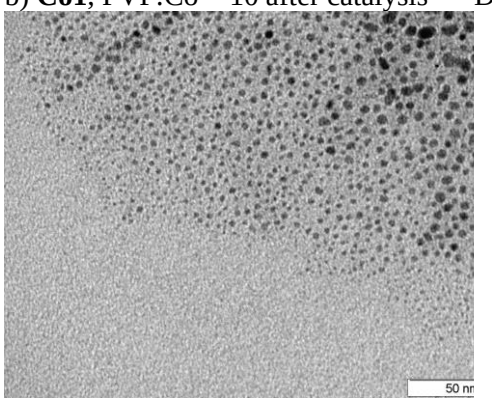

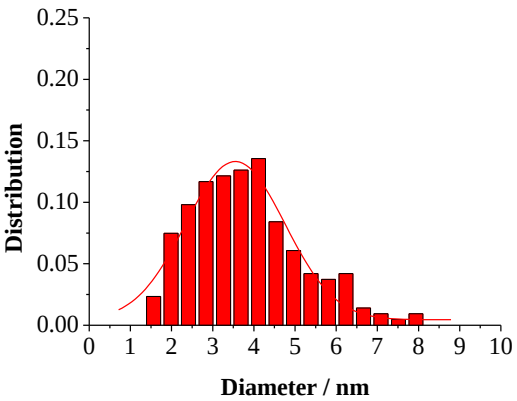

c) **Co2** , PVP:Co = 20 before catalysis D = 2.64 ± 0.92 nm.

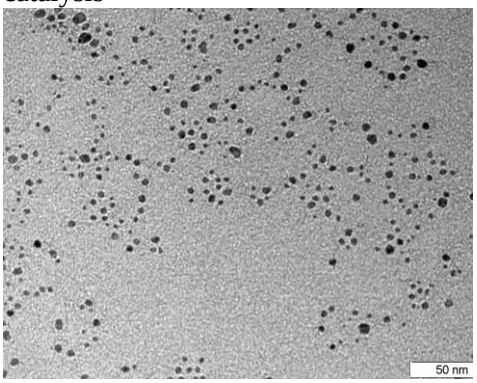

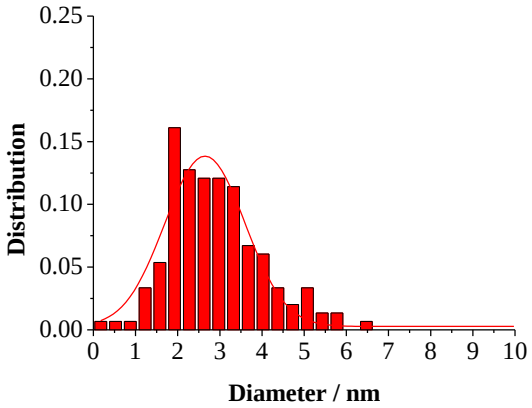

d) **Co2**, PVP:Co = 20 after catalysis D = 3.28 ± 1.17 nm.

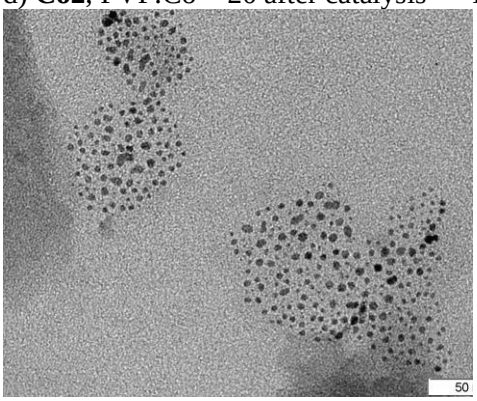

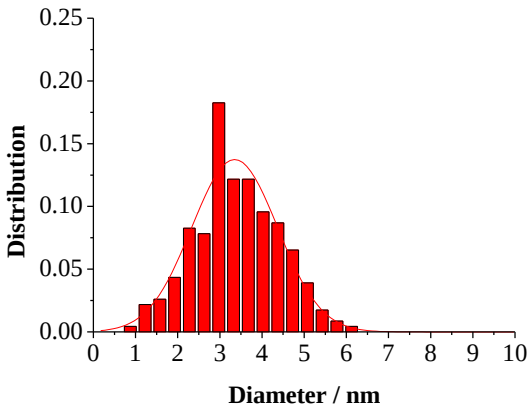

e) **Co3**, PVP:Co = 40 before catalysis D = 2.11 ± 0.41 nm.

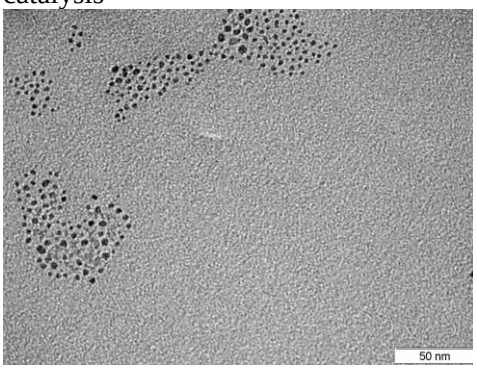

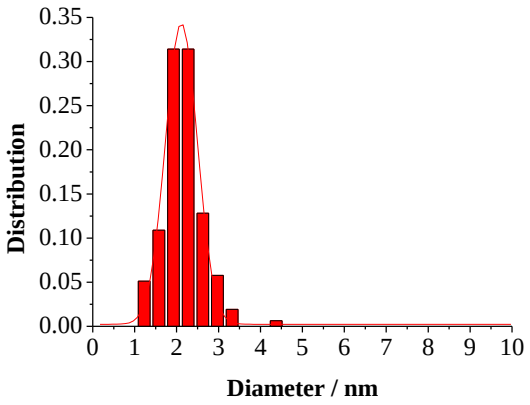

f) **Co3**, PVP:Co = 40 after catalysis D = 2.55 ± 0.98 nm.

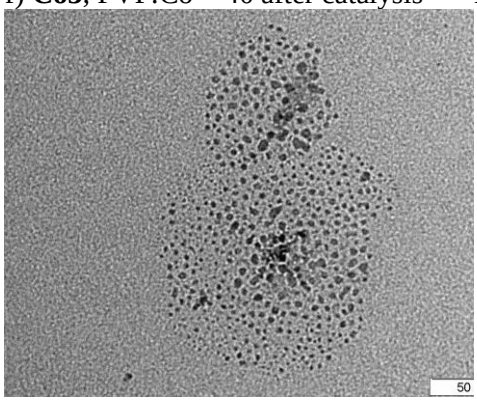

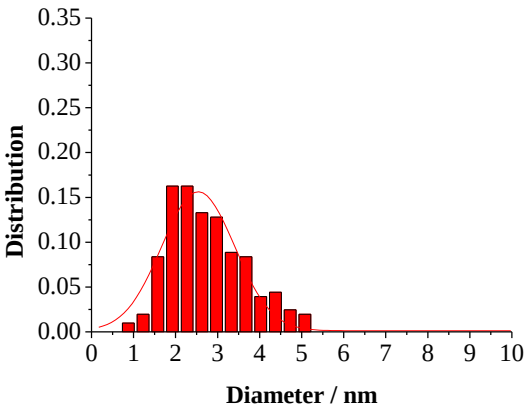

g) **Co4**, PVP:Co = 80 before catalysis D = 1.71 ± 0.73 nm.

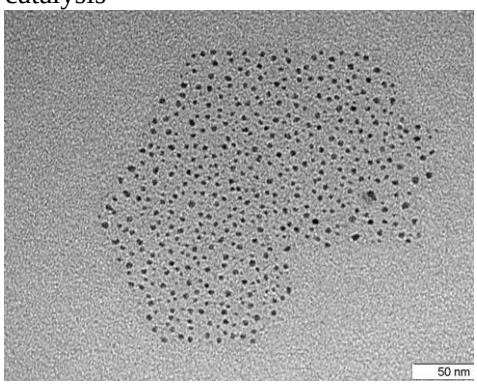

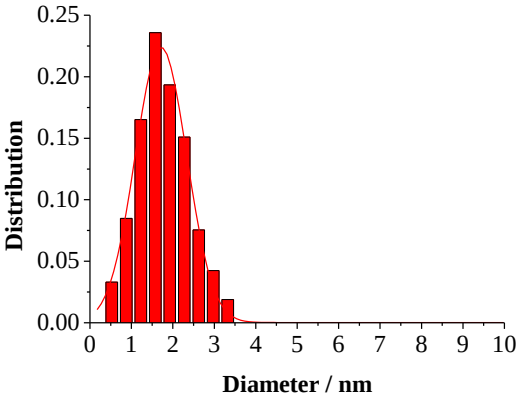

h) **Co4**, PVP:Co = 80 after catalysis D = 2.67 ± 0.81 nm.

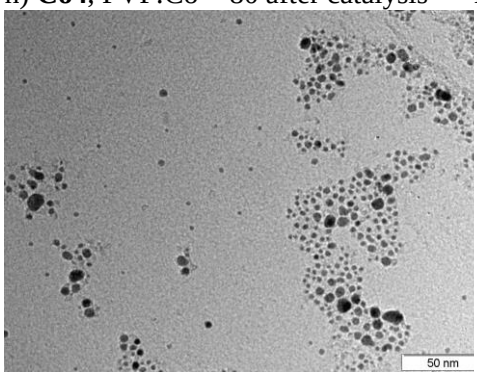

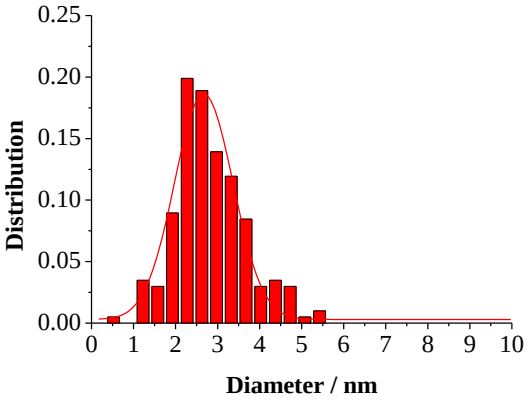

Table S1. Size of CoNPs before and after catalysis

Entry	NP	PVP:Co	Before, D(nm)	After, D(nm)
1	**Co1**	10	3.13 ± 1.58	3.54 ± 1.41
2	**Co2**	20	2.64 ± 0.92	3.28 ± 1.17
3	**Co3**	40	2.11 ± 0.41	2.55 ± 0.98
4	**Co4**	80	1.71 ± 0.73	2.67 ± 0.81

[a] Conditions: 0.93 mmol of $CoCl_2.6H_2O$; PVP (K-30); 9.31mmol $NaBH_4$.

Figure S2. (a) Full XPS spectra of CoNPs: (1) **Co1**, PVP:Co = 10; (2) **Co2**, PVP:Co = 20; (3) **Co3**, PVP:Co = 40 and (4) **Co4**, PVP:Co = 80. (b) Co 2p XPS spectra of (1) **Co2** freshly synthesized; (2) **Co2** oxidized under air during 3 months and (3) **Co2** after FTS using water as solvent. (c) C1s XPS spectra of **Co2** (1) before and (2) after catalysis. (d) B1s XPS spectra of **Co2** (1) before and (2) after catalysis.

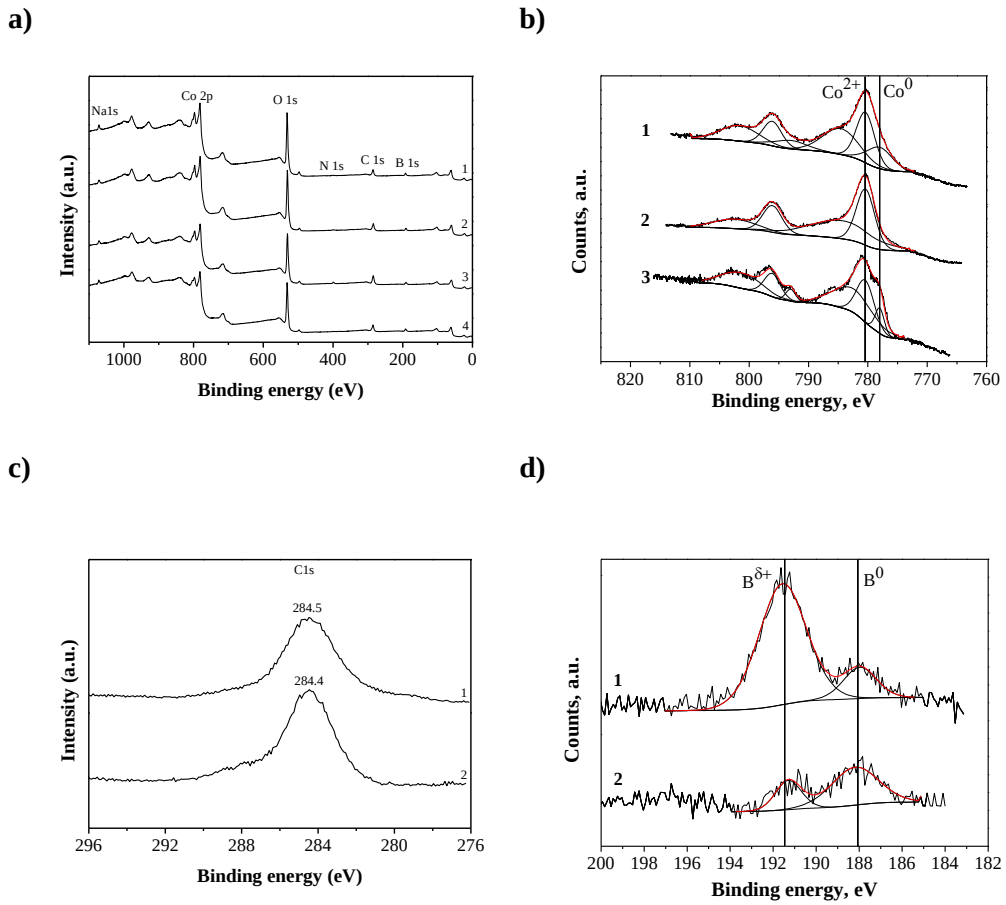

Table S2. Chemical composition analysis of CoNPs by XPS .

		Quantification regions (%Atom)						
Name	PVP:Co	Na 1s	C 1s	N 1s	O 1s	Co 2p	B 1s	Co/B
Co1	10	0.9	17.8	0.8	52.5	15.5	12.5	1.2
Co2	20		20.9		48.6	18.0	12.5	1.4
Co3	40	0.9	26.8	1.9	46.1	13.2	11.1	1.2
Co4	80	1.1	19.7	0.2	53.4	15.0	10.5	1.4
Co2[a]	20		54.9	2.4	31.6	9.0	2.1	4.3

[a] Analysis of **Co2** NPs after catalysis.

Table S3. Microanalysis by Energy-dispersive X-ray spectroscopy, EDX (%Atom) of **Co1-4**

		Element/ shell		
Name	PVP:Co	C K	O K	Co K
Co1	10	14.6	35.2	50.1
Co2	20	36.5	33.1	30.5
Co3	40	52.8	32.8	14.4
Co4	80	60.4	30.2	9.4

Scheme S1. Reaction of formation of CoNPs by reduction of $CoCl_2$ using $NaBH_4$ as reducing agent.

$$1\ CoCl_2 + 10\ NaBH_4 + PVP \longrightarrow CoNPs + H_2 + 10\ BO_3^{3-} + 10\ Na^+ + 2\ Cl^- + 8.1\ OH^- + PVP$$

Figure S3. Raman spectra of (1) **Co1**, PVP:Co = 10; (2) **Co2**, PVP:Co = 20; (3) **Co3**, PVP:Co = 40 and (4) **Co4**, PVP:Co = 80. Spectra acquired by scattering of a 514 nm Ar lamp.

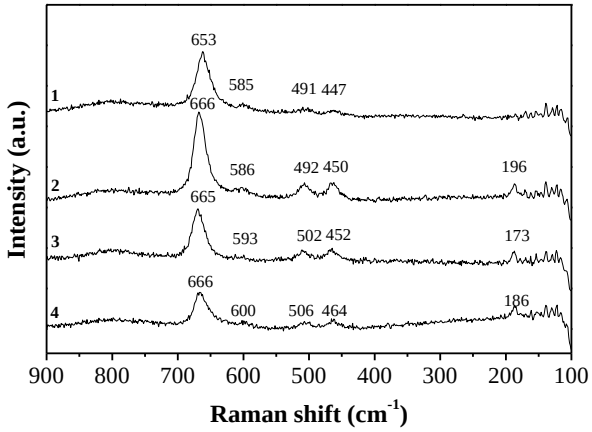

Figure S4. XRD analysis of **Co2** before (1) and after (2) catalysis.

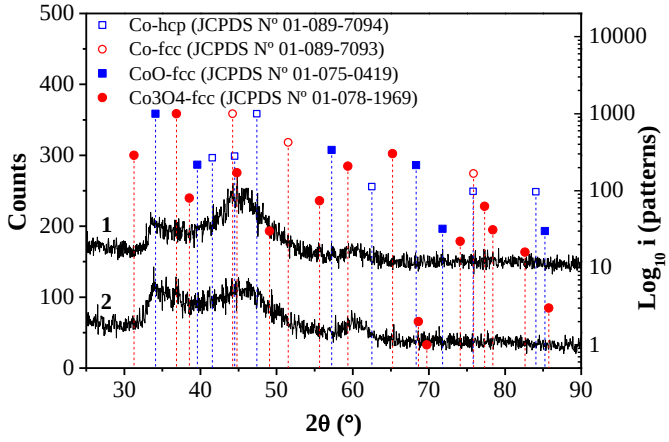

Figure S5. FTIR spectra of (1) **Co1**, PVP:Co = 10; (2) **Co2**, PVP:Co = 20; (3) **Co3**, PVP:Co = 40 and (4) **Co4**, PVP:Co = 80.

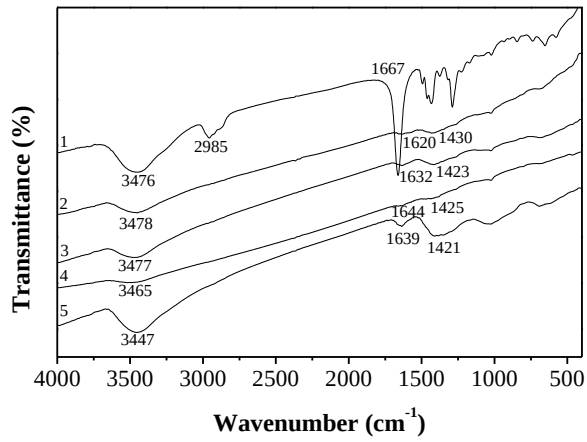

Figure S6. Potentiometric titration of the synthesis solution of **Co2** using HCl solution (2.007 M).

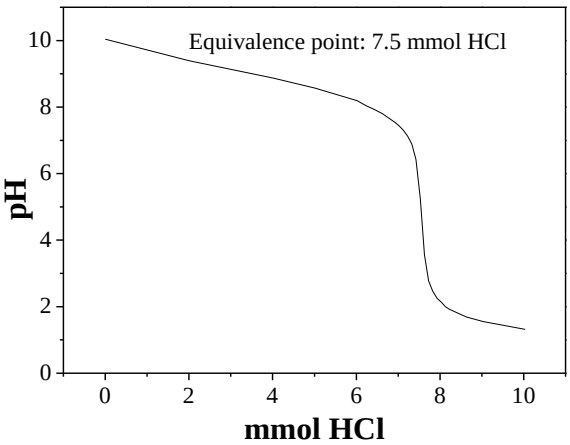

Figure S7. (a) TGA thermogram of PVP and **Co2**; (b) TGA thermograms of CoNPs synthesized by chemical reduction in presence of different PVP:Co ratios: (1) **Co1**, PVP:Co = 10; (2) **Co2**, PVP:Co = 20; (3) **Co3**, PVP:Co = 40 and (4) **Co4**, PVP:Co = 80 (c) TGA thermograms of **Co2** carried out under nitrogen or air flux.

a)

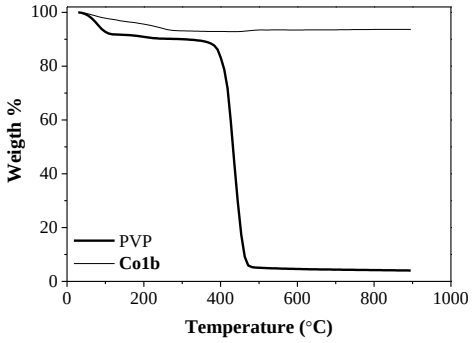

b)

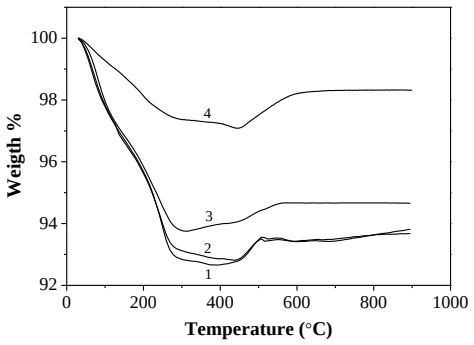

c)

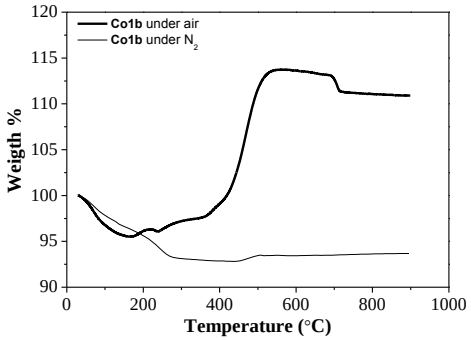

Figure S8. ^{13}C NMR in D_2O of solid residue obtained from reactions: (1) FT experiment at pH 13.1 and (2) Hydrogenation of $NaHCO_3$ by **Co2**.

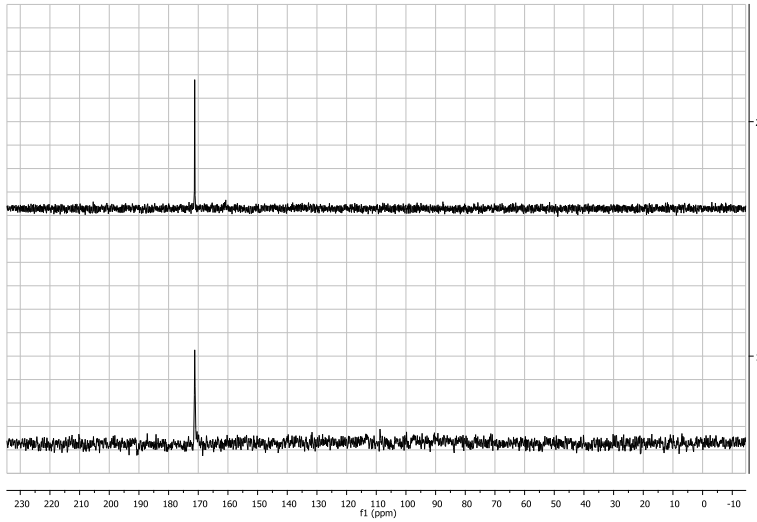

CHAPTER V

Correlation Between Hydrocarbon Products Distribution and Solvent Composition in the Colloidal Co-catalyzed Fischer-Tropsch Synthesis

Table of Contents

V.1. Abstract

Colloidal cobalt nanoparticles with well-defined particle size (*ca*. 2.7 nm) were synthesized, characterized and tested in Fischer-Tropsch Synthesis (FTS) using water and binary mixtures as solvent. The catalytic results revealed that activity and selectivity strongly depend on the nature and composition of the solvent mixture: the tests in pure water produced light hydrocarbons (C_2-C_4), while the addition of organic co-solvents increased the activity and shifted the selectivity to higher hydrocarbons (C_{13}-C_{30}). The observed variations in activity and selectivity were correlated to syngas solubility in the medium used for catalysis. Under the tested conditions, ethanol/water (93/7 v/v) appeared to be the optimum binary solvent in terms of FT activity.

Keywords: Fischer-Tropsch, cobalt nanoparticles, solvent effect, product distribution.

V.2. Introduction

Due to the recent crude oil crisis, the Fischer-Tropsch synthesis has gained renewed scientific interest because of its potential capacity to produce high quality synthetic fuels.[1] Through this reaction, synthesis gas (a mixture of carbon monoxide and hydrogen) is transformed into a series of linear hydrocarbon products.[2] At the same time, synthesis gas can be produced from alternative feedstocks such as coal, natural gas, and more recently biomass, making of this transformation a key process of the solid-to-liquid technologies (STL), gas-to-liquid (GTL) and biomass-to-liquid (BTL).[3]

Currently, one of the main challenges in FT research is the design of not only active and stable catalysts but also highly selective active phases that provide hydrocarbons with narrow chain length distributions.[4] Among the parameters that were shown to affect the selectivity of FT catalysts, the conditions used (T, P, H_2/CO ratio), the particle size of the catalysts and the presence of additives at the catalyst surface are probably the most relevant.[5] The presence of the FT products (water and

hydrocarbons) at the catalysts surface was also reported to influence the output of the reaction.[6] For instance, Van Steen and Claeys reported the effect of the presence of water during Fischer–Tropsch synthesis using a supported ruthenium catalyst.[6b] This study showed that the addition of water during catalysis led to a significant increase in product formation rates and to relevant variations in hydrocarbon selectivity, in particular lower methane selectivity and improved chain growth.

The effect of other solvents in Fischer-Tropsch synthesis was also identified in several reports as a key parameter to enhance the catalytic performance of the catalysts. Fujimoto and co-workers studied the influence of additional linear hydrocarbons on the selectivity to α-olefin products in FTS using a supported Co catalyst in a fixed-bed reactor system.[7] With these solvents, no relevant effect on the catalytic activity nor the chain growth probability (α-value) was observed, although a significant decrease in selectivity to α-olefins was described when long chain hydrocarbon solvents such as hexadecane were used. The same group reported the effect of solvent on the selectivity to long chain linear α-olefins over cobalt Fischer-Tropsch catalysts.[8] Interestingly, *ca*. 40% selectivity to α-olefins was obtained in the presence of n-decane, in comparison to *ca*. 2% in the presence of n-hexane and it was concluded that hydrogenation of α-olefins is more efficient in n-hexane.[5] According to the authors, this phenomenon indicates that the primary α-olefin products can be more effectively removed from the catalyst bed in n-decane due to the higher affinity for heavy aliphatic hydrocarbons expected for this solvent according to the longer carbon chain in comparison to n-hexane.

Burton and co-workers also investigated the effect of solvent on the performance of supported cobalt-based catalysts in Fischer–Tropsch synthesis using a continuously stirred tank reactor.[9] They observed an increase in conversion when the molecular weight of the solvent decreased. According to the authors, the decrease in conversion with time is likely to be a result of pore filling with solvent into the interior of the catalyst, which increases with increasing molecular weight of the start-up solvent.

For the study of solvent effects in FTS, the use of unsupported nanoparticles is of high interest due to the suppression of support-related issues such as internal

mass transport. Moreover, the synthesis of nanocatalysts by colloidal methods provides a better control of their size and shape compared to that of classical supported heterogeneous catalysts. The first example of colloidal nanoparticles applied as catalysts in the Aqueous FT Synthesis (AFTS) was reported by Kou, who used ruthenium nanoclusters stabilized by poly(N-vinyl-2-pyrrolidone) (PVP).[10] Using these nanocatalysts, they described a 35-fold increase in activity over traditional supported Ru catalysts. The smaller size and high dispersion, and the three-dimensional freedom of the particles in water were discussed as the key factors for such increase of the catalytic activity at 180°C. In addition, as the products of FTS are insoluble in water, they can be easily separated from the reaction mixture.[11] The same authors later reported the effect of ionic additives on the performance of these colloidal catalysts.[12] The same catalyst was also tested by van Santen and co-workers in the low temperature AFTS and high selectivity to oxygenates were obtained. The authors attributed this effect to a higher CO coverage at the NP surface under these conditions.[13] Recently, our research group reported the catalytic performance of colloidal Ru-NPs stabilised by various polymers such as PVP and lignins and showed that the nature of the NPs stabilisers influence the selectivity of Ru catalysts in AFTS.[14]

Concerning cobalt catalysts, Kou and co-workers recently reported the use of cobalt/platinum alloy nanoparticles stabilized by PVP as catalysts of the AFTS.[11] According to this report, activity up to 1.1 $mol_{CO}mol_{Suf\text{-}Co}^{-1}h^{-1}$ with a growth factor (α) of 0.8 was obtained at 160ºC. This outstanding activity was rationalized by the formation of Co overlayer structures on Pt NPs or Pt-Co alloy NPs. The same author tested Co nanoparticles reduced by $LiBEt_3H$ and $NaBH_4$, in the aqueous-phase Fischer-Tropsch synthesis.[15] Better catalytic performance was observed for the former case, and comparing the particle size distribution of the catalysts before and after reaction, it was suggested that catalyst reconstruction occurs during the reaction. In addition it was proposed the B-doping could affect the catalytic performance of these NPs. In a previous study, Kou and co-workers reported an activity of $0.12mol_{CO}mol_{Co}^{-1}h^{-1}$ at 170ºC in the AFTS for CoNPs synthesized by chemical reduction using sodium borohydride as reducing agent in water.[16] Other

colloidal Co nanocatalysts for FTS were reported in ionic liquids[17] and squalane[18] although in these cases generally low activity and agglomeration issues were described. Dupont and co-workers reported the synthesis of Co nanocubes (54 ± 22 nm)[17a] and nanospheres (7.7 ± 1.2 nm)[17b] by thermal decomposition of $Co_2(CO)_8$ in [DMI][NTf_2] and [BMI][NTf_2], respectively. The obtained materials resulted active in the FTS. Very recently, the same author reported the synthesis of bimetallic Co/Pt NPs in [BMI][PF_6], this time through an organometallic approach.[19] The isolated bimetallic NPs resulted active catalysts for the Fischer–Tropsch synthesis, with selectivity for naphtha products.

Nowadays, while the activity of FT catalysts can be efficiently tuned by several parameters such as the type of support or the addition of promoters, etc… the control of the selectivity for a selected hydrocarbon fraction is less documented and remains a challenge.[20] The study of parameters that could shift the product distribution in FT is therefore of high interest for the rational design of catalytic systems providing selectively diesel or gasoline fractions, for instance.

Here, we describe the synthesis and characterization of monometallic CoNPs stabilized with poly(N-vinyl-2-pyrrolidone) and their application as nanocatalysts in FTS. The effect of solvent composition on the catalytic performance of these NPs was investigated. Varying the composition of the solvent caused striking effects on the product distribution of the reaction from light to heavier hydrocarbons, which were correlated to the relative CO and H_2 solubility under these reaction conditions.

V.3. Results and Discussion

V.3.1. Synthesis and characterization of CoNPs

The cobalt nanoparticles **Co1** were synthesized in water by chemical reduction of $CoCl_2.6H_2O$ in the presence of $NaBH_4$ using PVP as stabilizer (PVP:Co = 20) while **Co2** were produced by thermal decomposition of $Co_2(CO)_8$ in butylether at 150 °C in the presence of 10 equivalents of PVP. In this latter case, the amount of

PVP was lower than for the chemical reduction method due to solubility issues. Both methodologies are schematically represented in Scheme 1.

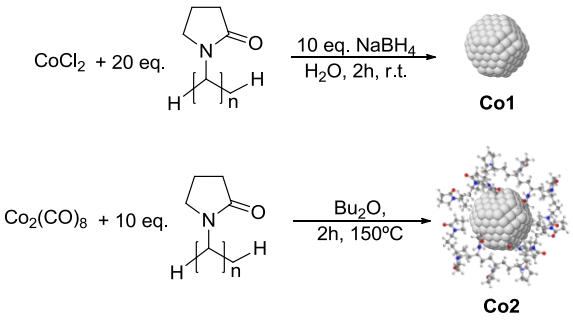

Scheme 1. Methodologies used for the synthesis of CoNPs **Co1-Co2**

According to the TEM micrographs and size histograms of **Co1** and **Co2** displayed in **Figure 1**, both methodologies resulted in the formation of spherical CoNPs of similar sizes *ca.* 2.7 nm (**Co1**: 2.64 ± 0.92 nm; **Co2**: 2.78 ± 0.71 nm).

Co1, 2.64 ± 0.92 nm. **Co2, 2.78 ± 0.71 nm.**

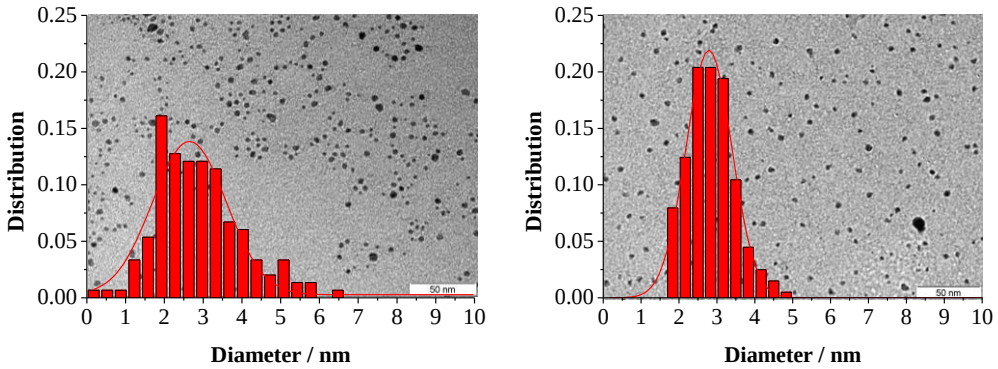

Figure 1. Size histograms and TEM micrographs of **Co1** and **Co2**.

The fine structure of the CoNPs **Co1** and **Co2** was studied by high-resolution transmission electron microscopy (HR-TEM). The corresponding micrographs are displayed in Figure 2, where the insets represent the electron diffraction of the NPs. In the micrograph of **Co1** (Figure 2, left), single particles of

ca. 2.6 nm diameter were observed, in agreement with TEM measurements. Analysis of the diffraction pattern revealed the presence of crystalline Co_3O_4-fcc (space group *Fd3m(227)*). Curiously, no crystalline metallic cobalt phase was identified .The diffuse rings present in the diffraction pattern of these NPs (**Co1)** suggest an amorphous structure for the cobalt faces, in agreement with previously reported synthesis of amorphous CoNPs via similar synthetic methods.[21]

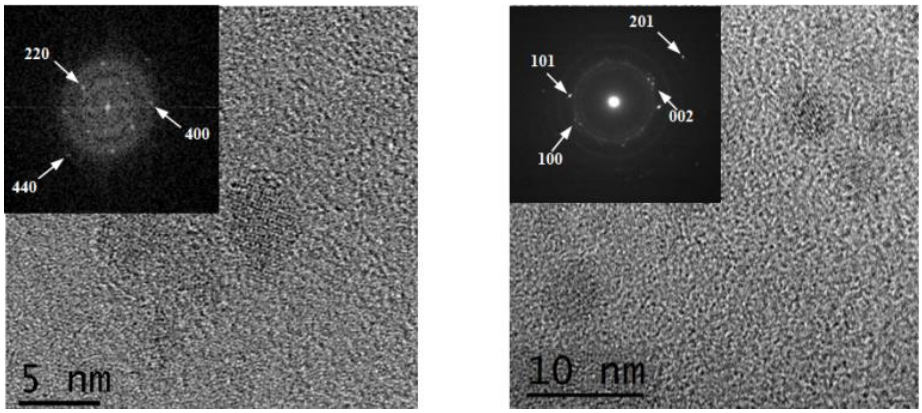

Figure 2. HRTEM image of **Co1** (left) and **Co2** (right) NPs and their corresponding electron diffraction pattern.

In contrast, the analysis of the diffraction pattern of **Co2** revealed the presence of crystalline Co-hcp (space group *P63/mmc*) while crystalline cobalt oxides were not detected in this case.

When the crystalline structure of the CoNPs was studied using X-ray diffraction (XRD) technique, the XRD pattern of **Co1** revealed the presence of two broad bands centred at 34º and 45º which cannot be attributed to any defined crystalline pattern unambiguously (Figure 3). In contrast, in the diffractogram of **Co2**, low intensity peaks were observed at 42, 45, 47 and 76º which were readily attributed to Co-hcp and Co-fcc crystalline phases. Additionally, a broad feature centred at 20º was also observed corresponding to large amounts of amorphous PVP at NPs surface. These results therefore indicated that the synthetic method used for the formation of NPs affects their crystalline structure and the oxidation state of Co.

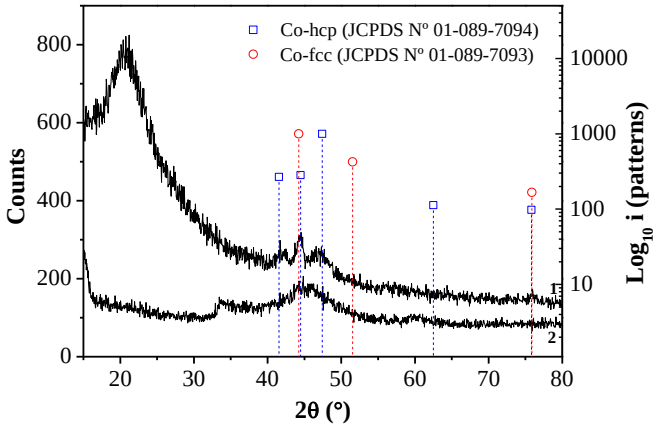

Figure 3. XRD patterns of (1) **Co1** and (2) **Co2**.

Surface analysis of the CoNPs **Co1** and **Co2** was performed by X-ray photoelectron spectroscopy (XPS). The full XPS spectra of **Co1** revealed the presence of Na, Co, O, N, C and B, according to the peaks observed at their characteristic binding energies (1071.6; 781.5; 530.9; 399.2; 284.5 and 191.1 eV respectively). The Co XPS spectrum of **Co1** exhibits two prominent peaks at 779.7 and 795.6 eV corresponding to Co $2p_{3/2}$ and Co $2p_{1/2}$, respectively. A low intensity shoulder detected at 777.9 eV can also be distinguished and suggests the presence of cobalt metal phase in low abundance (*ca.* 37% of Co^0 according to deconvolution of the Co XPS spectra). In contrast, for **Co2,** only characteristic peaks of PVP (O, N and C) were detected in the full XPS spectra, suggesting again the abundant coverage of **Co2** by PVP, and subsequently no information about the reduction state of cobalt at the metal surface could be obtained from this technique. Further analysis of **Co1** by ICP revealed a boron content of 5.9 wt%, which corresponded to a Co/B ratio of 2.8.

The presence of PVP at the surface of these CoNPs was also investigated by FTIR, TGA and ICP-OES techniques. The IR spectra of **Co1** didn´t exhibited absorption bands of PVP whereas for the case of **Co2,** characteristic absorption bands of PVP at 3460, 2955 and 1663 cm^{-1} were detected. To quantify the exact cobalt content of these NPs, ICP-OES analyses were performed, obtaining 82.4 and

5.8 wt % for **Co1** and **Co2,** respectively, in agreement with the weight losses observed by TGA. These results therefore confirmed that the coverage of the surface of these NPs by PVP is also affected by the synthetic method used for their formation, and is much more important in the case of **Co2** than in that of **Co1**. Due to the large excess of PVP remaining at the surface of **Co2**, a sample was washed with water and subsequently analyzed by FTIR and TGA (Supporting Information, Figure S6 and Figure S8). Characteristic signals of PVP were still present in the IR spectra of the washed sample. Additionally, a weight loss of 13% of PVP was determined by TGA thus demonstrating the coordination of PVP at the surface of **Co2** after the suspension in water.

In summary, the characterization of **Co1** and **Co2** NPs revealed that the composition and structure of these CoNPs depend strongly on the synthetic methodology used for their formation. Despite that both **Co1** and **Co2** show similar particle size (*ca*. 2.6 nm), **Co1** are constituted of metal cobalt and cobalt oxide with an amorphous structure, while **Co2** is reduced cobalt with hcp and fcc crystalline phases. Furthermore, relevant differences in PVP coverage were observed and showed that **Co1** is poorly wrapped by PVP compared to **Co2**.

V.3.2. Fischer-Tropsch catalytic experiments

The synthesized Co NPs (**Co1** and **Co2**) were tested in the Fischer-Tropsch synthesis using various solvents (mono-component or binary mixtures) in order to study the effect of solvent on the activity and selectivity of the CoNPs.

V.3.2.1. Catalysis in water

The synthesized NPs **Co1** were first tested in AFTS using water as solvent at 150, 180 and 210°C under 30 bar of syngas (Table 1). Activity increased from 0.012 to 0.097 $mol_{CO}mol_{Co}^{-1}h^{-1}$ as the temperature increased from 150 to 210 ºC (note: CO_2 was not considered for the activity calculation). Methane selectivity steadily increased from 8 to 25 wt% as temperature increased, whereas C_{2+} selectivity initially increased from 48 w% at 150°C to 57% at 180 °C, but decreased to 21% when temperature was further increased to 210 °C. The rise in temperature

also caused a considerable shortening of the hydrocarbon chain (decrease of the α value from 0.60 to 0.50), and favored the methanation reaction, in agreement with trends previously reported for cobalt catalysts.[5].

For **Co2**, activity of 0.205 $mol_{CO}mol_{Co}^{-1}h^{-1}$ was observed at 180°C with selectivity of 27% for methane and 50% for C_{2+}. The activity of **Co2** resulted *ca.* 10 times higher than that of **Co1** at this temperature, and was attributed to the higher reduction degree of **Co2**. In contrast, the product selectivities observed for **Co1** and **Co2** were quite similar at 180 °C, indicating that under these conditions, the differences in structure and composition of these CoNPs do not affect significantly the selectivity of the reaction. The obtained activities for **Co1** and **Co2** are comparable to those recently reported by Kou and co-workers in the AFTS catalyzed by CoNPs (0.27 and 0.1 $mol_{CO}mol_{Co}^{-1}h^{-1}$ corresponding to NPs prepared by chemical reduction using $NaBH_4$).[15] The hydrocarbon selectivities as well as the α values observed in water were also comparable. In contrast, the CH_4 and CO_2 selectivities obtained in this study were 20 and 23 wt% differently to the reported by Kou, 40 and 7 wt% respectively. These differences could be attributed no only to variations in the structure of the catalysts but also to the composition (extent of B-doping, etc).

Table 1. Fischer-Tropsch synthesis catalyzed by **Co1** and **Co2** using water as solvent.[a]

			Selectivity, Wt%			HC selectivity, Wt%			
E.[b]	Temp. (°C)	Activity[c]	CO_2	CH_4	C_{2+}	C_{2-4}	C_{5-12}	C_{13-30}	α
1	150	0.012	44	8	48	41	45	0	0.60
2	180	0.026	23	20	57	43	31	0	0.59
3	210	0.097	54	25	21	30	16	0	0.50
4[d]	180	0.205	23	27	50	41	24	0	0.57

[a] Reaction conditions: 30 bar H_2/CO/Ar (2:1:0,15); 66 mL water, 1000 rpm, 180 ºC, 12h; [b] **Co1** (0.93 mmol Co) ; [c] Activity without CO_2 in $mol_{CO}mol_{Co}^{-1}h^{-1}$; [d] **Co2** (0.93 mmol Co).

It is noteworthy that in these catalytic experiments, most of the hydrocarbon products were in the C_{1-4} fraction and no products longer than C_{12} were obtained. Usually, the range of α for Co-catalysed FTS is *ca.* 0.70–0.80 depending on the reaction conditions and catalyst type. [22] Here, using water as solvent, α values of 0.50-0.60 were obtained in all cases. This significant difference in selectivity may

indicate that water is responsible for the shortening of the hydrocarbon chain, possibly due to the low solubility of syngas in water.[23]

V.3.2.2. Catalysis in mixtures of water and organic co-solvent

In view of these results, it was thought that the addition of an organic co-solvent could exert a direct effect on the selectivity of AFTS. Therefore catalytic experiments using mixtures of water and a series of organic solvents (15% v/v) were carried out (Table 2). The organic co-solvents were selected on the basis of their boiling point (similar to that of water), to minimize vapor pressure effects during catalysis. For this initial screening, aliphatic (linear and cyclic), aromatic and perfluorinated hydrocarbons and alcohols were tested.

When a 15% v/v of heptane/water was used as the solvent mixture, the activity of the **Co1** NPs at 180°C increased up to 0.067 $mol_{CO}mol_{Co}^{-1}h^{-1}$ (x 2.5 compared to that obtained in pure water) with a clear shift of the hydrocarbon selectivity from C_{2-4} to C_{13-30} (Table 2, Entry 2 *versus* entry 1). Furthermore, a significant decrease of the methane and CO_2 selectivities, to 11% and 23 % respectively, was also observed (Table 2, Entry 2). In methylcyclohexane and toluene (Entries 3 and 4), similar results were obtained with activities of *ca*. 0.06-0.07 $mol_{CO}mol_{Co}^{-1}h^{-1}$, together with high selectivities to C_{13-30} and low selectivities to methane and CO_2.

Table 2. Screening of mixtures of organic solvents with water (15%) in the Fischer-Tropsch synthesis catalyzed by **Co1**.[a]

				Selectivity, Wt%			HC sel., Wt%			
E.[b]	Solvent (% v/v)	b.p ,ºC	Activity[c]	CO_2	CH_4	C_{2+}	C_{2-4}	C_{5-12}	C_{13-30}	α
1	Water (100%)	100	0.026	23	20	57	43	31	0	0.59
2	Heptane (15%)	99	0.067	23	11	66	7	19	59	0.92
3	Methylcyclohex.(15%)	101	0.058	19	15	66	11	22	49	0.92
4	Toluene (15%)	111	0.071	20	12	68	10	22	53	0.91
5	Perfluorooctane (15%)	103	0.076	10	10	80	11	21	57	0.91
6	Propanol (15%)	98	0.052	19	18	63	37	28	13	0.79

[a] Conditions: 0.93 mmol Co, 30 bar H_2/CO/Ar (2:1:0,15); 66mL total volume, 1000rpm, 180 ºC, 12h ; [b] **Co1** (0.93 mmol Co) ; [c] Activity without CO_2: $mol_{CO}mol_{Co}^{-1}h^{-1}$

Hydrogenation of toluene was not observed when the FT catalysis was performed in this aromatic solvent. The catalysis in perfluorooctane (Entry 5) gave

the highest activity of the series, up to 0.076 $mol_{CO}mol_{Co}^{-1}h^{-1}$, the highest C_{2+} selectivity (80%) and the lowest CO_2 and CH_4 selectivities (10% for both). Long chain hydrocarbons (C_{13+}) were again the main reaction products under these conditions.

When the catalysis was performed in 15% v/v of propanol/water (entry 6), intermediate results between those in water and heptane (15% v/v) were obtained. It is noteworthy that the hydrocarbon selectivity increased in the order water < heptane < perfluorooctane (57 < 66 < 80%), which suggested that these variations could be caused by the increasing solubility of H_2 and CO in these solvents.[23-24]

To summarize, when the catalysis was performed in water the growth of the hydrocarbon chain was restricted to C_{1-12} products whereas upon addition of 15% of an organic co-solvent such as heptane, catalytic activity increased and chain lengthening was observed (C_{13}-C_{30}).

In view of the results obtained with this series of co-solvents, and since water and hydrocarbons are products of the FTS reaction, the composition of the water/heptane mixture was optimized.

V.3.2.3. Optimization of the composition of water/heptane mixtures

To further investigate the effect of the co-solvent, the water/heptane mixture was investigated at various heptane contents.

In these experiments, rising the heptane content resulted in an increase in activity of **Co1** (Figure 4, solid line) up to a maximum of 0.095 $mol_{CO}mol_{Co}^{-1}h^{-1}$ at v/v 50%; however the activity decreased down to 0.009 $mol_{CO}mol_{Co}^{-1}h^{-1}$ as heptane content was further increased. The same behavior was observed for **Co2** (Figure 4, dotted line) although much higher activities (up to 0.27 $mol_{CO}mol_{Co}^{-1}h^{-1}$) than those for **Co1** were measured. The higher activity of **Co2** can be attributed to the higher reduction degree of the **Co2** catalyst, as previously indicated.

On the other hand, at high heptane content, important agglomeration of **Co1** and **Co2** was observed by TEM analysis performed after the catalytic tests. The low activity observed for both catalysts at high heptane content was therefore explained by the agglomeration of the nanocatalysts in such an apolar solvent (Figure 5).

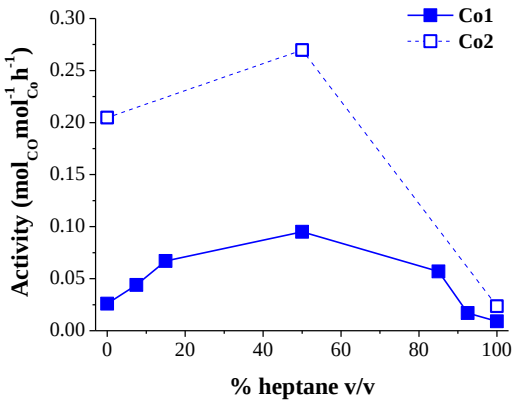

Figure 4. Activity in $mol_{CO}.mol_{Co}^{-1}.h^{-1}$ of **Co1** and **Co2** NPs as a function of the % heptane in water. Conditions: 0.949 mmol Co, 30 bar H_2/CO/Ar (2:1:0,15); 66 ml water, 1000 rpm, 180 ºC, 12h

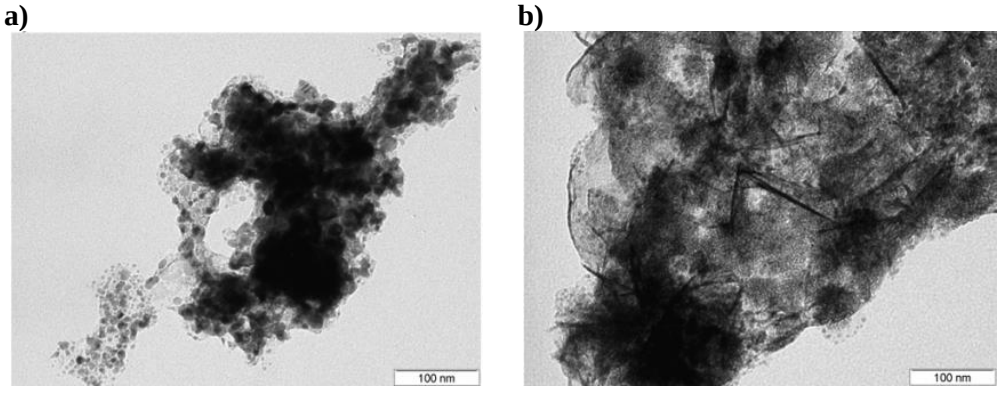

Figure 5. TEM micrographs of (a) **Co1** and (b) **Co2** after catalysis performed in heptane as the solvent.

The selectivity was also strongly affected by the composition of the solvent. The selectivity profiles for **Co1** as a function of the heptane/water ratio are displayed in Figure 6a. The hydrocarbon selectivity (C_{2+}) increased up to 82% when the heptane content was increased to 50%. Simultaneously, the CO_2 and CH_4 selectivity decreased from 23 to 11% and from 20 to 7%, respectively. At higher heptane contents, C_{2+} selectivity decreased down to 21% while CO_2 and CH_4 both increased to 45 and 34%, respectively. In 50/50 heptane/water mixture, the use of **Co2** as

catalyst provided slightly higher selectivities to hydrocarbons (84%, Suppl. Information).

The hydrocarbon product distribution was also considerably affected when the heptane content in the solvent mixture was varied (Figure 6b). The variation of solvent composition from pure water to a water/heptane mixture of 85/15 caused a strong shift of the product distribution from C_2-C_{12} towards the heavy fraction $C_{13\text{-}30}$ (Figure 6b), which is reflected in the increase of α value from 0.59 to *ca.* 0.90. This level of selectivity remained constant at heptane contents between 15 and 93% and dropped drastically when pure heptane was used as solvent.

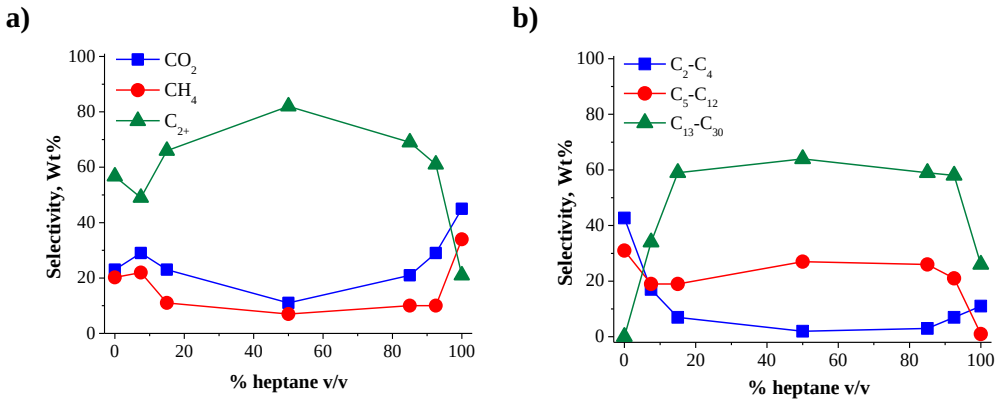

Figure 6. Selectivity (**a**) and hydrocarbon selectivity (**b**) in wt% of **Co1** NPs as a function of the heptane content in the solvent used for catalysis. Conditions: 0.949 mmol Co, 30 bar H_2/CO/Ar (2:1:0,15); 66 ml water, 1000 rpm, 180 ºC, 12h

The selectivity drop observed for pure heptane was attributed to the agglomeration of the NPs described above (Figure 5). It is also noteworthy that no C_{30+} products were detected in these experiments. Similar trends were observed for **Co2** (see Suppl. Information).

The dependence of the activity on the percentage of heptane in water can be rationalized by the variation of the solubilities of hydrogen and carbon monoxide in the different solvent mixtures. According to literature data, the solubility of hydrogen is higher in decane than in water by a factor of *ca.* 7 (3.348 mLH_2/L [25] *vs.* 0.488 mLH_2/L[23]) under reaction conditions (180ºC and 20 bar of H_2). A higher

solubility in heptane would represent a higher coverage of the metal surface by both gases, resulting in an increase in activity when the heptane content increases from 0 to 50%. The shift in product distribution from C_{2-4} to C_{13+} could also be explained by the increase solubility of syngas.

To confirm this hypothesis, the solubilities of H_2 and CO were measured in various heptane/water mixtures at room temperature using the method described by Deimling *et al*.[26] The results are displayed in Figure 6a. Solubility of both gases increased linearly as the heptane content increased. In all cases, CO solubility was higher than that of H_2 and the H_2:CO solubilities ratio (Figure 7a) decreased at higher heptane content. Interestingly, an inverse correlation was observed between the variation in H_2:CO solubility ratio and the chain growth probability of the FT products (Figure 7b). Indeed, when the heptane content is increased from 0 to 15%, a drastic drop in H_2:CO ratio is observed, and concomitantly, an increase in the α value was measured. At higher heptane content, the H_2:CO solubilities ratio is less affected, which is reflected in an almost constant α value. From these results, it was concluded that the variations observed in hydrocarbon product distribution were mainly controlled by the H_2:CO ratio in solution. At low H_2:CO solubilities ratio, long chain hydrocarbons are formed (C_{13+}) while at higher ratios, lighter hydrocarbons are preferably produced. These results are in agreement with previous reports which described that variations of the syngas composition affect the product distribution in FTS.[5]

These results therefore indicated that the presence of water and hydrocarbon at the surface of cobalt nanocatalysts produced by FTS strongly influences their subsequent selectivity by affecting the solubility of syngas and the CO coverage of these catalysts. The results described here suggest that the presence of water at the NP surface shortens the chain of the hydrocarbon products.

Next, to investigate the effect of the carbon chain length of the co-solvent on the selectivity, a series of mixture of hydrocarbons and water was tested in the Fischer-Tropsch reaction.

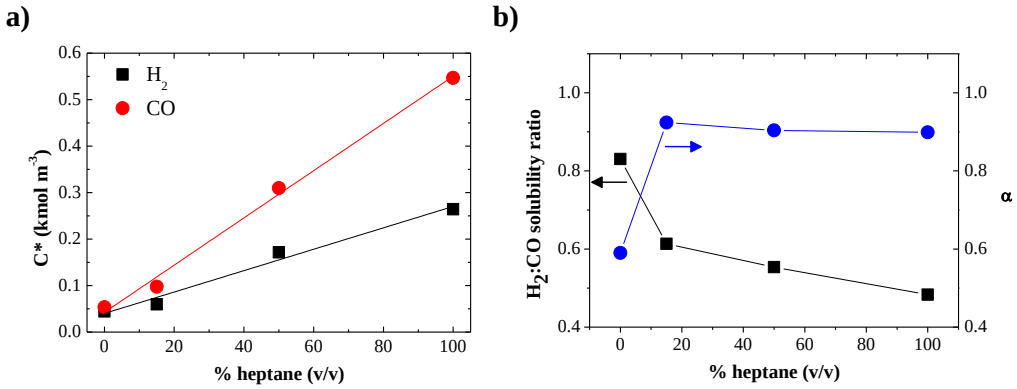

Figure 7. (a) Solubility of H_2 and CO at 20 and 10 bar respectively and r.t. in heptane/water mixtures (b) Measured H_2:CO solubility ratio and α values obtained in catalysis using different heptane/water mixtures.

V.3.2.4. Screening of hydrocarbons as co-solvents (50% v/v)

In view of the results obtained with the 50% v/v heptane/water mixture, the effect of the hydrocarbon chain length was studied with solvent mixtures composed by water and n-octane, n-decane and n-hexadecane in the same proportions (Figure 8).

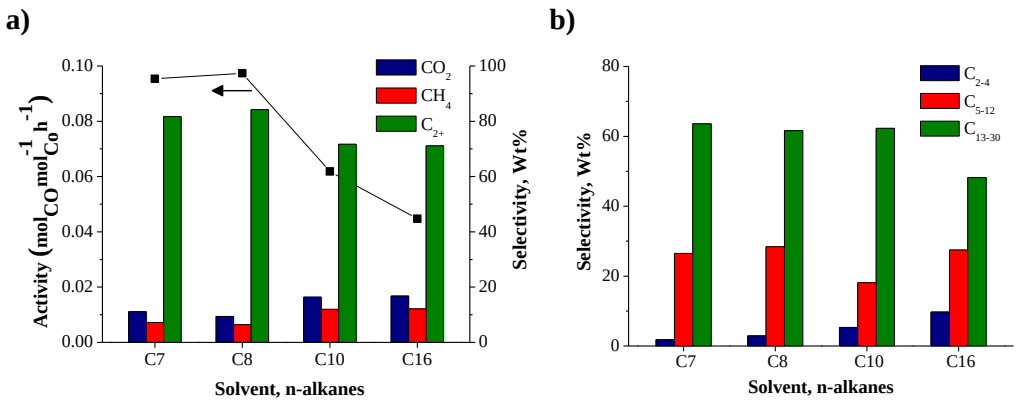

Figure 8. Activity and selectivity (a) and hydrocarbon selectivity (b) in wt% of **Co1** NPs as a function of the carbon chain length of the alkane co-solvent. Conditions: 0.949 mmol Co, 30 bar H_2/CO/Ar (2:1:0,15); 66 ml water, 1000 rpm, 180 ºC, 12h

The catalytic tests using heptane or octane in 50% v/v showed similar activity; however, activity decreased as chain length further increased in the series from octane to hexadecane. The activity observed for hexadecane was half (0.045 $mol_{CO}mol_{Co}^{-1}h^{-1}$) of that observed for heptane (0.095 $mol_{CO}mol_{Co}^{-1}h^{-1}$). Agglomeration was not observed in any case, and TEM images showed that dispersion of the CoNPs was similar independently of the co-solvent. This decrease in activity was therefore attributed to the lower solubility of syngas in heavier *n*-alkanes, as previously reported.[25]

In terms of selectivity, the amount of methane and CO_2 formed during the reactions slightly increased with longer chain co-solvents. Simultaneously, only a small shift towards lighter products was observed for octane and hexadecane, although it became more relevant for hexadecane. These small variations in selectivity could be attributed to the expected similarity of the H_2/CO ratio in these media. Interestingly, these trends are in contrast with those previously reported for supported CoNPs on SiO_2, for which no changes in activity nor in chain growth probability were observed when the same series of solvents were tested in slurry-type FT systems.[7]

V.3.2.5. Screening of alcohols as solvents for FTS

According to the initial screening of solvents (Table 2), the extent of chain growth in propanol/water mixture was somewhat intermediate between those obtained in water and heptane/water, according to their α values (0.79, 0.59 and 0.92 respectively). This suggested that performing the catalytic reaction in alcohols could be of interest for the modulation of the product distribution. Moreover, alcohols have the capacity to disperse efficiently CoNPs such as **Co1** and **Co2**, even in the absence of water.

It was therefore decided to investigate the effect of various alcohols and catalytic experiments using the series methanol, ethanol, 1-propanol, 1-butanol and 1-pentanol were performed (Table 3). The results of these experiments showed that when the FT reaction is performed in pure alcohols ($>C_1$), three types of products are formed (Scheme 2): a) FT products, b) FT-acetal products formed by reaction of

FT intermediate species with 2 molecules of solvent and c) C_n-acetals formed from 3 molecules of solvent and where C_n is the carbon number contained in the alcohol structure. The formation of FT-acetal products was previously observed by Kou and co-workers under FT conditions using ethylene glycol as solvent with the formation of a series of dioxolanes.[27] Here, the detection of two types of acetals were produced: those involving the reaction of a product formed by FT reaction with two molecules of solvent (route b, Scheme 2) and those formed by reaction of 3 molecules of solvents (route b, Scheme 2). It is noteworthy that these acetal products corresponded to less than 1% in alcohol conversion in all cases.

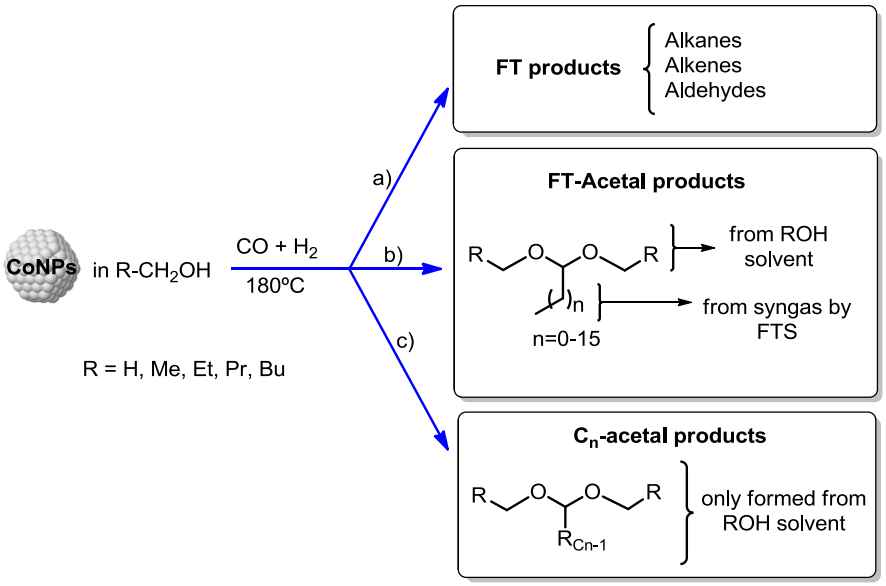

Scheme 2. Products formed under FT conditions using **Co1** as catalyst and alcohols as solvent.

The selectivities obtained in these reactions are summarized in **Table 3**. It should be noted that these selectivities were obtained by integration of the corresponding GC-MS peaks, since no calibration could be performed on these compounds.

Table 3. Fischer-Tropsch synthesis catalyzed by **Co1** in different n-alcohols.[a]

Entry	Alcohol	Selectivity (%)[b]			Final H_2/CO
		FT-products	FT-acetals	C_n acetal	
1	Methanol	100	0	0	1.3
2	Ethanol	69	13	18	1.8
3	1-Propanol	35	35	30	2.1
4	1-Butanol	2	44	54	2.7
5	1-Pentanol	1	27	73	2.5

[a] Conditions: 0.93 mmol Co, 30 bar H_2/CO/Ar (2:1:0,15); 66ml total volume, 1000rpm, 180 ºC, 12h; [b] Selectivity calculated from GC-MS data by peak integration.

Interestingly, among the series of alcohols used, only the FT experiments carried out in methanol produced selectively FT products since no acetals were detected (Entry 1). When the solvent was ethanol, *ca.* 15% of FT-acetals and C_n-acetals were detected (Entry 2) while the FT products were still mainly formed. However, when longer chain alcohols were used, an increasing amount of C_n-acetals was produced up to 73% in 1-pentanol with the FT products only detected as traces (Entry 5).

The classical mechanism of formation of acetals involves the reaction of one molecule of aldehyde with two molecules of alcohol under acidic conditions with elimination of one equivalent of water.[28] Recently, Milstein and co-workers reported the use of an homogeneous alcohol dehydrogenation Ru catalyst for the formation of acetals in pure alcohols.[29] In the present case, the role of Co in the C_n-acetal formation was confirmed when a blank experiment was performed: when alcohols were heated under the same conditions but in absence of Co catalyst, no acetals were formed. The generation of aldehyde thus requires the presence of Co, and it is proposed that oxidation of one equivalent of alcohol to the corresponding aldehyde proceeds via the concomitant reduction of a cobalt centre. The oxidation of the alcohols with H_2 release is supported by the observation of an increase in H_2:CO ratio in the gas phase when higher amounts of C_n-acetals are formed. Furthermore, it was previously reported that Co-hydride species present an acidic character and could therefore catalyze the formation of the C_n-acetals.[30]

The higher selectivity to C_n-acetals in long chain alcohols can be explained by the lower free Gibbs energy of formation for long chain aldehydes from the

corresponding alcohols.[31] Interestingly, when the selectivity to C_n-acetals was plotted against the free Gibbs energy of formation of the aldehyde, a linear relationship was obtained (see Suppl. Info).

These results therefore indicate that when FTS is completed in alcohols as solvents, a competition between the hydrocarbon and acetals formation is observed and depends on the chain length of the alcoholic solvent. This effect is remarkable since in MeOH, hydrocarbons are mainly formed while in 1-pentanol, acetals are selectively produced.

The detailed distributions of FT products formed during these catalytic experiments are described in Table 4.

Table 4. Fischer-Tropsch synthesis catalyzed by **Co1** using n-alcohols as solvent.[a]

			Selectivity, Wt%			HC selectivity, Wt%			
E.	Alcohol	Activity [b]	CO_2	CH_4	C_{2+}	C_{2-4}	C_{5-12}	C_{13-30}	Final H_2/CO
1	Methanol	0.046	7	8	84	2	21	66	1.3
2	Ethanol	0.189	3	5	92	2	26	67	1.8
3	1-Propanol	0.053	7	12	80	5	40	42	2.1
4	1-Butanol	0.027	13	31	56	14	1[c]	49	2.7
5	1-Pentanol	0.043	11	32	56	16	1[c]	46	2.5

[a] Conditions: 0.93 mmol Co, 30 bar H_2/CO/Ar (2:1:0,15); 66mL total volume, 1000rpm, 180 °C, 12h; [b] Activity without CO_2: $mol_{CO}mol_{Co}^{-1}h^{-1}$; [c] C_{5-12} hydrocarbons overlapped by the solvent peak in GC spectra.

Among the tested solvents, the highest activity was achieved in ethanol (up to 0.189 $mol_{CO}mol_{Co}^{-1}h^{-1}$) while for the other alcohols, FT activities between 0.027 – 0.053 $mol_{CO}mol_{Co}^{-1}h^{-1}$ were obtained. The results in longer alcohols could be explained by the competitive coordination of syngas and alcohols at the NPs surface, since high selectivity to acetals was observed in these solvents (Table 4).

The product selectivity was also affected by the chain length of the alcoholic solvents with high selectivity to C_{2+} when methanol, ethanol and propanol were used with a maximum of 92% in ethanol. In contrast for longer chain alcohols, the selectivity decreased considerably (down to 56%) while the methane selectivity increased to *ca.* 30%. In all solvent, low CO_2 selectivity was observed, indicating low WGS activity under these conditions. Similarly, the hydrocarbon distribution

showed high selectivity to C_{13+} in short chain alcohols, namely methanol and ethanol with a maximum of 67% in this latter solvent. For longer chain alcohols (Table 4, Entry 3-5), this selectivity was lower (*ca.* 45%) with a shift to lighter products. These results can be correlated with the H_2:CO ratio measured in the gas phase at the end of the catalytic experiments, which increases with heavier alcohols due to acetal formation (Table 4). In light alcohols (Entry 1 and 2), lower H_2:CO ratios were observed, resulting in low methane selectivity and high C_{13+} selectivity. In heavier alcohols, higher values were obtained, explaining the higher methane selectivity and the formation of short chain hydrocarbon products (Table 4, entry 4 and 5). In propanol, somewhat intermediate H_2:CO ratio and selectivity results were measured.

Interestingly, the catalysis in methanol exhibited a high olefin selectivity (65%) which decreased when the chain length of the alcohol increased, which was attributed to the lower H_2/CO ratio in the shorter alcohols that is in turn related to the lower amounts of acetals formed in these solvents.

As a conclusion, when alcohols are used as solvent for FTS, the formation of acetals catalysed by CoNPs is observed together with hydrocarbon products. When the chain length of the alcoholic solvent increases, the formation of acetal progressively becomes the major process. In the case of short alcohols such as ethanol, however, high FT activity (up to 0.189 $mol_{CO}mol_{Co}^{-1}h^{-1}$) was observed with excellent product selectivity (80% hydrocarbons).

V.3.2.6. Optimization of the composition of ethanol/water mixtures

In view of the excellent results obtained using ethanol as the solvent, the influence of water was tested through a series of catalytic FT experiments in several water / ethanol mixtures using **Co1** as catalyst. The results in terms of activity are summarized in Figure 9a.

Comparing the activity obtained in pure water as the solvent, the increase in ethanol content from 0 to 93% resulted in a significant increase of the activity from 0.026 to 0.278 $mol_{CO}mol_{Co}^{-1}h^{-1}$. These results can be correlated to the increased solubility of syngas at higher ethanol content (Figure 9b). [32] At higher ethanol

content, a decrease of the activity was observed down to 0.189 $mol_{CO}mol_{Co}^{-1}h^{-1}$ due to the competitive formation of FT-acetals.

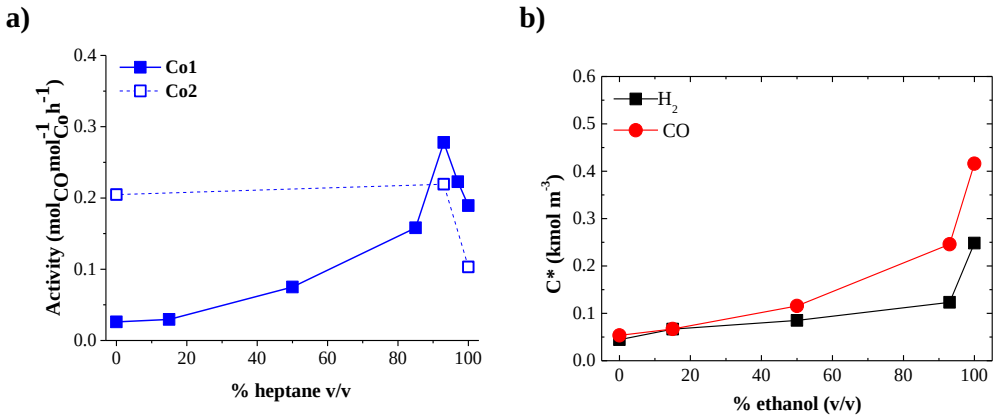

Figure 9. (**a**) Activity in $mol_{CO}.mol_{Co}^{-1}.h^{-1}$ of **Co1** and **Co2** NPs as a function of the % ethanol. Conditions: 0.949 mmol Co, 30 bar H_2/CO/Ar (2:1:0,15); 66 ml water, 1000 rpm, 180 ºC, 12h. (**b**) Solubility of H_2 and CO at 20 and 10 bar respectively and r.t. in heptane/water mixtures.

Importantly, in these experiments, acetal products (FT-acetals and Cn-acetals) were only detected when the content of water was ≤3%, which indicated that rapid hydrolysis of the acetals occurred at higher water content. To the best of our knowledge the activity observed for **Co1** when using 93% ethanol/water mixture (0.278 $mol_{CO}mol_{Co}^{-1}h\text{-}^{1}$) is the highest reported up to date for an aqueous colloidal FT system using CoNPs synthesized by a chemical reduction method. This result highlights the possibility to enhance the catalytic activity of a catalyst through the modification of their environment.

When **Co2** was used as the catalyst, similar activities were obtained in pure water and in 93% ethanol/water mixture. As previously mentioned, the higher activities observed for **Co2** in water and hydrocarbon/water mixtures were attributed to its higher content in metallic cobalt when compared to **Co1**. In alcohols, however, similar activities were observed for both catalysts. As the reduction of cobalt salts was previously reported in alcohols at similar temperature,[33] it was concluded that the similar activities observed for both catalysts could be explained by the *in situ*

reduction of **Co1** under these reaction conditions. In terms of selectivity (Figure 10a), the increase in ethanol content from 0 to *ca*. 90% led to a progressive increase in hydrocarbon selectivity from 57 to *ca*. 90% while the CO_2 and CH_4 selectivities decreased from 23 to 5% and from 20 to 5%, respectively. At higher ethanol content, these selectivities remained unchanged. It is noteworthy that in heptane/water mixtures, the increase in hydrocarbon selectivity was more accentuated than in ethanol/water mixtures, which can be explained by the rapid increase in syngas solubility when heptane is introduced compared to ethanol (Figure 7a vs. Figure 9a).

The hydrocarbon products distribution (Figure 10b) was also clearly affected by the composition of the solvent. When the ethanol content was increased from 0 to 15%, no changes in selectivity were observed. However, at higher ethanol content, the product distribution was progressively shifted from short chain (C_{2-4}) to long chain hydrocarbons (C_{13-30}) with variation in selectivity from 40% to 0% and from 0% to 73%, respectively. Further increase in ethanol content did not affect these selectivities. Interestingly, while the solvent composition clearly affected the C_{2-4} and C_{13-30} selectivities, the relative amount of C_{5-12} hydrocarbon remained unchanged at *ca.* 25%. When **Co2** was used as the catalyst, the same selectivity trends were observed (See Supporting Information).

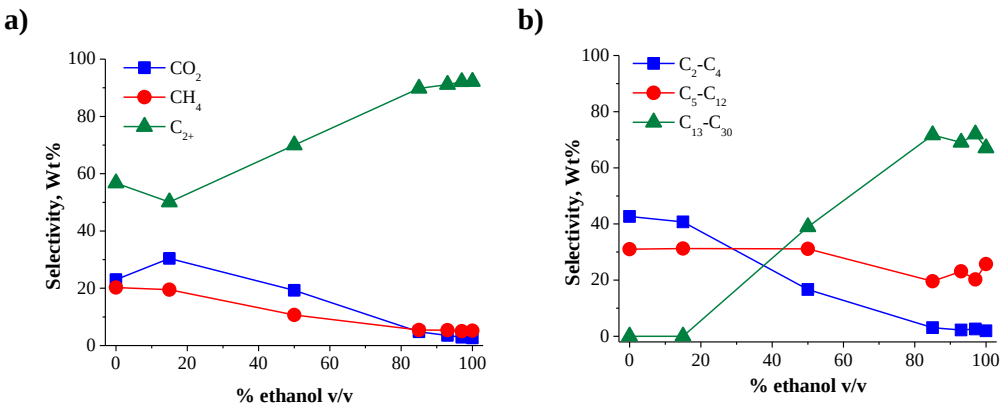

Figure 10. Selectivity (**a**) and hydrocarbon distribution (**b**) in wt% of FT experiments catalysed by **Co1** NPs as a function of the % ethanol. Conditions: 0.949 mmol Co, 30 bar H_2/CO/Ar (2:1:0,15); 66 ml water, 1000 rpm, 180 ºC, 12h

These variations in product distribution, reflected in the variations in chain growth probability, can be rationalized by the changes in H_2:CO solubility ratio as a function of the ethanol content (Figure 11). Indeed, at ethanol contents up to 15%, an increase in H_2:CO solubility ratio was measured, resulting in the lowering of the α value and the formation of light products ($C_{2\text{-}4}$ and $C_{5\text{-}12}$). At higher ethanol content, the H_2:CO solubility ratio decreased linearly, resulting in a concomitant increase of the chain growth probability and thus, in a higher C_{13+} selectivity. These results again indicated that the main parameter governing the FT product distribution is the relative solubilities of H_2 and Co in these solvents.

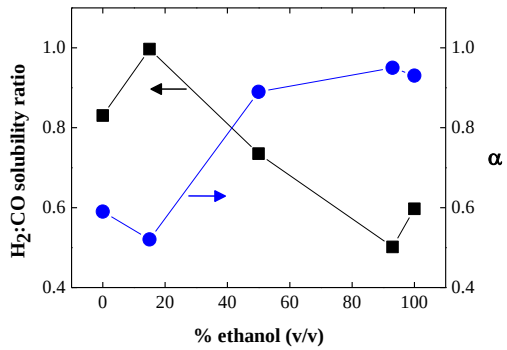

Figure 11. (a) Solubility of H_2 and CO at 20 and 10 bar respectively and r.t. in heptane/water mixtures (b) Measured H_2:CO solubility ratio and corresponding α values obtained for catalysis using different heptane/water mixtures.

Finally, from the comparison of **Co1** and **Co2** in the different solvent systems it is notheworthy that the presence of boron in **Co1** did not exhibit a clear effect in its catalytic performance.

V.4. Conclusions

The results described here show that the addition of co-solvents such as hydrocarbons and alcohols in AFTS strongly affects the selectivity and the FT product distribution. It was shown that the hydrocarbon distribution mainly depends

on the solubility of syngas and on the H_2:CO ratio, and can be tuned from light to heavy hydrocarbons with the selection of the appropriate aqueous solvent mixture.

In hydrocarbon/water mixtures, a compromise between the higher solubility of syngas in hydrocarbons and the better dispersion of the catalyst in water revealed to be crucial to reach high activity and selectivity to C_{13+} hydrocarbons. No effect of the chain length (C_7-C_{16}) of the hydrocarbon co-solvents was observed on the selectivity of FTS while the activity was slightly affected. This also indicates that the presence of water and hydrocarbons at the surface of such Co nanocatalysts directly influence their selectivity in FTS by affecting their H_2/CO coverage. These results also suggest that the presence of water can significantly shorten the chain length of the hydrocarbons produced by FTS.

In alcohols, significant effect was also observed; when the chain length of the alcoholic solvent increases, the formation of FT-acetal products progressively becomes the major process. In the case of short alcohols such as ethanol, however, high FT activity (up to 0.189 $mol_{CO}mol_{Co}^{-1}h^{-1}$) was observed with excellent product selectivity (80% hydrocarbons).

V.5. Experimental Section

Synthesis of cobalt nanoparticles by chemical reduction method (Co1)

Co1 was synthesized by chemical reduction of cobalt(II) chloride in the presence of polyvinylpyrrolidone (PVP) as stabilizer (PVP:Co ratio of 20) using sodium borohydride as reducing agent. As a standard procedure, 0.226 g of $CoCl_2.6H_2O$ (0.93 mmol) was dissolved in 50 mL of H_2O containing the 2.066 g of PVPK30 (18.6 mmol based on monomer units, PVP:Co ratio of 20). Then, a solution of 0.358 g of $NaBH_4$ (9.30 mmol) in 16 mL of H_2O was added at room temperature during 5 minutes. The solution was maintained under vigorous mechanical stirring for 2 h. Then 100 µl of the colloidal solution was centrifuged, washed with water and re-dispersed by sonication. Three drops of the obtained colloidal solution were deposited on a Cu-formvar or holey carbon grids for TEM and HR-TEM analysis. For the isolation of the CoNPs, the freshly prepared NPs

were initially precipitated by a strong magnetic field (using a neodymium magnet) and the supernatant was decanted. Then, the precipitated NPs were washed with water to remove the excess of salts and PVP. The decantation and washing process was repeated three times with water, then three times with ethanol and three times with hexane. The resulted CoNPs were finally dried under vacuum and stored in a glove-box.

TEM: D = 2.64 ± 0.92 nm.

HR-TEM: *ca.* 2.6 nm; detection of CoO-fcc and Co_3O_4-fcc.

XRD: 45, 35 and 60º

XPS: Co^0, 37%; Co^{2+}, 63%.

TGA: Temperature ºC/Δ wt. % (attribution); 70/-3.5 (solvent), 244/-3.7 (polymer), 900end/+0.92.

ICP: Co, 82.4 wt%, B, 5.9 wt%; Co/B atom ratio, 2.79

FTIR: 3478, 1614 cm^{-1}.

RAMAN: 666, 586, 492, 450, 196 cm^{-1}.

Synthesis of cobalt nanoparticles by thermal decomposition method (Co2)

Co2 was synthesized by thermal decomposition of $Co_2(CO)_8$ in presence of the PVP (PVP:Co ratio of 10) using butylether as solvent. As a standard procedure, 0.352 g of $Co_2(CO)_8$ (1.86 mmol) and 2.066 g of PVP (18.6 mmol based on monomer units, PVP:Co ratio of 10) were placed in a 500 mL Fischer-Porter and dissolved with 130 mL of butyl ether. The Fischer-Porter bottle was closed and then heated at 150ºC during 2h to give a black suspension. The CoNPs were then precipitated using a strong magnet and the solvent was decanted. The CoNPs were washed with with butylether, followed by THF and hexane and finally dried under vacuum and stored in glove box. For characterization purposes, a part of the isolated NPs was washed with water in order to remove any PVP excess, followed by ethanol and hexane washing prior to vacuum drying and storage in the glove box. Samples of **Co2** was centrifuged, washed with water and re-dispersed by sonication several times. Three drops of the obtained colloidal solution were deposited on a Cu-formvar or holey carbon grids for TEM and HR-TEM analysis.

TEM: D = 2.78 ± 0.71 nm.

HR-TEM: *ca.* 2.8 nm; detection of Co-hcp.

XRD: 41.5, 44.6, 46.7 and 75.8º

XPS: For fresh NPs, presence of C, N and O and absence of Co signal due to large PVP coverage of the CoNPs.

TGA: Temperature ºC/Δ wt. % (attribution); For fresh NPs, 150/-6.4 (solvent); 433/-75.1 (polymer); 900end/-4.8. For water washed NPs, 76/-3.6 (solvent); 219/-4.74 (polymer); 361/-8.3 (polymer); 900end/+5.20;

ICP: Fresh NPs, Co^0, 5.8%; water washed NPs, Co^{2+}, 39.0%.

FTIR: 3460, 2955, 1663 cm^{-1}.

General method for Fischer-Tropsch catalytic experiments

In a typical catalytic experiment, freshly prepared CoNPs (0.931 mmol of Co) were re-dispersed in the desired solvent and the suspension placed in a Teflon liner within a 100 mL stainless steel autoclave which was purged three times with Ar, and pressurized at an Ar pressure of 1.5 bar. Additional 10 bar CO and 20 bar H_2 were further added giving a final pressure of 31.5 bar (H_2:CO:Ar = 2:1:0.15). The autoclave was then heated to 180 ºC under mechanical stirring at 1000 rpm during 12h. At this point, the autoclave was cooled to room temperature prior to gas analysis. All the components contained in the gas phase (CO, H_2, Ar, CO_2, and C_1-C_8 hydrocarbons) were analyzed by GC-TCD and the quantification was performed using calibration curves for each component. The compounds present in the liquid phase were analyzed directly from the hydrocarbon phase or extracted with cyclohexane (10 mL) containing 1 µl of bicyclohexyl as internal standard. The organic phase containing the hydrocarbon and oxygenated products were analyzed by GC-MS. The identification and quantification of products was performed by comparison with standards using calibration curves for each compound.

V.6. Acknowledgements

The authors are grateful to Total S.A., the Spanish Ministerio de Economía y Competitividad (CTQ2013-43438-R, and *Ramon y Cajal* fellowship to C. Godard) and the Generalitat de Catalunya (2014SGR670) for financial support.

V.7. References

[1] Calderone, V. R.; Shiju, N. R.; Curulla-Ferré, D.; Chambrey, S.; Khodakov, A.; Rose, A.; Thiessen, J.; Jess, A.; Rothenberg, G. *Angew. Chem. Int. Ed.* **2013**, *52*, 4397-4401.

[2] (a) A. Steynberg; Dry., M.; Elsevier, 152: 2006.(b) *Fischer-Tropsch synthesis, catalysts and catalysis*; B.H. Davis; Occelli, M. L., Eds.; Elsevier, 163, 2007.(c) Zhang, Q.; Kang, J.; Wang, Y. *ChemCatChem* **2010**, *2*, 1030-1058.

[3] Khodakov, A. Y. *Catal. Today* **2009**, *144*, 251-257.

[4] Gual, A.; Godard, C.; Castillón, S.; Curulla-Ferré, D.; Claver, C. *Catal. Today* **2012**, *183*, 154-171.

[5] Van Der Laan; and, G. P.; Beenackers, A. A. C. M. *Catal. Rev.* **1999**, *41*, 255-318.

[6] (a) Hibbitts, D. D.; Loveless, B. T.; Neurock, M.; Iglesia, E. *Angew. Chem. Int. Ed.* **2013**, *52*, 12273-12278.(b) Claeys, M.; van Steen, E. *Catal. Today* **2002**, *71*, 419-427.

[7] Liu, X.; Linghu, W.; Li, X.; Asami, K.; Fujimoto, K. *App. Catal. A-Gen* **2006**, *303*, 251-257.

[8] Linghu, W.; Liu, X.; Li, X.; Fujimoto, K. *Catal. Lett.* **2006**, *108*, 11-13.

[9] Pendyala, V.; Jacobs, G.; Luo, M.; Davis, B. *Catal. Lett.* **2013**, *143*, 395-400.

[10] Xiao, C.-x.; Cai, Z.-p.; Wang, T.; Kou, Y.; Yan, N. *Angew. Chem. Int. Ed.* **2008**, *47*, 746-749.

[11] Wang, H.; Zhou, W.; Liu, J.-X.; Si, R.; Sun, G.; Zhong, M.-Q.; Su, H.-Y.; Zhao, H.-B.; Rodriguez, J. A.; Pennycook, S. J.; Idrobo, J.-C.; Li, W.-X.; Kou, Y.; Ma, D. *J. Am. Chem. Soc.* **2013**, *135*, 4149-4158.

[12] Wang, C.; Zhao, H.; Wang, H.; Liu, L.; Xiao, C.; Ma, D. *Catal. Today* **2012**, *183*, 143-153.

[13] Quek, X.-Y.; Guan , Y.; van Santen, R. A.; Hensen, E. J. M. *ChemCatChem* **2011**, *3*, 1735-1738.

[14] Gual, A.; Delgado, J. A.; Godard, C.; Castillón, S.; Curulla-Ferré, D.; Claver, C. *Top. Catal.* **2013**, *56*, 1208-1219.

[15] Wang, H.; Kou, Y. *Chin. J. Catal.* **2013**, *34*, 1914-1925.

[16] Fan, X.-B.; Tao, Z.-Y.; Xiao, C.-X.; Liu, F.; Kou, Y. *Green Chem.* **2010**, *12*, 795-797.

[17] (a) Scariot, M.; Silva, D. O.; Scholten, J. D.; Machado, G.; Teixeira, S. R.; Novak, M. A.; Ebeling, G.; Dupont, J. *Angew. Chem. Int. Ed.* **2008**, *47*, 9075-9078.(b) Silva, D. O.; Scholten, J. D.; Gelesky, M. A.; Teixeira, S. R.; Dos Santos, A. C. B.; Souza-Aguiar, E. F.; Dupont, J. *ChemSusChem* **2008**, *1*, 291-294.

[18] Yan, N.; Zhang, J.-g.; Tong, Y.; Yao, S.; Xiao, C.; Li, Z.; Kou, Y. *Chem. Commun.* **2009**, 4423-4425.

[19] Silva, D. O.; Luza, L.; Gual, A.; Baptista, D. L.; Bernardi, F.; Zapata, M. J. M.; Morais, J.; Dupont, J. *Nanoscale* **2014**, *6*, 9085-9092.

[20] (a) Bligaard, T.; Nørskov, J. K.; Dahl, S.; Matthiesen, J.; Christensen, C. H.; Sehested, J. *J. Catal.* **2004**, *224*, 206-217.(b) Khodakov, A. Y.; Chu, W.; Fongarland, P. *Chem. Rev.* **2007**, *107*, 1692-1744.(c) Schulz, H. *App. Catal. A-Gen* **1999**, *186*, 3-12.

[21] (a) Chuan Wu; Chun Hui Pang; Feng Wu; Ying Bai; Chi Chen; Zhong, Y. *Adv. Mat. Res.* **2011**, *391-392*, 1085.(b) Mitov, M.; Popov, A.; Dragieva, I. *J. Appl. Electrochem.* **1999**, *29*, 59-63.(c) Petit, C.; Wang, Z. L.; Pileni, M. P. *J. Phys. Chem. B* **2005**, *109*, 15309-15316.

[22] Dry, M. E. *J. Mol. Catal.* **1982**, *17*, 133.

[23] Pray, H. A.; Schweickert, C. E.; Minnich, B. H. *Ind. Eng. Chem.* **1952**, *44*, 1146-1151.

[24] Matsumoto, D. K.; Satterfield, C. N. *Ind. Eng. Chem. Proc. Des. Dev.* **1985**, *24*, 1297-1300.

[25] Florusse, L. J.; Peters, C. J.; Pàmies, J. C.; Vega, L. F.; Meijer, H. *AlChE J.* **2003**, *49*, 3260-3269.

[26] Deimling, A.; Karandikar, B. M.; Shah, Y. T.; Carr, N. L. *Chem. Eng. J.* **1984**, *29*, 127-140.

[27] Fan, X.-B.; Yan, N.; Tao, Z.-Y.; Evans, D.; Xiao, C.-X.; Kou, Y. *ChemSusChem* **2009**, *2*, 941-943.

[28] Carey, F. A. *Organic chemistry*; 4th ed.; McGraw-Hill, 2000.

[29] Gunanathan, C.; Shimon, L. J. W.; Milstein, D. *J. Am. Chem. Soc.* **2009**, *131*, 3146-3147.

[30] Moore, E. J.; Sullivan, J. M.; Norton, J. R. *J. Am. Chem. Soc.* **1986**, *108*, 2257-2263.

[31] (a) Lide, D. R. *CRC Handbook of Chemistry and Physics, Internet Version 2006*; Taylor and Francis: Boca Raton, FL, 2006.(b) Levine, I. N. *Physical Chemistry*; 4th ed.; McGraw-Hill: USA, 1996.

[32] Purwanto; Deshpande, R. M.; Chaudhari, R. V.; Delmas, H. *J. Chem. Eng. Data* **1996**, *41*, 1414-1417.

[33] (a) Fiévet, F.; Brayner, R. In *Nanomaterials: A Danger or a Promise?*; Brayner, R., Fiévet, F., Coradin, T., Eds.; Springer London: 2013, p 1-25.(b) Montiel, M. G.; Santiago-Jacinto, P. P.; Góngora, J. A. I. D.; Reguera, E.; Gattorno, G. R. *Nano-Micro Lett.* **2011**, *3*, 12-19.

Supporting Information for:

Correlation Between Hydrocarbon Products Distribution and Solvent Composition in the Colloidal Co-catalyzed Fischer-Tropsch Synthesis

Materials and Methods

Solvents were purchased from Merck or Sigma-Aldrich and used as received. $CoCl_2 \cdot 6H_2O$, $Co_2(CO)_8$, $NaBH_4$ and PVP K-30 were purchased from Sigma-Aldrich. Hydrogen (5.0) was purchased from Air Liquide and CO (4.7) and argon (5.0) from Carburos Metálicos.

The syntheses of CoNPs by chemical reduction were carried under aerobic conditions using a mechanical stirrer while the syntheses of CoNPs by thermal decomposition were carried out under inert conditions using Fischer-Porter bottles. Milli-Q water was used for all the experiments.

Transmission electron microscopy (TEM) measurements were performed at the "Unitat de Microscopia dels Serveis Cientificotècnics de la Universitat Rovira I Virgili" in Tarragona with Zeiss 10 CA electron microscope operated at 100 kV with resolution of 3 Å. High resolution electron microscopy (HRTEM) measurements were performed at the "Centres Científics i Tecnològics de la UB" in Barcelona with a JEOL 2011(FEG) electron microscope operated at 200 kV with a point resolution of 2 Å. FTIR spectra were acquired from KBr discs on a Bruker Equinox 55 Spectrometer using Opus software. XPS experiments were performed in a PHI 5500 Multitechnique System (from Physical Electronics) with a monochromatic X-ray source (Aluminium Kalfa line of 1486.6 eV energy and 350 W), placed perpendicular to the analyzer axis and calibrated using the 3d5/2 line of Ag with a full width at half maximum (FWHM) of 0.8 eV. The analyzed area was a circle of 0.8 mm diameter, and the selected resolution for the spectra was 187.5eV of Pass Energy and 0.8 eV/step for the general spectra and 23.5 eV of Pass Energy and 0.1 eV/step for the spectra of the different elements in the depth profile spectra. A low energy electron gun (less than 10 eV) was used in order to discharge the surface when necessary. All Measurements were made in a ultra high vacuum (UHV) chamber pressure between $5x10^{-9}$ and $2x10^{-8}$ torr. XRD measurements were made using a Siemens D5000 diffractometer (Bragg-Brentano parafocusing geometry and vertical θ-θ goniometer) fitted with a curved graphite diffracted-beam monochromator, incident and diffracted -beam Soller slits, a 0.06º receiving slit and scintillation counter as a detector. The angular 2θ diffraction range was between 25 and 120º. The data were collected with an angular step of 0.05º at 16s per step and sample rotation. A low background Si(510) wafer was used as sample holder. $Cu_{k\alpha}$ radiation was obtained from a copper X-ray tube operated at 40 kV and 30 mA. Thermogravimetric analysis (TGA) were performed with a thermobalance (Mettler TGA/SDTA851e) equipped with a gas flow

system. A 2-6 mg sample was heated in a 70 ul alumina crisol in a flow of nitrogen. Then the catalyst was heated under a 50 mL/min of nitrogen flow from 30 ºC to 900 ºC (heat rate: 10 ºC/min). The analysis resulted from the subtraction of a blank run under the same conditions. Analysis of cobalt were performed by inductively coupled plasma optical emission spectrometry (ICP-OES) with a Spectro Arcos FHS-16 spectrometer at the Servei Cientificotècnics de la Universitat Rovira i Virgili in Tarragona

The catalytic experiments were carried out using a 100mL stirred tank reactor operated in batch mode (Autoclave Engineers EZE-Seal-100ML). Analysis of the gas phase was performed using a GC-TCD connected online to the autoclave.

GC-TCD analyses were carried out on a Agilent 7890A GC using a system of three columns: Hayesep Q (3ft x 1/8 in), HP-Molesieve (30m x 0.320mm x 12µm) and HP-Plot/Q (30m x 0.320mm x 20µm) using helium as carrier gas. GC-MS analyses were performed on a 9575C MSD system (Agilent) using a HP-Innowax capillary column (30m x0.250 mm x0.15 µm), using helium as carrier gas. Standard reference of gases (CO, CO_2, H_2, N_2) and hydrocarbons (C_1-C_5) was purchased from Abello Linde.

Product analysis

All the hydrocarbon products were identified by comparison with reference samples.

The components contained in the gas phase (CO, H_2, Ar, CO_2, and C_1-C_8 hydrocarbons) were analysed on a Agilent 7890A GC using a system of three columns: Hayesep Q (3ft x 1/8 in), HP-Molesieve (30m x 0.320 mm x 12 µm) and HP-Plot/Q (30m x 0.320 mm x 20 µm) using helium as carrier gas. The quantification was carried out using calibration curves for each gas. Mixtures at different concentration of gases were prepared by gas blending from a standard reference of gases (Avello Linde).

The compounds present in the aqueous phase were extracted with cyclohexane (10 ml) containing 1µl of bicyclohexyl as internal standard. The organic phase containing the hydrocarbon and oxygenated products were analyzed immediately by GC-MS on a 9575C MSD system using a using a HP-Innowax capillary column (30m x 0.250 mm x 0.15 µm), and helium as carrier gas.

The identification and quantification of products was performed by comparison with standards using calibration curves for each compound.

Activity and Selectivity Calculations

The activity and selectivity was calculated based on the number of moles of carbon being formed as products according to the following formulas:

$$\text{Activity} = \frac{\text{total mol of C formed as products}}{\text{mol of Co} * \text{reaction time (h)}}$$

$$\text{Selectivity } Cn, wt\% = \frac{\text{Wt } C_n}{\text{Wt of all products}} \; x\; 100$$

$$\text{HC Sel. } Cn, wt\% = \frac{\text{Wt } C_n}{\text{Wt of all hydrocarbons (from } C_1 \text{ to } C_x)} \; x\; 100$$

Figure S1. Size histograms and TEM micrographs of **Co1** and **Co2** after catalysis using 50% heptane/water mixture as solvent.

Co1, 3.86 ± 0.95 nm.

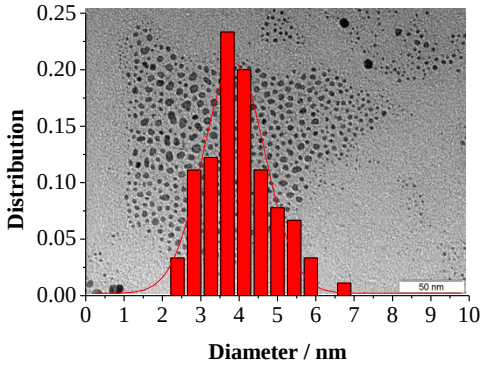

Co2, 2.74 ± 0.90 nm.

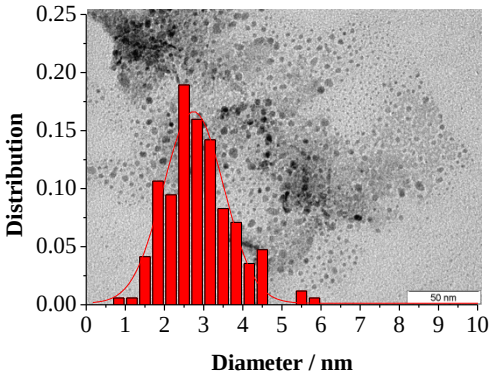

Figure S2. Typical GC-MS spectrum of hydrocarbon products contained in the liquid phase after FT synthesis catalysed by **Co1** and **Co2**. Reaction conditions: 0.931 mmol of Co; 30 bar H_2:CO:Ar (2:1:0.15); 180 ºC; 12h.

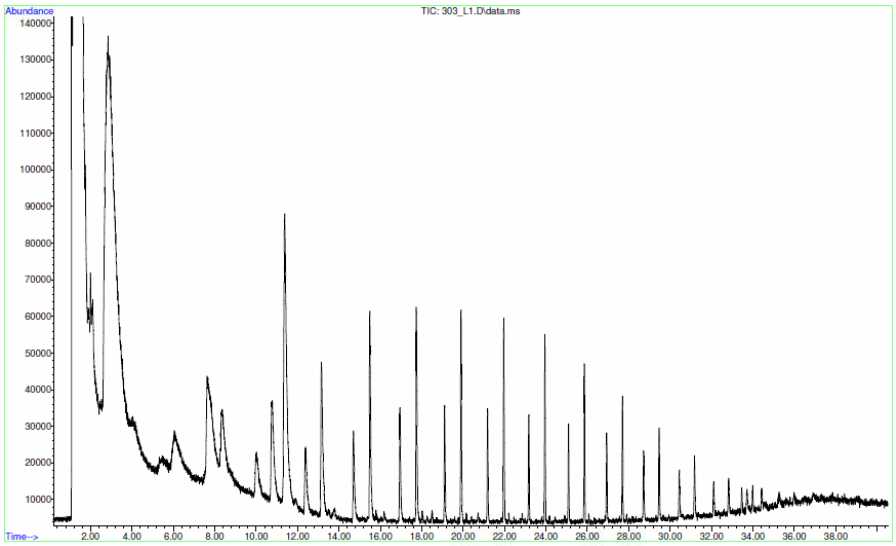

Figure S3. (a) XRD patterns of **Co1** (1) fresh catalyst and (2) after catalysis in water. **(b)** XRD pattern of **Co2** (1) fresh catalyst, (2) washed with water and (3) after catalysis in water.

Co1 **Co2**

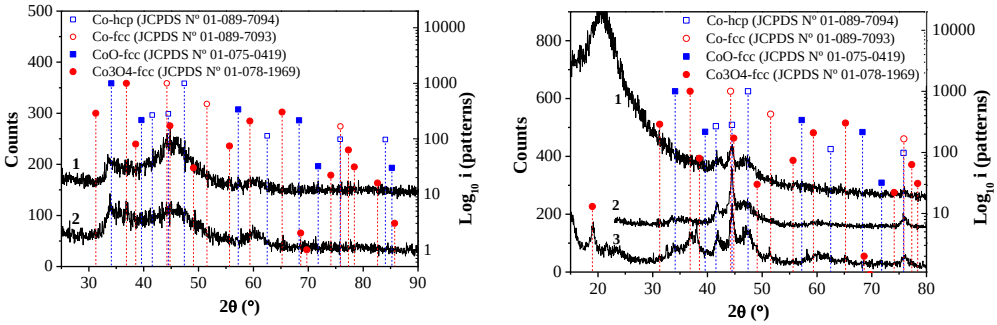

Figure S4. Full XPS spectra of CoNPs: (1) **Co1** and (2) **Co2.**

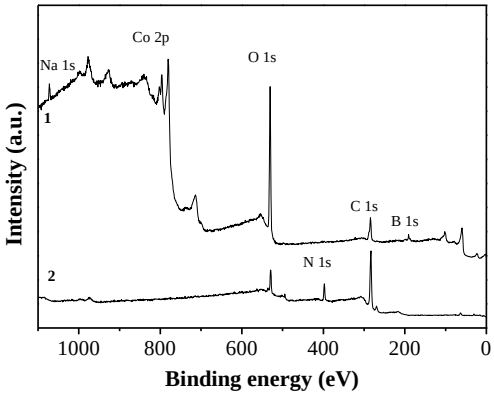

Figure S5. Co 2p and C 1s XPS spectra of (1) **Co1** and (2) **Co2**

Co 2p **C 1s**

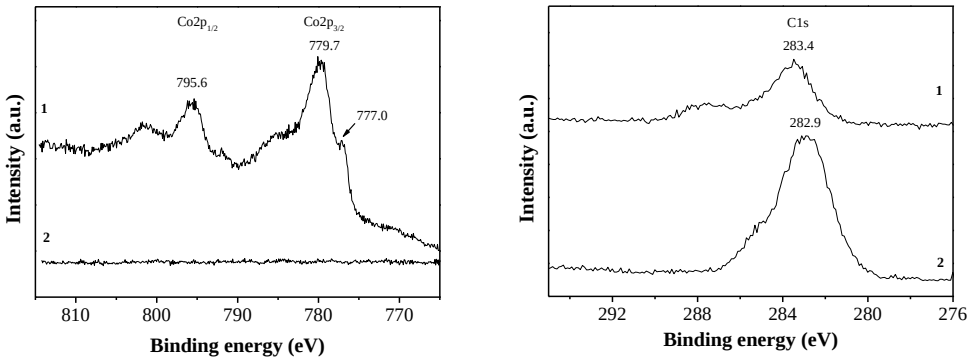

Figure S6. IR spectra of (1) PVP ; (2) **Co1**; (3) **Co2** in KBr disks.

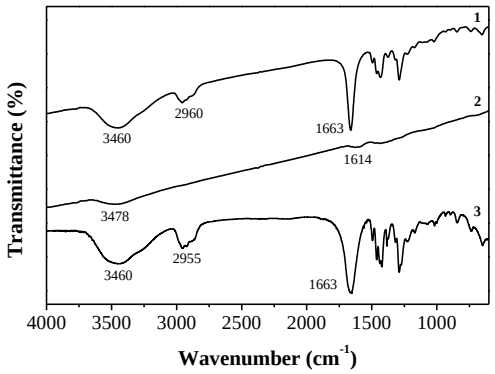

Figure S7. IR spectra of (1) PVP and **Co1** or **Co2** NPs before (2) and after (3) catalysis using water as solvent.

Co1 **Co2**

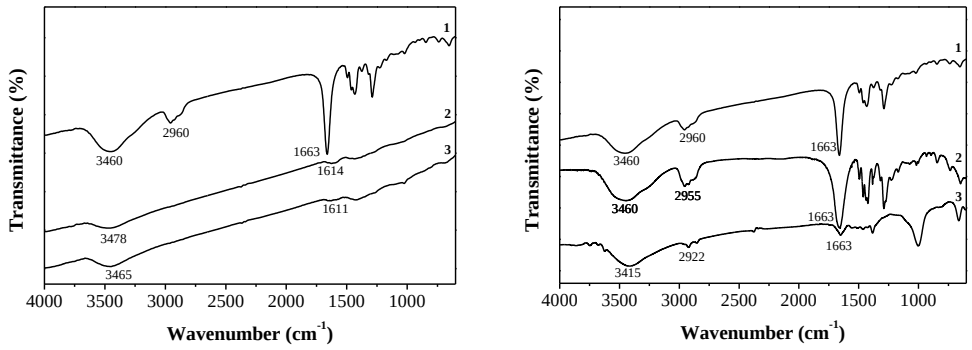

Figure S8. (a) TGA thermograms over N_2 flow of (1) **Co1** (2) **Co2** and (3) PVP. **(b)** TGA thermograms over N_2 flow of (1) **Co2** after water washing and (2) fresh **Co2**.

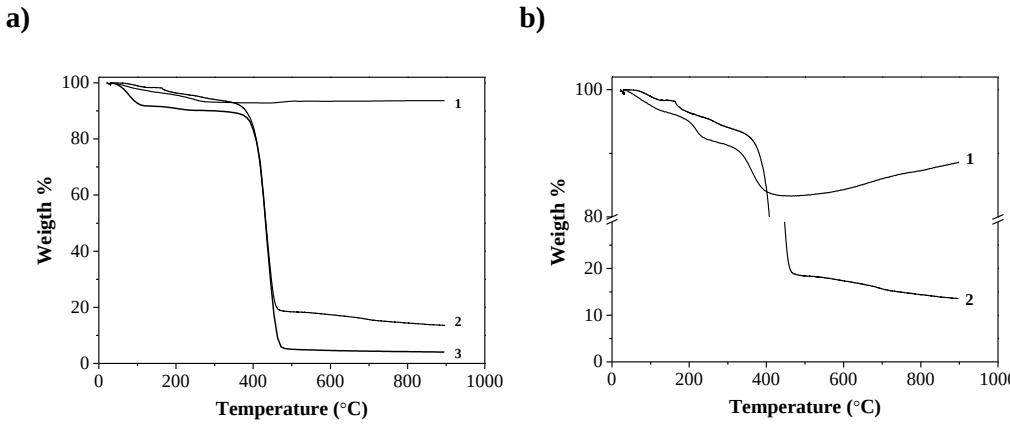

Figure S9. (**a**) Selectivity in wt% and (**b**) hydrocarbon selectivity in wt% of **Co2** as a function of the % heptane.

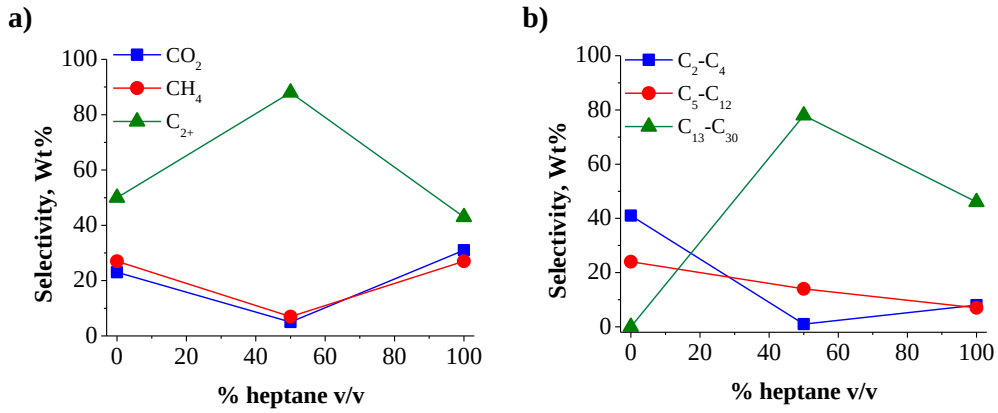

Figure S10. (**a**) Selectivity in wt% and (**b**) hydrocarbon selectivity in wt% of **Co2** as a function of the % ethanol.

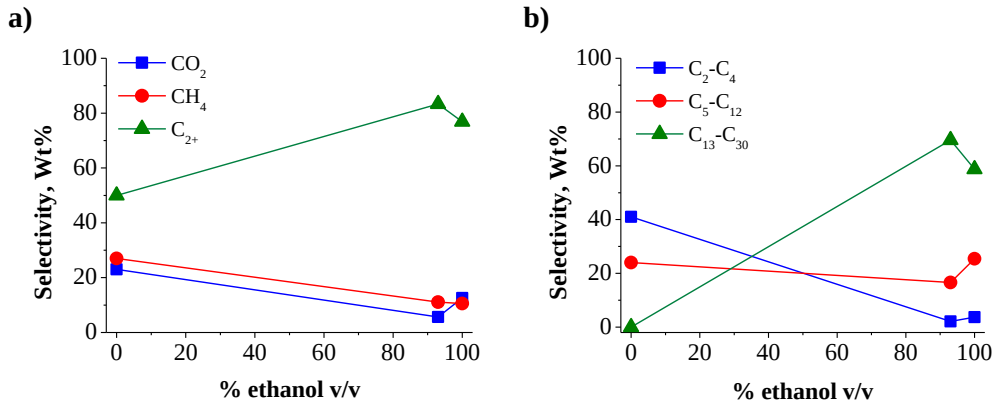

Measurement of H_2 and CO solubility in different solvent mixtures

The experimental set-up used for the solubility measurements was the same stirred tank rector used for the FT catalytic experiments. The experimental technique was the reported by Deimling *et al.*[26] and involves batch gas absorption (by surface aeration) in a liquid. The pressure of the enclosed gas phase in the reactor decreases with time because of the absorption. This decrease in pressure with time allows the estimation of mass transfer rate and the volumetric mass transfer coefficient (k_La). The total pressure decrease until equilibrium is reached gives the equilibrium solubility C*.

Experimental procedure

The autoclave was filled with 66 ml of the corresponding solvent, sealed and totally degassed by evacuation using a vacuum pump. The reactor was then pressurized with the gas which is to be absorbed. A pressure step of about 10 bar was established for satisfactory operation as recommended in the literature.[26] The stirrer was then set motion as soon as the reactor was filled with gas. The pressure decrease in the reactor during the absorption process was followed with a pressure transducer and recorded with the reactor software. The equilibrium pressure after absorption is the pressure of pre-saturation for the next experiment. The pressure in the vessel can then be increased to the next higher pressure level. The procedure was be repeated until the whole pressure range of interest was covered (7-36 bar). This procedure was repeated separately for H_2 and CO, using different liquids and liquid mixtures.

Figure S11. Solubility of H_2 and CO in heptane/water mixtures (**a**) and ethanol/water mixtures (**b**). Conditions for the measurement of gas solubilities: 100ml STR, 1000 rpm, r.t, V_l= 66.6 ml, V_g= 36.2 ml.

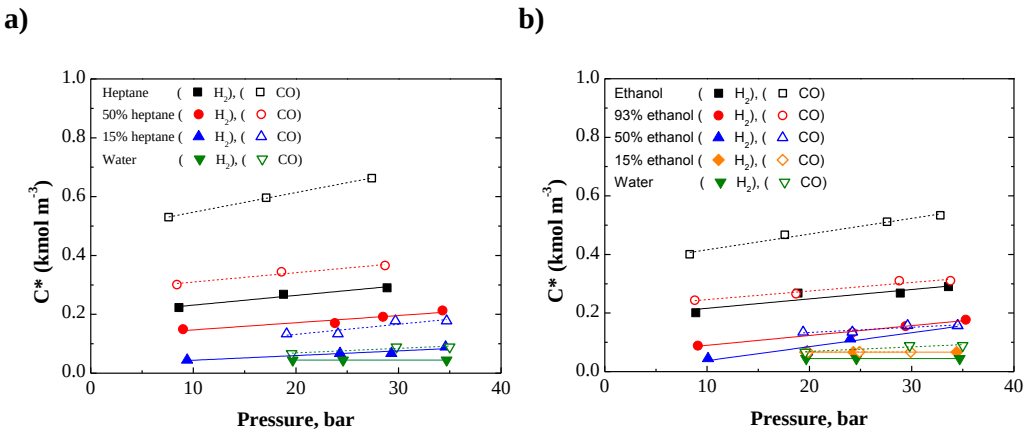

CHAPTER VI

Particle Size Effects in the Fischer-Tropsch Synthesis Over Cobalt Nanoparticles Prepared by Sodium Borohydride Reduction

Table of Contents

VI.1. Abstract

Small cobalt nanoparticles were synthesized in water using sodium borohydride as reducing agent and polyvinylpyrrolidone as stabilizer. Modulation of the particle size in the range of 1.7-7 nm was possible by varying the concentration of the borohydride solution. The colloidal NPs were immobilized on TiO_2 yielding 10 wt% Co/TiO_2 catalysts. Both colloidal and TiO_2 supported NPs were characterized by TEM, XRD, HRTEM, XPS, TGA, ICP techniques and their catalytic performance in the FTS were evaluated. As a general trend, an increase of the activity was observed when the particle size decreased. These results were rationalized based on several interconnected parameters: size effect, reduction degree of cobalt and the presence of boron species.

Keywords: Fischer-Tropsch synthesis, cobalt nanoparticles, size effect, polyvinylpyrrolidone.

VI.2. Introduction

The increasing worldwide energy demand has made major companies to consider alternative feedstocks such as natural gas, coal and biomass to replace fossil fuels.[1] In this context, the Fischer-Tropsch Synthesis (FTS) has been considered a key process of the biomass-to-liquid (BTL), gas-to-liquid (GTL) and solid-to-liquid technologies (STL)[2] since through this catalytic reaction, syngas can be transformed into high quality synthetic fuels (Scheme 1).[3] FTS is catalyzed by several transition metals including Ru, Co and Fe. However, cobalt based catalysts are more attractive from an industrial point of view due to their higher hydrocarbon productivity, good stability and commercial availability.[1]

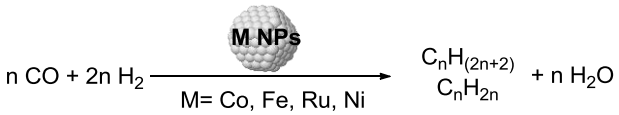

Scheme 1. Fischer-Tropsch synthesis catalyzed by metal nanoparticles

Currently, one of the main challenges in FTS research is the design of not only active and stable catalysts but also highly selective active phases that provide hydrocarbons with narrow chain length distributions.[4] Among the parameters that were shown to affect the selectivity of FTS catalysts such as the conditions used (T, P, H_2/CO ratio), the particle size of the catalysts is probably one of the most relevant.[5] The activity of the cobalt catalysts in FTS depends upon the number of active sites on the surface,[6] which is determined by the cobalt crystal size, loading amount, reduction degree and support-cobalt interactions.[7] Iglesia *et al.* reported a large increase in the FTS activity when the cobalt particle size was decreased from 200 to 9 nm.[8] On the other hand, small metal particles are highly susceptible to metal-support interaction, leading to the formation of difficultly reducible cobalt species.[9] Hence the synthesis of catalysts with uniform size and homogeneous distribution of metal is important for the FTS activity.

During the last decades, many efforts have been has been dedicated to study the cobalt particle size effects in the FTS.[6,10] Although many of these studies pointed that cobalt nanoparticles (CoNPs) below 10-6 nm resulted in less active catalysts compared to cobalt particles of larger sizes, there are some reports showing the opposite trend.

J. P. den Breejen *et al.* applied a Steady-State Isotopic Transient Kinetic Analysis (SSITKA) to provide information on surface residence times and coverage of reaction intermediates as a function of the cobalt particles size (2-16 nm).[10i] They concluded that the lower TOF measured for small cobalt particles (<6 nm) compared to larger ones is the result of a significant increase in the CH_x residence time combined with a decrease of the CH_x coverage. Yun-Jo Lee and co-workers studied the Co particle size effect in the range of 3-16 nm on catalytic activity, selectivity and stability.[6] They reported an increase of the CO conversion and TOF values as the crystal size increases from 4.8 to 9.3 nm. However for larger CoNPs, lower TOF were measured, indicating that under these conditions, the optimal size was *ca*. 9 nm in terms of activity. In another report, de Jong and co-workers using carbon nanofiber supported catalysts[10b] described that the turnover frequency decreased when the particle size was decreased from 6 to 2.6 nm. In this case, the

cobalt particle size effect was ascribed as a combination of CO-induced surface reconstruction and non-classical structure sensitivity. Among the different views on the origin of the cobalt particle size effect, numerous publications reported that oxidation of cobalt crystallites in the presence of water during FTS will also depend on the NPs size, which in return will affect the catalytic performance.[11] van Steen and co-workers concluded that the stability of nanosized crystallites is governed by the contribution of the surface energy to the overall energy of the system from a thermodynamic analysis of oxidation and re-reduction of cobalt in water/hydrogen mixtures.[11b] Small metal cobalt crystallites exposed to a water/hydrogen atmosphere as experienced during FTS were shown to be oxidized to Co(II)O depending on the crystallite size, morphology, the starting crystal phase, and the ratio of the partial pressure of water relative to the partial pressure of hydrogen.

However, the surface dependent activity of cobalt nanoclusters also has been reported in the FTS. Kikuchi *et al*. observed an increase of the CO conversion from 10 to 40 % when the cobalt particle size decreased from 54.8 to 20.1 nm respectively. The CoNPs used in this stidu were prepared by chemical reduction of cobalt salts using $NaBH_4$ as reducing agent.[10e] The observed behavior in catalysis was rationalized due to the contamination by sodium, more significant with lager particles. More recently, a similar trend in the FTS activity as a function of the particle size has been reported.[12] JinLin and co-workers studied the effect of catalyst confinement and pore size on FTS over CoNPs supported on carbon nanotubes (CNTs).[12b] Cobalt particle sizes of 4.2, 6.3 and 9.4nm were obtained for the catalysts prepared on the CNTs with average pore size of 5, 11 and 17 nm respectively. TPR analysis indicated that the reducibility of cobalt oxide particles inside the CNTs decreased with the increasing of the particle size. In catalysis, CNTs of smaller pore size (resulting in smaller cobalt particle size) appeared to enhance the FTS activity due to little interaction between the cobalt oxide and carbon and the electron shift on the non-planar carbon tube surface. In a different report, Housaindokht and Pour used also CNTs as support of cobalt nanoparticles to study the cobalt particle size effect in FTS. In catalysis it was observed that the cobalt time yields increases substantially (from 2.9 to 3.5 $x10^{-3}$ $mol_{CO}molCo^{-1}s^{-1}$

while the site-time yield (TOF) decreased when decreasing of cobalt particle size.[12a]

With the aim to enhance the productivity of the process, many efforts have been dedicated to the preparation of ultrafine particle catalyst and the study of their interactions with the supports.[10c,13] Currently, the control of the selectivity is one of the main goals in FTS investigation.[14] In this context, the use of unsupported nanoparticles is of high interest as they mimic metal surface activation and catalysis at the nanoscale, and shed some light on the role of the support during catalysis.[15] The first report of the aqueous phase Fischer-Tropsch Synthesis (AFTS) was reported using ruthenium nanoparticles (RuNPs) stabilized with poly(N-vinyl-2-pyrrolidone) (PVP) as catalysts.[16] In this study, the particle size of the RuNPs was modulated between 1.6 and 4.5 nm through the seeded growth method (Chapter I), and the series tested in the AFTS. Surprisingly, the Ru nanocatalyst of 2.0 nm exhibited the highest activity of the series; however no explanation of this unusual behaviour was given.[16] The structure sensitivity of PVP stabilized RuNPs in the AFTS has been also reported by Claver and co-workers[17] and Quek *et al*.[18]

Recently, the effect of the polymer stabilizer was studied in our group in the AFTS catalysed by RuNPs.[17] It was observed that PVP stabilized RuNPs were more active and selective towards hydrocarbons compared to those stabilized by lignins, indicating that the nature of the stabilizing polymer does affect the catalytic performance in AFTS influencing strongly the production of CO_2 by WGS reaction.

Concerning cobalt catalysts, Kou and co-workers recently reported the use of cobalt/platinum alloy nanoparticles stabilized by PVP as catalysts of the AFTS.[19] According to this report, activity up to 1.1 $mol_{CO}mol_{Suf\text{-}Co}^{-1}h^{-1}$ with a growth factor (α) of 0.8 was obtained at 160ºC. This outstanding activity was rationalized by the formation of Co overlayer structures on Pt NPs or Pt-Co alloy NPs. The same author tested Co nanoparticles reduced by $LiBEt_3H$ and $NaBH_4$, in the AFTS, obtaining a better catalytic performance in the former case.[20] It was suggested that catalyst reconstruction occurs during the reaction by comparing the particle size distribution of the catalysts before and after reaction. In addition it was proposed the B-doping could affect the catalytic performance of these NPs, however, no detailed study of

the nanoparticle structure or cobalt-boron interaction was given. The same author previously reported the synthesis of CoNPs by a chemical reduction method using sodium borohydride as reducing agent in water. The resulted NPs were active in the AFTS ($0.12 mol_{CO} mol_{Suf\text{-}Co}^{-1} h^{-1}$ at 170ºC).[21]

In the present work, the easy synthesis of reproducible and well size defined cobalt nanoparticles by chemical reduction using sodium borohydride in aqueous media is described. The aim of this investigation firstly is to understand the structure, composition and possible cobalt-boron interactions involved in these B-doped cobalt nanoparticles and secondly, to evaluate its catalytic performance in the FTS at the lower limit of the nanoscale (1-10 nm). The colloidal NPs were additionally immobilized on TiO_2 support, to allow the comparison between two catalytic systems: the classical FTS in fixed bed reactors and the AFTS using colloidal catalysts. This approach allowed us to give insights in the real parameters affecting the catalytic performance of these NPs and to clarify the possible interaction of the metal particles with the support.

VI.3. Results and Discussion

VI.3.1. Synthesis and characterization of CoNPs

The cobalt nanoparticles synthesized in this work were prepared by chemical reduction of $CoCl_2$ in water using $NaBH_4$ as reductant and PVP as stabilizer. CoNPs with distinct size were obtained varying the concentration of the $NaBH_4$ solutions as depicted in Scheme 2.

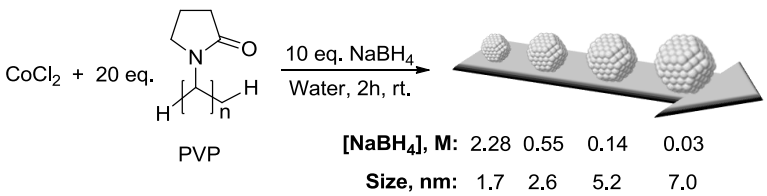

Scheme 2. Preparation of variable size CoNPs by chemical reduction method, varying the concentration of the $NaBH_4$ solution.

The TEM micrographs and size histograms of **Co1-4** are displayed in Figure 1. According to TEM analysis spherical cobalt nanoparticles of diameters between 1.7 to 7.0 nm were obtained respectively.

As a general trend, it was found that increasing the concentrations of both $NaBH_4$ and $CoCl_2$/PVP solutions, resulted in a decrease of the CoNPs size. Figure 2 summarises the size of **Co1-4** as a function of the concentration of the $NaBH_4$ and $CoCl_2$/PVP solutions.

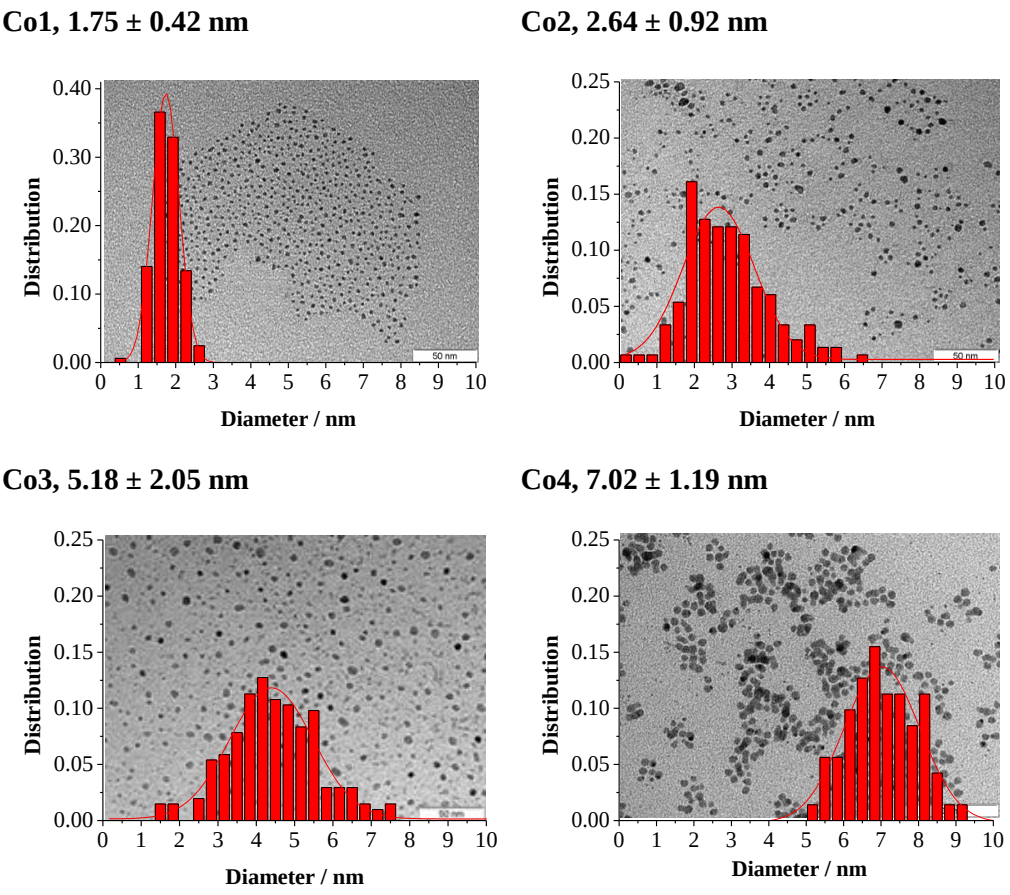

Figure 1. Size histograms and TEM micrographs of **Co1**-4.

The formation of smaller particles under high $NaBH_4$ concentrations is explained in terms of the higher nucleation rate, which is the responsible of the

formation of a large number of cobalt seeds, in comparison to the growth rate (Figure 2).

A similar relation between the concentration of $NaBH_4$ with the cobalt particle size was noticed by Wang *et al.* who reported the synthesis of 1-2 nm cobalt nanoparticles by using a high concentration of $NaBH_4$ aqueous solution (10 M), while lower concentrations resulted in the formation of larger particles (>10 nm).[22]

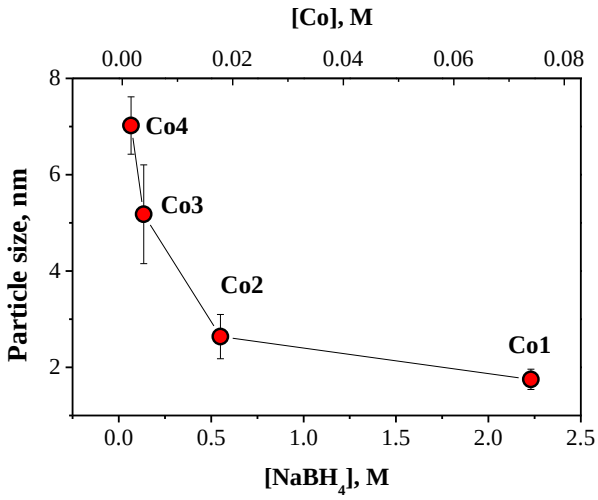

Figure 2. Variation of the particle size of the CoNPs as a function of $NaBH_4$ concentration during the synthesis.

The size and the fine structure of **Co2** were also studied by high-resolution transmission electron microscopy (Supporting Information, Figure S2). With this technique, single particles of 2.6 nm diameter were observed, in agreement with previous TEM analysis (2.64 ± 0.92 nm). Analysis of the diffraction pattern on these NPs revealed the presence of crystalline CoO-fcc and Co_3O_4-fcc.

The XRD pattern of the smallest CoNPs (**Co1,** 1.7 nm**)** revealed the presence of a single broad band centred at 45º and such band became sharper when the particle size increased up to 7.0 nm (Figure 3). The largest NPs of the series, (**Co4**, 7.0 nm) exhibited at least two additional small bands at 34 and 60º. However, these bands could not be unambiguously attributed to either cobalt or cobalt oxide

phases. The broadening of XRD lines is frequently related to the decrease of the crystallite size but also to the presence of strained and imperfect crystals. Similar XRD patterns have been reported in the literature for CoNPs synthesized by chemical reduction using $NaBH_4$ as reducing agent.[23] For instance, Torres *et al.* reported the synthesis of CoNPs of 1 nm exhibiting XRD patterns with broad bands and attributed this effect to the small size of the CoNPs.[23a] However, Pileni and co-workers attributed the broadness of XRD patterns of 7 nm CoNPs (also synthesized by chemical reduction) to their amorphous structure.[23b] Therefore, in view of these reports, the broad bands observed here could arise from the amorphous structure and/or due to the small size of the CoNPs.

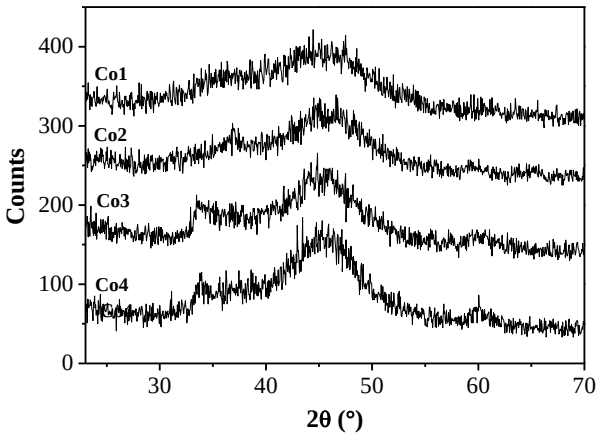

Figure 3. XRD patterns of **Co1-4** NPs.

Other authors reported a similar diffraction pattern for amorphous Co-B alloys also synthesized by chemical reduction of cobalt salts using $NaBH_4$.[24] The identity of the CoNPs was described previously (Chapter 3) using a methodology reported by Glavee *et al*. which consisted in the thermal treatment of the CoNPs under Ar atmosphere. (Supporting Information, Figure S3 b).[25] As displayed in Figure 4, this procedure forced the crystallization of the CoNPs thus elucidating the presence of a defined crystalline pattern of metallic cobalt phases (fcc and hcp),

together with a defined pattern of $B(OH)_3$ located at 28º. Particularly, **Co1** exhibited additional peaks corresponding to Co_2B-bct, which did not appear in the other samples. As a general trend, it was observed that the broad band located at 45º decayed in the series **Co1-4,** which could suggest the progressive decrease of the Co_2B content as the particle size of the CoNPs decrease.[25-26] It was therefore concluded that **Co1-4** correspond to a mixture of cobalt, cobalt oxide, $B(OH)_3$ and Co_2B amorphous phases and presumably, the proportion vary with the particle size.

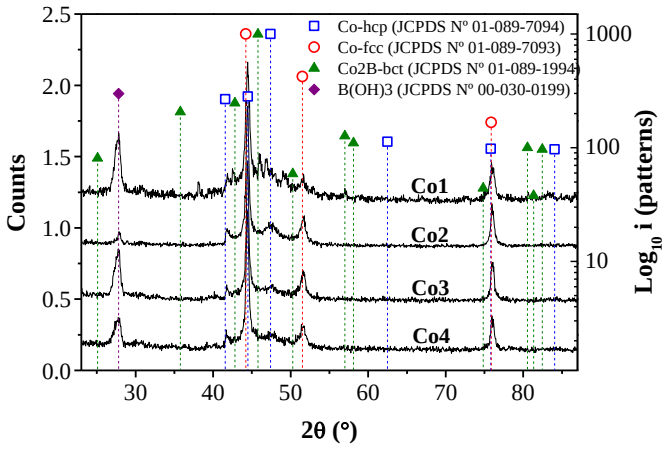

Figure 4. XRD patterns of **Co1-4** treated at 500 ºC for 2h under argon.

Surface analysis of the CoNPs synthesised in this study was performed by X-ray photoelectron spectroscopy (XPS). The full XPS spectra of **Co1-4** revealed the presence of Na, Co, O, N, C and B, according to the peaks observed at their characteristic binding energies (1071.6; 781.5; 530.9; 399.2; 284.5 and 191.1 eV respectively). The Co 2p XPS spectrum of the series **Co1-4** exhibited two prominent sets of peaks at *ca.* 777-794 and 795-806 eV readily assigned to Co $2p_{3/2}$ and Co $2p_{1/2}$, respectively. Each region was deconvoluted into three bands corresponding to metallic cobalt, Co^{2+} (CoO) and a prominent shake-up satellite located at higher binding energy (Figure 5a).[27]

The fractions of Co^0 and Co^{2+} extracted from the decomposition of the Co $2p_{3/2}$ spin orbit peaks are displayed in Table 1. It is noteworthy that the fraction of metallic cobalt decreases from 38 to 12% in the series **Co1-4**, according to the increase of the particle size from 1.7 to 7 nm. The low content of metallic cobalt suggests the presence of important amounts of cobalt oxide in agreement with the observed by Raman spectroscopy (Supporting Information, Figure S5).

The B 1s XPS spectra of the series **Co1-4** revealed the presence of two bands at 187.97 and 191.5 eV (Supporting Information, Figure S4 d) which were assigned to elemental boron (or Co_xB) and borates respectively according to reported data.[28] Deconvolution of the B 1s XPS revealed the abundance of the high valent boron species in comparison to the elemental one (>70 %).

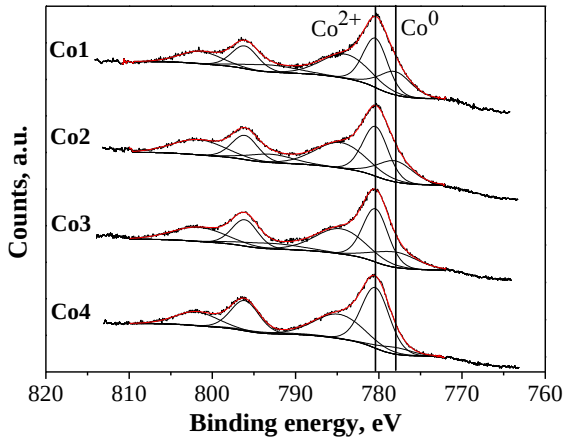

Figure 5. Co 2p XPS spectra of **Co1-4** NPs.

Table 1. Percentage of Co and B species in colloidal NPs from XPS spectra decomposition.[a]

Catalyst	Size, nm	Co^0	Co^{2+}	B^0	$B^{\delta+}$
Co1	1.75 ± 0.42	38	62	23	77
Co2	2.64 ± 0.92	37	63	15	85
Co3	5.18 ± 2.05	33	67		
Co4	7.02 ± 1.19	12	88	14	86

[a] Percentages corresponding to the Co $2p_{3/2}$ and B 1b spin orbit peaks.

Quantification of the content of cobalt and boron of **Co1-4** was performed by ICP (Table S1) The Co/B atom ratio for the series of CoNPs was in the range between 2.1-2.8 according to ICP analysis. Many studies have enlightened the dependence of the final composition of the cobalt nanoparticles[29] and cobalt amorphous borides[30] on the reaction temperature,[31] the pH, and the borohydride concentration or ratio versus the cobalt source.[22,31-32] For instance, Glavee *et al.* reported that the boron content in Co-B amorphous alloys increased with the BH_4^- concentration.[25] From ICP analysis it was therefore concluded that boron is present in the series of NPs **Co1-4**, and the atomic Co/B ratios resulted to be *ca.* 2.3 according to ICP analysis, however, there is not a clear dependence of the content of boron with the particle size of the CoNPs.

The presence of PVP and the thermal stability of **Co1-4** were examined by thermogravimetric analysis. The thermograms of **Co1-4** exhibited a first weight loss in the region of 90-110ºC (-5 wt% aprox. attributed to the loss of adsorbed solvent) followed by almost depreciable weigh loses at higher temperature (near -2 wt% aprox.) however no weight loss was observed at the decomposition temperature of PVP (430 ºC). In addition, no characteristic signals of PVP were detected by FTIR in the CoNPs. With these observations was therefore concluded that there is no evidence of presence of PVP in the series **Co1-4.**

To summarize, CoNPs of sizes between 1.7 to 7.0 nm were synthesized by controlling the concentration of the $NaBH_4$ solution. Structural analysis by HR-TEM revealed the presence of CoO-fcc and Co_3O_4-fcc crystalline phases in **Co2,** a representative CoNPs, while the diffraction pattern observed by XRD, suggested the amorphous structure and the small size of the NPs. The surface analysis by XPS indicated the considerable oxidation degree of the NPs and its dependence with the size: more reduced CoNPs were obtained at smaller sizes. Finally, the analysis by FTIR and TGA demonstrated that no PVP is present on these NPs after the work-up.

Characterization of TiO_2 supported catalysts (Co1-4/TiO_2)

Supported Co/TiO_2 catalysts were prepared by direct immobilization of the colloidal CoNPs by mixing suspensions of both the CoNPs and the TiO_2 support in

hexane. After immobilization of **Co1-4** on TiO_2, the particle size of the nanoclusters was maintained the same as the initial colloidal NPs as displayed in Figure 6. According to the TEM micrographs of the supported catalysts, the CoNPs were dispersed on TiO_2 crystals of *ca.* 10-60 nm (Aeroxide® P25).

Co1/TiO_2, 1.75 ± 0.42 nm. **Co2/TiO_2, 2.64 ± 0.92 nm.**

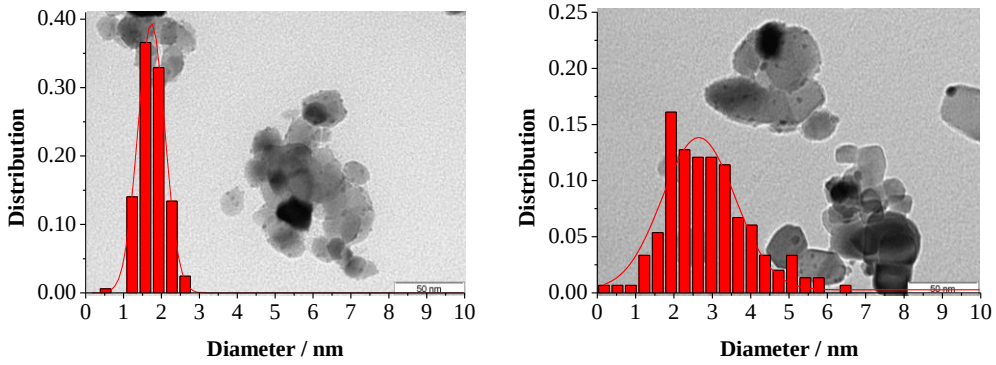

Co3/TiO_2, 5.18 ± 2.05 nm. **Co4/TiO_2, 7.02 ± 1.19 nm.**

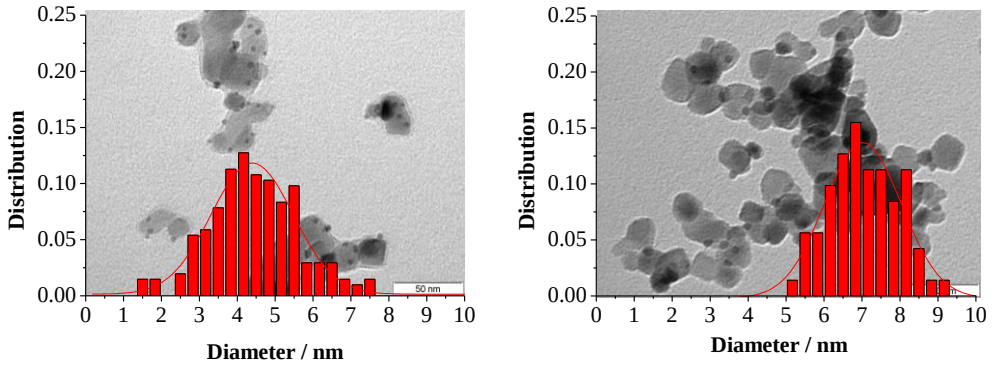

Figure 6. Size histograms and TEM micrographs of **Co1-4/TiO_2**

According to the HR-TEM micrograph of **Co2/TiO_2** catalyst displayed in Figure 7, the CoNPs are located at the borders of a TiO_2 crystal as indicated by arrows, however the distinction of the metal particles and the solid support is quite difficult in bright field analysis. The fine structure of the support is appreciated and the electron diffraction of the dotted area present characteristic signals of anatase planes (hkl: 101 and 004, Sys: Tetragonal, S.G: $I4_1/amd$).

XRD of the fresh catalysts was performed as complementary technique for the structure analysis, in addition to HR-TEM analysis. As displayed in Figure 8, in the series of catalyst the anatase crystalline phase predominates over rutile phase (85 vs 15%) however, the characteristic band of the CoNPs at 45º overlapped with support signals.

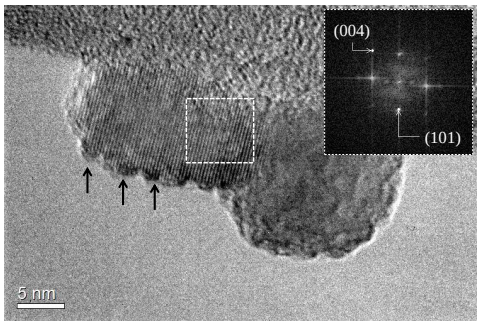

Figure 7. HR-TEM micrograph and electron diffraction of **Co2/TiO$_2$.**

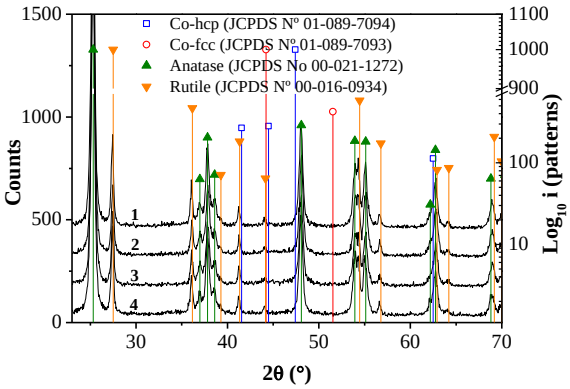

Figure 8. XRD patterns of TiO_2 supported CoNPs: (1) **Co1/TiO$_2$**; (2) **Co2/TiO$_2$**; (3) **Co3/TiO$_2$** and (4) **Co4/TiO$_2$**.

Surface analysis of the supported catalysts was performed also by XPS. Despite the low signal/noise explained by the low cobalt loading in the catalysts (*ca.* 10 wt%), deconvolution of the Co $2p_{3/2}$ spin orbit peaks (Supporting Information, Figure S10) confirmed the observed trend in the single CoNPs according to which

the reduction degree of the nanoparticles increased with the decrease of the particle size.

The reducibility of the fresh supported catalysts **Co1-4/TiO_2** was analyzed by temperature programmed reduction (TPR). At least two reduction bands were observed from their TPR profile at around 300-450 and 450-600 ºC (Figure 9). It has been reported that the peak at 300-400 ºC corresponds to the reduction of Co_3O_4 to CoO and that at 400-600 ºC to the reduction of CoO to Co metal.[33] As displayed in Figure 9, the TPR spectra of **Co1/TiO_2** corresponding to the NPs of 1.7 nm, shifted to lower temperatures when compared to the catalyst containing the largest cobalt NPs, 7.0 nm (**Co4/TiO_2**). Possibly, the lower reduction temperature over 1.7 nm sample might be the result of the higher contribution of already reduced Co in the core of the particle which facilitates the reduction process, in comparison to larger particles with lower initial content of metallic cobalt (according to XPS analysis).It is noteworthy that low detection issues occurred during the analysis due to the partially reduced nature of the NPs intrinsic to its preparation methodology discussed by XPS above.

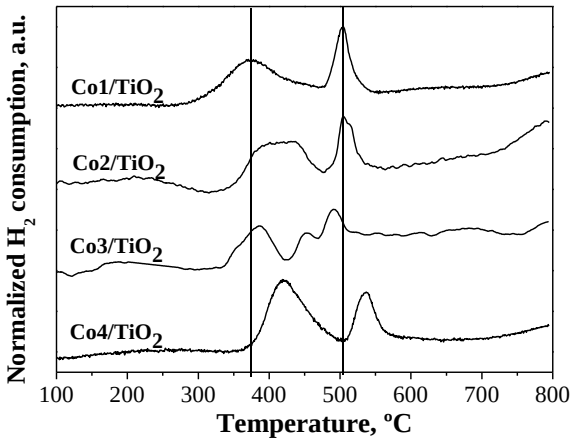

Figure 9. H_2-TPR profiles of **Co1-4/TiO_2** catalysts.

N_2 physisorption analyses were also realized on fresh catalysts. The BET areas of the series of catalysts **Co1-4/TiO_2** ranged between 44 and 62 m^2/g, values which are slightly larger than that measured for TiO_2 alone (43 m^2/g). ICP analysis of the supported catalysts revealed that the cobalt loading for the series ranged between 7-10 wt% (Supporting Information, Table S4).

To summarize, supported catalysts **Co1-4/TiO_2** were prepared by immobilization of the corresponding colloidal NPs **Co1-4** on TiO_2. Analysis of the supported catalysts by TEM and XPS confirmed the order of particle sizes and the reduction degree determined in the colloidal NPs. Finally, analysis of **Co1-4/TiO_2** by TPR suggests that the reducibility of the catalysts increased with the decrease of the cobalt particle size.

VI.3.2. Fischer-Tropsch catalytic experiments

VI.3.2.1. Aqueous phase Fischer-Tropsch synthesis using colloidal CoNPs (Co1-4)

In order to evaluate the effect of the particle size in FTS without possible effects derived from support interactions, catalytic experiments were carried out using the unsupported catalysts (**Co1-4**) suspended in water and the results are displayed in Table 2. The decrease of the particles size from 7.0 to 1.7 nm resulted in the linear increase of the time yield of the CoNPs from 0.006 to 0.035 h^{-1} (Figure 10a).

Table 2. Aqueous phase Fischer-Tropsch synthesis catalyzed by **Co1-4** evaluating the size effect of the CoNPs.[a]

				Selectivity, Wt%					
E.	**Catalyst**	**Size, nm**	**Cobalt time yield, h^{-1}[b]**	**CO_2**	**CH_4**	**C_{2-4}**	**C_{5-12}**	**C_{12+}**	***α***
1	**Co1**	1.75	0.035	23.8	23.7	31.9	20.6	0	0.56
2	**Co2**	2.64	0.026	23.0	20.3	32.9	23.9	0	0.59
3	**Co3**	5.18	0.019	36.2	22.4	27.5	13.9	0	0.64
4	**Co4**	7.02	0.006	64.7	11.5	13.3	10.5	0	0.66

[a] Conditions: 0.949 mmol Co, 30 bar H_2/CO/Ar (2:1:0,15); 66 ml water, 1000 rpm, 180 ºC, 12h [b] metal time yield = mol of CO converted per mol of Co, per unit of time.

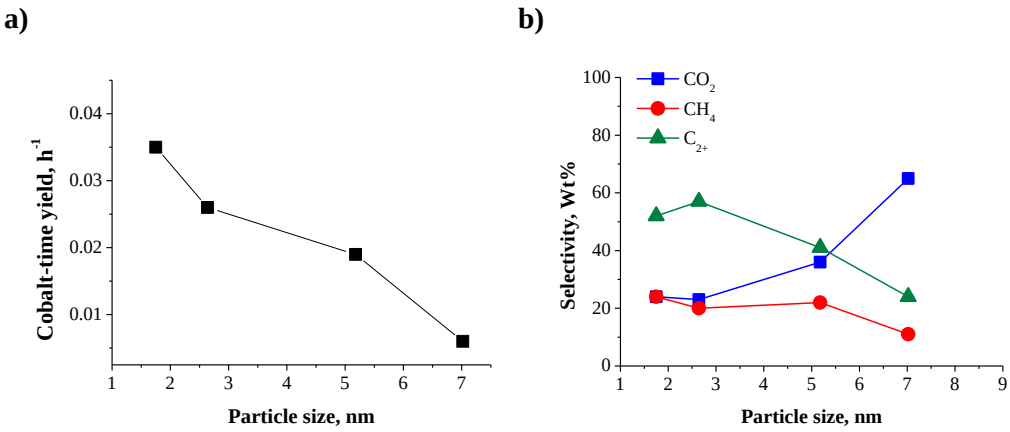

Figure 10. (**a**) Cobalt-time yield and (**b**) product selectivity in wt% of unsupported catalysts, **Co1-4** as a function of the particle size measured by TEM. Conditions: 0.949 mmol Co, 30 bar H_2/CO/Ar (2:1:0,15); 66 ml water, 1000 rpm, 180 ºC, 12h

In terms of product selectivity (Figure 10b), the increase of the particle size resulted in the increase of the CO_2 selectivity, reaching a maximum value of 65% for the 7.0 nm CoNPs (**Co4**). In contrast the methane selectivity slightly increased from 11 to 23 % with the decrease of the particle size. Moreover, when the particle size decreased from 7.0 to 2.6 nm, the C_{2+} fraction increased from 24 to 57 %, and remained almost constant for the smallest CoNPs (52% for **Co1**). It is noteworthy that under the current colloidal conditions using water as solvent, the chain length of the hydrocarbon products was not longer than C_{12}, as can be appreciated in the ASF distributions (Supporting Information, Figure S8). The observed trend was that the α values increased from 0.56 to 0.66 in the series **Co1-4** as the particle size of the CoNPs increased from 1.7 to 7.0 nm.

The observed trend in activity as a function of the particle size depend on at least three parameters which could be interconnected:

- Boron doping
- Reducibility of cobalt
- Cobalt particle size effect in relation to the surface area

- Concerning the first parameter, Kou and co-workers analyzed by ICP the cobalt and boron content of CoNPs prepared from $NaBH_4$ and $LiBEt_3H$ determining Co/B atom ratios of 0.2 and 2 respectively.[20] They proposed that the large boron content in the Co-$NaBH_4$ explained the lower catalytic performance in comparison to Co-$LiBEt_3H$ considering that the excess of B could noticeably reduce the activity and selectivity in FTS (0.10 vs. 0.27 $mol_{CO}mol_{Co}^{-1}h^{-1}$).[34] Additionally, CoB_x phases were detected by XRD in the fresh Co-$NaBH_4$ catalyst, thus revealing that the nature of the active phase was a cobalt boride species instead of cobalt. Glavee *et al*. reported the favored production of cobalt borides when the synthesis of the NPs was performed under inert conditions, similarly to the procedure described by Kou and co-workers for the Co-$NaBH_4$ catalyst. In our particular case the boron content of **Co1-4** resulted to be *ca.* ten times lower than that reported by Kou for Co-$NaBH_4$ NPs (Co/B atom ratios of 2.3 vs. 0.2). More importantly, the Co/B atom ratio for the series **Co1-4** were of similar order (2.1-2.7 according to ICP analysis, Table S1), thus suggesting that the amount of boron did not affect largely the activity of these catalysts.
- Secondly, considering that the colloidal catalysts are tested without activation pretreatment, the initial content of metallic cobalt in the NPs seems to be directly related to the activity. According to this, the increase of activity observed when the particle size decreased could be rationalized through the increasing content of metallic cobalt for this series as measured by XPS.
- Finally, the decrease of the surface to total atoms ratio with the increasing of the size, also agrees with the trend observed in catalysis. The size dependent activity has been reported in the literature for other reactions catalyzed by metal nanoparticles.[35]

In terms of product selectivity, similar C_{2-4} selectivity (*ca.* 30 wt%), alpha values (α *ca.* 0.6) and olefin to paraffin ratios (*ca* 0.75 for C_{2-12}) were observed in the present study in agreement with the Co-$NaBH_4$ catalyst reported by Kou and co-workers.[34] The increase of the CO_2 selectivity with the particle size could be rationalized considering the reported activity of oxidized cobalt species in WGS,[36] since a greater content in oxidized cobalt was detected in the large particles

according to XPS analysis (Table 1). The rationalization of the higher methane selectivity with small Co particles has been usually based on a higher coverage of hydrogen, as previously evidenced by P. B. Radstake *et al*. through SSITKA (Steady-State Isotopic Transient Kinetic Analysis) measurements.[10i] The higher H_2 coverage for the smallest NPs was shown to lead to rapid hydrogenation of CO to methane, rather than polymerization towards C_{2+} products, thus also affecting the chain growth by a more efficient termination.

VI.3.2.2. Fischer-Tropsch synthesis using TiO_2 supported CoNPs (Co1-4/TiO_2)

With the aim to investigate the possible effect of the support by comparison with the colloidal system, Fischer-Tropsch catalytic experiments were also performed using the TiO_2 supported catalysts (**Co1-4/TiO_2**) in fixed bed reactors. The FTS catalytic results obtained at 240 ºC after 46 h of reaction are displayed in Table 3.

Table 3. Fischer-Tropsch synthesis in fixed bed reactor catalyzed by TiO_2 supported CoNPs (**Co1-4/TiO_2**)[a]

				Selectivity, Wt%					
E.	**Catalyst**	**Size, nm**	**Cobalt time yield, h^{-1},b**	**CO_2**	**CH_4**	**C_{2-4}**	**C_{5-12}**	**C_{12+}**	***α***
1	**Co1/TiO_2**	1.75	10.62	0.3	12.1	16.5	19.8	51.3	0.71
2	**Co2/TiO_2**	2.64	5.27	0	10.5	17.4	19.0	53.0	0.76
3	**Co3/TiO_2**	5.18	1.52	0	17.4	23.6	27.0	32.1	*
4	**Co4/TiO_2**	7.02	0.36	*	*	*	*	*	0.87

[a] Conditions: Catalyst loading=8-12wt%, 20 bar H_2/CO/N_2 (2:1:0.15), 5.62 ml/min, 240 ºC, CO conversions at 46h; [b] metal time yield = mol of CO converted per mol of Co, per unit of time. [c] Site yield calculated for CoNPs of 2.15 nm as measured in the used catalyst by TEM. * Not available information.

Since the catalysts had not exactly the same cobalt content, cobalt time yields were used instead of CO conversions to represent the catalytic activity. The evolution of the cobalt time yield of the catalysts during time is displayed in Figure 11. Comparing the series of catalysts (Table 3, entry 1-4), it is clearly observed that increasing the cobalt particle size (**Co1/TiO_2** to **Co4/TiO_2**) resulted in the progressive decrease of the cobalt time yield from 10.6 to almost 0.3 h^{-1}.

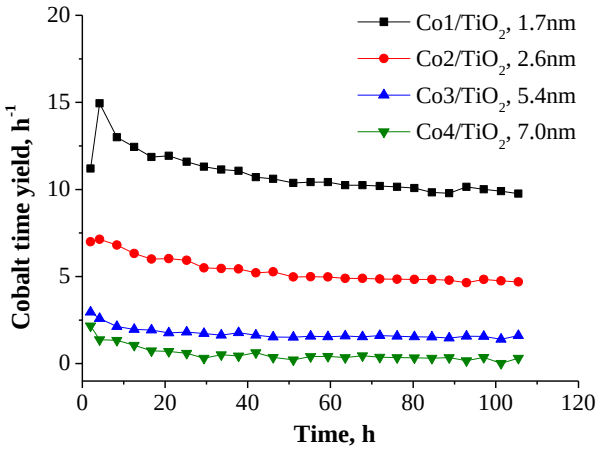

Figure 11. Evolution of cobalt time yield in FT experiments. Cobalt time yield: mol of CO converted per mol of Co, per hour. Conditions: 7-10 wt% Co/TiO_2, 20 bar $H_2/CO/N_2$ (2:1:0.15), 5.62 ml/min, 240 ºC.

Deactivation rates were calculated for the series of tested catalysts computing the time yields at 2h and 46h (Table 4). Comparing the series **Co2-4/TiO_2** the increase of the deactivation rate (from -25 to -83%) is evident as the particle size of the CoNPs increased from 2.6 to 7.0nm.

It should be noted that due to the low activity of the catalyst **Co4/TiO_2**, some of the products could not be quantified. The CO_2 and CH_4 selectivity for the series of TiO_2 supported catalysts were below 0.4 % and in the range of 10-17% respectively. The C_{2-4} selectivity was observed to increase from 16.5 to 23.6% for the catalysts **Co1-3/TiO_2** in which the cobalt particle size increased from 1.7 to 5.2 nm.

Table 4. Deactivation rate of cobalt catalysts at 240 ºC

Catalyst	Co-time yield at 2h	Co-time yield at 46h	Δ Co-time yield, %
Co1/TiO_2	14.9	10.6	-28.9
Co2/TiO_2	7.0	5.3	-24.6
Co3/TiO_2	3.0	1.5	-48.5
Co4/TiO_2	2.2	0.4	-83.6

Concerning the chain growth probability, the alpha values increased from 0.71 to 0.87 when the particle size of the CoNPs increased (**Co1-4/TiO_2**) according to the ASF distributions displayed in Figure 12.

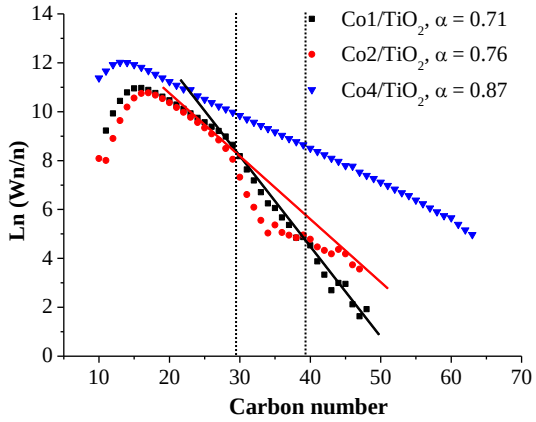

Figure 12. ASF distributions of **Co1-4/TiO_2 .**

It is noteworthy that the catalyst bearing the smallest CoNPs, **Co1/TiO_2** and **Co2/TiO_2** (1.7 and 2.6 nm) exhibited an inflexion in the distribution near C_{30} according to that, products containing more than $C_{40\text{-}50}$ were not detected. In contrast, the catalysts with the largest cobalt nanoclusters, **Co4/TiO_2** (7.0 nm) exhibited a classical continuous ASF distributions (with hydrocarbon chains up to C_{70}) with only one slope.

Characterization of used TiO_2 supported catalysts

Since the fresh catalysts suffers a series of transformations during the activation and the initial hours of reaction (e.g. sintering) the characterization of the catalyst once it reaches the steady state (which could be considered as the truly FT catalysts), is important. For this purpose TEM, XRD and XPS analysis were performed on the used catalysts to study variations of the cobalt particle size, crystalline structure and oxidation degree after reaction, respectively.

TEM analysis of the used catalysts **Co2-4/TiO_2** exhibited small variations in the cobalt particle size compared to the fresh catalyst (Supporting Information, Table S2). Curiously, the cobalt particle size for the catalysts **Co3,4/TiO_2** appeared to decrease more substantially during catalysis (5.18 vs. 3.65 nm for **Co3/TiO_2** and 7.02 vs. 4.85 nm for **Co4/TiO_2**).

The particle size and proportion of Co-fcc/Co-hcp crystallites were calculated from the XRD diffraction pattern in the used catalysts and Scherer equation at 51.5º (Supporting Information, Table S5). Analysis of the phase content for metallic cobalt demonstrated that the contribution of Co-hcp is almost twice the content of Co-fcc.

Surface analysis of the used catalysts was performed by XPS in order to study the reduction degree and the deactivation of the catalyst during FTS. Deconvolution of the Co $2p_{3/2}$ spin orbit peaks (Supporting Information, Table S7) revealed that the percentage of Co^0 after the activation process increased from 15 to 69%. However, after FTS, the Co^0 of the used catalyst was only 28%, thus suggesting an important degree of deactivation during catalysis.

The trend in activity as a function of the particle size resulted similar to the obtained for the colloidal system. This observation suggests that the factors that determined the activity for the colloidal NPs are also valid for the supported catalysts, since they are composed by the same active phase. In addition, the reducibility of the series of supported catalysts (**Co1-4/TiO_2**) agrees with the observed trend in activity. The higher contribution of already reduced Co in the core of the smallest NPs (**Co1/TiO_2**, according to XPS, Supporting Information, Table S6) could facilitate the reduction during the activation process in comparison to the larger ones thus resulting in a higher content of active phase in the case of the smallest CoNPs.

Similar particle size effects on activity were previously observed in FT literature.[10e,12,22] For instance, Wang and co-workers prepared a series of faujasite zeolite supported cobalt catalysts by borohydride reduction with cobalt particle sizes ranging from 1-2 to 30 nm. They observed that small cobalt particles (1–2 nm) were still active in the Fischer-Tropsch synthesis exhibiting higher CO conversions than

larger NPs.[22] In spite of these studies, other authors have concluded that cobalt particles with sizes smaller than a critical value (6-9 nm) are less active in Fischer–Tropsch synthesis than larger cobalt particles.[6,10b,10i] This phenomenon may, however, result from the lower reducibility and stability of small cobalt species.[11]

In relation to the observed decrease of the α values when decreasing the particle size, Wang and co-workers also evidenced the decrease of the C_{21+} selectivity from 17.5 to 3.1% with the decrease of the cobalt particle size from *ca*. 30 to 1-2 nm.[22]

It was concluded that the observed trend in activity as a function of the cobalt particle size was common for both the colloidal and the supported catalysts. This observation suggests that the effects observed in catalysis can be attributed to an intrinsic size effect of the cobalt nanoparticles and not to interactions between the metal and support. In our particular case, it was observed the highest activity for the catalysts with the smallest cobalt diameter. These results provide evidence on the intrinsic catalytic activity of cobalt nanoparticles below 5 nm in Fischer–Tropsch synthesis. This unconventional size behavior might be related to the preparation method for these NPs using sodium borohydride as reducing agent.

VI.4. Conclusions

CoNPs of sizes between 1.7 to 7.0 nm were synthesized in water using $NaBH_4$ as reducing agent. Structural analysis by XRD suggested amorphous structures for the cobalt and cobalt oxide phases. The broadening of XRD signals were also attributed to the small size of these CoNPs. Analysis of thermally treated NPs revealed the presence of cobalt and cobalt-boron. Surface analysis by XPS indicated the considerable oxidation degree of the NPs depending on the size: more reduced CoNPs were obtained for smaller NPs. Finally, the analysis by FTIR and TGA showed no evidence of the presence of PVP in the series of NPs, **Co1-4**. TEM and TPR analysis of the TiO_2 supported catalysts demonstrated that the particle size of the CoNPs remained unchanged after immobilization on TiO_2 and that the reducibility of the catalyst decreased with the increase of the particle size.

The AFTS catalytic performances of unsupported cobalt nanoparticles were observed to depend on the reduction degree and the size of the NPs, with a decrease of the activity with the particle size. For the supported catalysts, the observed trend was in agreement with the observed for the colloidal catalysts. This observation suggests that the effects observed in catalysis can be attributed to an intrinsic size effect of the cobalt nanoparticles and not to interactions between the metal and the support.

VI.5. Experimental Section

Synthesis of colloidal cobalt nanoparticles by chemical reduction (Co1-4)

CoNPs were synthesized by chemical reduction of cobalt dichloride in the presence of polyvinylpyrrolidone (PVP) as stabilizer and using sodium borohydride as reducing agent. The size of the **Co1-4** was modulated through the variation of the concentration of reagents.

As a standard procedure, 0.226g of $CoCl_2.6H_2O$ (0.931 mmol) was dissolved in H_2O containing the polymer stabilizant (2.066 g of PVP-K30). The volume of water used to dissolve both PVP and the cobalt salt was 12.5, 50, 200 and 800 ml for **Co1-4** respectively. Then, a freshly prepared solution of 0.358 g of $NaBH_4$ (9.31 mmol) in H_2O was added at room temperature during at a rate of 3 ml/min. The volume of water used to dissolve the $NaBH_4$ was 4.1, 16.6, 66 and 264 ml for **Co1-4** respectively. The solution was maintained with a vigorous mechanical stirring for 2 h. Then 100 µl of the colloidal solution was centrifuged, washed with water and re-dispersed by sonication. Three drops of the obtained colloidal solution was deposited on a Cu-formvar or holey carbon grids for TEM or HR-TEM analysis. For the isolation of the CoNPs, the freshly prepared NPs were initially precipitated by a strong magnetic field and the supernatant was decanted. Then, the precipited NPs were rinsed with water to remove the excess of salts and PVP. The decantation and washing process was repeated three times with water, then three times with ethanol and three times with hexane. The resulted CoNPs were finally dried under vacuum and kept in the glove box.

- **Co1:** was synthesized according to the general procedure using $CoCl_2 6H_2O$ (0.226 g, 0.931 mmol) in presence of PVP-K30 (2.066 g, PVP:Co=20) dissolved in 12.5 ml of deionized water ([37] = 0.0740 M). $NaBH_4$ (0.358 g, 9.369 mmol) was dissolved in 4.1 ml of water ([$NaBH_4$] = 2.285 M).

  TEM: D = 1.75 ± 0.42 nm.

  XRD: 45, 35 and 60º

  XPS: Co^0, 38%; Co^{2+}, 62%.

  TGA: Temperature ºC/Δ wt. % (attribution); 106/-11 (solvent); [430/-0.67; 511/-0.97; 633/-0.33 (PVP, total: -1.97)]; 900end/+1.53

  ICP: Co, 77.3 wt%, B, 7.4 wt%; Co/B atom ratio, 2.11

  FTIR: 3479, 1644, 1425 cm^{-1}.

  RAMAN: 661, 593, 497, 457, 185 cm^{-1}.

- **Co2:** was synthesized according to the general procedure using $CoCl_2 6H_2O$ (0.226 g, 0.931 mmol) in presence of PVP-K30 (2.066 g, PVP:Co=20) dissolved in 50 ml of deionized water ([Co] = 0.0180 M). $NaBH_4$ (0.358 g, 9.369 mmol) was dissolved in 16.6 ml of water ([$NaBH_4$] = 0.550 M).

  TEM: D = 2.64 ± 0.92 nm.

  HR-TEM: *ca.* 2.6 nm; detection of CoO-fcc and Co_3O_4-fcc.

  XRD: 45, 35 and 60º

  XPS: Co^0, 37%; Co^{2+}, 63%.

  TGA: Temperature ºC/Δ wt. % (attribution); 70/-3.5 (solvent), 244/-3.7 (polymer), 900end/+0.92.

  ICP: Co, 82.4 wt%, B, 5.9 wt%; Co/B atom ratio, 2.79

  FTIR: 3477, 1644, 1425 cm^{-1}.

  RAMAN: 666, 586, 492, 450, 196 cm^{-1}.

- **Co3:** was synthesized according to the general procedure using $CoCl_2 6H_2O$ (0.226 g, 0.931 mmol) in presence of PVP-K30 (2.066 g, PVP:Co=20) dissolved in 200 ml of deionized water ([Co] = 0.0045 M). $NaBH_4$ (0.358 g, 9.369 mmol) was dissolved in 66 ml of water ([$NaBH_4$] = 0.141 M).

  TEM: D = 5.18 ± 2.05 nm.

  XRD: 45, 33 and 60º

XPS: Co^0, 33%; Co^{2+}, 67%.

TGA: Temperature ºC/Δ wt. % (attribution); 201/-1.35 (solvent); 900end/+8.4.

ICP: Co, 88.0 wt%, B, 7.5 wt%; Co/B atom ratio, 2.36.

FTIR: 3482, 1644, 1425 cm^{-1}.

RAMAN: 662, 598, 501, 456 cm^{-1}.

- **Co4:** was synthesized according to the general procedure using $CoCl_26H_2O$ (0.226 g, 0.931 mmol) in presence of PVP-K30 (2.066 g, PVP:Co=20) dissolved in 800 ml of deionized water ([Co] = 0.018 M). $NaBH_4$ (0.358 g, 9.369 mmol) was dissolved in 264 ml of water ([$NaBH_4$] = 0.035 M).

  TEM: D = 7.02 ± 1.19 nm.

  XRD: 45, 34 and 60º

  XPS: Co^0, 12%; Co^{2+}, 88%.

  TGA: Temperature ºC/Δ wt. % (attribution); 104/-1.7 (solvent); 216/-1.8 (polymer); 900end/+6.15.

  ICP: Co, 90.3 wt%, B, 8.3 wt%; Co/B atom ratio, 2.18.

  FTIR: 3475, 1644, 1425 cm^{-1}.

  RAMAN: 662, 592, 499, 460, 184 cm^{-1}.

The size, the crystalline structure and oxidation state of the CoNPs were studied using transmission electron microscopy (TEM), HR-TEM, X-ray diffraction (XRD), and X-ray photoelectron spectroscopy (XPS) respectively. The composition of the CoNPs was studied using FTIR, TGA and ICP-OES.

Immobilization of colloidal cobalt nanoparticles on TiO_2 (Co1-4/TiO_2)

55 mg aprox. of the corresponding isolated CoNPs were re-suspended in 20ml of hexane and sonicated during 3 minutes. Separately, a suspension of TiO_2 (0.490 g of 20 nm nanopowder, Degussa P25, 35-65 m^2/g) in 40 ml of hexane was firstly sonicated during 1 min and then mechanically stirred. The amount of TiO_2 was the corresponding to obtain a 10wt% Co catalyst. Then the suspension of CoNPs in hexane was added dropwise over the stirred suspension of TiO_2 and the resultant stirred during 30min more. The gray suspension was then sonicated during

3 min to homogenize the dispersion of the CoNPs on the support and the resultant was magnetically precipitated, the hexane removed and the solid dried under vacuum.

Since the catalyst were powders too fine to be suitable for the reactor, they were pelletized using a press then crushed and sieved to get grain sizes between the 0.300 - 0.150 mm. The obtained materials were then used for the catalytic test.

Fischer-Tropsch catalytic experiments in water using the colloidal catalysts

Catalytic experiments were performed according to reported methods.[16,38] Fischer-Tropsch reactions using the colloidal catalysts were carried out in a 100 ml stainless steel autoclave operated in bath mode. 0.55mg of the isolated CoNPs (0.931 mmol of Co) were redispersed in 66 ml of water, and placed inside a Teflon liner in the autoclave. The autoclave was purged three times with Ar, and sealed at an Ar pressure of 1.5 bar. Additional 10 bar CO and 20 bar H_2 were further added giving a final pressure of 31.5 bar (H_2:CO:Ar = 2:1:0.15). Then the autoclave was heated at 180 ºC under mechanical stirring at 1000 rpm during 12h. After reaction the autoclave was cooled to room temperature prior to gas analysis. All the components contained in the gas phase (CO, H_2, Ar, CO_2, and C_1-C_8 hydrocarbons) were analyzed by GC-TCD and the quantification was performed using calibration curves for each component. The compounds present in the aqueous phase were extracted with dichloromethane (10 ml) containing 1 µl of bicyclohexyl as internal standard. The organic phase containing the hydrocarbon and oxygenated products were analyzed by GC-MS. The identification and quantification of products was performed by comparison with standards using calibration curves for each compound.

Fischer-Tropsch catalytic experiments using the TiO_2 supported catalysts

Carbon monoxide hydrogenation was carried out in a Flowrence high throughput unit[38] equipped with 16 parallel milli-fixed reactors (d_{int} = 2 mm) operating at a total pressure of 20 bar, H_2/CO = 2 molar ratio and GHSV = 6700 cm^3/g h. The catalyst loading was 100 mg. Prior to the catalytic test,

all the samples were activated in a flow of pure hydrogen at atmospheric pressure during 10 h at 673 K with at GHSV = 2 NL h^{-1} g^{-1}. During the reduction, the temperature ramp was 1 K/min. After the reduction, the catalysts were cooled down to 433 K and a flow of premixed syngas was gradually introduced through the catalysts. When pressure attained 20 bar, the temperature was slowly increased to 513 K with a ramp of 1 K/min. Gaseous reaction products were analyzed by on-line gas chromatography. Analysis of permanent gases was performed using a Molecular Sieve column and a thermal conductivity detector. Carbon dioxide and C_1–C_4 hydrocarbons were separated in a PPQ column and analyzed by a thermoconductivity detector. C_5–C_{12} hydrocarbons were analyzed using CP-Sil5 column and a flame-ionization detector. The carbon monoxide contained 5% of helium, which was used as an internal standard for calculating carbon monoxide conversion. Catalytic rates and selectivities were measured at the steady-state regime after 46 h time-on-stream. The reaction rates expressed in cobalt time yield h^{-1}, are defined as the moles of CO converted per mol of Co per hour. The product selectivity (*S*) is reported as the wt% of a given product.

VI.6. Acknowledgements

The authors are grateful to Total S.A., the Spanish Ministerio de Economía y Competitividad (CTQ2013-43438-R, and *Ramon y Cajal* fellowship to C. Godard) and the Generalitat de Catalunya (2014SGR670) for financial support. We acknowledge with thanks the collaboration with Prof. Andrei Khodakov and Dr. Vitaly Ordomsky from the Universite Lille 1 and UCCS in relation to the experiments with supported catalysts.

VI.7. References

[1] Calderone, V. R.; Shiju, N. R.; Curulla-Ferré, D.; Chambrey, S.; Khodakov, A.; Rose, A.; Thiessen, J.; Jess, A.; Rothenberg, G. *Angew. Chem. Int. Ed.* **2013**, *52*, 4397-4401.

[2] Khodakov, A. Y. *Catal. Today* **2009**, *144*, 251-257.

[3] (a) A. Steynberg; Dry., M.; Elsevier, 152: 2006.(b) *Fischer-Tropsch synthesis, catalysts and catalysis*; B.H. Davis; Occelli, M. L., Eds.; Elsevier, 163, 2007.(c) Zhang, Q.; Kang, J.; Wang, Y. *ChemCatChem* **2010**, *2*, 1030-1058.

[4] Gual, A.; Godard, C.; Castillón, S.; Curulla-Ferré, D.; Claver, C. *Catal. Today* **2012**, *183*, 154-171.

[5] Van Der Laan; and, G. P.; Beenackers, A. A. C. M. *Catal. Rev.* **1999**, *41*, 255-318.

[6] Park, J.-Y.; Lee, Y.-J.; Karandikar, P. R.; Jun, K.-W.; Ha, K.-S.; Park, H.-G. *App. Catal. A-Gen* **2012**, *411–412*, 15-23.

[7] Jacobs, G.; Ji, Y.; Davis, B. H.; Cronauer, D.; Kropf, A. J.; Marshall, C. L. *App. Catal. A-Gen* **2007**, *333*, 177-191.

[8] Iglesia, E. *App. Catal. A-Gen* **1997**, *161*, 59-78.

[9] Jacobs, G.; Das, T. K.; Zhang, Y.; Li, J.; Racoillet, G.; Davis, B. H. *App. Catal. A-Gen* **2002**, *233*, 263-281.

[10] (a) Azzam, K.; Jacobs, G.; Ma, W.; Davis, B. *Catal. Lett.* **2014**, *144*, 389-394.(b) Bezemer, G. L.; Bitter, J. H.; Kuipers, H. P. C. E.; Oosterbeek, H.; Holewijn, J. E.; Xu, X.; Kapteijn, F.; van Dillen, A. J.; de Jong, K. P. *J. Am. Chem. Soc.* **2006**, *128*, 3956-3964.(c) Borg, Ø.; Dietzel, P. D. C.; Spjelkavik, A. I.; Tveten, E. Z.; Walmsley, J. C.; Diplas, S.; Eri, S.; Holmen, A.; Rytter, E. *J. Catal.* **2008**, *259*, 161-164.(d) den Breejen, J. P.; Radstake, P. B.; Bezemer, G. L.; Bitter, J. H.; Frøseth, V.; Holmen, A.; Jong, K. P. d. *J. Am. Chem. Soc.* **2009**, *131*, 7197-7203.(e) Kikuchi, E.; Sorita, R.; Takahashi, H.; Matsuda, T. *App. Catal. A-Gen* **1999**, *186*, 121-128.(f) Ma, W.; Jacobs, G.; Sparks, D. E.; Gnanamani, M. K.; Pendyala, V. R. R.; Yen, C. H.; Klettlinger, J. L. S.; Tomsik, T. M.; Davis, B. H. *Fuel* **2011**, *90*, 756-765.(g) Melaet, G.; Lindeman, A.; Somorjai, G. *Top. Catal.* **2014**, *57*, 500-507.(h) Prieto, G.; Martínez, A.; Concepción, P.; Moreno-Tost, R. *J. Catal.* **2009**, *266*, 129-144.(i) Radstake, P. B.; Breejen, J. P. d.; Bezemer, G. L.; Bitter, J. H.; Jong, K. P. d.; Frøseth, V.; Holmen, A. In *Stud. Surf. Sci. Catal.*; Fábio Bellot Noronha, M. S., Eduardo Falabella, S.-A., Eds.; Elsevier: 2007; Vol. Volume 167, p 85-90.(j) van Santen, R. A.; Markvoort, A. J. *Faraday Discuss.* **2013**, *162*, 267-279.(k) Wang, Z.-j.; Skiles, S.; Yang, F.; Yan, Z.; Goodman, D. W. *Catal. Today* **2012**, *181*, 75-81.(l) Yang, J.; Tveten, E. Z.; Chen, D.; Holmen, A. *Langmuir* **2010**, *26*, 16558-16567.(m) Zeng, B.; Hou, B.; Jia, L.; Wang, J.; Chen, C.; Sun, Y.; Li, D. *ChemCatChem* **2013**, *5*, 3794-3801.

[11] (a) van de Loosdrecht, J.; Balzhinimaev, B.; Dalmon, J. A.; Niemantsverdriet, J. W.; Tsybulya, S. V.; Saib, A. M.; van Berge, P. J.; Visagie, J. L. *Catal. Today* **2007**, *123*, 293-302.(b) van Steen, E.; Claeys, M.; Dry, M. E.; van de Loosdrecht, J.; Viljoen, E. L.; Visagie, J. L. *J. Phys. Chem. B* **2005**, *109*, 3575-3577.

[12] (a) Nakhaei Pour, A.; Housaindokht, M. *Catal. Lett.* **2013**, *143*, 1328-1338.(b) Xie, W.; Zhang, Y.; Liew, K.; Li, J. *Science China Chemistry* **2012**, *55*, 1811-1818.

[13] (a) Bechara, R.; Balloy, D.; Vanhove, D. *App. Catal. A-Gen* **2001**, *207*, 343-353.(b) Borg, Ø.; Eri, S.; Blekkan, E. A.; Storsæter, S.; Wigum, H.; Rytter, E.; Holmen, A. *J. Catal.* **2007**, *248*, 89-100.(c) Xiong, H.; Zhang, Y.; Wang, S.; Li, J. *Catal. Commun.* **2005**, *6*, 512-516.

[14] Sousa-Aguiar, E. F.; Noronha, F. B.; Faro, J. A. *Catal. Sci. Technol.* **2011**, *1*, 698-713.

[15] Astruc, D.; Lu, F.; Aranzaes, J. R. *Angew. Chem. Int. Ed.* **2005**, *44*, 7852-7872.

[16] Xiao, C.-x.; Cai, Z.-p.; Wang, T.; Kou, Y.; Yan, N. *Angew. Chem. Int. Ed.* **2008**, *47*, 746-749.

[17] Gual, A.; Delgado, J. A.; Godard, C.; Castillón, S.; Curulla-Ferré, D.; Claver, C. *Top. Catal.* **2013**, *56*, 1208-1219.

[18] Quek, X.-Y.; Pestman, R.; van Santen, R. A.; Hensen, E. J. M. *Catal. Sci. Technol.* **2014**.
[19] Wang, H.; Zhou, W.; Liu, J.-X.; Si, R.; Sun, G.; Zhong, M.-Q.; Su, H.-Y.; Zhao, H.-B.; Rodriguez, J. A.; Pennycook, S. J.; Idrobo, J.-C.; Li, W.-X.; Kou, Y.; Ma, D. *J. Am. Chem. Soc.* **2013**, *135*, 4149-4158.
[20] Wang, H.; Kou, Y. *Chin. J. Catal.* **2013**, *34*, 1914-1925.
[21] Fan, X.-B.; Tao, Z.-Y.; Xiao, C.-X.; Liu, F.; Kou, Y. *Green Chem.* **2010**, *12*, 795-797.
[22] Wang, Y.; Wu, H.; Zhang, Q.; Tang, Q. *Micropor. Mesopor. Mat.* **2005**, *86*, 38-49.
[23] (a) Garcia-Torres, J.; Vallés, E.; Gómez, E. *J. Nanopart. Res.* **2010**, *12*, 2189-2199.(b) Petit, C.; Wang, Z. L.; Pileni, M. P. *J. Phys. Chem. B* **2005**, *109*, 15309-15316.
[24] (a) Mitov, M.; Popov, A.; Dragieva, I. *J. Appl. Electrochem.* **1999**, *29*, 59-63.(b) Patel, N.; Fernandes, R.; Miotello, A. *J. Catal.* **2010**, *271*, 315-324.
[25] Glavee, G. N.; Klabunde, K. J.; Sorensen, C. M.; Hadjipanayis, G. C. *Langmuir* **1993**, *9*, 162-169.
[26] (a) Glavee, G. N.; Klabunde, K. J.; Sorensen, C. M.; Hadjapanayis, G. C. *Langmuir* **1992**, *8*, 771-773.(b) Glavee, G. N.; Klabunde, K. J.; Sorensen, C. M.; Hadjipanayis, G. C. *Inorg. Chem.* **1993**, *32*, 474-477.
[27] Khodakov, A. Y.; Chu, W.; Fongarland, P. *Chem. Rev.* **2007**, *107*, 1692-1744.
[28] Arzac, G. M.; Rojas, T. C.; Fernández, A. *ChemCatChem* **2011**, *3*, 1305-1313.
[29] Demirci, U. B.; Miele, P. *Phys. Chem. Chem. Phys.* **2014**, *16*, 6872-6885.
[30] Carenco, S.; Portehault, D.; Boissière, C.; Mézailles, N.; Sanchez, C. *Chem. Rev.* **2013**, *113*, 7981-8065.
[31] Dragieva, I.; Gavrilov, G.; Buchkov, D.; Slavcheva, M. *J. Less Common Met.* **1979**, *67*, 375-379.
[32] (a) Linderoth, S. r.; Mo/rup, S. *J. Appl. Phys.* **1991**, *69*, 5256-5261.(b) Yiping, L.; Hadjipanayis, G. C.; Sorensen, C. M.; Klabunde, K. J. *J. Magn. Magn. Mater.* **1989**, *79*, 321-326.
[33] Khodakov, A. Y.; Chu, W.; Fongarland, P. *Chem. Rev.* **2007**, *107*, 1692-1744.
[34] Li, J.; Coville, N. J. *App. Catal. A-Gen* **1999**, *181*, 201-208.
[35] Astruc, D.; Lu, F.; Aranzaes, J. R. *ChemInform* **2006**, *37*, no-no.
[36] Jacobs, G.; Das, T. K.; Li, J.; Luo, M.; Patterson, P. M.; Davis, B. H. In *Stud. Surf. Sci. Catal.*; Davis, B. H., Occelli, M. L., Eds.; Elsevier: 2007; Vol. 163, p 217-253.
[37] In *Catalysis*; Spivey, J. J., Dooley, K. M., Eds.; The Royal Society of Chemistry: 2006; Vol. 19, p 1-40.
[38] http://avantium.com/catalysis/R-D-solutions/systems/Flowrence.html.

Supporting Information for:

Particle Size Effects in the Fischer-Tropsch Synthesis Over Cobalt Nanoparticles Prepared by Sodium Borohydride Reduction

Materials and Methods

All syntheses of CoNPs were carried under aerobic conditions using a mechanical stirrer. Milli-Q water was used for all the experiments. Solvents were purchased from Merck and used as received. $CoCl_2 \cdot 6H_2O$, $NaBH_4$ and PVP K-30 and were purchased from Sigma-Aldrich. Hydrogen (5.0) was purchased from Air Liquide and CO (4.7) and argon (5.0) from Carburos Metálicos.

Transmission electron microscopy (TEM) measurements were performed at the "Unitat de Microscopia dels Serveis Cientificotècnics de la Universitat Rovira I Virgili" in Tarragona with Zeiss 10 CA electron microscope operated at 100 kV with resolution of 3 Å. High resolution electron microscopy (HR-TEM) measurements were performed at the "Centres Científics i Tecnològics de la UB" in Barcelona with a JEOL 2011(FEG) electron microscope operated at 200 kV with a point resolution of 2 Å.

XRD measurements were acquired using a Siemens D5000 diffractometer (Bragg-Brentano parafocusing geometry and vertical θ-θ goniometer) fitted with a curved graphite diffracted-beam monochromator, incident and diffracted -beam Soller slits, a 0.06º receiving slit and scintillation counter as a detector. The angular 2θ diffraction range was between 25 and 120º. The data were collected with an angular step of 0.05º at 16s per step and sample rotation. A low background Si(510) wafer was used as sample holder. $Cu_{k\alpha}$ radiation was obtained from a copper X-ray tube operated at 40 kV and 30 mA.

XPS experiments were performed in a PHI 5500 Multitechnique System (from Physical Electronics) with a monochromatic X-ray source (Aluminium Kalfa line of 1486.6 eV energy and 350 W), placed perpendicular to the analyzer axis and calibrated using the 3d5/2 line of Ag with a full width at half maximum (FWHM) of 0.8 eV. The analized area was a circle of 0.8 mm diameter, and the selected resolution for the spectra was 187.5eV of Pass Energy and 0.8 eV/step for the general spectra and 23.5 eV of Pass Energy and 0.1 eV/step for the spectra of the different elements in the depth profile spectra. A low energy electron gun (less than 10 eV) was used in order to discharge the surface when necessary. All Measurements were made in an ultra-high vacuum (UHV) chamber pressure between $5x10^{-9}$ and $2x10^{-8}$ torr.

FTIR spectra were acquired from KBr discs on a Bruker Equinox 55 Spectrometer using Opus software. Raman spectra was acquired by scattering of a 514nm Ar lamp on a Renishaw InVia Raman microscope using a x50LW objective, 60s of exposition time and 100% of laser intensity.

Thermogravimetric analysis (TGA) were performed at the "Centres Científics i Tecnològics de la UB" in Barcelona with a thermobalance (Mettler TGA/SDTA851e) equipped with a gas flow system. A 2-6 mg sample was heated in an alumina crisol in a flow of nitrogen. Then the catalyst was heated under a 50 ml/min of nitrogen flow from 30 ºC to 900 ºC (heat rate: 10 ºC/min).

Temperature programmed reduction under H_2 (TPR) was carried out using a ChemBET™ TPR/TPD (Quantachrome). The catalyst (0.1 g) was mounted in a quartz cell and heated up to 900 ºC in a flow of 5% H_2/Ar (30 cm^3min^{-1}). The rate of temperature ramp was 10 ºC min^{-1}.

GC-TCD analyses were carried out on an Agilent 7890A GC using a system with three columns: Hayesep Q (3ft x 1/8 in), HP-Molesieve (30m x 0.320 mm x 12 µm) and HP-Plot/Q (30m x 0.320 mm x 20 µm) using helium as carrier gas. GC-MS analyses were performed on a 9575C MSD system (Agilent) using a HP-Innowax capillary column (30m x 0.250 mm x 0.15 µm), using helium as carrier gas. Standard reference of gases (CO, CO_2, H_2, N_2) and hydrocarbons (C_1-C_5) was purchased from Avello Linde.

TEM characterization

Immediately after each synthesis, 100 µl of the colloidal solution of CoNPs was centrifuged at 600 rpm during 5 minutes. The supernatant was removed and the CoNPs then washed with deionized water and re-dispersed by 1 min of sonication. The colloidal solution was appropriately diluted with deionized water to obtain a pale grey solution. Then, three drops of the obtained colloidal solution was deposited on a Cu-formvar grid and the grid was dried during 24 h prior TEM analysis. The TEM measurements were performed on a Zeiss 10 CA electron microscope operated at 100 kV with resolution of 3 Å. The particles size distributions were determined by a manual analysis of enlarged images. At least 200 particles on a given grid were measured in order to obtain a statistical size distribution. Nanoparticle mean diameter was estimated using Gaussian analysis.

Fischer-Tropsch catalytic experiments in water using the colloidal catalysts

Catalytic experiments were performed according to reported methods.[16,38]

Fischer-Tropsch reactions using the colloidal catalysts were carried out in a 100 ml stainless steel autoclave operated in bath mode. 0.55mg of the isolated CoNPs (0.931 mmol of Co) were redispersed in 66 ml of water, and placed inside a Teflon liner in the autoclave. The autoclave was purged three times with Ar, and sealed at an Ar pressure of 1.5 bar. Additional 10 bar CO and 20 bar H_2 were further added giving a final pressure of 31.5 bar

(H_2:CO:Ar = 2:1:0.15). Then the autoclave was heated at 180 ºC under mechanical stirring at 1000 rpm during 12h. After reaction the autoclave was cooled to room temperature prior to gas analysis. All the components contained in the gas phase (CO, H_2, Ar, CO_2, and C_1-C_8 hydrocarbons) were analyzed by GC-TCD and the quantification was performed using calibration curves for each component. The compounds present in the aqueous phase were extracted with dichloromethane (10 ml) containing 1µl of bicyclohexyl as internal standard. The organic phase containing the hydrocarbon and oxygenated products were analyzed by GC-MS. The identification and quantification of products was performed by comparison with standards using calibration curves for each compound.

Fischer-Tropsch catalytic experiments using the TiO_2 supported catalysts

Carbon monoxide hydrogenation was carried out in a Flowrence high throughput unit[38] equipped with 16 parallel milli-fixed reactors (d_{int} = 2 mm) operating at a total pressure of 20 bar, H_2/CO = 2 molar ratio and GHSV = 6700 cm^3/g h. The catalyst loading was 100 mg. Prior to the catalytic test, all the samples were activated in a flow of pure hydrogen at atmospheric pressure during 10 h at 673 K with at GHSV = 2 NL h^{-1} g^{-1}. During the reduction, the temperature ramp was 1 K/min. After the reduction, the catalysts were cooled down to 433 K and a flow of premixed syngas was gradually introduced through the catalysts. When pressure attained 20 bar, the temperature was slowly increased to 513 K with a ramp of 1 K/min. Gaseous reaction products were analyzed by on-line gas chromatography. Analysis of permanent gases was performed using a Molecular Sieve column and a thermal conductivity detector. Carbon dioxide and C_1–C_4 hydrocarbons were separated in a PPQ column and analyzed by a thermoconductivity detector. C_5–C_{12} hydrocarbons were analyzed using CP-Sil5 column and a flame-ionization detector. The carbon monoxide contained 5% of helium, which was used as an internal standard for calculating carbon monoxide conversion. Catalytic rates and selectivities were measured at the steady-state regime after 46 h time-on-stream.

The reaction rates expressed in cobalt time yield h^{-1}, are defined as the moles of CO converted per mol of Co per hour. The product selectivity (*S*) is reported as the wt% of a given product.

Product analysis

All the hydrocarbon products were identified by comparison with reference samples.

The components contained in the gas phase (CO, H_2, Ar, CO_2, and C_1-C_8 hydrocarbons) were analysed on a Agilent 7890A GC using a system of three columns: Hayesep Q (3ft x 1/8 in), HP-Molesieve (30m x 0.320 mm x 12 µm) and HP-Plot/Q (30m x 0.320 mm x 20 µm) using helium as carrier gas. The quantification was carried out using calibration curves for each gas. Mixtures at different concentration of gases were prepared by gas blending from a standard reference of gases (Avello Linde).

The compounds present in the aqueous phase were extracted with dichloromethane (10 ml) containing 1µl of bicyclohexyl as internal standard. The bottom organic phase containing the hydrocarbon and oxygenated products were analyzed immediately by GC-MS on a 9575C MSD system using a using a HP-Innowax capillary column (30m x 0.250 mm x 0.15 µm), and helium as carrier gas.

The identification and quantification of products was performed by comparison with standards using calibration curves for each compound.

Activity and Selectivity Calculations

The activity and selectivity was calculated based on the number of moles of carbon being formed as products according to the following formulas:

$$\text{Time yield} = \frac{\text{mol of CO converted}}{\text{mol of Co} * \text{reaction time (h)}}$$

$$\text{Selectivity } Cn = \frac{\text{Wt } C_n}{\text{Wt of all products}} \; x \; 100$$

Figure S1. Size histograms and TEM micrographs of **Co1-4** after catalysis.

Co1, 2.83 ± 0.97 nm.

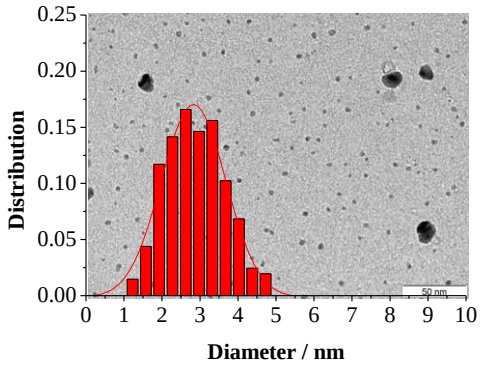

Co2, 3.28 ± 1.17 nm.

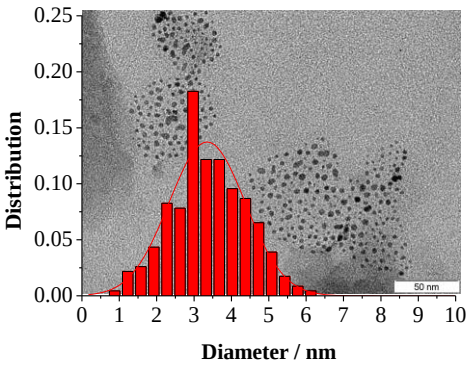

Co3, 2.81 ± 0.85 nm.

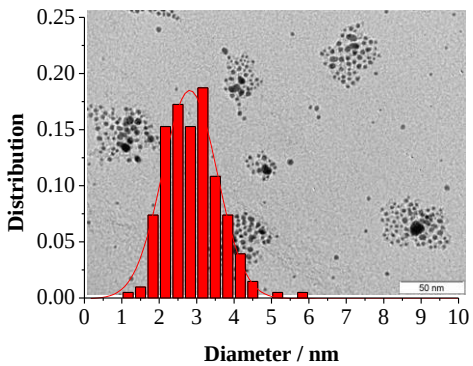

Co4, 1.77 ± 0.64 nm.

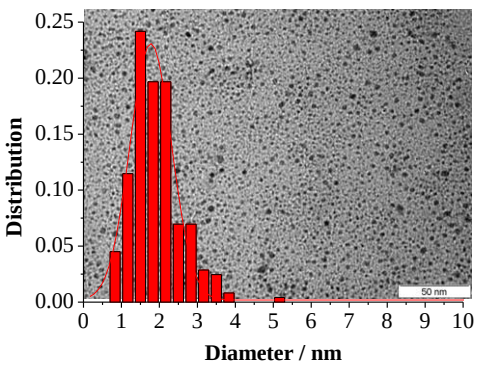

Figure S2. HRTEM image of **Co2** NPs and electron diffraction pattern.

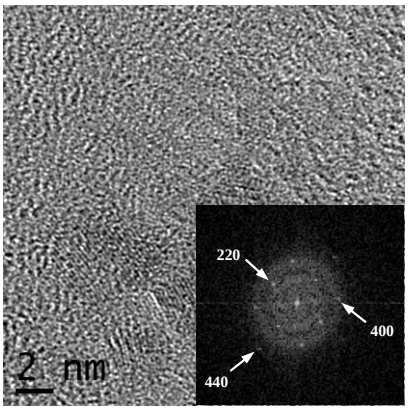

Figure S3. (a) **Co2** before (1) and after (2) catalysis.(b) XRD patterns of **Co2** before (1) and after (2) thermal treatment at 500 ºC for 2h under argon.

a)

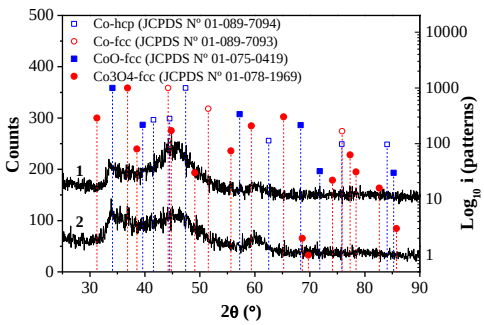

b)

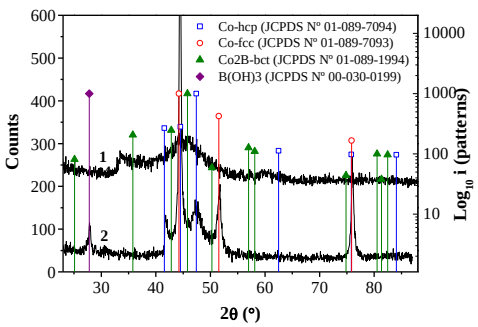

Figure S4. (a) Full XPS spectra of CoNPs: (1) **Co1**, 1.75 ± 0.42 nm; (2) **Co2**, D = 2.64 ± 0.92 nm; (3) **Co3**, D = 5.18 ± 2.05 nm; (4) **Co4**, D = 7.02 ± 1.19 nm. **(b)** C1s XPS spectra of **Co2** (1) before and (2) after catalysis. **(c)** Co 2p XPS spectra of (1) **Co2** freshly synthesized; (2) **Co2** oxidized under air during 3 months and (3) **Co2** after FTS using water as solvent (d) B1s XPS spectra of **Co1,2,4** and**.**

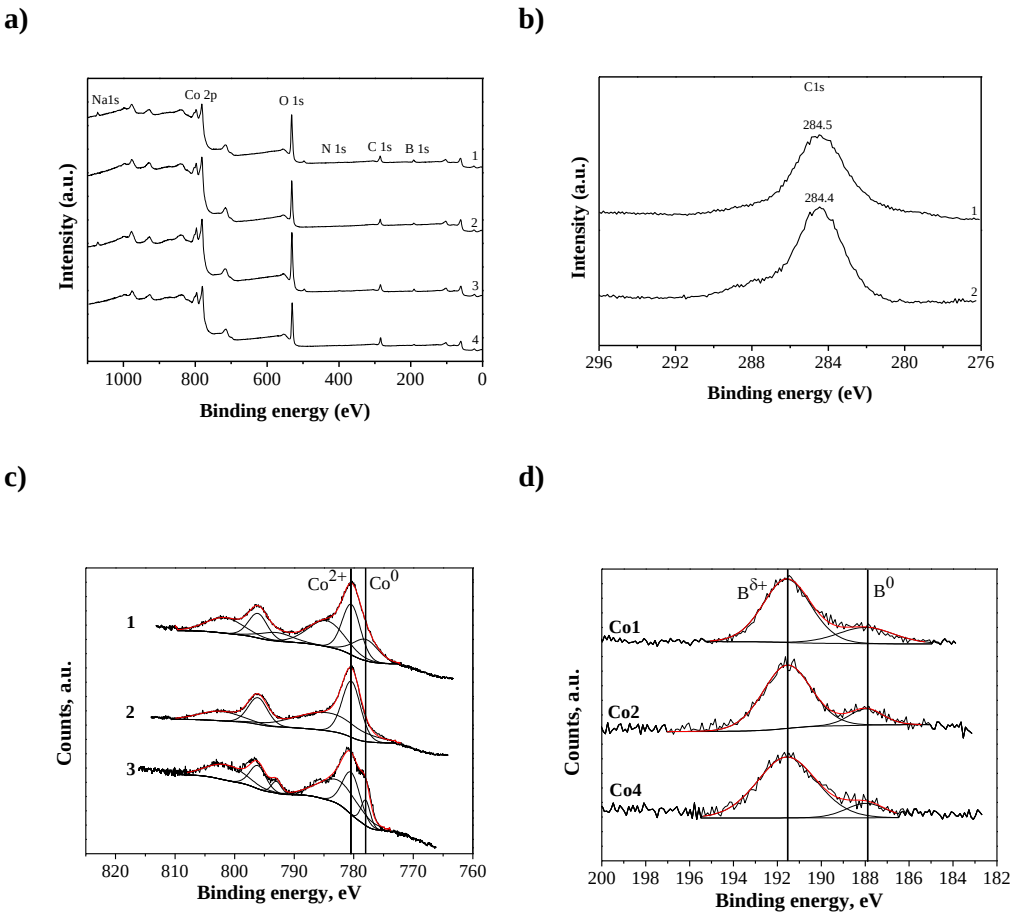

Table S1. ICP and XPS data of **Co1-4** catalysts.

		Co/B (atom ratio)	
NPs	Size, nm	ICP	XPS
Co1	1.75 ± 0.42	2.11	0.83
Co2	2.64 ± 0.92	2.79	1.44
Co3	5.18 ± 2.05	2.36	1.49
Co4	7.02 ± 1.19	2.18	2.19
Co2[a]	2.64 ± 0.92	3.56	4.34

[a] **Co2** after catalysis.

Table S2. Chemical composition analysis of CoNPs by XPS .

		Quantification regions (%Atom)						
Name	Size, nm	Na 1s	C 1s	N 1s	O 1s	Co 2p	B 1s	Co/B
Co1	1.75 ± 0.42	1.2	22.8	0.3	48.4	12.4	14.9	0.8
Co2	2.64 ± 0.92		20.9		48.6	18.0	12.5	1.4
Co3	5.18 ± 2.05	0.9	20.2	0.4	51.7	16.0	10.8	1.5
Co4	7.02 ± 1.19		27.2		48.5	16.6	7.6	2.2
Co2[a]	2.64 ± 0.92		54.9	2.4	31.6	9.0	2.1	4.3

[a] Analysis of **Co2** after catalysis

Table S3. Microanalysis by Energy-dispersive X-ray spectroscopy, EDX (%Mass) of **Co1-4**

		Element/ shell		
Name	Size, nm	C K	O K	Co K
Co1	1.75 ± 0.42	47.6	40.8	11.7
Co2	2.64 ± 0.92	19.9	31.6	48.6
Co3	5.18 ± 2.05	36.5	33.1	30.5
Co4	7.02 ± 1.19	50.0	31.3	18.8

Figure S5. Raman spectra of (1) **Co1**, 1.75 ± 0.42 nm; (2) **Co2**, D = 2.64 ± 0.92 nm; (3) **Co3**, D = 5.18 ± 2.05 nm; (4) **Co4**, D = 7.02 ± 1.19 nm. Spectra acquired by scattering of a 514 nm Ar lamp.

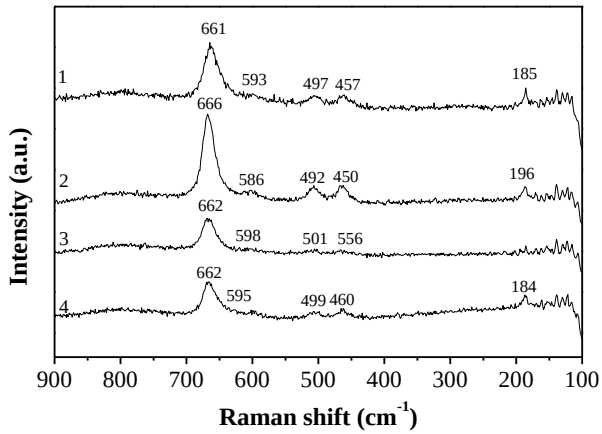

Figure S6. FTIR spectra of (1) **Co1**, 1.75 ± 0.42 nm; (2) **Co2**, D = 2.64 ± 0.92 nm; (3) **Co3**, D = 5.18 ± 2.05 nm; (4) **Co4**, D = 7.02 ± 1.19 nm.

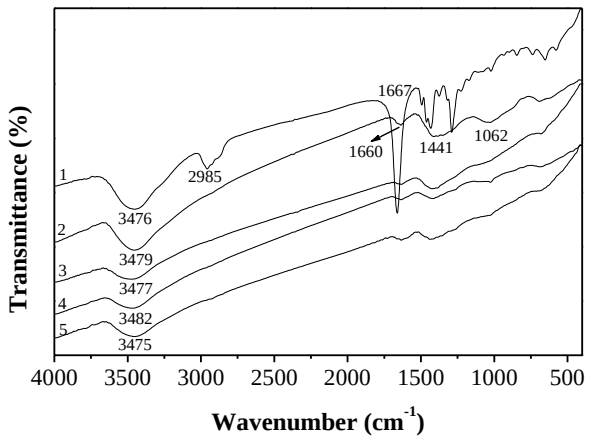

Figure S7. (a) TGA thermogram of PVP and **Co2**; (b) TGA thermograms of **Co1-4.** and 80 (c) TGA thermograms of **Co2** carried out under nitrogen or air flux.

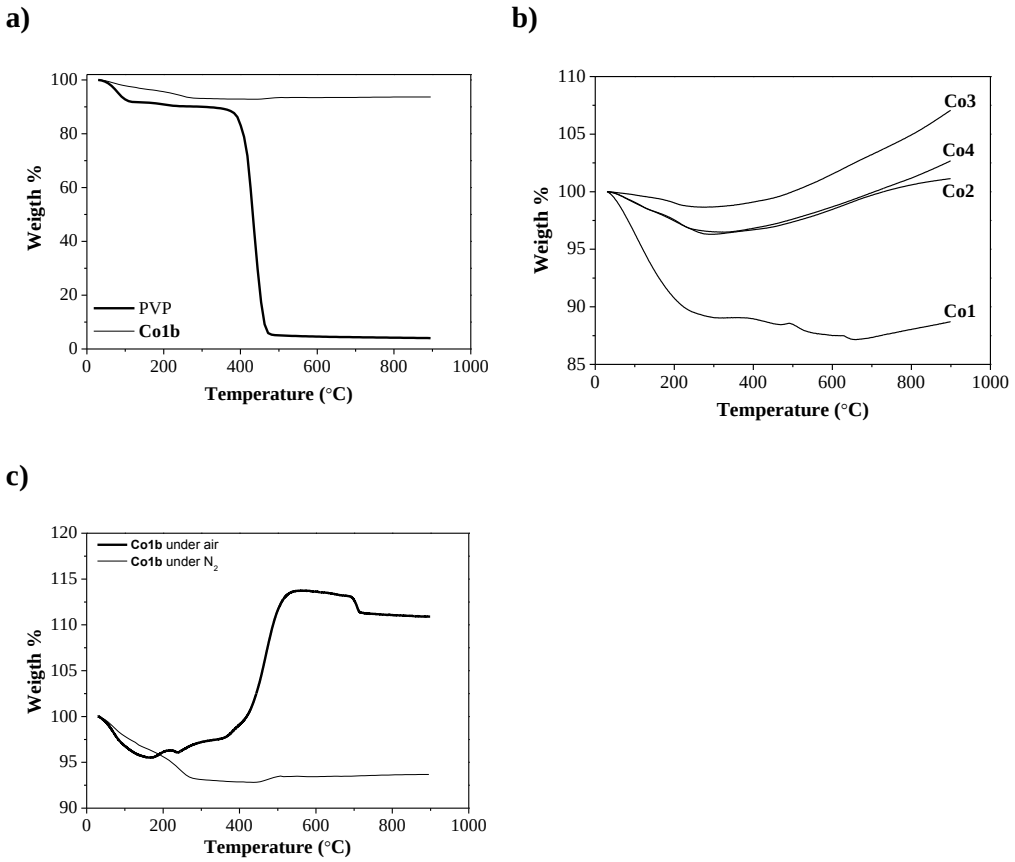

Figure S8. ASF distributions of **Co1-4** nanocatalysts

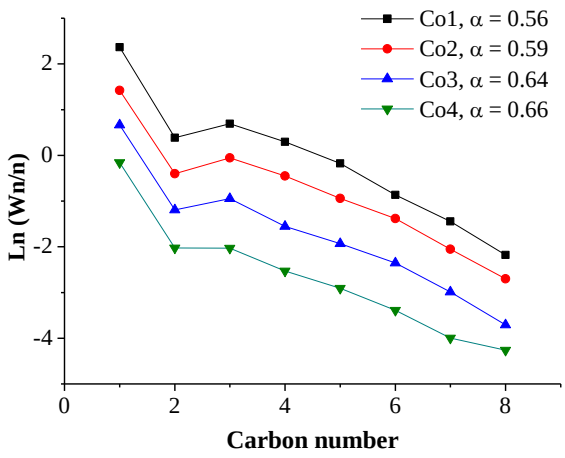

Figure S9. (a) XRD patterns of TiO_2 supported catalysts after calcination process (1 ºC/min up to 500 ºC, 5h): (1) **Co1/TiO$_2$**; (2) **Co2/TiO$_2$**; (3) **Co3/TiO$_2$** and (4) **Co4/TiO$_2$**. In dotted line the peak of 31.2 used for particle size estimation of Co_3O_4. (b) Amplification of dotted region from a. (c) XRD patterns of TiO_2 supported catalysts after the reduction process: (1) **Co2/TiO$_2$**; (2) **Co3/TiO$_2$**; (3) **Co4/TiO$_2$**. In dotted line the peak of 51.5 used for particle size estimation of Co-fcc. (d) Amplification of dotted region from **c**.

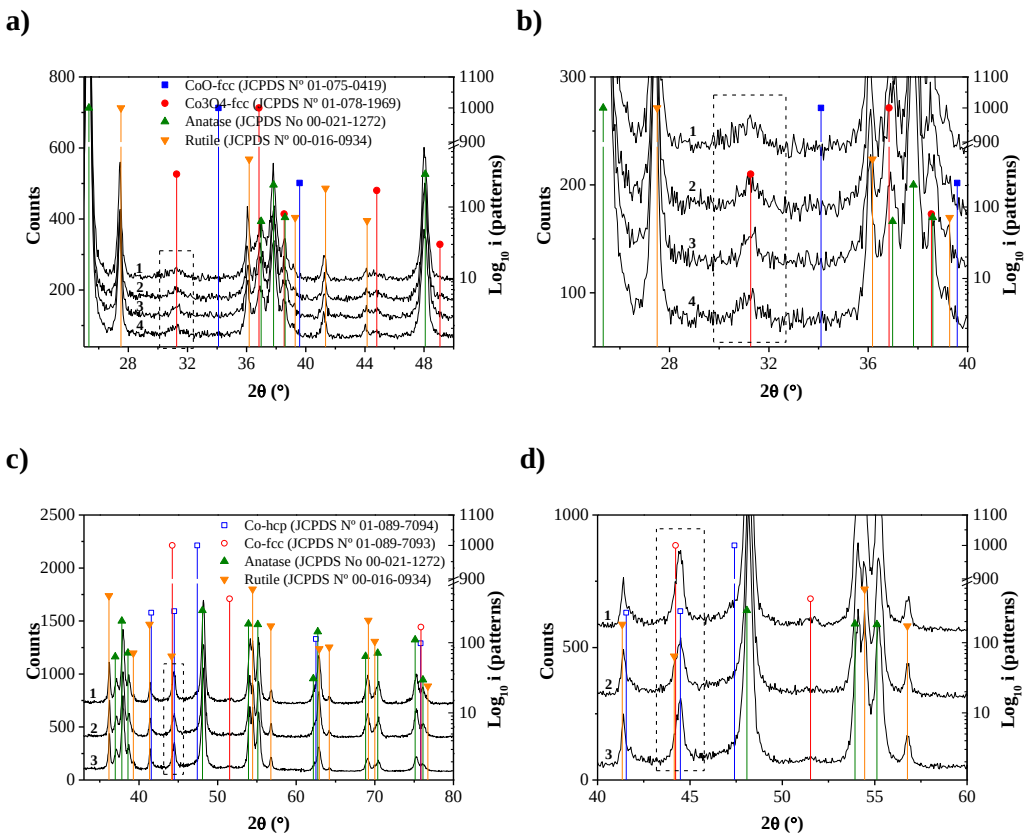

Table S4. Cobalt particle size measured by XRD and TEM, BET surface area and sodium content measured by ICP of supported catalysts.

		XRD (particle size) fresh catalyst		TEM (particle size) fresh catalyst	N_2 fisi. (Surf. Area)	ICP, wt%/catalyst	
E.	Catalyst	d (Co_3O_4)(nm)	d (Co^0)[a] (nm)	(nm)	BET (m^2/g)	Co	Na
1	**Co1**/TiO_2	4.8	3.6	1.75 ± 0.42	44.51	7.69	0.23
2	**Co2**/TiO_2	5.2	3.9	2.64 ± 0.92	50.16	8.05	0.19
3	**Co3**/TiO_2	6.9	5.2	5.18 ± 2.05	62.13	10.37	0.18
4	**Co4**/TiO_2	5.5	4.1	7.02 ± 1.19	59.57	6.90	0.32
5	TiO_2 [b]				43.08	0	0

[a] Mean Co^0 particle size as estimated from the corresponding d(Co_3O_4-fcc) by applying the molar volume correction: d(Co^0) = 3/4 d(Co_3O_4). [b] According to XRD the composition of TiO_2 corresponded to 17% rutile and 83% anatase.

Table S5. Cobalt particle size of the fresh and used catalysts determined by XRD and TEM

		XRD			TEM (nm)	
E.	Catalyst	Fresh[a] (nm)	Used, (nm) Co-fcc/Co-hcp[b]	Used, (wt%)[c] Co-fcc/Co-hcp	Fresh	Used
1	**Co1/TiO_2**	3.6	*	*	1.75 ± 0.42	1.85 ± 0.40
2	**Co2/TiO_2**	3.9	13.8/3.2	2.6/5.1	2.64 ± 0.92	2.59 ± 0.53
3	**Co3/TiO_2**	5.2	10.1/3.2	2.6/5.5	5.18 ± 2.05	3.65 ± 0.66
4	**Co4/TiO_2**	4.3	14.4/3.2	2.2/5.2	7.02 ± 1.19	4.85 ± 1.38

[a] Co particle size estimated from the corresponding d(Co_3O_4-fcc) by applying the molar volume correction: d(Co^0) = 3/4 d(Co_3O_4). [b] Particle size of Co-fcc crystallites calculated using the Scherer equation at 51.5º. A Co-hcp crystallite size was fixed to 3.2nm to fit properly the simulated diffractogram to the experimental. [c] Content of Co-fcc/Co-hcp phases in wt%/catalyst calculated from XRD.

The particle size of Co-fcc/Co-hcp crystallites were calculated from the XRD diffraction pattern and Scherer equation at 51.5º Table S5. This peak was selected for the analysis because was almost the only peak free of overlapping with peaks of anatase and rutile from the support. It is noteworthy that the simulated diffractogram (as computed by Topas software), required the contribution of both Co-fcc and Co-hcp to fit properly the experimental pattern, for that reason in Table S5 is displayed the computed sizes for both Co-fcc and Co-hcp as well as the calculated content for both phases. For comparison purposes it was fixed the Co-hcp crystallite size to 3.2nm for the series of analysis.

The particle sizes determined for Co-fcc crystallites in the case of **Co2-4 /TiO_2** resulted considerable larger (+5-10nm) than the estimated for the fresh catalysts. The substantial differences in the particle size determined by XRD for the used catalysts compared to the fresh catalyst or even its equivalents by TEM could be attributed to some approximations considered in the calculation. On the one hand, for the calculation of the particle size the Scherer equation assumes a single crystalline phase when the reality is that a mixture of both

fcc and hcp crystalline phases are present in the catalyst. On the other hand the crystallite size of Co-hcp fixed to 3.2 was an approximation suitable for the simulation but which not necessarily should be true, so that depending on the fixed value the corresponding size of Co-fcc crystallite would change. The contents of Co-fcc/Co-hcp displayed in Table S5 demonstrates also that the contribution of Co-hcp is not depreciable, in contrary, it corresponds to almost twice the content of Co-fcc.

Figure S10. Co 2p XPS spectra of **Co1-4**/TiO_2 catalysts.

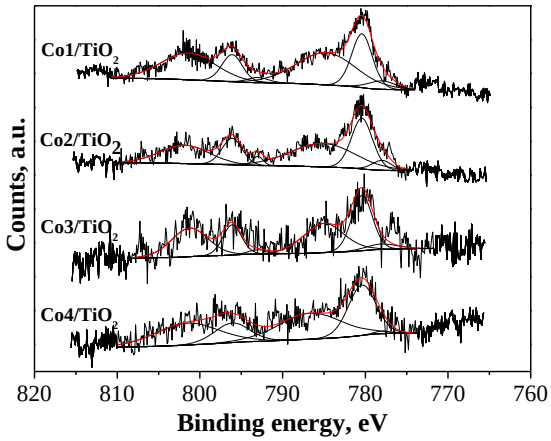

Table S6. Percentage of Co species in supported catalysts from XPS spectra decomposition.[a]		
Catalyst	Co^0	Co^{2+}
Co1/TiO_2	17	83
Co2/TiO_2	15	85
Co3/TiO_2	13	87
Co4/TiO_2	3	97

[a] Percentages corresponding to the Co $2p_{3/2}$ spin orbit peaks. [b] Reduced under H_2 at 400ºC during 10h. [c] After FTS in fixed bed.

Figure S11. Co 2p XPS spectra of **Co2/TiO$_2$** (1) freshly synthesized; (2) reduced under H_2 at 400ºC during 10h and (3) after FTS in fixed bed.

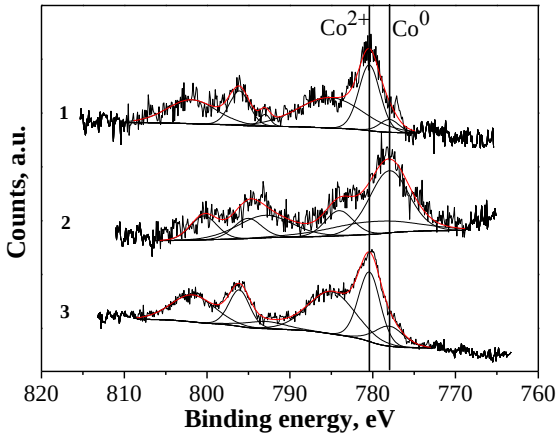

Table S7. Percentage of Co species in supported catalysts from XPS spectra decomposition.[a]		
Catalyst	Co^0	Co^{2+}
Co2/TiO_2	15	85
Co2/TiO_2, [b]	69	31
Co2/TiO_2, [c]	28	72

[a] Percentages corresponding to the Co $2p_{3/2}$ spin orbit peaks. [b] Reduced under H_2 at 400ºC during 10h. [c] After FTS in fixed bed.

Table S8. Aqueous phase Fischer-Tropsch synthesis catalyzed by **Co1-4** evaluating the size effect of the CoNPs.[a]

E.	Catalyst	Size, nm	O/P ratio		
			O/P C_{2-12}	**O/P C_{2-4}**	**O/P C_{5-12}**
1	**Co1**	1.75	0.75	1.23	0.32
2	**Co2**	2.64	0.79	1.33	0.28
3	**Co3**	5.18	0.80	1.12	0.37
4	**Co4**	7.02	0.51	1.00	0.16

[a] Conditions: 0.949 mmol Co, 30 bar H_2/CO/Ar (2:1:0,15); 66ml water (100 ml autoclave), 1000rpm, 180 ºC, 12h

Table S9. Fischer-Tropsch synthesis in fixed bed reactor catalyzed by TiO_2 supported CoNPs (**Co1-4/TiO_2**)[a]

E.	Catalyst	Size, nm	O/P ratio		
			O/P C_{2-12}	**O/P C_{2-4}**	**O/P C_{5-12}**
1	**Co1/TiO_2**	1.75	0.17	0.3	0.08
2	**Co2/TiO_2**	2.64	0.30	0.58	0.12
3	**Co3/TiO_2**	5.18	0.63	1.13	0.35
4	**Co4/TiO_2**	7.02	*	*	*

[a] Conditions: Catalyst loading=8-12wt%, 20 bar H_2/CO/N_2 (2:1:0.15), 5.62 ml/min, 240 ºC, CO conversions at 46h; * Not available information.

CHAPTER VII

Fischer-Tropsch Synthesis Over Cobalt Nanoparticles Prepared by Sodium Borohydride Reduction: Effect of the Polymeric Stabilizer

Table of Contents

VII.1. Abstract

A series of cobalt nanoparticles were synthesized by chemical reduction of cobalt salts using $NaBH_4$ as reduction agent in water, in the presence of a series of polymers as stabilizers. The polymer/cobalt ratio was observed to affect the size of the CoNPs. Cobalt nanoparticles of *ca.* 2.6 nm were immobilized on TiO_2 yielding approximately 10 wt% Co/TiO_2 catalysts. Both colloidal and TiO_2 supported NPs were characterized by TEM, XRD, HRTEM, XPS, TGA, ICP techniques and their catalytic performance in the AFTS and FTS were evaluated respectively. For both catalytic systems relevant differences in FTS were observed as a function of the polymeric stabilizer used during the synthesis of the CoNPs. The reduction degree of the cobalt particles, the interaction strength between the polymer and the metal surface and B-doping are propose as ruling parameters of the performance of the colloidal catalysts. In contrast, the catalytic activity of supported catalysts revealed to be influenced by the presence of polymer stabilizer at the metal surface, its thermal stability and B-doping.

Keywords: Fischer-Tropsch synthesis, cobalt nanoparticles, polymer stabilizers.

VII.2. Introduction

Fischer-Tropsch Synthesis (FTS) is considered a key process of the XTL technologies (biomass-to-liquid, BTL, gas-to-liquid, GTL, and solid-to-liquid, STL) since through this catalytic reaction, syngas (a mixture of H_2 and CO) can be transformed into clean fuels.[1] Among the different metals active in FTS, there is a renewed interest in cobalt catalysts due to its higher activity and stability compared to iron.[2] These, in conjunction with the convenient gas stoichiometry obtained from methane reformed syngas, are the reasons why recent gas to liquid facilities in Malaysia (Shell) and Qatar (Sasol and Qatar Petroleum) use cobalt based catalysts.[1b]

Currently, one of the main challenges in FT research is the design of not only active and stable catalysts but also highly selective active phases that provide hydrocarbons with narrow chain length distributions.[3] In this context, the advances in colloidal nanoscience have allowed a more efficient control over the size and morphology of metallic nanoparticles with potential applications in the field of catalysis.[4] Considering that most catalysts applied in FTS are anchored onto a support, an additional advantage of colloidal particles is that the effect of the support could be excluded.[5] However when colloidal NPs are used, the effect of the stabilizing agent arises as an intrinsic characteristic for these catalysts. It is often considered that the activity of NPs tends to decrease with increasing coordination strength of the organic stabilizing agent to the metal surface.[5] There are examples reported for hydrogenation,[6] and C-C coupling reactions.[7] For instance, the possibility to tune the selectivity in the Ru and RhNPs catalyzed hydrogenation of aromatic ketones through the phosphorus stabilizing ligand has been recently reported in our research group.[6a] For the particular case of the FTS, the only study dedicated to the rationalization of the effect of the stabilizing agent was recently reported by Hensen and co-workers using RuNPs.[5] To avoid changes in the size and morphology of the initial Ru particles, the organic stabilizing agents: trimethyl(tetradecyl)ammonium bromide (TTAB), polyvinylpyrrolidone (PVP) and sodium 3-mercapto-1-propanesulfonate (SMPS), were deposited onto a previously prepared Ru/CNF (carbon nanofiber) catalyst. In catalysis, the activity for the FT reaction decreased in the order: Ru>Ru-TTAB>Ru-PVP>>Ru-SMPS. It was proposed that this activity order coincides with increasing the interaction strength between the organic stabilizing agent and the Ru surface.

Kou and co-workers tested in the Aqueous phase Fischer-Tropsch Synthesis (AFTS) RuNPs stabilized by PVP-K15, K30 and K90, corresponding to polymers of molecular weights of 10000, 40000 and 36000 respectively.[8] A fast aggregation and deactivation of the catalysts prepared using the PVP-K15 was observed in catalysis. Interestingly, the activity of the catalyst prepared in presence of the polymer of highest molecular weight, PVP-K90, was slightly lower than the stabilized by PVP-K30. It was proposed that too strong coverage by PVP (which is

the case of PVP-K90) may block the route for the reactants to diffuse and react over the metal surface, thus resulting in an inferior catalytic activity.

For the case of cobalt, much less information concerning the effect of the stabilizing agent is documented in the literature. All the reports on FTS catalyzed by colloidal CoNPs involve the use of PVP or ionic liquids as stabilizing agent. For instance, Kou and co-workers have reported several studies concerning the application of monometallic CoNPs,[9] and bimetallic Pt-Co NPs,[10] as catalysts of the AFTS. The same author also reported the effect of the reducing agent ($LiBEt_3H$ and $NaBH_4$) used for the preparation of CoNPs in the AFTS,[11] and proposed that doping by boron could affect the catalytic performance of these NPs. Despite these studies, no reports on the effect of the stabilizing agent have been described for Co-catalyzed FTS. Dupont and co-workers reported the synthesis of Co nanocubes (54 ± 22 nm)[12] and nanospheres (7.7 ± 1.2 nm)[13] by thermal decomposition of $Co_2(CO)_8$ in [DMI][NTf_2] and [BMI][NTf_2] respectively. The obtained materials resulted active in FTS. In these studies, since the stabilizer was the same solvent of reaction, no direct correlation with the stabilizer effect could be extracted.

In the present work, a new step forward for the understanding of the effect of the polymer stabilizer on cobalt nanoparticles for the FT reaction is described. The aim of this investigation firstly is to understand the structure, composition and possible cobalt-boron interactions involved in these B-doped cobalt nanoparticles and secondly, to evaluate their catalytic performance in FTS. The colloidal NPs were additionally immobilized on TiO_2 support for comparison between the classical Fischer-Tropsch Synthesis in fixed bed reactors and the Aqueous phase Fischer-Tropsch Synthesis using the single colloidal catalyst. This approach allowed us to investigate the effect of the polymeric stabilizer on FTS and to look at the possible interaction of the cobalt nanoparticles with the support.

VII.3. Results and Discussion

VII.3.1. Synthesis and characterization of CoNPs

CoNPs were synthesized in water by chemical reduction of cobalt chloride in the presence of polymers as stabilizers and sodium borohydride as reducing agent. The structures of the water soluble polymers used to stabilize the CoNPs are displayed in Figure 1.

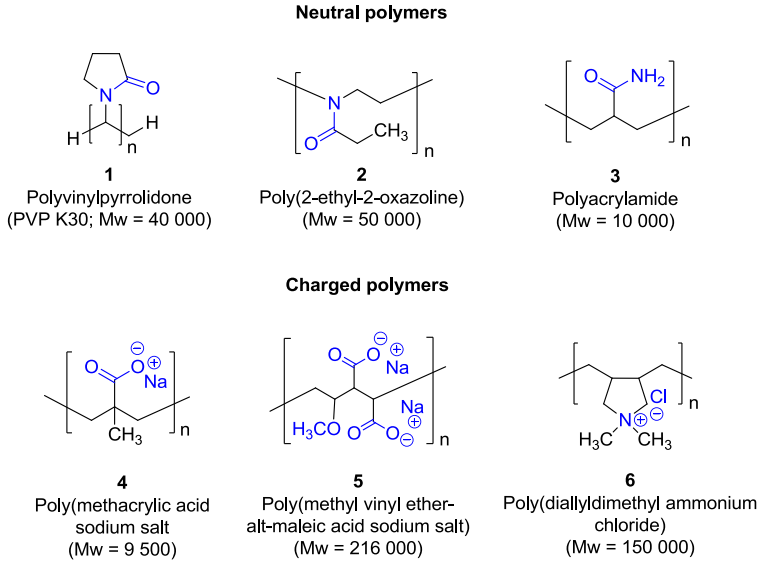

Figure 1. Structures of the water soluble polymers used as stabilizers for CoNPs.

Additionally, for each polymer, three sets of CoNPs were synthesized varying the polymer:Co ratio between 1 and 40. The TEM micrographs and size histograms of the NPs synthesized using a polymer:Co ratio of 20 for the case of **Co1b**, **Co2b**, **Co3b**, **Co4b** and **Co6b** and a ratio of 1 for **Co5a** NPs are displayed in Figure 2. The whole series of TEM micrographs and size histograms for the six sets of NPs are displayed in the Supporting Information (Figure S1).

According to Figure 2, spherical nanoparticles with diameters of *ca.* 2.6 nm were obtained under the corresponding polymer:Co ratios. The variations in particle

size as a function of the polymer and the polymer:Co ratio are summarized in Table 1.

Co1b (2.64 ± 0.92 nm)
Polymer1:Co = 20

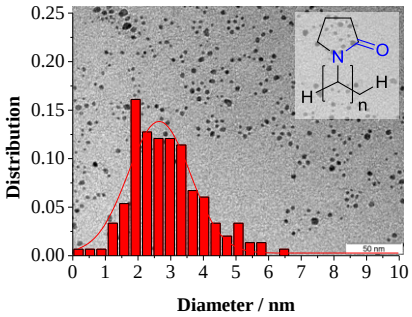

Co2b (2.74 ± 0.75 nm)
Polymer2:Co = 20

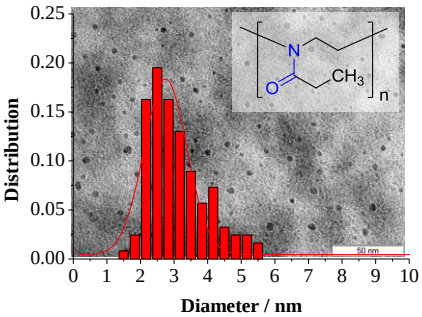

Co3b (2.83 ± 0.98 nm)
Polymer3:Co = 20

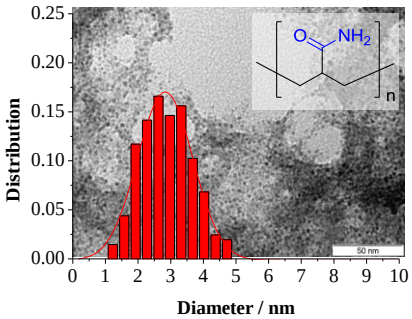

Co4b (2.75 ± 0.57 nm)
Polymer4:Co = 20

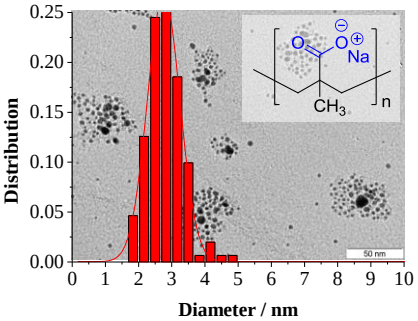

Co5b (2.55 ± 0.49 nm)
Polymer5:Co = 1

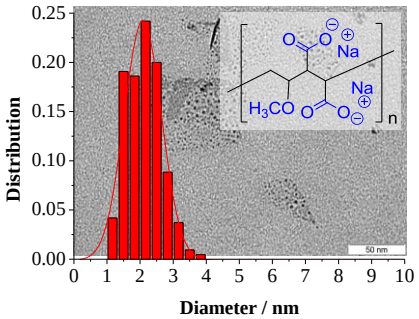

Co6b (2.69 ± 0.58 nm)
Polymer6:Co = 20

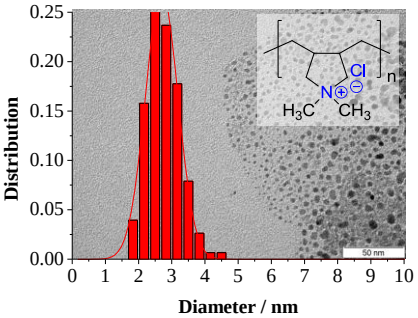

Figure 2. TEM micrographs and size histograms of **Co1-6** NPs.

Table 1. Conditions for the synthesis of **Co1-6** by chemical reduction method.[a]

Entry	CoNPs	Stabilizer	Polymer:Co[b]	Size, nm
1	**Co1a**	1	10	3.13 ± 1.58
2	**Co1b**	1	20	2.64 ± 0.92
3	**Co1c**	1	40	2.11 ± 0.41
4	**Co2a**	2	10	6.73 ± 1.58
5	**Co2b**	2	20	2.74 ± 0.75
6	**Co2c**	2	40	1.84 ± 0.74
7	**Co3a**	3	10	3.26 ± 1.12
8	**Co3b**	3	20	2.83 ± 0.98
9	**Co3c**	3	40	1.67 ± 0.46
10	**Co4a**	4	10	4.12 ± 1.58
11	**Co4b**	4	20	2.75 ± 0.57
12	**Co4c**	4	40	1.61 ± 0.67
13	**Co5a**	5	1	2.55 ± 0.49
14	**Co5b**	5	5	2.07 ± 0.68
15	**Co5c**	5	10	1.69 ± 0.51
16	**Co6a**	6	10	4.92 ± 1.15
17	**Co6b**	6	20	2.69 ± 0.58
18	**Co6c**	6	40	1.91 ± 0.56

[a] Conditions: 0.93 mmol of $CoCl_2.6H_2O$, 9.31mmol $NaBH_4$, water, 2h, rt. [b] Polymer:Co ratio based on mol of monomer units per mol of Co.

In most cases, large particle sizes (3-7 nm) and broad distributions (up to ± 1.6 nm) were obtained when a polymer:Co of 10 ratio was employed. The broad size distribution under those conditions was attributed to the poor stabilization of the NPs due to the low polymer concentration during the synthesis. Only for the case of **Polymer5**, NPs of small size and sharp distribution were obtained when even a low polymer:Co ratio of 1 was used (**Co5a**, 2.55 ± 0.49 nm), thus demonstrating the good stabilization capacity of this polymer. Figure 3 summarizes the mean diameter for the series of **Co1-6** NPs as a function of the polymer:Co ratio.

According to Figure 3, for all the stabilizers, when the polymer:Co ratio was increased, smaller NPs with sharper distributions were obtained (Table 1). The convergence in size to a value of *ca.* 2.6 and 1.8-2 nm when polymer:Co ratios of 20 and 40 were used respectively, is noteworthy. It was therefore concluded that at

polymer:Co ratio of 20 or higher, similar size CoNPs are formed. However at lower ratios, large differences in size and distribution are observed.

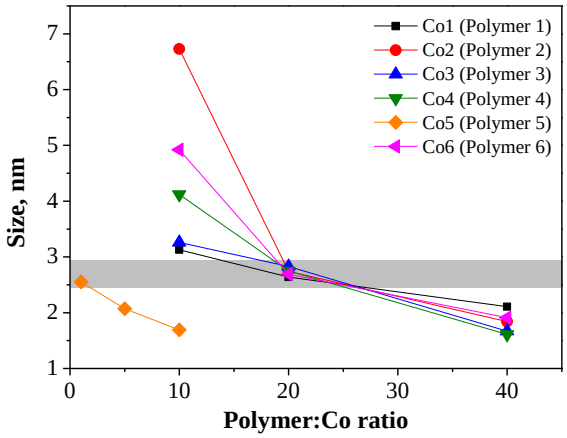

Figure 3. Mean diameter for the series of **Co1-6** stabilized by polymers 1-6 as a function of the polymer:Co ratio.

The variation of the stabilizer amount is a method widely applied for the synthesis of size controllable metal nanoparticles.[14] For instance, Lu *et al*. reported the tuning of the size of the spherical cobalt nanoparticles between 2–7.5 nm by changing the concentration of the polymer stabilizer, end-functionalized poly(methacrylic acid).[15] The decreasing size of the cobalt nanoparticles agrees with a slower growth relative to nucleation when higher concentration of PVP are used.[16]

It is also remarkable that the lower particle sizes of the series of NPs were obtained with **Polymer5**. The enhanced stabilization capacity of this polymer could rely on the presence of several potential coordinating groups per monomer unit as displayed in Figure 1. The particularly small sizes observed for CoNPs stabilized by **Polymer5**, could be also attributed to the large molecular weight of this polymer (Mw = 216000). The relation between the particle size of AuNPs and the molecular weight of the stabilizing polymeric thiol were described by Braun and co-workers.[17] According to the authors, the observation of the decreasing particle size with the increasing polymer molecular weight, suggests that the steric bulk of the

polymer may block the particle growth. The authors also proposed that the presence of polar polymeric thiols may accelerate nanoparticle nucleation, yielding smaller particles rather than fewer large ones.

Subsequent structural characterization and composition analysis was carried out on **Co1b, Co2b, Co3b, Co4b, Co5a** and **Co6b** NPs. We focused on these NPs due to their similar particle size (*ca.* 2.6 nm), important for their comparison in catalysis considering the structure sensitivity of FTS at such small cobalt particle sizes.[18]

The size and the fine structure of the CoNPs **Co1b** and **Co5a** were studied by high-resolution transmission electron microscopy (HR-TEM). In the micrograph of **Co1b** displayed in Figure 4, single particles of *ca.* 2.6 nm were observed in agreement with previous TEM observations (2.64 ± 0.92 nm).

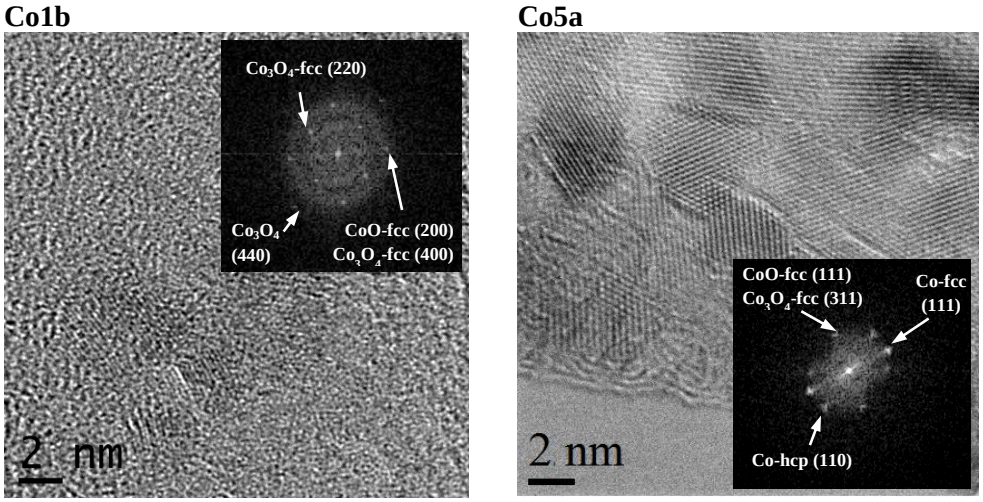

Figure 4. HR-TEM image of **Co1b** and **Co5a** NPs and their electron diffraction patterns.

Analysis of the diffraction pattern of these NPs revealed the presence of crystalline CoO-fcc and Co_3O_4-fcc, although no crystalline metallic cobalt phase were identified. In contrast, the micrograph of **Co5a** evidenced the fine crystalline structure of CoNPs of *ca.* 2.7 nm, revealing the presence of CoO-fcc, Co_3O_4-fcc and also Co-fcc. From the analysis by HR-TEM, the influence of the polymer stabilizer

on the fine structure of the NPs was suggested, since **Co5a** was more crystalline than **Co1b**. Possibly, the excellent stabilization capacity of **Polymer5** (demonstrated by the requirement of small amounts of this polymer to obtain well defined small CoNPs) could result in a more ordered structure during the reduction process.

Analysis of the crystalline structure of the catalysts **Co1-6** was performed by XRD. According to Figure 5, the diffraction pattern of these materials was characterized by the presence of broad signals which did not allowed the unambiguous identification of either cobalt, cobalt oxide or boride phases.

For instance, in the diffractograms of **Co1b**, **Co2b**, **Co3b** three bands centered at *ca.* 45º, 35 and 60º were appreciated. In contrast, **Co5a** and **Co6b** exhibited a prominent band at 45º similarly to that observed in **Co1b**. Finally, almost no signal was detected in the diffractogram of **Co4b**. The broadening of XRD peaks in cobalt nanoparticles is frequently associated to the small size and/or to the amorphous structure of the NPs.[19] For instance, Torres *et al.* reported the synthesis of CoNPs of 1 nm exhibiting XRD patterns with broad signals and attributed this effect to the small size of the CoNPs.[19a] However, Pileni and co-workers attributed the broadness of XRD patterns of 7 nm CoNPs (also synthesized by chemical reduction) to their amorphous structure.[19b]

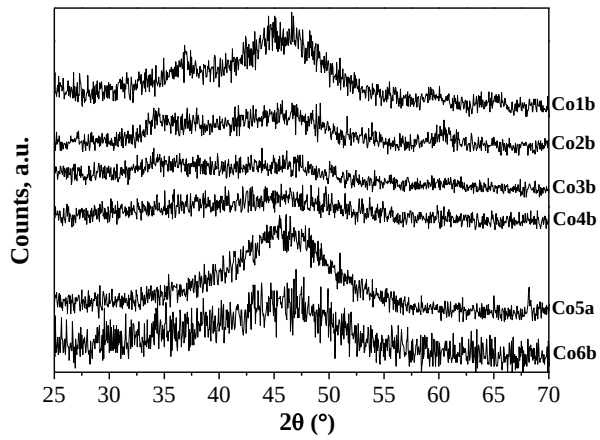

Figure 5. X-ray diffraction patterns of **Co1-6.**

Other authors ascribed a similar broad band centered at 45º to the amorphous structure of Co_2B synthesized from chemical reduction of cobalt salts using sodium borohydride as reducing agent.[20] Structural information of the CoNPs was obtained as described previously (Chapter 5 and 6) using a methodology reported by Glavee *et al*. which consisted in the thermal treatment of the CoNPs under Ar atmosphere.[21] Through this procedure, the CoNPs are forced to crystallize (or increase in size) then elucidating a defined crystalline pattern of their components. According to Figure 6, after the thermal treatment, **Co1b**, **Co2b**, **Co5a** and **Co6b** evidenced the presence of metallic cobalt phases (fcc and hcp), and presumably a boron species located at 28º for the case of **Co1b**. In contrast, **Co3b** and **Co4b**, exhibited a mixture of metallic cobalt (fcc and hcp) and important amounts of cobalt oxide phases (CoO-fcc). It was therefore concluded that the series, **Co1-6**, were effectively constituted by metallic cobalt, however for the case of **Co3b** and **Co4b** important amounts of cobalt oxide were present. These observations suggest that the protection of the polymer stabilizer can affect the reduction/oxidation degree of the resulting CoNPs.

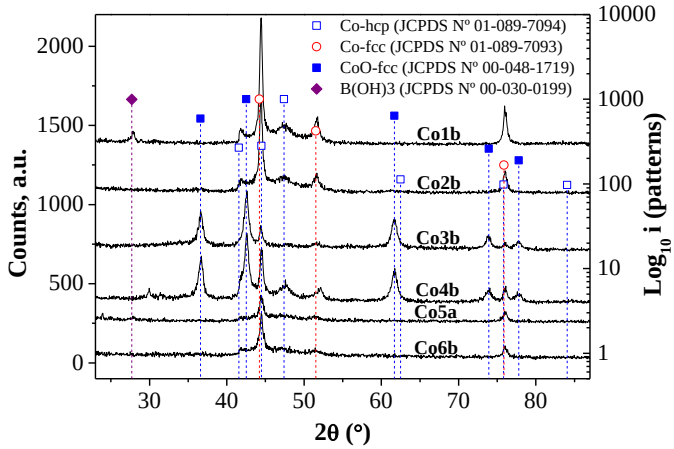

Figure 6. XRD patterns of **Co1a-d** treated at 500 ºC for 2h under argon.

Surface analysis of the CoNPs synthesized in this study was performed by X-ray photoelectron spectroscopy (XPS). The full XPS spectra of **Co1-6** revealed the presence of Na, Co, O, N, C and B, according to the peaks observed at their characteristic binding energies (1071.6; 781.5; 530.9; 399.2; 284.5 and 191.1 eV respectively). The Co 2p XPS spectra of the series **Co1-6** exhibited two prominent sets of peaks at *ca.* 777-794 and 795-806 eV readily assigned to Co $2p_{3/2}$ and Co $2p_{1/2}$, respectively (Figure 7). The fractions of Co^0 and Co^{2+} extracted from the decomposition of the Co $2p_{3/2}$ spin orbit peaks are displayed in Table 2.[22] A wide range of metallic cobalt content from 6 to 67% were calculated for the series of NPs. **Co5a** exhibited the highest value of metallic cobalt content with 67 %. **Co2b**, **Co3b** and **Co4b**, presented similar values in the range of 25-30%. Finally for the case of **Co6b**, only 6% of metallic cobalt content was determined.

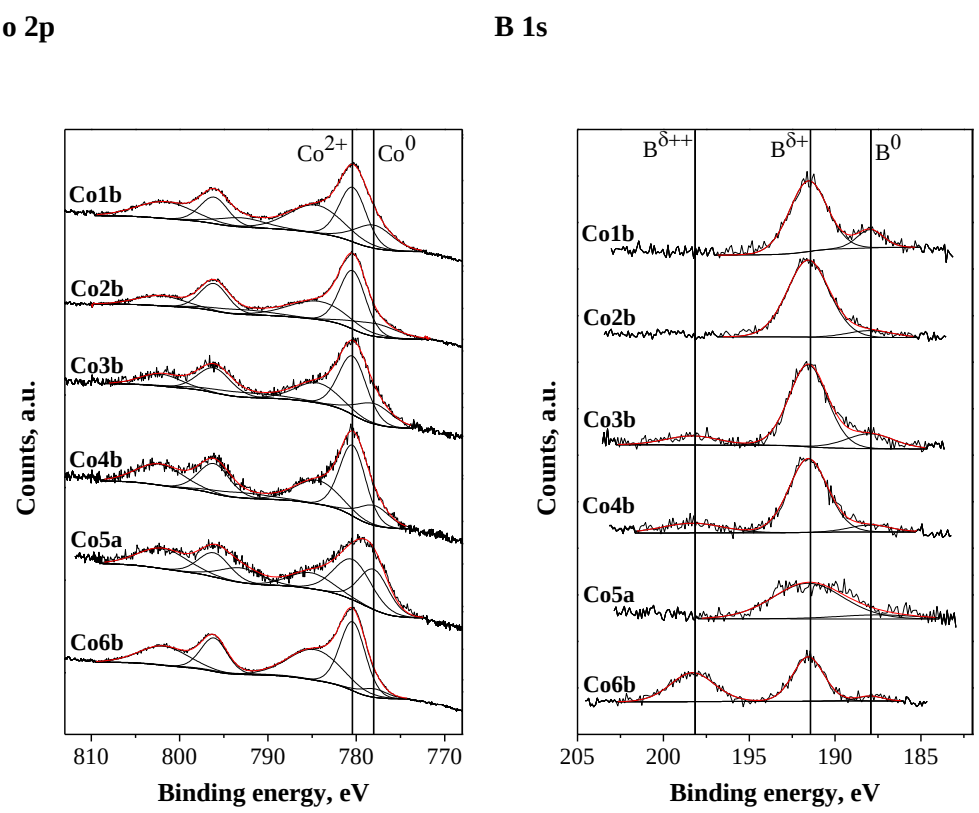

Figure 7. Co 2p and B 1s XPS spectra of **Co1-6** NPs.

Table 2. Percentage of Co and B species in colloidal NPs from XPS spectra decomposition. [a]

		Co 2p		B 1s		
Catalyst	Polymer	Co^0	Co^{2+}	B^0	$B^{\delta+}$	$B^{\delta++}$
Co1b	1	37	63	15	85	
Co2b	2	28	72	9	91	
Co3b	3	31	69	16	72	11
Co4b	4	25	75	8	77	16
Co5a	5	67	33	12	88	
Co6b	6	6	94	4	50	46

[a] Percentages corresponding to the Co $2p_{3/2}$ and B 1s spin orbit peaks.

The low content of metallic cobalt in several of the samples suggests the presence of important amounts of cobalt oxide in agreement with the observed by Raman spectroscopy (Supporting Information, Figure S5). It was therefore concluded that the polymer stabilizer also affects the reduction degree of the final material. It is believed that the differences in the reduction degree of the CoNPs could derive from the capacity of the stabilizing agent to protect the NPs against oxidation. According to this, **Polymer5** would be the best stabilizing agent against oxidation while conversely, **Polymer6** would be the worst of the series of tested polymer stabilizers.

The role of the stabilizing agent in the protection of CoNPs against oxidation has been documented in the literature.[23] For instance, Schmidt and co-workers reported that the oxidation rate of cobalt nanoparticles stabilized by carboxylic acid-telechelic polystyrene (Co@PS) was lower than those stabilized by polycaprolactone (Co@PCL).[23b] According to the authors, the deceleration of oxidation was much more significant for PS than for a PCL shell, probably due to a difference in their molecular oxygen diffusion properties resulting from different polymer polarity and oxygen affinity.

Since B-doping frequently occurs during the synthesis of cobalt nanoparticles prepared by $NaBH_4$ reduction,[21,24] analysis of the boron species at the NPs surface were studied by XPS. According to Figure 7, the B 1s XPS spectra of the series **Co1-6** exhibited the presence of two bands at 187.97 and 191.5 eV which were assigned to elemental boron (or Co_xB) and borates respectively, according to

reported data.[25] Deconvolution of the B 1s XPS revealed in general the abundance of the high valent boron species (> 70%, 191.5 eV) in comparison to the lower valent one. Curiously, a third band was detected at higher binding energy (198.3 eV) in **Co3b**, **Co4b** and more pronouncedly in **Co6b** (46%) which would correspond to a higher valence boron species.

Quantification of the content of cobalt and boron in **Co1-6** was performed by ICP. The Co/B atom ratio for the series of CoNPs was in the range of 2.0-6.4, according to Table 3. The maximal and minimal values in Co/B atom ratio corresponded to **Co4b** (6.4) and **Co6b** (2.0) respectively, while the other NPs exhibited values of *ca.* 2.6. Several studies have described the dependence of the final composition of the cobalt nanoparticles[26] and cobalt amorphous borides[24a] on the reaction temperature,[27] the pH, and the borohydride concentration or ratio versus cobalt.[27-28] To our knowledge this is the first study revealing the influence of the polymer stabilizer on the final composition of boron doped cobalt nanoparticles synthesized from $NaBH_4$ reduction.

Table 3. Co/B atom ratios of **Co1-6** catalysts determined by ICP analysis.

Entry	NPs	**Polymer**	**Co/B (atom ratio)**
1	**Co1b**	1	2.79
2	**Co2b**	2	2.57
3	**Co3b**	3	2.39
4	**Co4b**	4	6.44
5	**Co5a**	5	2.45
6	**Co6b**	6	2.02

The thermal stability of **Co1-6** was examined by thermogravimetric analysis. The thermograms of **Co1-6** (Supporting Information, Figure S7) exhibited a first weight loss in the region of 90-120ºC attributed to the loss of adsorbed solvent, followed by one or several weigh losses at higher temperature (>150 ºC) corresponding to the decomposition of the polymer stabilizer. According to the TGA data summarized in Table 4, important polymer amounts were detected in **Co3**, **Co4**, **Co2** (26, 12 and 7 wt%) while negligible quantities or even the complete absence of polymer were detected in **Co1b**, **Co6b** and **Co5a** (3, 1.6 and 0 wt% respectively).

Table 4. Weight loses observed by TGA for **Co1-6** NPs.

Entry	NPs	Polymer	Wt% Solvent[a]	Wt% Polymer[b]
1	**Co1b**	1	-3.5	-3.1
2	**Co2b**	2	-7.7	-7.4
3	**Co3b**	3	-8.0	-26.0
4	**Co4b**	4	-3.4	-12.2
5	**Co5a**	5	-0.6	0.0
6	**Co6b**	6	-3.2	-1.6

[a] Weight losses at T < 120ºC. [b] Weight losses at T > 150ºC.

Analysis of the NPs by FTIR confirmed the presence of the polymer stabilizer in **Co3** and **Co4**, in agreement with TGA (Supporting Information, Figure S6). Curiously, the two CoNPs that exhibited the largest polymer content (**Co3b** and **Co4b**) were synthesized using the polymers with the lowest molecular weight of the series (10000 for **Polymer3** and 9500 g mol^{-1} for **Polymer4**). According to Golas *et al*. short polymeric chains tend to act as effective stabilizers, resulting in well dispersed and stable metal colloids.[29] Conversely, too large polymeric chains may behave as floculant at the same mass concentration in solution. Adapting this argument to our case, the particular low molecular weight of **Polymer3** and **Polymer4** in conjunction to the strong coordination ability of amide and carboxylate groups could explain the good stabilization of the metal NPs by these polymers thus evidenced by the large polymer content of the isolated NPs. The scenery is different for **Co5a**. Although **Polymer5** also bears carboxylate groups similarly to **Polymer4**, the molecular weight of the former polymer is almost twenty times the value of the later (Mw = 216000 vs. 9500 g mol^{-1}). Such large difference in molecular weight results in distinct stabilization behaviors for both polymers. In the present study the nanoparticles with the lowest polymer content (**Co5a** and **Co6b**) also coincided with the largest molecular weights of the tested polymer stabilizers (**Polymer5** and **Polymer6**). Curiously for the series of tested polymers it was observed in general that the polymer content determined by TGA in the CoNPS increased when the molecular weight of the polymer decreased.

To summarize, six families of CoNPs stabilized by water soluble polymers were synthesized. The particle sizes resulted inversely proportional to the amount of stabilizer. In most cases, the particle size converged to a value of *ca.* 2.6 nm when the polymer:Co ratio was 20. Analysis by HR-TEM revealed the influence of the polymer stabilizer on the fine structure of the NPs, being **Co5a** more crystalline than **Co1a**. While the XRD of the fresh NPs only suggested the amorphous structure, after the thermal treatment under argon, it was revealed that the polymer stabilizer can affect the final reduction/oxidation degree of the CoNPs, in agreement with the XPS results. After this procedure, metallic cobalt phases were observed in all the NPs, but only in **Co3b** and **Co4b**, CoO-fcc was also detected. Finally, analysis of the NPs by TGA, pointed that the polymer stabilizer interacts differently with the metal surface. Stronger interactions such as for **Polymer3** and **Polymer4** resulted in larger amounts of the polymer in the analysis of the corresponding NPs.

Characterization of TiO_2 supported catalysts (Co1-6/TiO_2)

Immobilization of isolated **Co1-6** NPs on TiO_2 was carried out by direct addition of a suspension of the NPs over a stirred suspension of TiO_2 in hexane. The amounts of NPs and TiO_2 were adjusted to obtain a cobalt loading of *ca.* 10 wt%. Subsequently, ultrasonication of the obtained material was performed to ensure a good dispersion of the NPs onto the support. According to the TEM micrographs of the supported catalysts (**Co1-6/TiO_2,** Figure 8), in all cases, the CoNPs resulted well dispersed on TiO_2 crystals of *ca.* 20-30nm (Aeroxide® P25, Figure 8). The particle size of the nanoclusters maintained unchanged during the immobilization process.

The fine structure of **Co1b/TiO_2** supported catalyst was studied by HR-TEM. According to Figure 9, CoNPs are located over a TiO_2 crystal as indicated by arrows; however the distinction of the metal particles and the solid support is quite difficult in bright field analysis. For the case of this supported NPs, the electron diffraction of the dotted area only exhibited signals of anatase planes.

Co1b/TiO_2 (2.64 ± 0.92 nm)

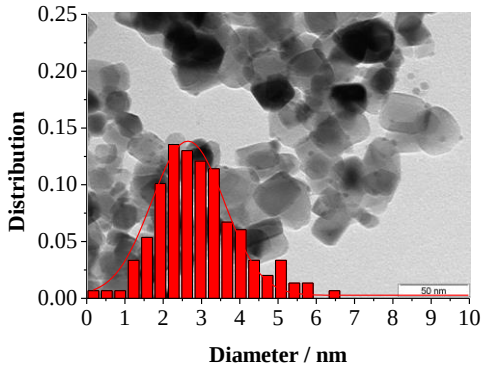

Co2b/TiO_2 (2.74 ± 0.75 nm)

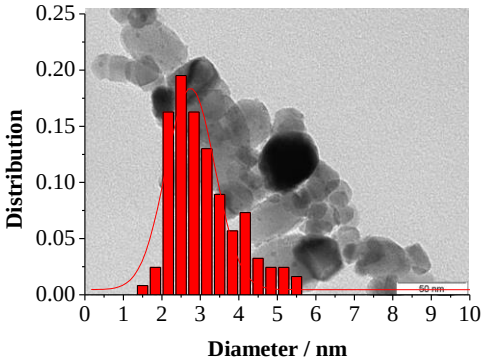

Co3b/TiO_2 (2.83 ± 0.98 nm)

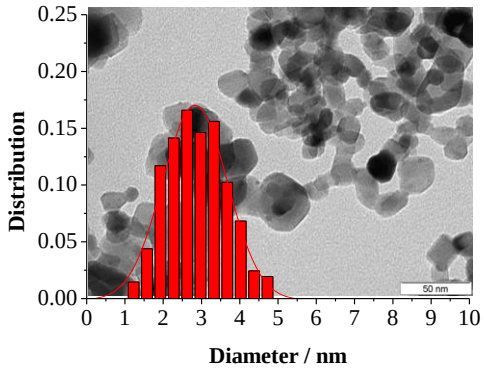

Co4b/TiO_2 (2.75 ± 0.57 nm)

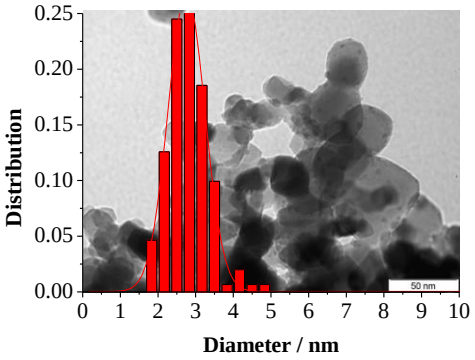

Co5a/TiO_2 (2.55 ± 0.49 nm)

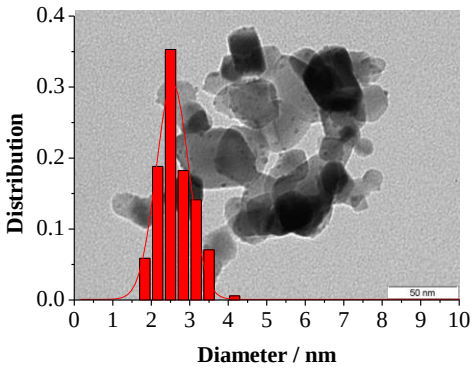

Co6b/TiO_2 (2.69 ± 0.58 nm)

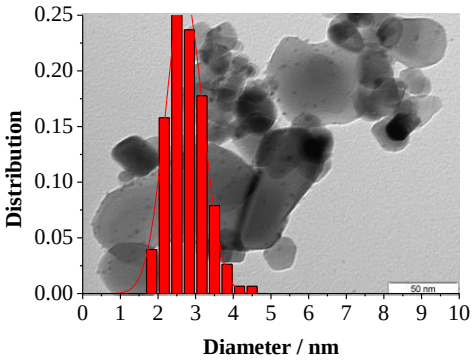

Figure 8. Size histograms and TEM micrographs of **Co1-6/TiO_2** catalysts.

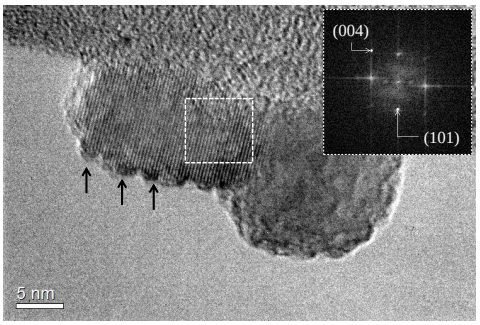

Figure 9. HR-TEM micrograph and electron diffraction of **Co1bTiO$_2$.**

XRD analysis was also performed on these supported catalysts. As displayed in Figure 10, in the series of catalysts, the anatase crystalline phase predominates over rutile phase (85 vs. 15%), however, the characteristic band of the CoNPs at 45º was practically overlapped by one of the rutile signals.

Surface analysis of the supported catalysts was also performed by XPS. Despite the low signal to noise observed due to the low cobalt loading in the catalysts (*ca.* 10 wt%), deconvolution of the Co $2p_{3/2}$ spin orbit peaks (Supporting Information, Figure S9) revealed metallic cobalt contents quite proportional to the values determined for the colloidal NPs (**Co5a/TiO$_2$** being the most reduced catalyst).

The reducibility of the supported catalysts **Co1-6/TiO$_2$** was analyzed by temperature programmed reduction (TPR), however, due to the partial reduction of the CoNPs, low signals were observed during the TPR analysis. For this reason, with the aim to increase the H_2 consumption, a soft passivation process was performed in all the catalysts prior to TPR analysis (100 ºC, 30 min). According to Figure 11, at least two reduction regions were observed in most of the samples at 300-450 and 450-600 ºC. The peak at 300–400 ºC corresponds to the reduction of Co_3O_4 to CoO and that at 400–600 ºC to the reduction of CoO to Co metal.[30]

The TPR profiles of **Co1-2/TiO$_2$** catalysts resulted quite similar with a broad band of low intensity in the region between 300-450 ºC, followed by a sharp band at 500 ºC. This suggests that the reducibility of the catalysts prepared using **Polymers**

1 and **2** is similar and was related to the structural similitude of both stabilizers (Figure 1).

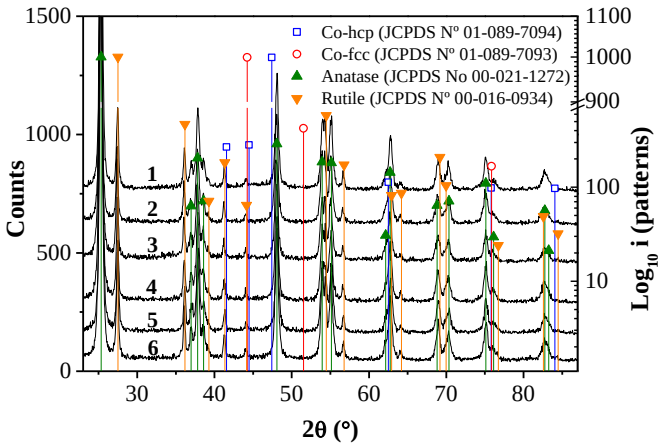

Figure 10. XRD patterns of TiO_2 supported CoNPs: (1) **Co1b/TiO$_2$**; (2) **Co2b/TiO$_2$**; (3) **Co3b/TiO$_2$**; (4) **Co4b/TiO$_2$**; (5) **Co5a/TiO$_2$**; and (6) **Co6b/TiO$_2$.**

In the case of **Co3b/TiO$_2$**, a broad band over the region of 350-580 ºC, indicated the pour reducibility of this catalyst. The important amounts of stabilizer determined for **Co3b** (26 wt%, Table 4, entry 3) in conjunction with the large residue that **Polymer3** could leave at the metal surface after its decomposition (31 wt% of residue at 900 ºC according to Table S5, Supporting Information), could be the responsible of the prolonged reduction temperature for this catalyst. In concordance with this hypothesis, the sudden increase of the H_2 consumption at 450 ºC coincides with the end of the main weight loss of **Polymer3** (Supporting Information, Figure S7), which could indicate that the presence of this polymer shifts the reduction temperature of the catalyst to higher values.

In contrast with the other catalysts, **Co4b/TiO$_2$**, displayed a single band with maximum at 405 ºC, and no H_2 absorption was observed for higher temperatures than 480 ºC. This observation suggests the good reducibility of **Co4b/TiO$_2$** catalyst in comparison with the others of the series. Finally, TPR spectra of **Co5a/TiO$_2$** displayed two defined bands at 460 and 540 ºC. The shift of the reduction

temperature to higher values indicated the low reducibility of **Co5a/TiO_2** in this series. Despite the structural relationship between **Polymer4-5**, large differences in reducibility were observed for their corresponding catalysts (**Co4-5/TiO_2**). The TPR profile of **Co6b/TiO_2** was similar to that for **Co5a/TiO_2** but with a less pronounced band below 500 ºC.

In conclusion, deep differences in reducibility were observed for the series of supported catalysts **Co1-6/TiO_2**. This indicated the role of the polymer stabilizer used during the synthesis of the CoNPs.

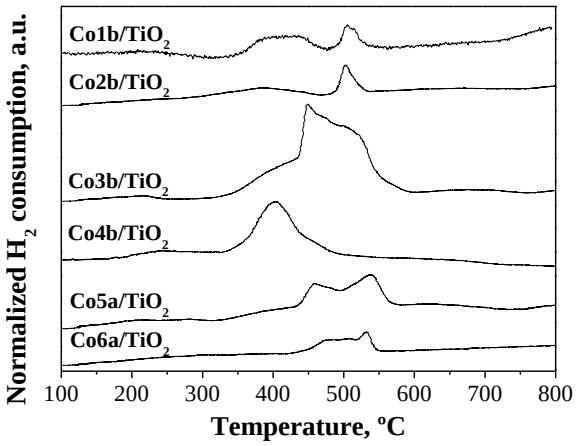

Figure 11. H_2-TPR profiles of **Co1-6/TiO_2** catalysts**.**

N_2 physisorption analyses were also realized on fresh catalysts. The BET areas of the series of catalysts **Co1-6/TiO_2** ranged between 42 and 56 m^2, values which are slightly larger than that measured for TiO_2 itself (43 m^2). ICP analysis of the supported catalysts revealed that the cobalt loadings ranged between 6.2-10.6 wt% (Supporting Information, Table S8).

To summarize, supported catalysts **Co1-6d/TiO_2** were prepared by immobilization of the corresponding colloidal NPs **Co1-6** on TiO_2. Analyses of the supported catalysts by XPS are in agreement with the results on the colloidal NPs in

terms of metallic cobalt content. Finally, the reducibility of the series of catalysts proved to be affected by the polymer stabilizer used during their synthesis.

VII.3.2. Fischer-Tropsch catalytic experiments

VII.3.2.1. Aqueous phase Fischer-Tropsch synthesis using colloidal CoNPs (Co1-6)

To evaluate the effect of the polymeric stabilizer in FTS, a series of catalytic experiments were carried out using the colloidal catalysts (**Co1-6**) suspended in water and the results are displayed in Table 5. The cobalt time yields discussed below are defined as mol of CO converted to hydrocarbon products per mol of Co per hour.

According to Figure 12a, moderate cobalt-time yields in the range between 0.002-0.061 h^{-1} were obtained for **Co4b** and **Co5b,** respectively. Similar activities were observed for catalysts **Co1b** and **Co2b** (*ca.* 0.025 h^{-1}), while **Co3b** exhibited slightly higher activity (0.033 h^{-1}). For the case of **Co4b**, although the time yield was almost depreciable, values up to 0.029 h^{-1} were calculated when the CO converted to CO_2 is included in the calculation. Finally, **Co5a** and **Co6b** exhibited the highest activities of the series with values of 0.061 and 0.051 h^{-1} respectively.

Concerning the product selectivity (Figure 12b), large variations were observed with these catalysts. For all the NPs except **Co4b**, the CO_2, CH_4, C_2-C_4 and C_5-C_{12} selectivites ranged between 23-43, 18-47, 16-40 and 8-24 wt% respectively.

Table 5. Aqueous phase Fischer-Tropsch synthesis catalyzed by **Co1-6** evaluating the effect of the polymer stabilizer on the NPs.[a]

E.	Catalyst	Polymer	Cobalt time yield, h^{-1} (+CO_2)[b]	Selectivity, Wt%					α
				CO_2	CH_4	C_{2-4}	C_{5-12}	C_{12+}	
1	**Co1b**	1	0.026 (0.029)	23.0	20.3	32.9	23.9	0.0	0.59
2	**Co2b**	2	0.021 (0.027)	43.0	18.5	24.3	14.2	0.0	0.66
3	**Co3b**	3	0.033 (0.040)	41.6	12.8	29.8	15.7	0.0	0.60
4	**Co4b**	4	0.002 (0.029)	96.9	1.7	0.8	0.6	0.0	0.65
5	**Co5a**	5	0.061 (0.068)	27.1	18.7	39.7	14.5	0.0	0.50
6	**Co6b**	6	0.051 (0.058)	28.9	47.5	15.9	7.7	0.0	0.53

[a] Conditions: 0.949 mmol Co, 30 bar H_2/CO/Ar (2:1:0,15); 66ml water (100 ml autoclave), 1000rpm, 180 ºC, 12h [b] metal time yield = mol of CO converted to hydrocarbon products per mol of Co, per unit of time (in parenthesis the CO converted to CO_2 is included)

a)

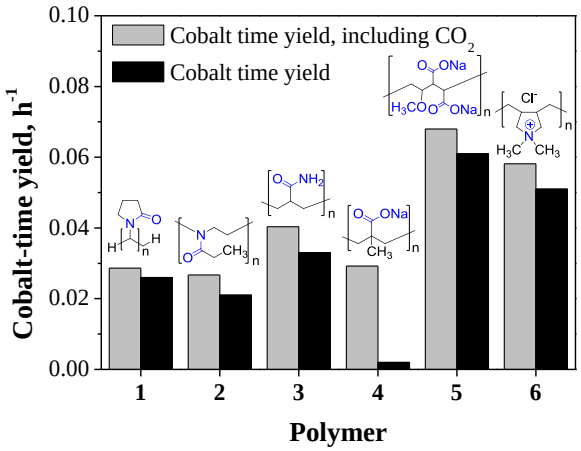

b)

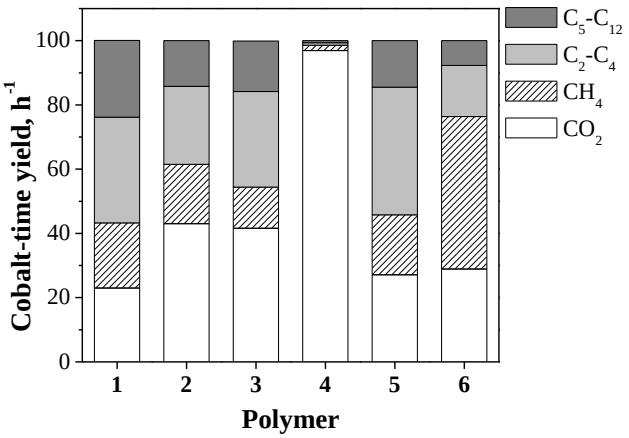

Figure 12. (**a**) Cobalt time yield and (**b**) product selectivity in the AFTS catalyzed by unsupported CoNPs, as a function of the polymer stabilizer. Conditions: 0.949 mmol Co, 30 bar H_2/CO/Ar (2:1:0.15), 66 ml water, 1000 rpm, 180 ºC, 12h.

Curiously, **Co4b** displayed an almost quantitative selectivity towards CO_2 (97 wt%). Comparable selectivities in terms of CO_2, CH_4 and C_{2+} (*ca.* 24, 20, 55 wt%) were obtained for **Co5a** and **Co1b** but the former case displayed a higher C_2-C_4 fraction (40 vs. 33%) in conjunction with a slightly lower α value (0.50 vs. 0.59) respectively. The catalysts **Co2b** and **Co3b** exhibited similar CO_2, CH_4 and C_{2+}

selectivities (*ca*. 40, 16 and 45 wt%). Finally, a large CH_4 selectivity (48 wt%) was observed for **Co6b** in agreement with a low α value of 0.53.

It is noteworthy that under the current colloidal conditions using water as solvent, the chain length of the hydrocarbon products was not longer than C_9 (See the ASF distributions in Supporting Information). From the series of tested catalysts, **Co5a** and **Co2b** exhibited the lowest and the highest α value (0.50 vs. 0.66 respectively).

The reduction degree of the fresh CoNPs is of paramount importance for their activity since in the absence of activation pretreatment, it determines the amount of active phase at the beginning of the reaction. The relationship between the activity and the reduction degree of the CoNPs is represented in Figure 13. According to this plot, it is evident the correlation between the percentage of reduced cobalt with the activity for the majority of the NPs (**Co1-5**). For the case of **Co6b,** it was concluded that additional factors must affect the activity of theses NPs.

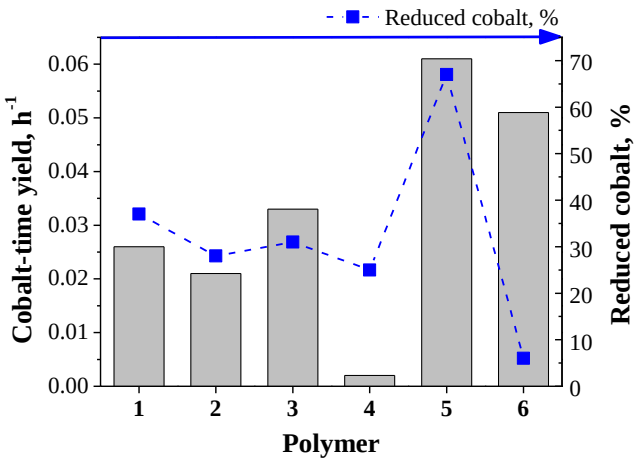

Figure 13. Correlation between the activity and the reduction degree of cobalt (Co^0 determined by XPS).

Indeed, the amount of polymer coordinated to the metal surface may also affect negatively the activity via the blocking of active sites.[5,7] The extent of this kind of polymer effect can be related with the amount of polymer measured by

TGA. Therefore, the catalytic performance of CoNPs with large polymer content would be affected negatively. The relationship between the activity and the polymer content of the CoNPs is represented in Figure 14. According to this plot, the inverse relationship between the polymer content and the activity is only evident for **Co5b** (for which no polymer was detected by TGA). However, this was not clear for all the other catalysts.

B-doping could also affect negatively the catalytic activity and the reducibility of cobalt based FT catalysts according to reported data.[31] For instance, Kou and co-workers analyzed by ICP the cobalt and boron content of CoNPs prepared from $NaBH_4$ and $LiBEt_3H$, determining Co/B atom ratios of 0.2 and 2 respectively.[11] They proposed that the large boron content in the Co-$NaBH_4$ explained the lower catalytic performance in comparison to Co-$LiBEt_3H$ considering that the excess of B could noticeably reduce the activity and selectivity of Fischer-Tropsch synthesis (0.10 vs. 0.27 $mol_{CO}mol_{Co}^{-1}h^{-1}$).[31] Conversely, recent studies demonstrated that boron can act as a promoter to enhance the stability of cobalt based catalysts during Fischer-Tropsch synthesis.[32]

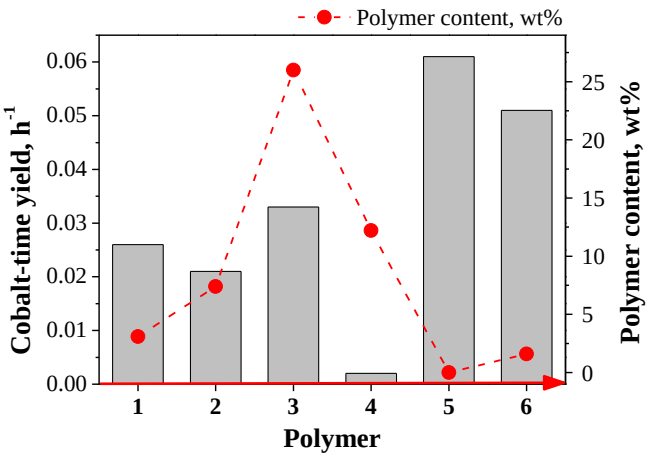

Figure 14. Correlation between the activity and the amount of polymer at the NPs surface (TGA).

According to computational calculations carried out in this study, the boron promotion can selectively block the deposition, nucleation, and growth of resilient carbon species, thus reducing the deactivation rate.

From the results obtained in this study, the relationship between the activity and the Co/B ratio (measured by XPS) of the CoNPs is depicted in Figure 15. However, no direct relationship between the activity and the boron content is evident.

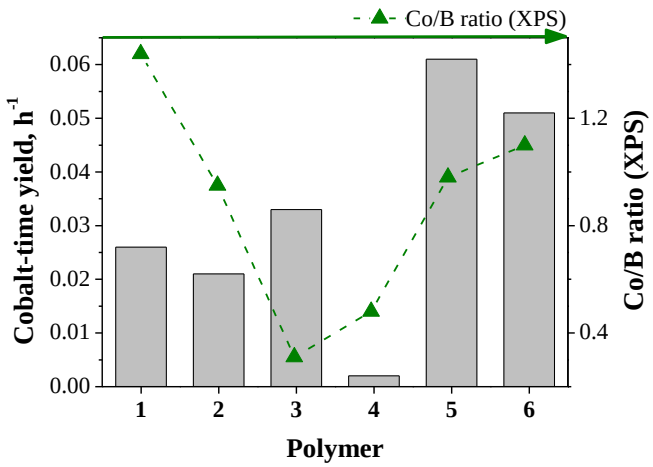

Figure 15. Correlation between the activity and the B-doping at the surface of the NPs (Co/B atom ratio calculated from XPS data).

The elemental composition of the fresh and used catalysts after AFTS was performed by XPS. According to Figure 16, in the absence of wax deposition, the variance in the elemental abundances between the fresh and used catalysts demonstrates the change of the metal surface during reaction. For instance, trace amounts of sodium observed in most of the fresh catalysts disappeared completely after catalysis. Similarly, the amounts of B and N decreased substantially (or even disappeared) after catalysis. The decrease of these elements at the metal surface can be considered a kind of "cleaning" under reaction conditions.

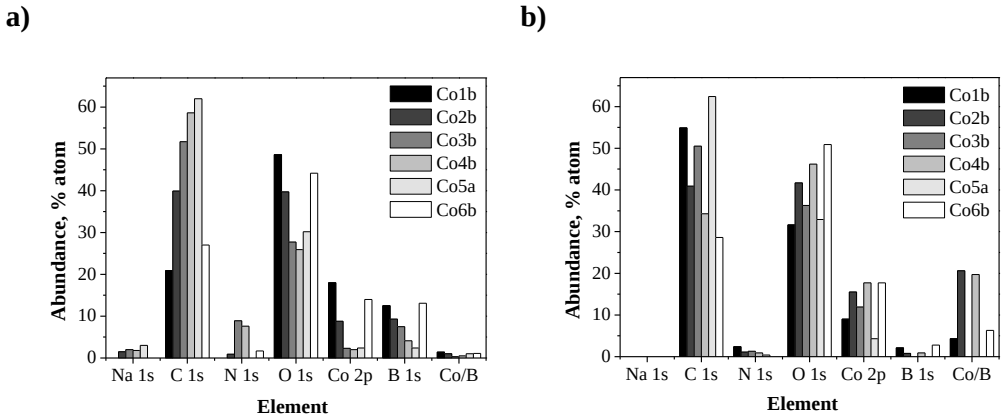

Figure 16. Surface elemental composition of **(a)** fresh and **(b)** used catalysts after AFTS determined by XPS analysis.

Although the restructuration of CoNPs during AFTS conditions was mentioned by Kou, the present study evidences the evolution of the metal particles in terms of variation of sodium and boron contents at the metal surface during catalysis. This is in contrast with the results reported by Kou and co-workers since they observed no variation of the Co/B ratio before and after catalysis for borohydride reduced CoNPs.[11]

Since the amount of boron present at the metal surface decreases during catalysis, a low Co/B ratio in the fresh catalysts does not represent necessarily a negative effect on the catalytic performance. If the effect associated to Co/B ratio is ignored, the moderate activity exhibited by **Co3b** proves that at least in the AFTS, the presence of important amounts of **Polymer3** coordinated at the NPs surface (25%) does not block the access of reactants to the active sites.

Conversely, although **Co4b** presents a lower polymer content in comparison with **Co3b** (12 vs. 26 wt%), since **Polymer4** contained sodium as counterion is believed to be the responsible of the complete suppression of FT activity. The increase of the CO_2 selectivity is a typical effect of the sodium poisoning of cobalt based catalysts.[33] In the case of **Co4b** the sodium effect is so marked that full selectivity towards CO_2 was obtained (97 wt%, Table 5).

Due to the excellent results obtained for the catalyst stabilized by **Polymer5**, further optimization was carried out varying the **Polymer5**:Co ratio (0.25, 5 and 20) during the synthesis of the NPs, and catalytic variables such as the temperature (150 and 210 ºC) and the solvent of reaction (n-buthylether and squalane) (See results in the Supporting Information, Figure S12-S14).

As a summary, lower activities were observed when **Polymer5**:Co ratios higher than 1 were used. In addition, lowering the reaction temperature from 210 to 150 ºC resulted in an increase of the gasoline fraction (C_5-C_{12}) from 13 to 22% while the oxygenate selectivity (mainly aldehydes) increased from 5 to 14%. The favorable oxygenate selectivity at low temperatures agrees with the results reported by van Santen *et al*. in the AFTS catalyzed by RuNPs.[34] According to this report, at low reaction temperatures the chain termination through the CO insertion FT mechanism becomes important due to the higher CO coverage (favored also at low temperatures), thus resulting in a higher oxygenate selectivity, particularly aldehydes.

The last catalyst, **Co6b**, also exhibited a moderate activity (0.51 h^{-1}) in agreement with the low polymer content (1.6 wt%). The good activity of these NPs despite the low initial content of Co^0 (only 6 %) suggests the easy reducibility of this catalyst under reaction conditions.

To conclude, relevant differences in the catalytic performance in the AFTS were observed for the series of catalysts **Co1-6** as a function of the polymer stabilizer used during the synthesis of the NPs. The results in catalysis suggested that the activity was clearly influenced by the reduction degree of the CoNPs. Correlation between the activity and other parameters such as the polymer content and B-doping resulted less evident.

VII.3.2.2. Fischer-Tropsch synthesis using TiO_2 supported CoNPs (Co1-6/TiO_2)

Fischer-Tropsch experiments were also performed using the TiO_2 supported catalysts in fixed bed reactors at 240 ºC and 20 bar of syngas. The FT catalytic results at 46 h for the series of catalysts **Co1-6/TiO_2** (entry 1-4) are displayed in Table 6.

Strong variations in the activity were observed as a function of the polymer stabilizer used during the synthesis of the CoNPs. The series of catalysts exhibited the following order of decreasing activities at 46 h of reaction: **Co2b/TiO_2** > **Co5a/TiO_2** > **Co1b/TiO_2** > **Co6a/TiO_2** > **Co4b/TiO_2** > **Co3b/TiO_2** with the corresponding values of cobalt time yield of 11.76, 8.62, 5.27, 3.20, 0.04 and 0 h^{-1}, respectively. Negligible activities were observed for catalysts **Co3b/TiO_2** and **Co4b/TiO_2**. The evolution of the cobalt time yield of the catalysts during time is displayed in Figure 17.

Table 6. Fischer-Tropsch synthesis in fixed bed reactor using TiO_2 supported CoNPs[a]

E.	Catalyst	Polymer	Cobalt time yield[b]	Selectivity, Wt%					α
				CO_2	CH_4	C_{2-4}	C_{5-12}	C_{12+}	
1	**Co1b/TiO_2**	1	5.27	0.0	10.5	17.4	19.0	53.0	0.76
2	**Co2b/TiO_2**	2	11.76	0.3	13.1	16.0	25.9	44.7	0.81
3	**Co3b/TiO_2**	3	0	0	0	0	0	0	0
4	**Co4b/TiO_2**	4	0.04	0	0	0	0	0	0.88
5	**Co5a/TiO_2**	5	8.62	0.0	10.5	17.7	18.6	53.2	0.73
6	**Co6b/TiO_2**	6	3.20	0.0	13.6	18.2	22.9	45.3	0.81

[a] Conditions: Catalyst loading, 7-10 wt%, 20 bar $H_2/CO/N_2$ (2:1:0.15), 5.62 ml/min, 240 ºC; [b] metal time yield = mol of CO converted per mol of Co, per unit of time (46 h).

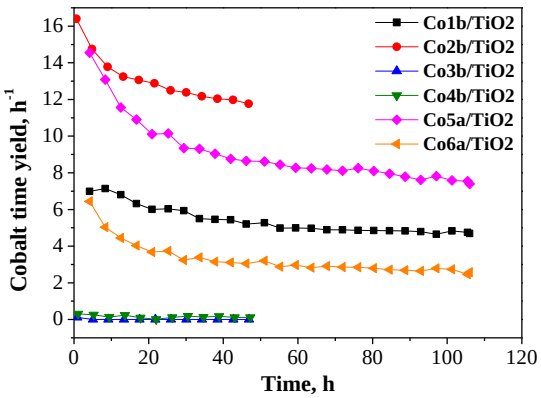

Figure 17. Evolution of cobalt time yield during time in FT experiments. Conditions: 7-10 wt% Co/TiO_2, 20 bar $H_2/CO/N_2$ (2:1:0.15), 5.62 ml/min, 240 ºC.

Deactivation rates were calculated for the series of tested catalysts computing the time yields at 2 h and 46 h (Table 7). Fast deactivation of **Co5a/TiO_2** and **Co6b/TiO_2** was observed during the first 20 h of reaction (-44 and -52 % after 46 h respectively). A similar deactivation profile, although less pronounced, was registered for **Co2b/TiO_2** (-26 % after 46 h). Other catalysts such as **Co1b/TiO_2** presented relatively stable time yields without a marked deactivation during the initial period of the reaction (-24 % after 46 h).

Table 7. Deactivation rate of cobalt catalysts at 240 ºC

Catalyst	Co-time yield at 2h	Co-time yield at 46h	Δ Co-time yield, %
Co1b/TiO_2	7.0	5.3	-24.6
Co2b/TiO_2	15.9	11.7	-26.3
Co3b/TiO_2	0.1	0	-100.0
Co4b/TiO_2	0.3	0.04	-86.2
Co5a/TiO_2	15.5	8.6	-44.3
Co6b/TiO_2	6.7	3.2	-52.3

It should be noted that due to the low activity of the catalyst **Co3-4/TiO_2**, some of the products could not be quantified. The CO_2 and CH_4 selectivities for the series of TiO_2 supported catalysts were below 0.4 % and in the range of 16-18 %, respectively.

Concerning the selectivity of the active catalysts (**Co1,2,5,6/TiO_2**), similar hydrocarbon fractions were obtained in all cases (10-13% CH_4, 16-18% C_{2-4}, 18-25% C_{5-12} and 44-53% C_{5+}; Table 6. and Figure 18). It is noteworthy that the production of CO_2 was negligible under the present catalytic conditions. For the particular case of **Co2b/TiO_2,** slightly higher selectivity for the gasoline fraction (26 wt%, C_5-C_{12}) was observed in comparison to the other catalysts (18-23 wt%).

Concerning the chain growth probability, the series of active catalysts exhibited α values between 0.73-0.81. The lowest α value was registered for the catalyst prepared from **Co5a** (0.73, **Co5a/TiO_2**) similarly to the results obtained for the colloidal catalytic system. According to the ASF distributions displayed in Figure 18, it is noteworthy that catalysts **Co1b/TiO_2** and **Co5a/TiO_2** presented an inflexion in the distribution near C_{30} after which the product fractions notably

decreased. This inflexion seems also to appear in **Co2b/TiO$_2$** but is clearly less pronounced. Curiously the ASF distribution of **Co6b/TiO$_2$** described an asymptotic decrease, which does not exhibited any inflexion in the distributions, as observed for the other catalysts.

Although the activity of **Co4b/TiO$_2$** was negligible, the accumulation of product during 46 h of reaction, allowed the analysis of the wax fraction. In this case, a typical ASF distribution was observed according to the straight line described, resulting in a chain growth factor of 0.88, which is the highest α value of the series.

It can therefore be concluded that the polymer used to stabilize the CoNPs, strongly affect not only the activity but also the stability and selectivity of the supported catalysts in the FTS. From the tested catalysts, **Co2b/TiO$_2$** resulted to be the most active of series, while **Co3-4/TiO$_2$** were almost inactive. In addition, similar selectivities were obtained for the active catalysts and particular ASF distributions with inflexion near C_{30} were also appreciated.

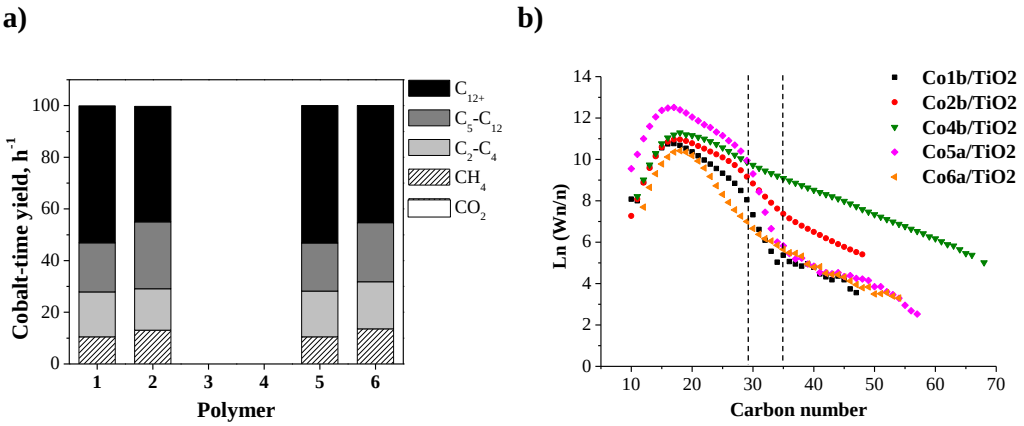

Figure 18. (a) Product selectivity in FTS and its corresponding **(b)** ASF distributions of **Co1-6/TiO$_2$**. Conditions: Catalyst loading=7-10wt%, 20 bar $H_2/CO/N_2$ (2:1:0.15), 5.62 ml/min, 240 ºC.

For the rationalization of the FT experiments using the supported catalysts, different parameters to those analyzed in the colloidal system, must be considered.

First, since activation of the catalysts was carried out prior to reaction, the content of metallic cobalt at the beginning of the catalysis will be related to its corresponding reducibility (TPR, Figure 11). The correlation between the activities of supported catalysts and the reduction temperatures is depicted in Figure 19, where the bars indicate the interval of reduction temperatures obtained from TPR data. According to this plot, a catalyst with a reduction temperature closer to the activation temperature (arrow) will exhibit a better reducibility compared to other with a larger reduction temperature value. Over this argument, the high activity observed for **Co2b/TiO_2** agrees with the good reducibility characterized by the low temperature at which this catalysts starts to reduce (309 ºC).

Conversely, **Co3b/TiO_2** which resulted inactive in catalysis, exhibited the highest reduction temperature value of the series of catalysts. In the case of **Co5a/TiO_2**, the relatively high activity obtained in catalysis (8.6 h^{-1}) agrees with the high reduction degree of the initial **Co5a** colloidal catalysts (67% of Co^0, Table 2). Analysis of **Co1b/TiO_2** by XPS demonstrated that the reduction degree of this catalyst increased up to 70% after the activation procedure (Supplementary Information, Table S7).

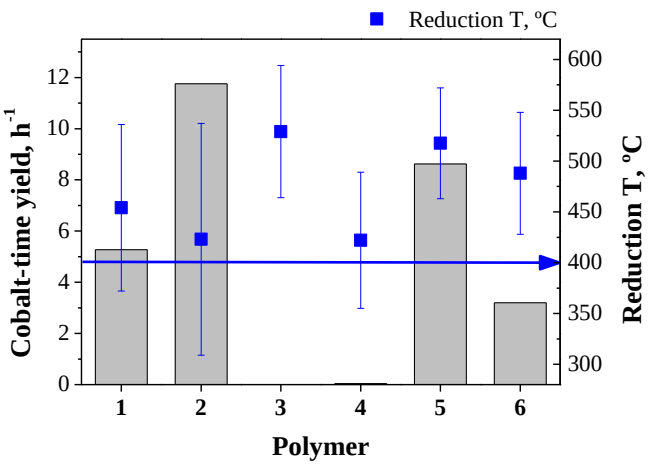

Figure 19. Correlation between the activity and the reduction temperature of the supported catalysts **Co1-6/TiO_2** (measured by TPR).

The correlation between the activity of the supported catalysts and the polymer content measured by TGA in the colloidal NPs is displayed in Figure 20. According to this plot, the lack of activity for catalysts **Co3-4/TiO_2** agrees with the high amount of polymer determined by TGA for the colloidal catalysts (26 and 12 wt% respectively, Table 4). In addition, the good catalytic performance observed for **Co5a/TiO_2** coincides with the absence of polymer stabilizer determined for the colloidal **Co5a** NPs. However, despite the important polymer content measured for **Co2b/TiO_2** (7.4 wt%, Table 4) the excellent performance observed for this catalyst suggests that other parameters are involved.

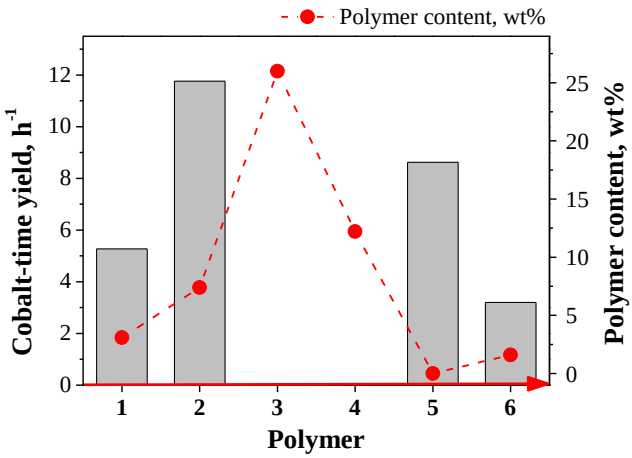

Figure 20. Correlation between the activity and the amount of polymer at the NPs surface (measured by TGA).

Finally, B-doping could affect also the catalytic performance of the supported catalysts. The detrimental effect of boron could even be more significant for the supported catalysts since the mechanism of "surface cleaning" observed in the colloidal catalysts during the reaction do not apply for the supported catalysts. The relationship between the Co/B ratio (calculated from XPS data) and the activity of the supported catalysts as a function of the polymer stabilizer is displayed in Figure 21.

According to this plot, active catalysts in FTS corresponded to those with Co/B ratios above of 1 (**Co1,2,5,6/TiO_2**) while the two inactive catalysts (**Co3-4/TiO_2**) exhibited Co/B ratios below of 0.5. In other words, active catalysts were obtained for those with relatively low amount of boron at the NPs surface. These observations agrees with the results of Jinlin *et al.* who reported that the introduction of 0.02-1.5% of boron as H_2BO_3 resulted in the decrease of the reducibility, the metal dispersion and the CO hydrogenation rate of a 10 wt% Co/TiO_2 catalyst.[31]

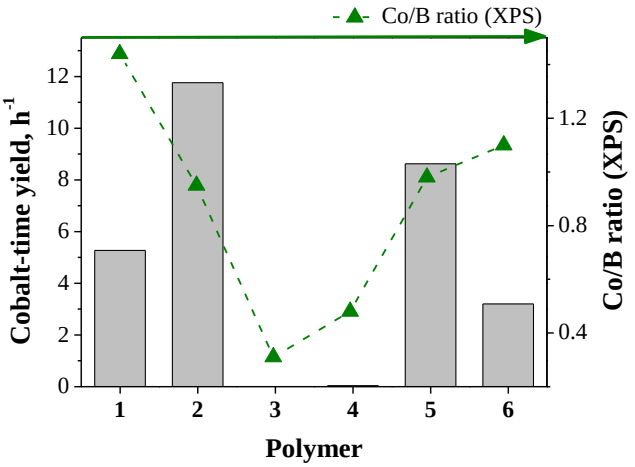

Figure 21. Correlation between the activity and the B-doping at the surface of the NPs (Co/B atom ratio calculated from XPS data).

Concerning possible effect of the B-doping on the reducibility, it should be noted that the catalyst with the highest reduction temperature (C**o3/TiO_2**, 570-600 ºC) exhibited also highest boron content of the series (Co/B atom ratio = 0.31). However, no clear trend between the B-doping and reducibility or activity was observed for the other catalysts.

In the case of **Co3b/TiO_2** and **Co4b/TiO_2**, the absence of activity observed for these catalysts is attributed to the important amounts of polymer stabilizer determined in **Co3b** and **Co4b** (26 and 12 wt% respectively). The large amount of residue measured by TGA after calcination of **Polymers3-4** (31 and 45 wt%) made impossible the cleaning of the metal surface through the activation process. In the

same line, the presence of important amounts of **Polymer3** was observed to shift the reduction of **Co3b/TiO_2** towards a high temperature interval (460-564 ºC) according to TPR analysis. Additionally, in spite of the good reducibility observed for **Co4b/TiO_2** (Figure 11) the performance of this catalyst can be deeply affected by sodium poisoning present in the NPs as counterion of **Polymer4**. The pour catalytic performance observed for this catalyst, agrees with the observed behavior for **Co4b** in the colloidal system.

To conclude, the catalytic performance of the supported catalysts tested in FTS was observed to be deeply affected by the polymer stabilizer used during the synthesis of the CoNPs. In this occasion, parameters such as the reducibility of the catalysts and B-doping were shown to be affected by the nature of the polymeric stabilizer and consequently influenced the performance of these catalysts during FTS.

VII.4. Conclusions

Six families of CoNPs stabilized by water soluble polymers were synthesized. In most cases, the particle size converged towards a value of *ca.* 2.6 nm when the polymer:Co ratio was 20. Notable differences in the fine structure, the crystallinity, the oxidation degree, the composition and the polymer content (polymer/surface interaction) were determined by HR-TEM, XRD, XPS, ICP and TGA, respectively. Supported catalysts were also prepared by immobilization of the colloidal NPs on TiO_2 and its reducibility evaluated by TPR. Both series of colloidal and supported catalysts were tested in the FTS using stirred tank (STR) and fixed bed reactors respectively. For the colloidal catalytic system, the nature of the polymeric stabilizer influenced the reduction degree of the CoNPs, which in turn affected the catalytic performance of the NPs. The good catalytic performance in terms of activity and selectivity observed for **Co5a** were attributed to minimal polymer content and their high reduction degree.

Similarly, the catalytic performance of supported catalysts resulted also deeply dependent on the nature of the polymeric stabilizer, since this mainly affected

the reducibility. Finally, the excellent catalytic performance of **Co2b/TiO_2** was mainly attributed to the easy reducibility of this catalyst.

VII.5. Experimental Section

Synthesis of colloidal cobalt nanoparticles by chemical reduction (Co1-6)

CoNPs were synthesized by chemical reduction of cobalt chloride in presence of different water soluble polymers as stabilizer and using sodium borohydride as reducing agent.

As standard procedure, 0.226 g of $CoCl_2.6H_2O$ (0.931 mmol) was dissolved in H_2O containing the corresponding amount of the polymer stabilizer. The volume of water for all the synthesis was completed to 50 ml to obtain a cobalt concentration of 0.018 M. Then, a freshly prepared solution of 0.358 g of $NaBH_4$ (9.31 mmol) in 16.6 ml H_2O was added at room temperature with a rate of 3 ml/min (5 min). The solution was maintained under vigorous mechanical stirring for 2 h. Then, 100 µl of the colloidal solution was centrifuged, washed with water and re-dispersed by sonication. Three drops of the obtained colloidal solution was deposited on a Cu-formvar or holey carbon grids for TEM or HR-TEM analysis. In order to isolate the CoNPs, freshly prepared NPs were initially precipitated by a strong magnetic field and the supernatant was decanted. Then, the precipitated NPs were rinsed with water to remove the excess of salts and polymer. This process was repeated three times with water, then three times with ethanol and finally, three times with hexane. The resulted CoNPs were finally dried under vacuum and kept in the glove box.

The size, the crystalline structure and oxidation state of the CoNPs were studied using transmission electron microscopy (TEM), HR-TEM, X-ray diffraction (XRD), and X-ray photoelectron spectroscopy (XPS) respectively. The composition of the CoNPs was studied using FTIR, TGA and ICP-OES.

- **Co1a:** was synthesized according to the general procedure using $CoCl_2 \cdot 6H_2O$ (0.226 g, 0.931 mmol) in presence of **Polymer1** (1.033 g of PVP-K30, **Polymer1**:Co=10) dissolved in 50 ml of deionized water ([Co] = 0.018 M). $NaBH_4$ (0.358 g, 9.369 mmol) was dissolved in 16.6 ml ([$NaBH_4$] = 0.550 M).

TEM: D = 3.13 ± 1.58 nm.

- **Co1b:** was synthesized according to the general procedure using $CoCl_2 \cdot 6H_2O$ (0.226 g, 0.931 mmol) in presence of **Polymer1** (2.066 g of PVP-K30, **Polymer1**:Co=20) dissolved in 50 ml of deionized water ([Co] = 0.018 M). $NaBH_4$ (0.358 g, 9.369 mmol) was dissolved in 16.6 ml ([$NaBH_4$] = 0.550 M).
  TEM: D = 2.64 ± 0.92 nm.
  HR-TEM: *ca.* 2.6 nm; detection of CoO-fcc and Co_3O_4-fcc.
  XRD: 45, 35 and 60º
  XPS: Co^0, 37%; Co^{2+}, 63%.
  TGA: Temperature ºC/Δ wt. % (attribution); 70/-3.5 (solvent), 244/-3.7 (polymer), 900end/+0.92.
  ICP: Co, 82.4 wt%, B, 5.9 wt%; Co/B atom ratio, 2.79
  FTIR: 3477, 1644, 1425 cm^{-1}.
  RAMAN: 666, 586, 492, 450, 196 cm^{-1}.
- **Co1c:** was synthesized according to the general procedure using $CoCl_2 \cdot 6H_2O$ (0.226 g, 0.931 mmol) in presence of **Polymer1** (4.132 g of PVP-K30, **Polymer1**:Co=40) dissolved in 50 ml of deionized water ([Co] = 0.018 M). $NaBH_4$ (0.358 g, 9.369 mmol) was dissolved in 16.6 ml ([$NaBH_4$] = 0.550 M).
  TEM: D = 2.11 ± 0.41 nm.
- **Co2a:** was synthesized according to the general procedure using $CoCl_2 \cdot 6H_2O$ (0.226 g, 0.931 mmol) in presence of **Polymer2** (0.432 g of poly(2-ethyl-2-oxazoline), **Polymer2**:Co=10) dissolved in 50 ml of deionized water ([Co] = 0.018 M). $NaBH_4$ (0.358 g, 9.369 mmol) was dissolved in 16.6 ml ([$NaBH_4$] = 0.550 M).
  TEM: D = 6.73 ± 1.58 nm.
- **Co2b:** was synthesized according to the general procedure using $CoCl_2 \cdot 6H_2O$ (0.226 g, 0.931 mmol) in presence of **Polymer2** (0.864 g of poly(2-ethyl-2-oxazoline), **Polymer2**:Co=20) dissolved in 50 ml of deionized water ([Co] = 0.018 M). $NaBH_4$ (0.358 g, 9.369 mmol) was dissolved in 16.6 ml ([$NaBH_4$] = 0.550 M).
  TEM: D = 2.74 ± 0.75 nm.

XRD: 34, 47 and 61º

XPS: Co^0, 28%; Co^{2+}, 72%.

TGA: Temperature ºC/Δ wt. % (attribution); 70/-7.7 (solvent); 285/-6.7 (polymer); 424/-0.7 (polymer); 900end/+2.74

ICP: Co, 81.0 wt%, B, 6.3 wt%; Co/B atom ratio, 2.57

FTIR: 3449, 1635, 1418, 1053 cm^{-1}.

RAMAN: 670, 605, 508, 464, 184 cm^{-1}.

- **Co2c:** was synthesized according to the general procedure using $CoCl_2 \cdot 6H_2O$ (0.226 g, 0.931 mmol) in presence of **Polymer2** (1.728 g of poly(2-ethyl-2-oxazoline), **Polymer2**:Co=40) dissolved in 50 ml of deionized water ([Co] = 0.018 M). $NaBH_4$ (0.358 g, 9.369 mmol) was dissolved in 16.6 ml ([$NaBH_4$] = 0.550 M).

  TEM: D = 1.84 ± 0.74 nm.

- **Co3a:** was synthesized according to the general procedure using $CoCl_2 \cdot 6H_2O$ (0.226 g, 0.931 mmol) in presence of **Polymer3** (0.659 g of 50 wt% sln. of polyacrylamide, **Polymer3**:Co=10) dissolved in 50 ml of deionized water ([Co] = 0.018 M). $NaBH_4$ (0.358 g, 9.369 mmol) was dissolved in 16.6 ml ([$NaBH_4$] = 0.550 M). D = 3.26±1.12 nm.

  TEM: D = 3.26 ± 1.12 nm.

- **Co3b:** was synthesized according to the general procedure using $CoCl_2 \cdot 6H_2O$ (0.226 g, 0.931 mmol) in presence of **Polymer3** (1.318 g of 50 wt% sln. of polyacrylamide, **Polymer3**:Co=20) dissolved in 50 ml of deionized water ([Co] = 0.018 M). $NaBH_4$ (0.358 g, 9.369 mmol) was dissolved in 16.6 ml ([$NaBH_4$] = 0.550 M).

  TEM: D = 2.83 ± 0.98 nm.

  XRD: 35, 46 and 60º

  XPS: Co^0, 31%; Co^{2+}, 69%.

  TGA: Temperature ºC/Δ wt. % (attribution); 89/-8 (solvent); 224/-6 (polymer); 318/-8; 434/-12; 524/-8 (polymer); 900end/-6.

  ICP: Co, 56.3 wt%, B, 4.7 wt%; Co/B atom ratio, 2.39

  FTIR: 3396, 3196, 2941, 1664, 1612, 1413 cm^{-1}.

RAMAN: 775, 671 cm^{-1}.

- **Co3c:** was synthesized according to the general procedure using $CoCl_2 \cdot 6H_2O$ (0.226 g, 0.931 mmol) in presence of **Polymer3** (2.635 g of 50 wt% sln. of polyacrylamide, **Polymer3**:Co=40) dissolved in 50 ml of deionized water ([Co] = 0.018 M). $NaBH_4$ (0.358 g, 9.369 mmol) was dissolved in 16.6 ml ([$NaBH_4$] = 0.550 M).

  TEM: D = 1.67 ± 0.46 nm.

- **Co4a:** was synthesized according to the general procedure using $CoCl_2 \cdot 6H_2O$ (0.226 g, 0.931 mmol) in presence of **Polymer4** (1.670 g of 50 wt% sln. of poly(methacrylicacid) sodium salt, **Polymer4**:Co=10) dissolved in 50 ml of deionized water ([Co] = 0.018 M). $NaBH_4$ (0.358 g, 9.369 mmol) was dissolved in 16.6 ml ([$NaBH_4$] = 0.550 M).

  TEM: D = 4.12 ± 1.58 nm.

- **Co4b:** was synthesized according to the general procedure using $CoCl_2 \cdot 6H_2O$ (0.226 g, 0.931 mmol) in presence of **Polymer4** (3.340 g of 50 wt% sln. of poly(methacrylicacid) sodium salt, **Polymer4**:Co=20) dissolved in 50 ml of deionized water ([Co] = 0.018 M). $NaBH_4$ (0.358 g, 9.369 mmol) was dissolved in 16.6 ml ([$NaBH_4$] = 0.550 M).

  TEM: D = 2.75 ± 0.57 nm.

  XRD: Not peaks detected.

  XPS: Co^0, 25%; Co^{2+}, 75%.

  TGA: Temperature ºC/Δ wt. % (attribution); 92/-3.4(solvent); 215/-6.2 (polymer low [386/-3.8; 623/-2.2 (polymer)]; 900end/+0.26

  ICP: Co, 81.9 wt%, B, 2.6 wt%; Co/B atom ratio, 6.44

  FTIR: 3430, 2923, 1555, 1399, 1205 cm^{-1}.

  RAMAN: 680 cm^{-1}.

- **Co4c:** was synthesized according to the general procedure using $CoCl_2 \cdot 6H_2O$ (0.226 g, 0.931 mmol) in presence of **Polymer4** (6.680 g of 50 wt% sln. of poly(methacrylicacid) sodium salt, **Polymer4**:Co=40) dissolved in 50 ml of deionized water ([Co] = 0.018 M). $NaBH_4$ (0.358 g, 9.369 mmol) was dissolved in 16.6 ml ([$NaBH_4$] = 0.550 M).

TEM: D = 1.61 ± 0.67 nm.

- **Co5a:** was synthesized according to the general procedure using $CoCl_2 \cdot 6H_2O$ (0.226 g, 0.931 mmol) in presence of **Polymer5** (2 ml of 0.375 mM sln. of poly(methylvinylether-alt-maleic acid) sodium salt, **Polymer5**:Co=1) dissolved in 48 ml of deionized water ([Co] = 0.018 M). $NaBH_4$ (0.358 g, 9.369 mmol) was dissolved in 16.6 ml ([$NaBH_4$] = 0.550 M).

  TEM: D = 2.55 ± 0.49 nm.

  HRTEM: *ca.* 2.6 nm; detection of CoO-fcc, Co_3O_4-fcc and Co-hcp.

  XRD: 46º

  XPS: Co^0, 67%; Co^{2+}, 33%.

  TGA: Temperature ºC/Δ wt. % (attribution); 114/-0.6 (solvent); 900end/+4.35.

  ICP: Co, 75.4 wt%, B, 6.2 wt%; Co/B atom ratio, 2.45

  FTIR: 3482 cm^{-1}.

  RAMAN: 825 cm^{-1}.

- **Co5b:** was synthesized according to the general procedure using $CoCl_2 \cdot 6H_2O$ (0.226 g, 0.931 mmol) in presence of **Polymer5** (10 ml of 0.375 mM sln. of poly(methylvinylether-alt-maleic acid) sodium salt, **Polymer5**:Co=5) dissolved in 40 ml of deionized water ([Co] = 0.018 M). $NaBH_4$ (0.358 g, 9.369 mmol) was dissolved in 16.6 ml ([$NaBH_4$] = 0.550 M).

  TEM: D = 2.07 ± 0.68 nm.

- **Co5c:** was synthesized according to the general procedure using $CoCl_2 \cdot 6H_2O$ (0.226 g, 0.931 mmol) in presence of **Polymer5** (20 ml of 0.375 mM sln. of poly(methylvinylether-alt-maleic acid) sodium salt, **Polymer5**:Co=10) dissolved in 30 ml of deionized water ([Co] = 0.018 M). $NaBH_4$ (0.358 g, 9.369 mmol) was dissolved in 16.6 ml ([$NaBH_4$] = 0.550 M).

  TEM: D = 1.69 ± 0.51 nm.

- **Co6a:** was synthesized according to the general procedure using $CoCl_2 \cdot 6H_2O$ (0.226 g, 0.931 mmol) in presence of **Polymer6** (1.670 g of 50 wt% sln. of poly(methacrylicacid) sodium salt, **Polymer6**:Co=10) dissolved in 50 ml of deionized water ([Co] = 0.018 M). $NaBH_4$ (0.358 g, 9.369 mmol) was dissolved in 16.6 ml ([$NaBH_4$] = 0.550 M).

TEM: D = 4.92 ± 1.15 nm.

- **Co6b:** was synthesized according to the general procedure using $CoCl_2 \cdot 6H_2O$ (0.226 g, 0.931 mmol) in presence of **Polymer6** (3.340 g of 50 wt% sln. of poly(methacrylicacid) sodium salt, **Polymer6**:Co=20) dissolved in 50 ml of deionized water ([Co] = 0.018 M). $NaBH_4$ (0.358 g, 9.369 mmol) was dissolved in 16.6 ml ([$NaBH_4$] = 0.550 M).

  TEM: D = 2.69 ± 0.58 nm.

  XRD: 46º

  XPS: Co^0, 6%; Co^{2+}, 94%.

  TGA: Temperature ºC/Δ wt. % (attribution); 102/-3.17 (solvent); 253/-1.64 (polymer low); 900end/+0.17.

  ICP: Co, 73.7 wt%, B, 7.3 wt%; Co/B atom ratio, 2.02

  FTIR: 3428, 2925, 1619, 684 cm^{-1}.

  RAMAN: 664 cm^{-1}.

- **Co6c:** was synthesized according to the general procedure using $CoCl_2 \cdot 6H_2O$ (0.226 g, 0.931 mmol) in presence of **Polymer6** (6.680 g of 50 wt% sln. of poly(methacrylicacid) sodium salt, **Polymer6**:Co=40) dissolved in 50 ml of deionized water ([Co] = 0.018 M). $NaBH_4$ (0.358 g, 9.369 mmol) was dissolved in 16.6 ml ([$NaBH_4$] = 0.550 M).

  TEM: D = 1.91 ± 0.56 nm.

Immobilization of colloidal cobalt nanoparticles on TiO_2 (Co1-6/TiO_2)

55 mg approximately of the isolated CoNPs were re-suspended in 20ml of hexane and sonicated during 3 minutes. Separately, a suspension of TiO_2 (0.2-0.5 g of 20 nm nanopowder, Degusa P25, 35-65 m^2/g) in 40 ml of hexane was firstly sonicated during 1min and then mechanically stirred. The amount of TiO_2 was the corresponding to obtain a 10 wt% Co catalyst. Then the suspension of CoNPs in hexane was added dropwise over the stirred suspension of TiO_2 and the resultant stirred during 30 min more. The grey suspension was then sonicated during 3min to homogenize the dispersion of the CoNPs on the support and the solid was magnetically precipitated, the hexane removed and the solid dried under vacuum.

Since the catalyst were powders too fine to be suitable for the micro-fixed bed reactor, they were pelletized using a press then crushed and sieved to get grain sizes between the 0.300 - 0.150 mm. The obtained materials were then used for catalytic testing.

Fischer-Tropsch catalytic experiments in water using the colloidal catalysts (Co1-6)

Catalytic experiments were performed according to reported methods.[35] Fischer-Tropsch reactions using the colloidal catalysts were carried out in a 100 ml stirred tank reactor operated in bath mode. A suitable amount of isolated CoNPs (*ca.* 0.60 mg corresponding to *ca.* 1 mmol of Co) were redispersed in 66 ml of water, and placed inside a Teflon liner in the autoclave. The autoclave was purged three times with Ar, and sealed at an Ar pressure of 1.5 bar. Additionally, 10 bar CO and 20 bar H_2 were added giving a final pressure of 31.5 bar (H_2:CO:Ar = 2:1:0.15). Then the autoclave was heated at 180 ºC under mechanical stirring at 1000 rpm during 12 h. After reaction the autoclave was cooled to room temperature prior to gas analysis. All the components contained in the gas phase (CO, H_2, Ar, CO_2, and C_{1-8} hydrocarbons) were analyzed by GC-TCD and the quantification was performed using calibration curves for each component. The compounds present in the aqueous phase were extracted with dichloromethane (10 ml) containing 1 µl of bicyclohexyl as internal standard. The organic phase containing the hydrocarbon and oxygenated products were analyzed by GC-MS. The identification and quantification of products was performed by comparison with standards using calibration curves for each compound.

Fischer-Tropsch catalytic experiments using the TiO_2 supported catalysts (Co1-6/TiO_2)

Carbon monoxide hydrogenation was carried out in a Flowrence high throughput unit[36] equipped with 16 parallel milli-fixed reactors (d_{int} = 2 mm) operating at a total pressure of 20 bar, H_2/CO = 2 molar ratio and GHSV = 6700 cm^3/g h. The catalyst loading was 100 mg. Prior to the catalytic test,

all the samples were activated in a flow of pure hydrogen at atmospheric pressure during 10 h at 673 K with at GHSV = 2 NL h^{-1} g^{-1}. During the reduction, the temperature ramp was 1 K/min. After the reduction, the catalysts were cooled down to 433 K and a flow of premixed syngas was gradually introduced through the catalysts. When pressure attained 20 bar, the temperature was slowly increased to 513 K with a ramp of 1 K/min. Gaseous reaction products were analyzed by on-line gas chromatography. Analysis of permanent gases was performed using a Molecular Sieve column and a thermal conductivity detector. Carbon dioxide and C_1–C_4 hydrocarbons were separated in a PPQ column and analyzed by a thermoconductivity detector. C_5–C_{12} hydrocarbons were analyzed using CP-Sil5 column and a flame-ionization detector. The carbon monoxide contained 5% of helium, which was used as an internal standard for calculating carbon monoxide conversion. Catalytic rates and selectivities were measured at the steady-state regime after 46 h time-on-stream.

The reaction rates expressed in cobalt-time yield h^{-1}, are defined as the moles of CO converted per mol of Co per hour. The product selectivity (*S*) is reported as the wt% of a given product.

VII.6. Acknowledgements

The authors are grateful to Total S.A., the Spanish Ministerio de Economía y Competitividad (CTQ2013-43438-R, and *Ramon y Cajal* fellowship to C. Godard) and the Generalitat de Catalunya (2014SGR670) for financial support. We acknowledge with thanks the collaboration with Prof. Andrei Khodakov and Dr. Vitaly Ordomsky from the Universite Lille 1 and UCCS in relation to the experiments with supported catalysts.

VII.7. References

[1] (a) A. Steynberg; Dry., M.; Elsevier, 152: 2006.(b) *Fischer-Tropsch synthesis, catalysts and catalysis*; B.H. Davis; Occelli, M. L., Eds.; Elsevier, 163, 2007.(c) Zhang, Q.; Kang, J.; Wang, Y. *ChemCatChem* **2010**, *2*, 1030-1058.

[2] Calderone, V. R.; Shiju, N. R.; Curulla-Ferré, D.; Chambrey, S.; Khodakov, A.; Rose, A.; Thiessen, J.; Jess, A.; Rothenberg, G. *Angew. Chem. Int. Ed.* **2013**, *52*, 4397-4401.

[3] Gual, A.; Godard, C.; Castillón, S.; Curulla-Ferré, D.; Claver, C. *Catal. Today* **2012**, *183*, 154-171.

[4] Ott, L. S.; Finke, R. G. *Coord. Chem. Rev.* **2007**, *251*, 1075-1100.

[5] Quek, X.-Y.; Pestman, R.; van Santen, R. A.; Hensen, E. J. M. *ChemCatChem* **2013**, *5*, 3148-3155.

[6] (a) Llop Castelbou, J.; Bresó-Femenia, E.; Blondeau, P.; Chaudret, B.; Castillón, S.; Claver, C.; Godard, C. *ChemCatChem* **2014**, *6*, 3160-3168 .(b) Wang, X.; Sonström, P.; Arndt, D.; Stöver, J.; Zielasek, V.; Borchert, H.; Thiel, K.; Al-Shamery, K.; Bäumer, M. *J. Catal.* **2011**, *278*, 143-152.

[7] Choi, H. R.; Woo, H.; Jang, S.; Cheon, J. Y.; Kim, C.; Park, J.; Park, K. H.; Joo, S. H. *ChemCatChem* **2012**, *4*, 1587-1594.

[8] Liu, L.; Sun, G.; Wang, C.; Yang, J.; Xiao, C.; Wang, H.; Ma, D.; Kou, Y. *Catal. Today* **2012**, *183*, 136-142.

[9] Fan, X.-B.; Tao, Z.-Y.; Xiao, C.-X.; Liu, F.; Kou, Y. *Green Chem.* **2010**, *12*, 795-797.

[10] Wang, H.; Zhou, W.; Liu, J.-X.; Si, R.; Sun, G.; Zhong, M.-Q.; Su, H.-Y.; Zhao, H.-B.; Rodriguez, J. A.; Pennycook, S. J.; Idrobo, J.-C.; Li, W.-X.; Kou, Y.; Ma, D. *J. Am. Chem. Soc.* **2013**, *135*, 4149-4158.

[11] Wang, H.; Kou, Y. *Chin. J. Catal.* **2013**, *34*, 1914-1925.

[12] Scariot, M.; Silva, D. O.; Scholten, J. D.; Machado, G.; Teixeira, S. R.; Novak, M. A.; Ebeling, G.; Dupont, J. *Angew. Chem. Int. Ed.* **2008**, *47*, 9075-9078.

[13] Silva, D. O.; Scholten, J. D.; Gelesky, M. A.; Teixeira, S. R.; Dos Santos, A. C. B.; Souza-Aguiar, E. F.; Dupont, J. *ChemSusChem* **2008**, *1*, 291-294.

[14] (a) Chen, Y.; Liew, K. Y.; Li, J. *Appl. Surf. Sci.* **2009**, *255*, 4039-4044.(b) Chou, K.-S.; Chang, Y.-C.; Chiu, L.-H. *Ind. Eng. Chem. Res.* **2012**, *51*, 4905-4910.(c) Seoudi, R.; Shabaka, A.; El Sayed, Z. A.; Anis, B. *Physica E* **2011**, *44*, 440-447.

[15] Lu, L. T.; Tung, L. D.; Robinson, I.; Ung, D.; Tan, B.; Long, J.; Cooper, A. I.; Fernig, D. G.; Thanh, N. T. K. *J. Mater. Chem.* **2008**, *18*, 2453-2458.

[16] Reetz, M. T. In *Nanoparticles and Catalysis*; Wiley-VCH Verlag GmbH & Co. KGaA: 2008, p 253-277.

[17] Shimmin, R. G.; Schoch, A. B.; Braun, P. V. *Langmuir* **2004**, *20*, 5613-5620.

[18] Bezemer, G. L.; Bitter, J. H.; Kuipers, H. P. C. E.; Oosterbeek, H.; Holewijn, J. E.; Xu, X.; Kapteijn, F.; van Dillen, A. J.; de Jong, K. P. *J. Am. Chem. Soc.* **2006**, *128*, 3956-3964.

[19] (a) Garcia-Torres, J.; Vallés, E.; Gómez, E. *J. Nanopart. Res.* **2010**, *12*, 2189-2199.(b) Petit, C.; Wang, Z. L.; Pileni, M. P. *J. Phys. Chem. B* **2005**, *109*, 15309-15316.

[20] (a) Mitov, M.; Popov, A.; Dragieva, I. *J. Appl. Electrochem.* **1999**, *29*, 59-63.(b) Patel, N.; Fernandes, R.; Miotello, A. *J. Catal.* **2010**, *271*, 315-324.

[21] Glavee, G. N.; Klabunde, K. J.; Sorensen, C. M.; Hadjipanayis, G. C. *Langmuir* **1993**, *9*, 162-169.

[22] Khodakov, A. Y.; Chu, W.; Fongarland, P. *Chem. Rev.* **2007**, *107*, 1692-1744.

[23] (a) Doan, N.; Kontturi, K.; Johans, C. *J. Colloid Interface Sci.* **2010**, *350*, 126-131.(b) Dobbrow, C.; Schmidt, A. M. *Beilstein J. Nanotechnol.* **2012**, *3*, 75-81.(c) Zhang, X.-H.; Ho, K. M.; Wu, A.-H.; Wong, K. H.; Li, P. *Langmuir* **2010**, *26*, 6009-6014.

[24] (a) Carenco, S.; Portehault, D.; Boissière, C.; Mézailles, N.; Sanchez, C. *Chem. Rev.* **2013**, *113*, 7981-8065.(b) Glavee, G. N.; Klabunde, K. J.; Sorensen, C. M.; Hadjipanayis, G. C. *Inorg. Chem.* **1993**, *32*, 474-477.

[25] Arzac, G. M.; Rojas, T. C.; Fernández, A. *ChemCatChem* **2011**, *3*, 1305-1313.

[26] Demirci, U. B.; Miele, P. *Phys. Chem. Chem. Phys.* **2014**, *16*, 6872-6885.

[27] Dragieva, I.; Gavrilov, G.; Buchkov, D.; Slavcheva, M. *J. Less Common Met.* **1979**, *67*, 375-379.

[28] (a) Linderoth, S. r.; Mo/rup, S. *J. Appl. Phys.* **1991**, *69*, 5256-5261.(b) Wang, Y.; Wu, H.; Zhang, Q.; Tang, Q. *Micropor. Mesopor. Mat.* **2005**, *86*, 38-49.(c) Yiping, L.; Hadjipanayis, G. C.; Sorensen, C. M.; Klabunde, K. J. *J. Magn. Magn. Mater.* **1989**, *79*, 321-326.

[29] Golas, P. L.; Louie, S.; Lowry, G. V.; Matyjaszewski, K.; Tilton, R. D. *Langmuir* **2010**, *26*, 16890-16900.

[30] Khodakov, A. Y.; Chu, W.; Fongarland, P. *Chem. Rev.* **2007**, *107*, 1692-1744.

[31] Li, J.; Coville, N. J. *App. Catal. A-Gen* **1999**, *181*, 201-208.

[32] (a) Saeys, M.; Tan, K. F.; Chang, J.; Borgna, A. *Ind. Eng. Chem. Res.* **2010**, *49*, 11098-11100.(b) Tan, K. F.; Chang, J.; Borgna, A.; Saeys, M. *J. Catal.* **2011**, *280*, 50-59.

[33] Lillebø, A. H.; Patanou, E.; Yang, J.; Blekkan, E. A.; Holmen, A. *Catal. Today* **2013**, *215*, 60-66.

[34] Quek, X.-Y.; Guan , Y.; van Santen, R. A.; Hensen, E. J. M. *ChemCatChem* **2011**, *3*, 1735-1738.

[35] Gual, A.; Delgado, J. A.; Godard, C.; Castillón, S.; Curulla-Ferré, D.; Claver, C. *Top. Catal.* **2013**, *56*, 1208-1219.

[36] http://avantium.com/catalysis/R-D-solutions/systems/Flowrence.html.

Supporting Information for:

Fischer-Tropsch Synthesis Over Cobalt Nanoparticles Prepared by Sodium Borohydride Reduction: Effect of the Polymeric Stabilizer

Materials and Methods

All syntheses of CoNPs were carried under aerobic conditions using a mechanical stirrer. Milli-Q water was used for all the experiments. Solvents were purchased from Merck and used as received. $CoCl_2 \cdot 6H_2O$, $NaBH_4$ and the polymers were purchased from Sigma-Aldrich. Hydrogen (5.0) was purchased from Air Liquide and CO (4.7) and argon (5.0) from Carburos Metálicos.

Transmission electron microscopy (TEM) measurements were performed at the "Unitat de Microscopia dels Serveis Cientificotècnics de la Universitat Rovira I Virgili" in Tarragona with Zeiss 10 CA electron microscope operated at 100 kV with resolution of 3 Å. High resolution electron microscopy (HRTEM) measurements were performed at the "Centres Científics i Tecnològics de la UB" in Barcelona with a JEOL 2011(FEG) electron microscope operated at 200 kV with a point resolution of 2 Å.

XRD measurements were made using a Siemens D5000 diffractometer (Bragg-Brentano parafocusing geometry and vertical θ-θ goniometer) fitted with a curved graphite diffracted-beam monochromator, incident and diffracted -beam Soller slits, a 0.06º receiving slit and scintillation counter as a detector. The angular 2θ diffraction range was between 25 and 120º. The data were collected with an angular step of 0.05º at 16s per step and sample rotation. A low background Si(510) wafer was used as sample holder. $Cu_{k\alpha}$ radiation was obtained from a copper X-ray tube operated at 40 kV and 30 mA.

XPS experiments were performed in a PHI 5500 Multitechnique System (from Physical Electronics) with a monochromatic X-ray source (Aluminium Kalfa line of 1486.6 eV energy and 350 W), placed perpendicular to the analyzer axis and calibrated using the 3d5/2 line of Ag with a full width at half maximum (FWHM) of 0.8 eV. The analized area was a circle of 0.8 mm diameter, and the selected resolution for the spectra was 187.5eV of Pass Energy and 0.8 eV/step for the general spectra and 23.5 eV of Pass Energy and 0.1 eV/step for the spectra of the different elements in the depth profile spectra. A low energy electron gun (less than 10 eV) was used in order to discharge the surface when necessary. All Measurements were made in a ultra high vacuum (UHV) chamber pressure between $5x10^{-9}$ and $2x10^{-8}$ torr.

FTIR spectra were acquired from KBr discs on a Bruker Equinox 55 Spectrometer using Opus software. Raman spectra was acquired by scattering of a 514nm Ar lamp on a Renishaw InVia Raman microscope using a x50LW objective, 60s of exposition time and 100% of laser intensity.

Thermogravimetric analysis (TGA) were performed at the "Centres Científics i Tecnològics de la UB" in Barcelona with a thermobalance (Mettler TGA/SDTA851e) equipped with a gas flow system. A 2-6 mg sample was heated in an alumina crisol in a flow of nitrogen. Then the catalyst was heated under a 50 ml/min of nitrogen flow from 30 ºC to 900 ºC (heat rate: 10 ºC/min).

Temperature programmed reduction under H_2 (TPR) was carried out using a ChemBET TPR/TPD (Quantachrome). The catalyst (0.1 g) was mounted in a quartz cell and heated up to 900 ºC in a flow of 5% H_2/Ar (30 cm^3min^{-1}). The rate of temperature ramp was 10 ºC min^{-1}.

GC-TCD analyses were carried out on an Agilent 7890A GC using a system with three columns: Hayesep Q (3ft x 1/8 in), HP-Molesieve (30m x 0.320 mm x 12 µm) and HP-Plot/Q (30m x 0.320 mm x 20 µm) using helium as carrier gas. GC-MS analyses were performed on a 9575C MSD system (Agilent) using a HP-Innowax capillary column (30m x 0.250 mm x 0.15 µm), using helium as carrier gas. Standard reference of gases (CO, CO_2, H_2, N_2) and hydrocarbons (C_1-C_5) was purchased from Avello Linde.

TEM characterization

Immediately after each synthesis, 100 µl of the colloidal solution of CoNPs was centrifuged at 600 rpm during 5 minutes. The supernatant was removed and the CoNPs then washed with deionized water and re-dispersed by 1 min of sonication. The colloidal solution was appropriately diluted with deionized water to obtain a pale grey solution. Then, three drops of the obtained colloidal solution was deposited on a Cu-formvar grid and the grid was dried during 24 h prior TEM analysis. The TEM measurements were performed on a Zeiss 10 CA electron microscope operated at 100 kV with resolution of 3 Å. The particles size distributions were determined by a manual analysis of enlarged images. At least 200 particles on a given grid were measured in order to obtain a statistical size distribution. Nanoparticle mean diameter was estimated using Gaussian analysis.

Product analysis

All the hydrocarbon products were identified by comparison with reference samples.

The components contained in the gas phase (CO, H_2, Ar, CO_2, and C_1-C_8 hydrocarbons) were analysed on a Agilent 7890A GC using a system of three columns: Hayesep Q (3ft x 1/8 in), HP-Molesieve (30m x 0.320 mm x 12 µm) and HP-Plot/Q (30m x 0.320 mm x 20 µm) using helium as carrier gas. The quantification was carried out using calibration curves

for each gas. Mixtures at different concentration of gases were prepared by gas blending from a standard reference of gases (Avello Linde).

The compounds present in the aqueous phase were extracted with dichloromethane (10 ml) containing 1µl of bicyclohexyl as internal standard. The bottom organic phase containing the hydrocarbon and oxygenated products were analysed immediately by GC-MS on a 9575C MSD system using a using a HP-Innowax capillary column (30m x 0.250 mm x 0.15 µm), and helium as carrier gas.

The identification and quantification of products was performed by comparison with standards using calibration curves for each compound.

Activity and Selectivity Calculations

The activity and selectivity was calculated based on the number of moles of carbon being formed as products according to the following formulas:

$$\text{Cobalt time yield} = \frac{\text{mol of CO converted}}{\text{mol of Co} * \text{reaction time (h)}}$$

$$\text{Selectivity } Cn = \frac{\text{Wt } C_n}{\text{Wt of all products}} \; x \; 100$$

Figure S1. Size histograms and TEM micrographs of **Co1-6** NPs.

Co1a (3.13 ± 1.58 nm) **Co1b** (2.64 ± 0.92 nm) **Co1c** (2.11 ± 0.41 nm)

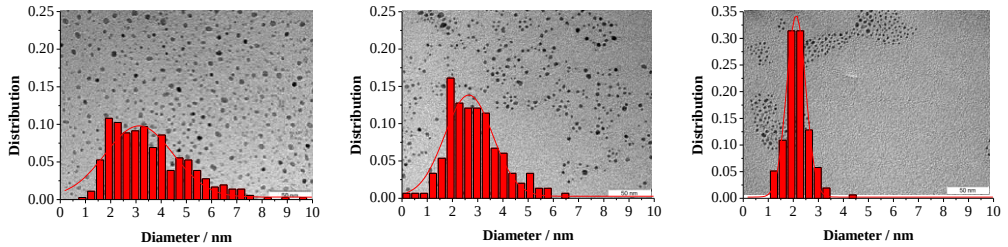

Co2a (6.73 ± 1.58 nm) **Co2b** (2.74 ± 0.75 nm) **Co2c** (1.84±0.74 nm)

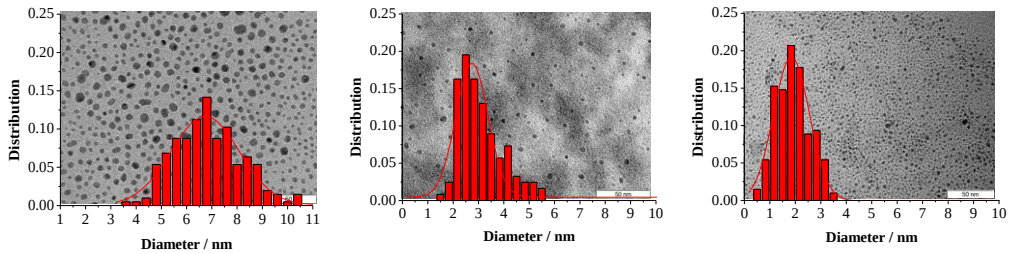

Co3a (3.26 ± 1.12 nm) **Co3b** (2.83 ± 0.98 nm) **Co3c** (1.67 ± 0.46 nm)

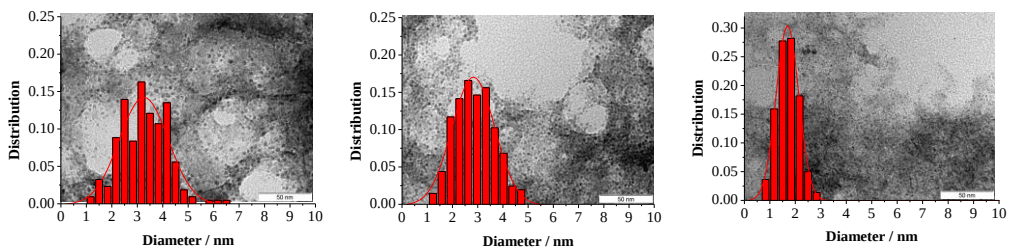

Co4a (4.12 ± 1.58 nm) **Co4b** (2.75 ± 0.57 nm) **Co4c** (1.61 ± 0.67 nm)

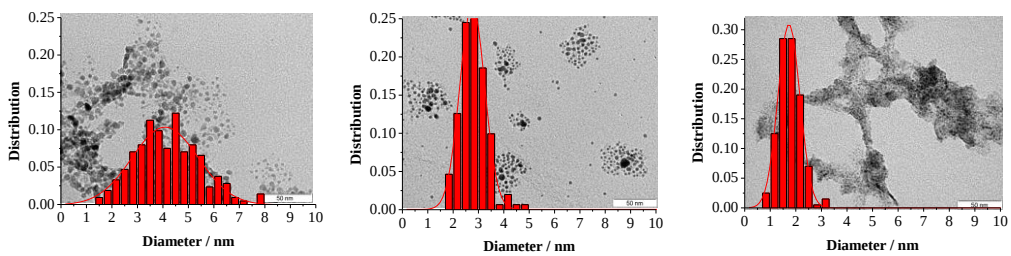

Co5a (2.55 ± 0.49 nm)

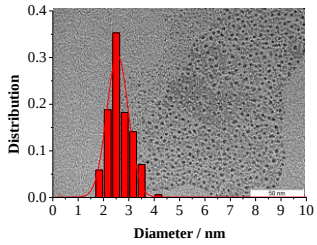

Co5b (2.07±0.68 nm)

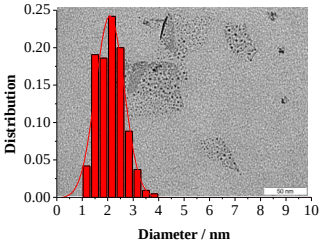

Co5c (1.69 ± 0.51 nm)

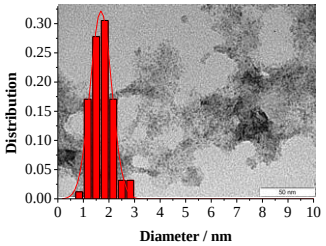

Co6a (4.92 ± 1.15 nm)

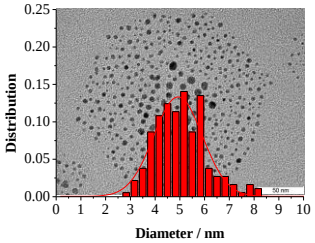

Co6b (2.69 ± 0.58 nm)

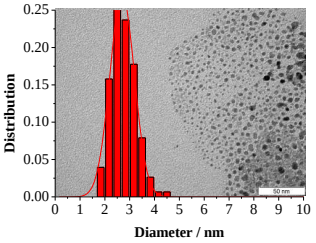

Co6c (1.91 ± 0.56 nm.)

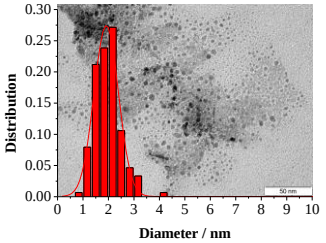

Figure S2. Co 2p XPS spectra of **Co1-6** CoNPs (1) before and (2) after catalysis.

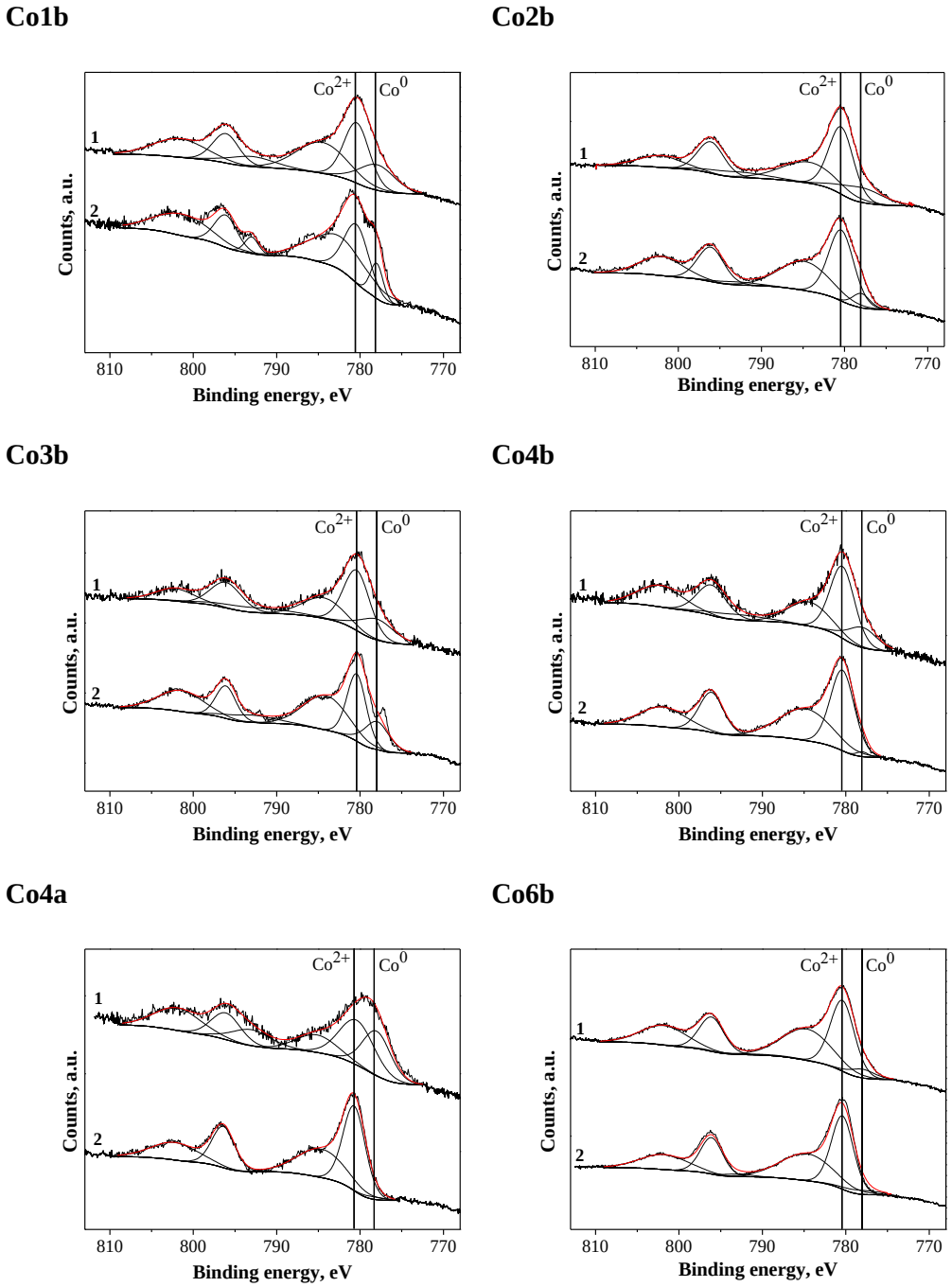

Figure S3. B 1s XPS spectra of **Co1-6** CoNPs (1) before and (2) after catalysis.

Co1b

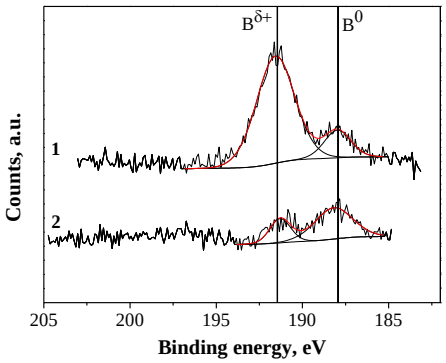

Co2b

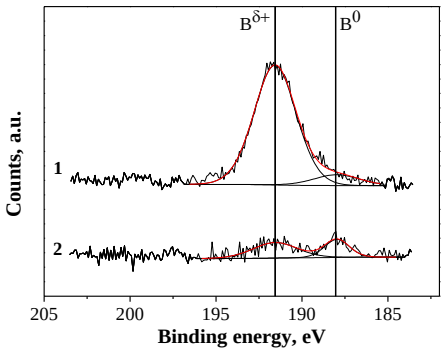

Co3b

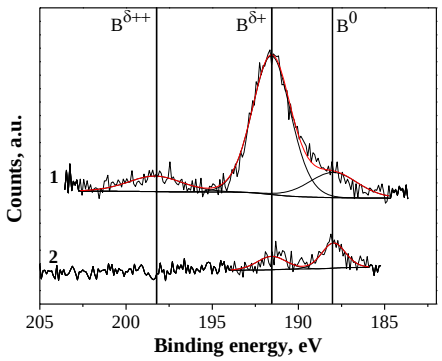

Co4b

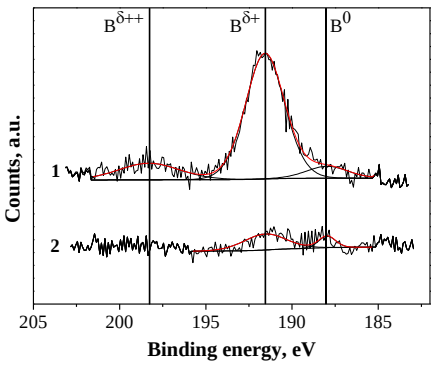

Co4a

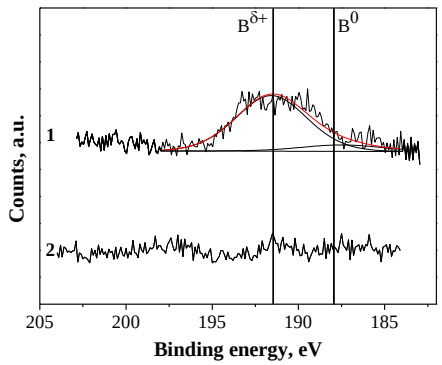

Co6b

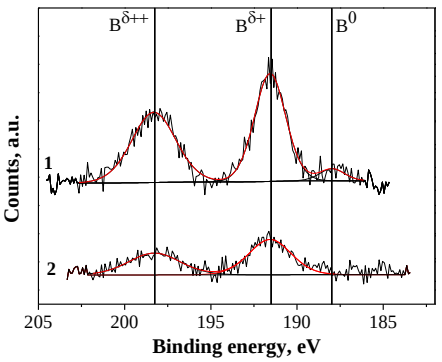

Table S1. Percentage of Co^0 and B^0 species in Co1-6 NPs for fresh and used catalysis, from XPS spectra decomposition.[a]

Catalyst	Polymer	Co^0			B^0		
		Fresh	Used	Δ%	Before	After	Δ%
Co1b	1	37	24	-13	15	70	+55
Co2b	2	28	12	-16	9	39	+30
Co3b	3	31	35	+4	16	61	+45
Co4b	4	25	3	-22	8	23	+15
Co5a	5	67	3	-64	12	0	-12
Co6b	6	6	4	-2	4	0	-4

[a] Percentages corresponding to the Co $2p_{3/2}$ and B 1b spin orbit peaks.

Figure S4. (a) Full XPS and **(b)** C1s XPS spectra of **Co1-6** NPs.

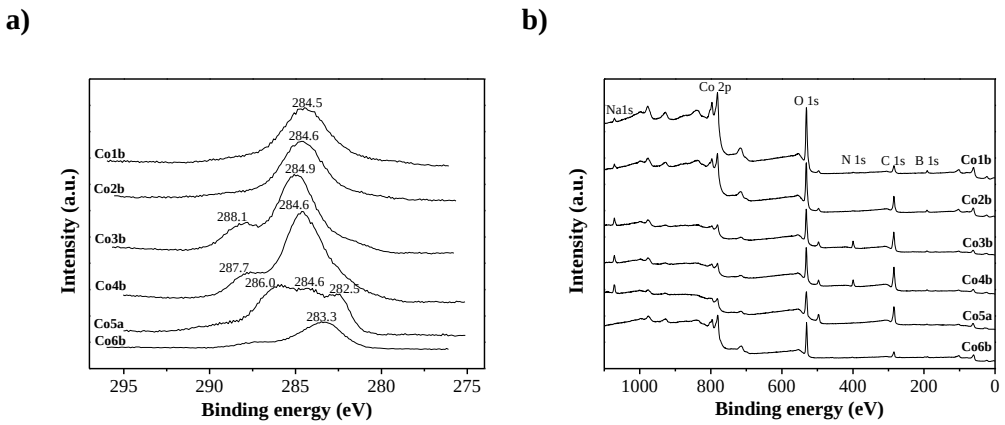

Table S2. Elemental quantification by XPS of fresh **Co1-6** NPs.

		Quantification regions (%Atom)						
NPs	Polymer	Na 1s	C 1s	N 1s	O 1s	Co 2p	B 1s	Co/B
Co1b	1		20.9		48.6	18.0	12.5	1.4
Co2b	2	1.5	39.9	0.9	39.7	8.8	9.3	1.0
Co3b	3	2.0	51.7	8.9	27.7	2.3	7.5	0.3
Co4b	4	1.8	58.6	7.6	25.9	2.0	4.1	0.5
Co5a	5	3.0	62.0		30.2	2.4	2.4	1.0
Co6b	6		27.0	1.7	44.2	14.0	13.1	1.1

Table S3. Elemental quantification by XPS of **Co1-6** NPs after AFTS.

		Quantification regions (%Atom)						
NPs	Polymer	Na 1s	C 1s	N 1s	O 1s	Co 2p	B 1s	Co/B
Co1b	1		54.9	2.4	31.6	9.0	2.1	4.3
Co2b	2		40.9	1.1	41.7	15.5	0.8	20.6
Co3b	3		50.5	1.3	36.3	11.9		
Co4b	4		34.3	0.9	46.2	17.7	0.9	19.7
Co5a	5		62.4	0.4	32.9	4.3		
Co6b	6		28.6		50.9	17.7	2.8	6.3

Table S4. Microanalysis by Energy-dispersive X-ray spectroscopy, EDX (%Mass)

		Element/ shell					
NPs	Polymer	C K	O K	Co K	Na K	Cl K	N K
Co1b	1	36.5	33.1	30.5			
Co2b	2	17.9	48.4	31.1	2.7		
Co3b	3	41.4	34.9	7.4	2.5	0.1	13.1
Co4b	4	34.1	38.9	21.7	2.6		
Co5a	5	48.1	17.4	34.5			

Figure S5. Raman spectra of **Co1-6**. Spectra acquired by scattering of a 514 nm Ar lamp

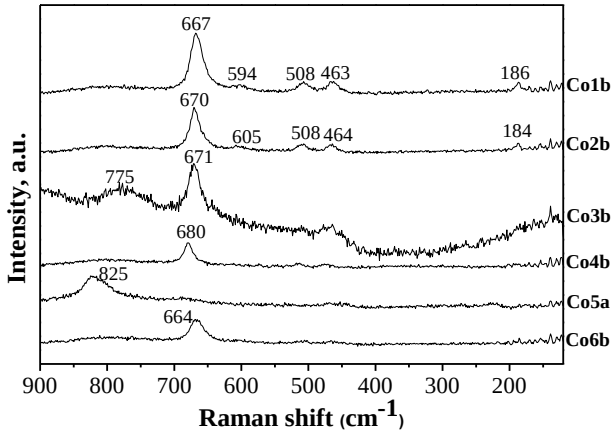

Figure S6. FTIR spectra of **Polymers1-6** (1) and its corresponding CoNPs, **Co1-6** (2)

Co1a

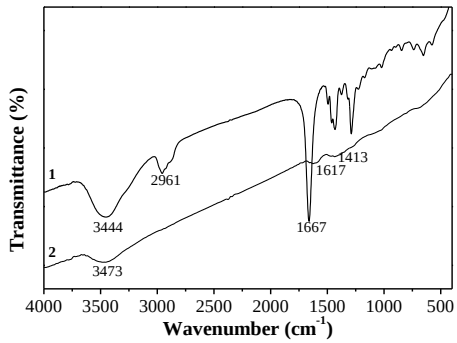

Co2b

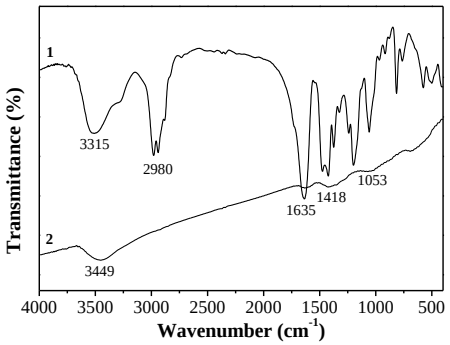

Co3b

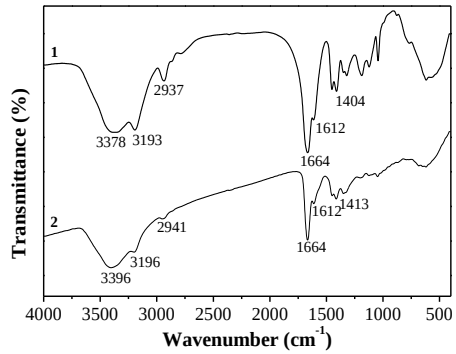

Co4b

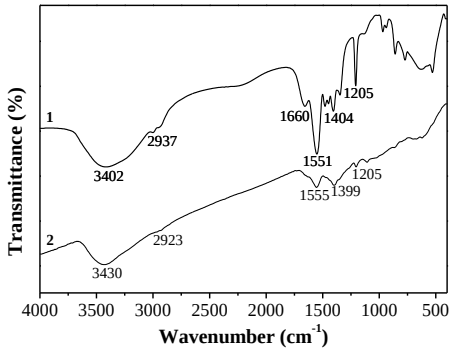

Co5a

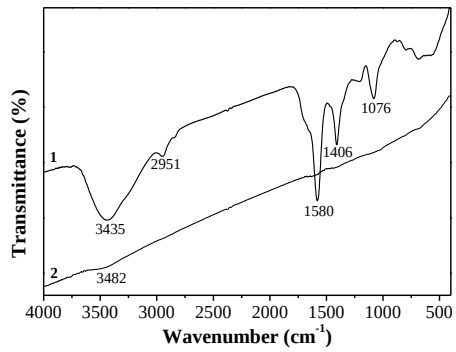

Co6b

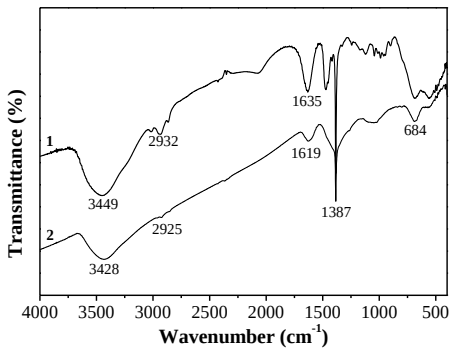

Figure S7. TGA thermograms under nitrogen flux of **Polymers1-6** (1) and its corresponding CoNPs, **Co1-6** (2)

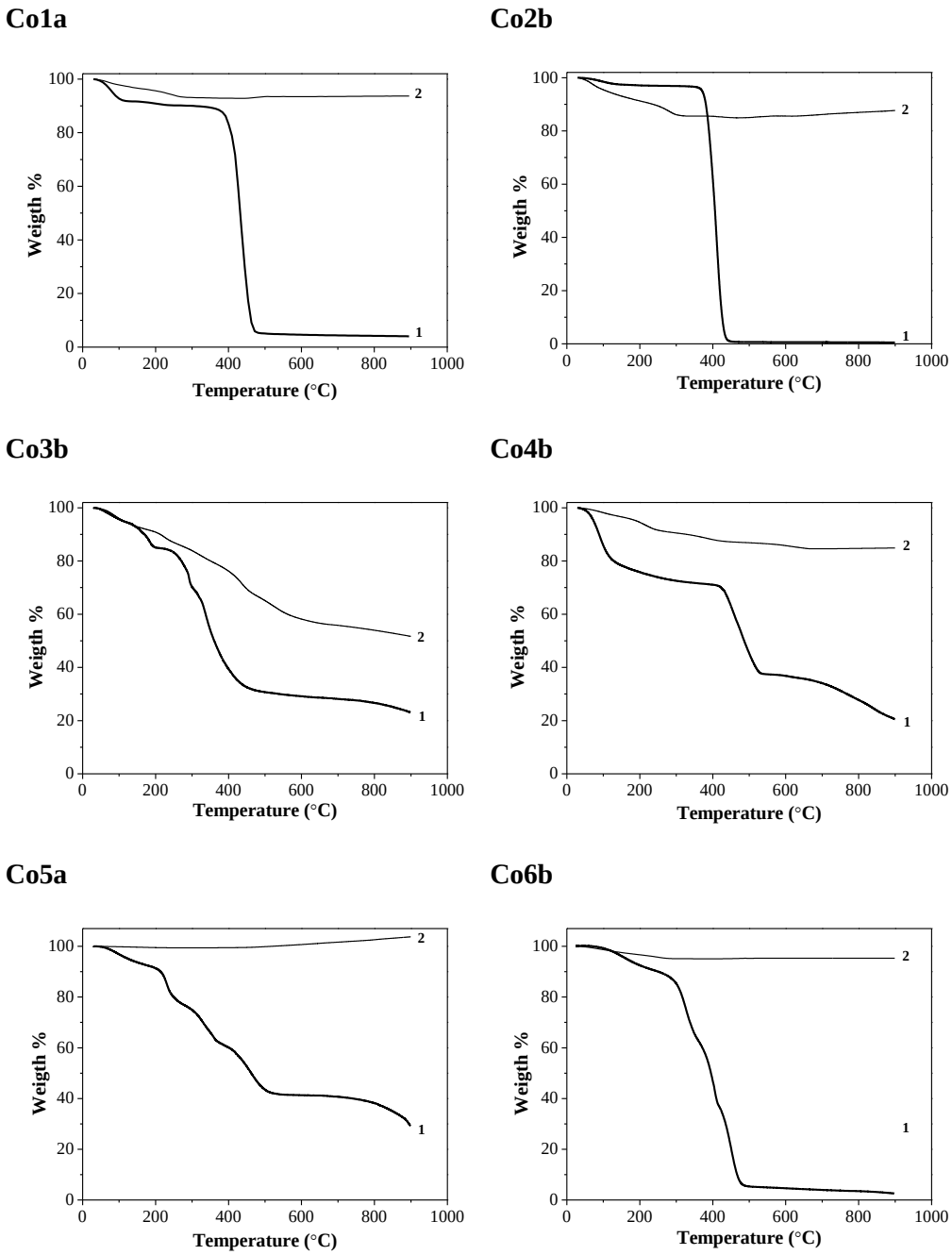

Table S5. Thermal stability properties of **Polymers 1-6** measured by TGA.

Entry	Polymer	T. dec.	Residue at 900ºC
1	1	435	4
2	2	407	1
3	3	290-340	31
4	4	468	45
5	5	136-462	42
6	6	328-449	6

Figure S8. (a) XRD patterns of TiO_2 supported catalysts after a calcination process: (1) **Co1b/TiO_2**; (2) **Co2b/TiO_2**; (3) **Co3b/TiO_2**; (4) **Co4b/TiO_2**; (5) **Co5a/TiO_2**; and (6) **Co6b/TiO_2**. In dotted line the peak of 31.2 used for particle size estimation of Co_3O_4. **(b)** Amplification of dotted region from a.

a) **b)**

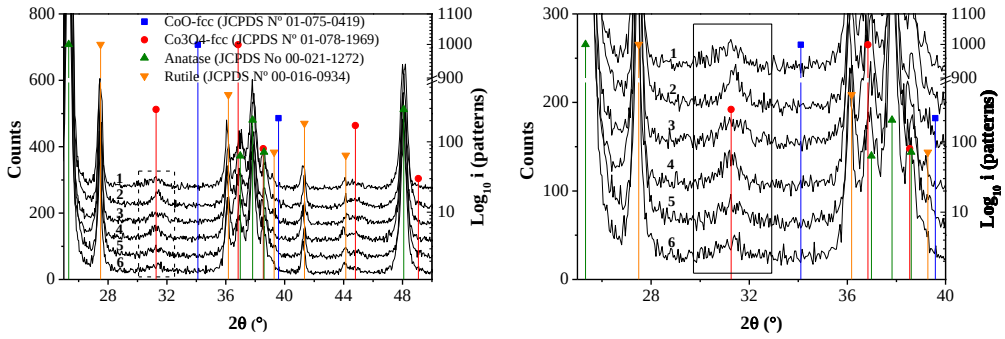

Figure S9. Co 2p XPS spectra of **Co1-5/TiO_2** catalysts.

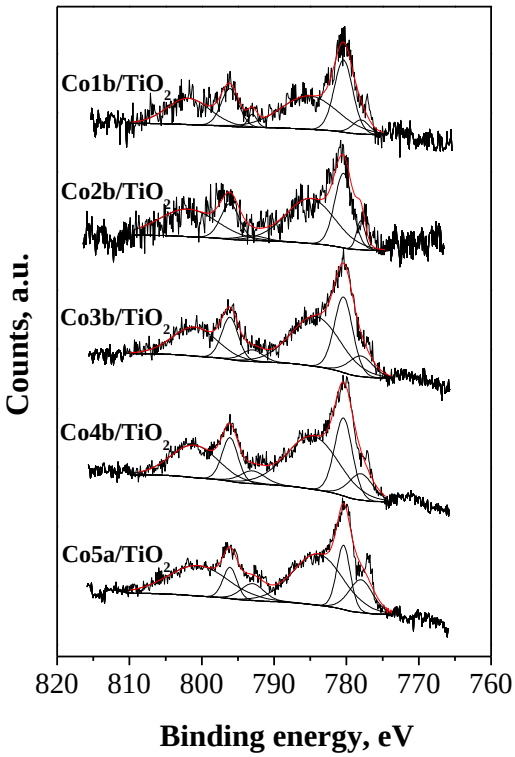

Table S6. Percentage of Co species from XPS spectra decomposition[a]			
Catalyst	Polymer	Co^0	Co^{2+}
Co1b/TiO_2	1	15	85
Co2b/TiO_2	2	16	84
Co3b/TiO_2	3	26	74
Co4b/TiO_2	4	31	69
Co5a/TiO_2	5	48	52
Co6b/TiO_2	6	*	*

[a] Percentages corresponding to the Co $2p_{3/2}$ spin orbit peaks.

Figure S10. Co 2p XPS spectra of **Co1b/TiO$_2$** (1) freshly synthesized; (2) reduced under H_2 at 400ºC during 10h and (3) after FTS in fixed bed.

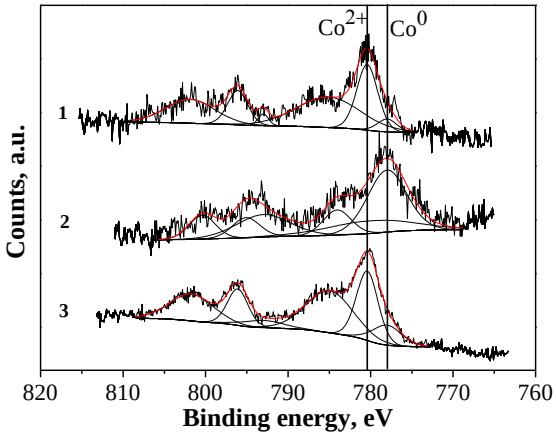

Table S7. Percentage of Co species in supported catalysts from XPS spectra decomposition.[a]		
Catalyst	Co^0	Co^{2+}
Co1b/TiO_2	15	85
Co1b/TiO_2[b]	69	31
Co1b/TiO_2[c]	28	72

[a] Percentages corresponding to the Co $2p_{3/2}$ spin orbit peaks. [b] Reduced under H_2 at 400ºC during 10h. [c] After FTS in fixed bed.

Table S8. BET surface area and Co loadings measured by ICP of supported catalysts.				
			N_2 fisi. (Surf. Area)	ICP, wt%/catalyst
E.	Catalyst	Polymer	BET (m^2/g)	Co
1	Co1b/TiO_2	1	50.16	8.05
2	Co2bTiO_2	2	46.91	7.07
3	Co3b/TiO_2	3	51.89	10.61
4	Co4b/TiO_2	4	42.16	7.26
5	Co5a/TiO_2	5	52.27	6.24
6	Co6b/TiO_{22}	6	56.15	7.50
8	TiO_2[b]		43.07	

[a] Mean Co^0 particle size as estimated from the corresponding d(Co_3O_4)by applying the molar volume correction: d(Co^0) = 3/4 d(Co_3O_4). [b] According to XRD the composition of TiO_2 corresponded to 17% rutile and 83% anatase.

Table S9. Aqueous phase Fischer-Tropsch synthesis catalyzed by **Co1-6** evaluating the effect of the polymer stabilizer on the NPs.[a]

E.	Catalyst	Polymer	O/P ratio		
			O/P C_{2-12}	O/P C_{2-4}	O/P C_{5-12}
1	**Co1b**	1	0.79	1.33	0.28
2	**Co2b**	2	0.98	1.38	0.35
3	**Co3b**	3	1.26	1.90	0.43
4	**Co4b**	4	0.31	0.71	0.00
5	**Co5a**	5	1.32	1.50	0.79
6	**Co6b**	6	0.92	1.39	0.37

[a] Conditions: 0.949 mmol Co, 30 bar H_2/CO/Ar (2:1:0,15); 66ml water (100 ml autoclave), 1000rpm, 180 ºC, 12h

Figure S11. ASF distributions of **Co1-6** nanocatalysts (Y-offset).

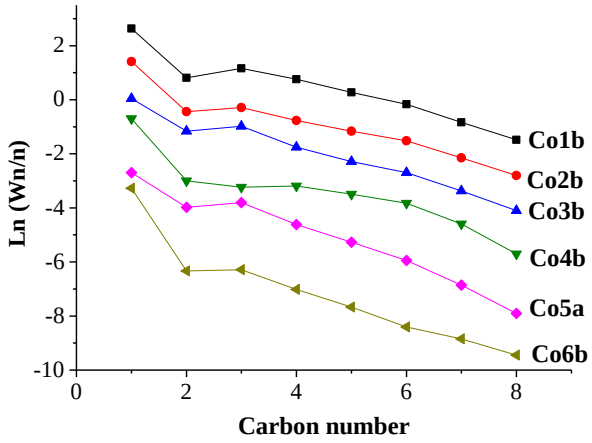

Figure S12. (**a**) Cobalt-time yield and (**b**) product selectivity in the AFTS catalyzed by **Co5** synthesized under different Polymer5:Co ratio. Conditions: 0.949 mmol Co, 30 bar H_2/CO/Ar (2:1:0,15); 66 ml water, 1000 rpm, 180 ºC, 12h.

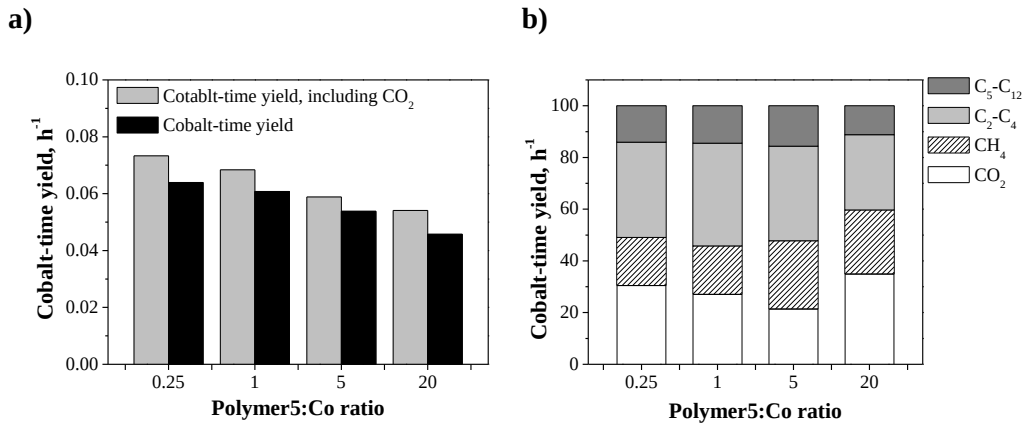

Figure S13. Effect of the temperature on (**a**) cobalt-time yield and (**b**) product selectivity in the AFTS catalyzed by **Co5**a. Conditions: 0.949 mmol Co, 30 bar H_2/CO/Ar (2:1:0,15); 66 ml water, 1000 rpm, 150-210 ºC, 12h.

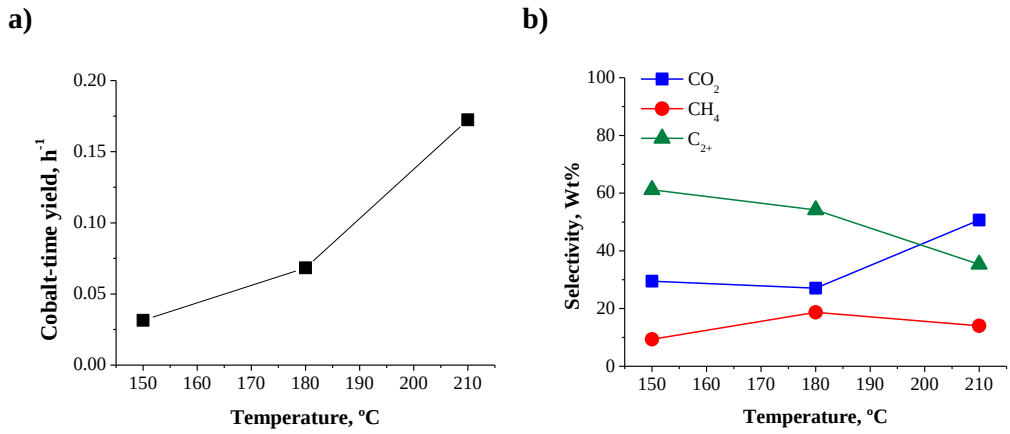

Figure S14. (**a**) Cobalt-time yield and (**b**) product selectivity in the FTS catalyzed by **Co5a** dispersed in different solvents. Conditions: 0.949 mmol Co, 30 bar H_2/CO/Ar (2:1:0,15); 66 ml water, 1000 rpm, 180 ºC, 12h.

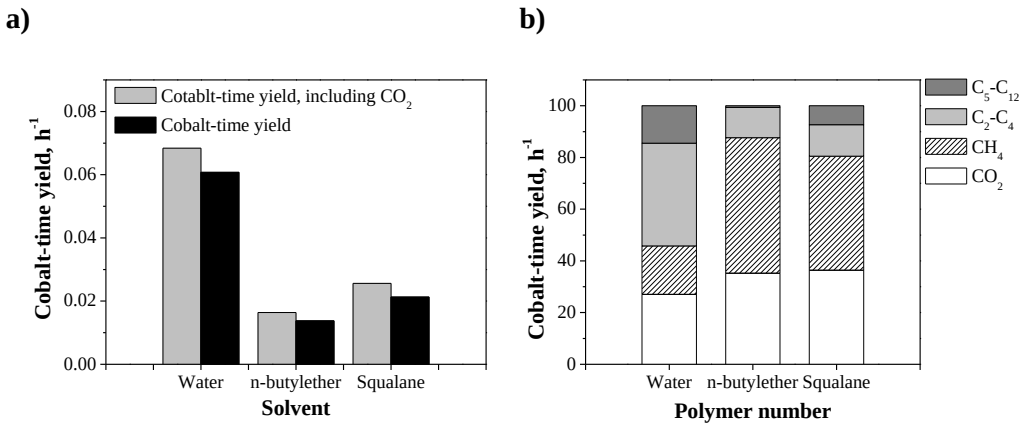

Table S10. Fischer-Tropsch synthesis in fixed bed reactor using TiO_2 supported CoNPs[a]

E.	Catalyst	Polymer	O/P ratio		
			O/P C_{2-12}	**O/P C_{2-4}**	**O/P C_{5-12}**
1	**Co1b/TiO2**	1	0.30	0.58	0.12
2	**Co2b/TiO2**	2	0.19	0.39	0.10
3	**Co3b/TiO2**	3	0	0	0
4	**Co4b/TiO2**	4	0	0	0
5	**Co5a/TiO2**	5	0.29	0.50	0.13
6	**Co6b/TiO2**	6	0.25	0.50	0.10

[a] Conditions: Catalyst loading=7-10wt%, 20 bar $H_2/CO/N_2$ (2:1:0.15), 5.62 ml/min, 240 ºC

CHAPTER VIII

Conclusions and Summary

Table of Contents

General Conclusions

A series of new polymer stabilized cobalt nanoparticles were synthesized through colloidal methodologies and their catalytic performance in the Fisher-Tropsch Synthesis was evaluated. Intrinsic properties of the cobalt nanoparticles such as the size, structure, composition, polymer stabilizer were shown to influence the catalytic performance of the nanocatalysts. Other external parameters proper of the reaction media such as the temperature, solvent, and the pH in the case of aqueous systems were demonstrated to influence strongly the activity and the selectivity of the CoNPs. Finally, similar trends in terms of activity were observed when compared the colloidal with the supported catalytic systems, thus suggesting the relevance of the nanoparticle structure in comparison to the influence of the support on the performance of the CoNPs.

Chapter IV.

This chapter focused on the Aqueous phase Fischer-Tropsch Synthesis (AFTS) catalyzed by CoNPs and the effect of NPs preparation and pH on catalyst activity and selectivity.

- Variations in the particle size (1.7 - 3.1 nm) were observed when the PVP:Co ratio varied from 10 to 80 for CoNPs synthesized by chemical reduction in water using PVP as stabilizer and $NaBH_4$ as reducing agent.
- Surface analysis of the CoNPs by XPS allowed to conclude that the oxidation degree of the CoNPs depends on the PVP:Co ratio with a higher content in metallic cobalt when high PVP:Co ratios are used during the synthesis. Analysis of the bulk and surface composition of the CoNPs revealed the presence of boron (cobalt/boron atom. ratio *ca.* 2) with certain enrichment at the metal surface. Analysis by FTIR and TGA demonstrated that after work-up, no PVP remained at the surface of the CoNPs.
- Relevant differences in activity and product selectivity were observed when *in-situ* or isolated CoNPs were tested in the AFTS. It was observed that the pH increased during the NPs synthesis, which consequently affected the catalytic

performance of the *in-situ* CoNPs. Indeed, at basic pH, the WGS activity was enhanced thus producing high amounts of H_2 and CO_2. The increase in H_2 partial pressure resulted in higher selectivity for methane while CO_2 reacts with hydroxide to form carbonate which is subsequently hydrogenated in the presence of CoNPs to form the corresponding formate. To the best of our knowledge, this is the first example of carbonate hydrogenation to formate catalyzed by CoNPs. This result opens the possibility to employ cobalt nanoparticles in the catalytic reduction of CO_2, a reaction of interest in current scientific research.

- Analysis of the used catalysts tested under neutral conditions demonstrated slight variations of the metal NPs in terms of size, structure and composition in contrast to the observed by other authors. In the present study it was observed the decrease of the boron content of the catalyst during the reaction.

Chapter V.

This chapter was dedicated to the study the effect of the addition of co-solvents in the CoNPs catalyzed AFTS.

- The addition of co-solvents such as hydrocarbons and alcohols in the AFTS catalyzed by colloidal cobalt nanoparticles strongly affects the activity, the selectivity and the distribution of the hydrocarbon products.
- It was concluded that the hydrocarbon distribution mainly depended on the solubility of syngas and on the H_2:CO ratio of the corresponding solvent, and can be tuned from light to heavy hydrocarbons with the selection of the appropriate aqueous solvent mixture.
- In hydrocarbon/water mixtures, a compromise between the high solubility of syngas in hydrocarbons and the better dispersion of the catalyst in water revealed to be crucial to reach high activity and selectivity to C_{13+} hydrocarbons. These results suggested that the presence of water can significantly shorten the chain length of the hydrocarbons produced by FTS.
- It was demonstrated that the chain length of the hydrocarbon co-solvents in the range of C_7-C_{16} not affected the selectivity but slightly the activity in AFTS.

- In alcohols, significant effects were also observed in catalysis. When the chain length of the alcoholic solvent increases, the formation of FT-acetal products progressively becomes the major process. In the case of short alcohols such as ethanol, however, high FT activity (up to 0.189 $mol_{CO}mol_{Co}^{-1}h^{-1}$) was observed with excellent product selectivity (80% hydrocarbons).

Chapter VI.

The effect of the cobalt particle size in FTS for CoNPs synthesized by borohydride reduction was dealt in this chapter.

- The size of the CoNPs synthesized by a chemical reduction methodology can be modulated between 1.7 to 7.0 nm by controlling the concentration of the $NaBH_4$ and Co/PVP solutions.
- The amorphous structure of the cobalt and cobalt oxide phases and the small size of the CoNPs were inferred from XRD analysis. Analysis of thermal treated NPs elucidated the presence of cobalt and cobalt-boron species as a function of the particle size. Surface analysis by XPS indicated the considerable oxidation degree of the NPs and its dependence with the size: more reduced CoNPs were obtained at smaller sizes. Finally, the analysis by FTIR and TGA demonstrated that there is no evidence of presence of PVP in the series of NPs, **Co1a-d**.
- TEM and TPR analysis of the TiO_2 supported catalysts demonstrated that the particle size of the CoNPs remained invariable after immobilization on TiO_2 and that the reducibility of the catalyst decreased with the particle size, respectively. The differences in reducibility probably are associated to contributions of the metallic cobalt phase as a function of the particle size.
- It was concluded that the catalytic performance of the cobalt nanoparticles prepared by borohydride reduction depended on the reduction degree and the size of the NPs, with a decrease of the activity with the particle size. This behavior has allowed us to investigate the catalytic performance of ultra-small CoNPs in the Fischer-Tropsch Synthesis, which is unique of NPs prepared by borohydride reduction.

Chapter VII.

This chapter described the effect of the stabilizing polymer on cobalt-nanoparticle-catalyzed Fischer-Tropsch Synthesis.

- The variation of the polymer:Co ratio allowed the modulation of the particle size of CoNPs for six different water soluble polymers.
- The particle sizes resulted inversely proportional to the concentration of the stabilizer. For most cases, the particle size converged in a value of *ca.* 2.6 nm when the polymer:Co ratio was 20.
- Notable differences in the fine structure, the crystallinity, the oxidation degree, the composition and the polymer content (polymer/surface interaction) were determined by HR-TEM, XRD, XPS, ICP and TGA respectively as a function of the polymer stabilizer.
- Supported catalysts were also prepared by immobilization of the colloidal NPs on TiO_2 and its reducibility evaluated by TPR.
- Both series of catalysts were tested in the AFTS and the classical FTS in fixed bed reactors and showed significant differences in the catalytic performance as a function of the polymer stabilizer.
- The reduction degree of the cobalt particles, the interaction strength between the polymer and the metal surface (defined in terms of the amount of polymer at the NPs) and boron doping were demonstrated to rule the performance of the colloidal catalysts.
- For the supported catalysts, the reducibility and the boron doping showed to be influenced by the polymer stabilizer thus affecting the catalytic performance of the catalysts.
- The outstanding catalytic performance observed for **Co5a** was attributed to a matched scenario of positive parameters: minimal polymer content and high reduction degree.

Summary

The increasing worldwide energy demand has made major companies to consider alternative feedstocks such as natural gas, coal and biomass to replace fossil fuels. In this context, the Fischer-Tropsch Synthesis (FTS) has been considered a key process of the biomass-to-liquid (BTL), gas-to-liquid (GTL) and solid-to-liquid technologies (STL) since through this catalytic reaction, syngas is transformed into high quality synthetic fuels. FTS is catalyzed by several transition metals but cobalt catalysts are more attractive from an industrial point of view.

This doctoral thesis describes the synthesis and characterization of cobalt nanoparticles and their application as colloidal and TiO_2-supported nanocatalysts in the Fischer-Tropsch synthesis.

Chapter I introduces the main concepts of the Fisher-Tropsch synthesis. The first part of this chapter describes a brief historical background of the synthetic fuels and of the Fischer-Tropsch synthesis process. General aspects of this reaction such as the thermodynamics and reaction mechanisms are also included. In the second part, the different types of cobalt catalysts reported in this reaction are discussed. First, general aspects related to cobalt based catalysts such as promoters, deactivation, effect of water and mass transfer limitations are treated. Subsequently, the most relevant methods of preparation of supported cobalt catalysts and the influence of the support on the catalytic performance in FTS are described. Finally, the use of cobalt nanoparticles as colloidal catalysts for this reaction is illustrated, with particular emphasis on their methods of preparation, types of stabilizer and catalytic performances in FTS.

Chapter II includes the general objectives of this work.

In **Chapter III,** the experimental set-up used for the catalytic experiments and the chromatographic methods that were applied for the analysis of reaction products are explained in details. It is noteworthy that a report entitled “Numerical and experimental Modelization of the two-phase mixing in a small scale vessel” that was elaborated by the group of Prof. Anton Vernet and describe a modelization study using the autoclave where the FTS experiments of this thesis were performed, is also included as Appendix IV.

In **Chapter IV**, the synthesis and characterization of colloidal CoNPs stabilized with polyvinylpyrrolidone are described and their application as nanocatalysts in the aqueous phase FT synthesis evaluated. Some parameters such as the PVP:Co ratio, the presence of base and the potential effect of the nanocatalyst size were taken under consideration in this study. Differences in the reduction degree of the CoNPs were observed when the PVP:Co ratio used during the synthesis was varied, while analysis of the bulk composition of the CoNPs revealed the presence of boron (cobalt/boron atom. ratio *ca.* 2). In FTS, a strong influence of the pH of the aqueous medium on the catalytic performance of the nanocatalysts (both activity and selectivity) was evidenced. At basic pH (> 13), the WGS was enhanced thus producing CO_2 and H_2. The CO_2 produced reacted with hydroxide producing carbonate which was subsequently hydrogenated to formate in the presence the cobalt nanoparticles. To the best of our knowledge, this is the first example of carbonate hydrogenation to formate catalyzed by CoNPs.

In **Chapter V**, our results on the effect of solvents in the AFTS catalyzed by colloidal cobalt nanoparticles are discussed. The addition of co-solvents such as hydrocarbons and alcohols strongly affected the activity, the selectivity and the distribution of the hydrocarbon products under the reaction conditions. The shift in product distribution observed was related to the variations of H_2 and CO solubility. These results demonstrated that the selectivity of this process can be tuned from light to heavy hydrocarbons with the selection of the appropriate aqueous solvent mixture. Interestingly, no effect of the chain length (C_7-C_{16}) of the hydrocarbon co-solvents was observed on the selectivity of FTS while the activity was slightly affected. The production of acetals was also observed when the reaction was performed using alcohols as solvents and such acetal selectivity became favored when the alcohol chain length was increased. In the case of short alcohols such as ethanol, however, high FT activity with excellent product selectivity was observed.

Chapter VI deals with the effects of particle size in the Fischer-Tropsch synthesis catalyzed by cobalt nanoparticles synthesized from sodium borohydride reduction. Cobalt nanoparticles of sizes between 1.7 to 7.0 nm were synthesized using a chemical reduction method by controlling the concentration of the Co/PVP

and $NaBH_4$ solutions. The CoNPs were immobilized on TiO_2 and both the colloidal and the supported catalysts were tested in the AFTS and the FTS respectively. For both systems the catalysts activity increased when the particle size of the CoNPs decreased. Furthermore, the catalytic performance of the cobalt nanoparticles prepared by borohydride reduction was shown to depend on several factors such as the boron doping, the reduction degree and the size of the NPs.

Finally, **Chapter VII** concerned the study of the effect of the polymer stabilizer on the catalytic performance of cobalt nanoparticles in the FTS. Several families of CoNPs stabilized by a series of water soluble polymers were synthesized at various polymer:Co ratios. Subsequently, some of these CoNPs were immobilized on TiO_2 and both the colloidal and the supported catalysts were tested in the AFTS and the FTS, respectively. Significant differences in the catalytic performance were observed for both sets of catalytic systems when the structure of the polymeric stabilizer was varied. The reduction degree of the cobalt particles, the amount of polymer at the NPs surface and the degree of boron doping were proposed as the most influential parameters affecting the performance of the colloidal catalysts. Similarly, the catalytic performance of the supported catalysts were interpreted in terms of the catalyst reducibility, amount of polymer stabilizer at the Co surface (and its removal ability during the reduction pretreatment) and the degree of boron doping.

Appendices

Appendix 1. Congress and Scientific Meetings

2012

- J. A. Delgado, A. Gual, C. Godard, C. Claver, S. Castillón, D. Curulla-Ferré. Synthesis of new water-soluble CoNPs and their application in the Fischer-Tropsch synthesis. *Grupo Especializado de Química Organometálica (XXXI GEQO)*. Castelló, Spain. 06/2012

- J. A. Delgado. Synthesis of water soluble Co-NPs and their application as nanocatalysts in the Fischer-Tropsch synthesis. *Synfuel 2012*. Munich, Germany. 07/2012. Oral presentation.

- J. A. Delgado. *International Congress on Catalysis (15th ICC)*. Munich, Germany. 07/2012.

2013

- J. A. Delgado, C. Godard, C. Claver, S. Castillón, D. Curulla-Ferré. Effects of the nature of colloidal CoNPs on the aqueous Fischer-Tropsch synthesis. *Natural Gas Conversion Symposium (NGCS 10)*. Doha, Qatar. 03/2013.

- J. A. Delgado, C. Godard, S. Castillón, D. Curulla-Ferré, C. Clave. Influence of the synthetic methodology for colloidal CoNPs on the aqueous Fischer-Tropsch process. *11th European Congress on Catalysis (EuropaCat-XI)*. Lyon, France. 09/2013.

2014

- J. A. Delgado, C. Godard, S. Castillón, D. Curulla-Ferré and C. Claver. Influence of the synthetic methodology and particle size of CoNPs and the reaction conditions (pH) on the aqueous Fischer-Tropsch synthesis. *Grupo Especializado de Química Organometálica (XXXII GEQO)*. Tarragona, Spain. 09/2014

Appendix 2. Stages

- **Internship Project:** "Synthesis of bimetallic nanoparticles, immobilization in solid supports and its application as catalysts in the Fischer-Tropsch synthesis in fixed bed reactors". Advised by Andrei Khodakov and Vitaly Ordomsky. Université Lille 1. 9-12/2013

Appendix 3. Publications based on the content of this thesis

- Gual, A., **Delgado, J. A.**; Godard, C.; Castillón, S.; Curulla-Ferré, D.; Claver, C. Novel polymer stabilized water soluble Ru-nanoparticles as aqueous colloidal Fischer-Tropsch catalysts. *Topics in Catalysis*, **2013**, 56, 13-14, 1208-1219.

- **Delgado, J. A.**; Godard, C.; Castillón, S.; Curulla-Ferré, D.; Claver, C. Aqueous phase Fischer-Tropsch synthesis catalyzed by Co nanoparticles: effect of NPs preparation and pH on catalyst activity and selectivity. To be submitted.

- **Delgado, J. A.**; Godard, C.; Castillón, S.; Curulla-Ferré, D.; Claver, C. Correlation between hydrocarbon products distribution and solvent composition in the colloidal Co-catalyzed Fischer-Tropsch Synthesis. To be submitted.

- **Delgado, J. A.**; Godard, C.; Castillón, S.; Curulla-Ferré, D.; Claver, C. Cobalt particle size effects in the Fischer-Tropsch synthesis: comparison between unsupported and TiO_2 supported nanocatalysts. Under preparation.

- **Delgado, J. A.**; Godard, C.; Castillón, S.; Curulla-Ferré, D.; Claver, C. Fischer-Tropsch Synthesis Catalyzed by Polymer Stabilized Co Nanoparticles: comparison between unsupported and TiO_2 supported nanocatalysts. Under preparation.

Appendix 4. Report: "Numerical and experimental Modelization of the two-phase mixing in a small scale stirred vessel"

Project developed by Sylvana Varela, Manuel Martínez, Jordi Pallarès and Anton Vernet in the "Grupo de Experimentación, Computación y Modelización en Mecánica de Fluidos y Turbulencia (ECOMMFIT)" at the Chemical Enginery Department of the URV. September of 2014.

NUMERICAL AND EXPERIMENTAL MODELIZATION OF THE TWO-PHASE MIXING IN A SMALL SCALE STIRRED VESSEL

Centre Tecnològic de la Química de Catalunya

Grupo de Experimentación, Computación y Modelización en Mecánica de Fluidos y Turbulencia

Universitat Rovira i Virgili

Sylvana Varela
Manuel Martínez
Jordi Pallarès
Anton Vernet

September 2014

NUMERICAL AND EXPERIMENTAL MODELIZATION OF THE TWO-PHASE MIXING IN A SMALL SCALE STIRRED VESSEL

Sylvana Varela Ballesta

Manuel Martínez del Álamo

Jordi Pallarès Curto

Anton Vernet Peña

CTQC
Centre Tecnològic de la Química de Catalunya
Carrer Marcel.lí Domingo, s/n
43007 Tarragona

ECoMMFiT
Experimentació, Computació i Modelització en Mecànica de Fluids i Turbulència
Departament d'Enginyeria Mecànica

Universitat Rovira i Virgili
Av. Països Catalans, 26
43007 Tarragona

Index

Page

Abstract

The main objective of this project is the prediction, using numerical simulations, of the mass transfer rate of gas components within the liquid phase in a stirred tank reactor. To reach this objective, experiments have been conducted in a transparent model of the reactor equipped with the stirrer used in the normal operation of the reactor. The visualization of the air-water two-phase flow in the model at different rotation rates of the stirrer allowed the determination of the size and number of the air bubbles, as well as the flow regime. This experimental information has been used in the numerical simulations to predict the mass transfer rates of gas components from the gas phase to the liquid phase. In particular simulations of the distribution of the liquid and gas phases at the operating conditions of the reactor were carried out and bubbles with the experimentally measured diameter were numerically tracked to determine the particle Reynolds number, which is an important parameter, together with the Schmidt number, to determine the mass transfer rates. The mass transfer rates of the gas components to the liquid phase were estimated using conventional mass transfer correlations.

Baffled and unbaffled reactor configurations were analyzed separately. It has been determined, experimentally, that the amount of bubbles inside the reactor increases with the rotation rate, while the bubble size decreases. The experimental results were compared with the ones obtained using analytical correlations for similar reactors. It has been estimated that the differences between the experiments and the predictions of correlations are about 8 %. For the unbaffled reactor an emulsion is formed for axis rotation rates between 991 and 1371 rpm, while bubbly flow remains for the baffled reactor in the whole range of rotation rates studied (up to 1721 rpm). Additionally, some

experiments for three phase flows (air-water-heptane) were conducted and the flow behavior was analyzed. Different compositions of the liquid mixture and rotation rates were studied.

The numerical simulations used the multiple reference frames approach with Eulerian multiphase flow model and the RNG k-ε turbulence model. The numerical model used was validated with the experimental data. The results predict that the flow pattern is dominated by the rotation, and as the rotation rate increases the free surface is displaced toward the top vessel. As long as the bubbly flow is established, the unbaffled reactor provides larger mass transfer rates (about 30%) than the baffled reactor. However, mass transfer rates drop of about 65 % when the emulsion is formed. Therefore, above the critical rotation rate at which the emulsion appears for the unbaffled reactor (between 1000 and 1400 rpm), the baffled reactor provides larger mass transfer rates. In all cases, mass transfer rates for hydrogen are larger than for carbon monoxide.

1. Objectives

The aim of this work is to analyze the two-phase mixing processes that occur in a small-scale batch reactor. The main objective is to determine the mass transfer rates for different gas components within the liquid phase of a stirred tank reactor. A numerical simulation approach was used in this study. Previously to the simulations some flow information was needed. For this reason the work has an initial step that implies an experimental part. All relevant information about how bubbles inside the liquid phase are formed, the amount and their sizes were extracted from these experiments and used in the numerical simulations. Additionally three-phase experiments were conducted to determine the flow behavior inside the reactor.

2. Experimental study

2.1. Experimental setup

The main objective of this part of the work was to estimate the amount and the mean diameter of the bubbles that show up in the liquid phase at different rotation speeds. The experiments were also useful for the understanding of the flow behavior inside the reactor for different rotation rates of the stirrer. The information obtained from the experimental work was used as input data and to validate the results from the numerical simulations of the reactor.

Experiments have been conducted in a two-phase system (air-water) at room temperature and atmospheric pressure. Additionally, the analysis of a three-phase system (air-water-heptane) was included to this work. The study of the three-phase system was qualitative and does not include a numerical simulation nor the computation of the mass transfer rate associated.

Figure 1 shows a schematic representation of the experimental setup. The flow images were obtained using monochromatic MotionPro digital camera (X3 Plus model). This camera is equipped with a 1" CMOS sensor with 1280×1024 pixels resolution with square pixels of 12µm. A macro Sigma lens of 28-300mm F3.5-6.3 was used with the camera.

Two different illumination systems were used in the experiments. The first system involves a pair of 300 Watts spotlights that allows a backside illumination. This system was used for the qualitative investigation of the flow behavior and in the previous analysis of the system. The other system consist

in a green Nd:Yag laser, linearly polarized with 532nm wavelength (Monocrom MP532-3W). This illumination system was the main light source used.

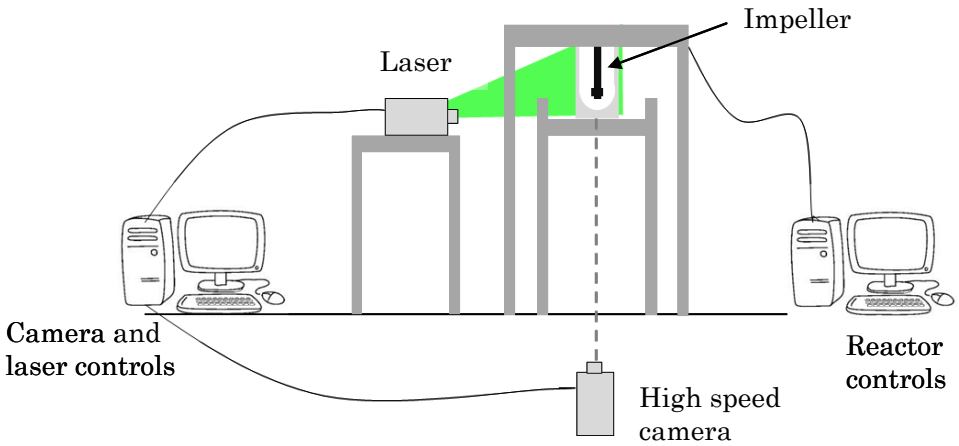

Figure 1. Experimental setup

The reactor analyzed consists in a vessel that is filled with liquid until a certain level. Usually this system operates at high temperature and pressure. The experimental analysis of the flow requires a transparent vessel to allow the visualization of the fluid inside that can not resist that working conditions. For this reason all the experiments where carried out at room temperature and atmospheric pressure. The vessel of the reactor was specifically made and was constructed in a transparent PMMA (Polymethyl methacrylate). The external part of the model was made with a square section to avoid image aberrations due to the curvature of the vessel wall (Figure 2).

Figure 2. PMMA model of the vessel: lateral view (left) and top view (right)

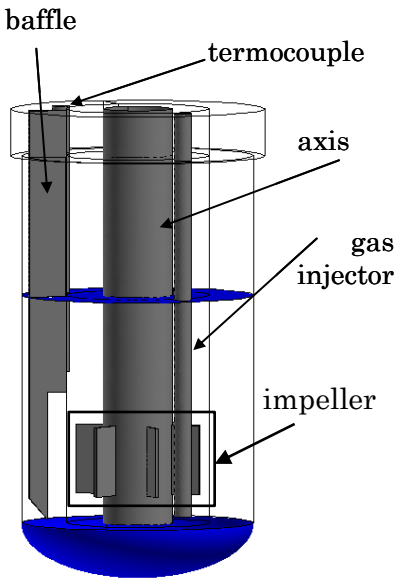

Figure 3. Scheme of the reactor

As shown in Figure 3 inside the vessel it can be found the rotating axis with blades, the thermocouple, the gas injector and the baffle. All these elements modify the flow dynamics, affecting the mixing and the emergence of bubbles. The internal diameter of the vessel is 42.2 mm and the height is 85.8 mm. The vessel is filled with 66 ml of water.

Two different impellers and reactor controls were used during the study. In both cases the same PMMA vessel was used. The first impeller (R1) was used to test the assembly and to obtain previous results needed to adapt the experimental setup. The second impeller (R2) was used to obtain the final parameters needed in the numerical simulations. Experiments with and without baffle were carried on. Figure 4 shows a picture of the experimental setup with a close look of the vessel installed.

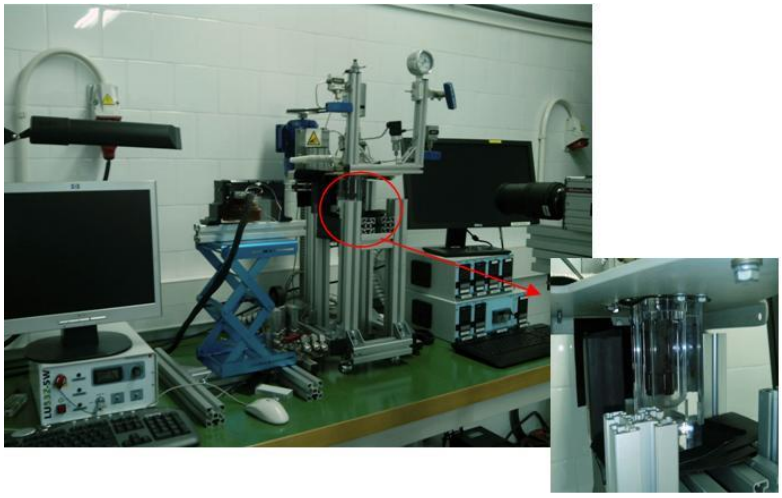

Figure 4. Picture of the experimental setup and detail of the vessel

2.2. Two-phase system

Experiments in two-phase system were carried on using air and water. All the experiments were done at room temperature and atmospheric pressure. The vessel was filled with 66 ml water. In all cases the experiment starts with the stirrer at rest and we wait several minutes until the system is stationary at the desired rotation rate. Only then the images are acquired and stored for latter processing.

Table 1 list the experiments done for the two-phase analysis using impeller R2. The Table 1 includes the total number of images acquired, the settings of the camera as the acquisition velocity (frames per second) and the exposure time for each image, the laser settings and it also indicates if the experiment has been done with or without baffle (see Figure 3). Previous experiments using the impeller R1 are not included in this list.

Table 1: Two-phase experiments

Rotation rate (Ω) (rpm)	fps (frame per second)	Number of images recorded	Exposure time (μs)	Laser power (W)	With baffle	Without baffle
606	75	3324	140	1.14	X	X
678	75	3324	140	1.50		X
754	75	3324	140	1.50		X
816	75	3324	140	1.50		X
909	75	3324	140	1.50		X
991	75	3324	140	1.50	X	X
1066	75	3324	140	1.50		X
1144	75	3324	140	1.50		X
1200	150	3272	231	1.14		X
1212	75	3324	140	1.50		X
1294	75	3324	140	1.50		X
1371	75	3324	140	1.50	X	X
1452	75	3324	140	1.50		X
1532	75	3324	140	1.50		X
1587	75	3324	140	1.50		X
1642	75	3324	140	1.50		X
1721	75	3324	140	1.50	X	X

2.3. Analysis of the free surface

The results obtained in this section were used to validate the numerical simulations. The shape of the free surface for specific system configurations will be obtained using numerical simulation and compared with the ones obtained experimentally. Figure 5.a shows one of the 2000 instantaneous images acquired for the case of Ω=800 rpm using an image acquisition velocity of 500 fps with laser illumination and without baffle. From all the images of this experiment the mean (figure 5.b), standard deviation (figure 5.c) and median were calculated. To improve the visualization of the free surface, the median has been subtracted to the mean as figure 5.d shows. This procedure allows subtracting all fixed reflections and fixed objects present in the image.

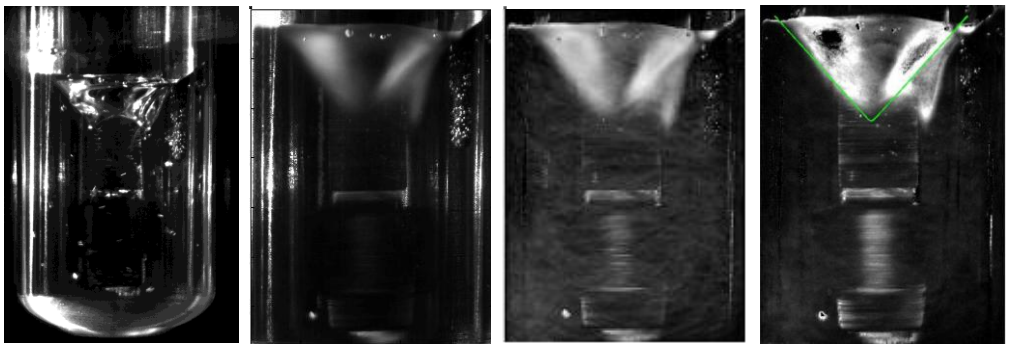

(a) (b) (c) (d)

Figure 5. Free surface zone, Ω=800 rpm, a) Original image, b) Mean image over 2000 images, c) standard deviation image, d) Mean – Median image with hyperbola fitting with coefficients show in Table 2

Theoretically the free surface of the liquid in a cylindrical mixing vessel agitated by a concentric paddle agitator is isobaric and shows a hyperbolic contour[18]. Table 2 shows the hyperbolic fitting of the experimental data obtained at different rotation rates with the equation 2.1:

$$\frac{y^2}{a^2} - \frac{x^2}{b^2} = 1 \qquad \text{Eq. 2.1}$$

Table 2: Rotation rates and hyperbola coefficients

Ω (rpm)	a	b
800	5	4.5
900	5	3.5
500	1	2.5

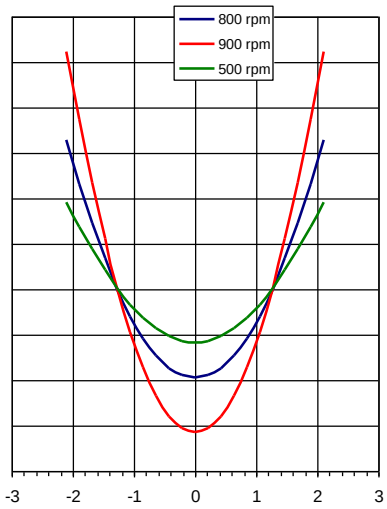

Figure 6. Hyperbola fitting with coefficients show in Table 2

As it can be expected the free surface changes with the rotation rate. An increase in rotation rate in the range studied results in the free surface being located at a higher position.

2.3.1. Analysis of the reactor without baffle

The analysis of the flow behavior inside the reactor has been conducted for rotation rates (Ω) ranging from 606 to 1721 rpm using reactor R2. The first step was to analyze the time evolution of the system. To characterize this evolution the "image intensity" is analyzed from different experimental conditions. Observing the acquired instantaneous images it can be seen that the bubbles inside the fluid are white while the rest remains black. Thus, the total image intensity is related with the number of bubbles inside the liquid. On the other hand, the settings of the camera and the laser affect the intensity of the images recorded. In order to compare the images from different experiments the same conditions need to be imposed. Accordingly, uniform laser intensity, acquisition rate and exposure time have been applied for all experiments used in this analysis. The image intensity has not been computed

employing the information of the entire image only a selected region of interest (the same for all the experiments) has been analyzed.

Figure 7 shows the time evolution of the number of bubbles (image intensity) from time zero where the stirrer is at rest. Due to equipments restrictions only 45 s have been recorded for each rotation rate. It can be observed that almost in all the cases the number of bubbles increases suddenly 10 s after the system starts to rotate. For larger rotation rates the gradient is high. Although after 45 s the stationary state is not reached in any case and it seems that the number of bubbles can grow more. Thus to obtain an estimate of the numbers and sizes of the bubbles for each case it will be necessary to wait more time to ensure that the system is stationary.

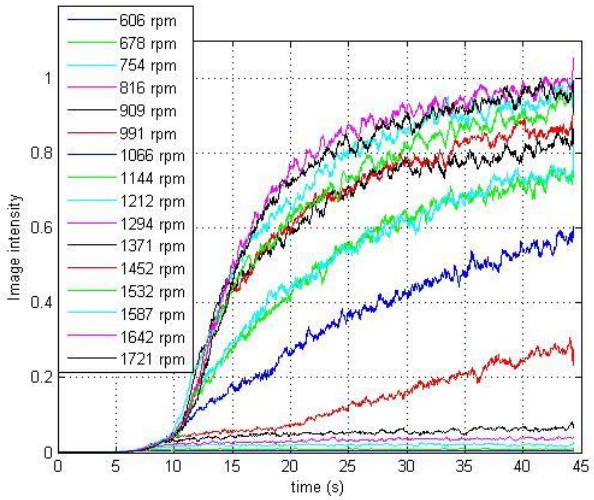

Figure 7. Time evolution of white pixels amount in a selected region

To obtain the time for which the system becomes stationary, experiments at 606, 991, 1371 and 1721 rpm were carried on in three consecutive time intervals (Figure 8). It can be seen that the number of bubbles do not significantly change for time higher than 400 s. It is also interesting to observe that the number of bubbles is practically the same for the three cases, even when velocities are different.

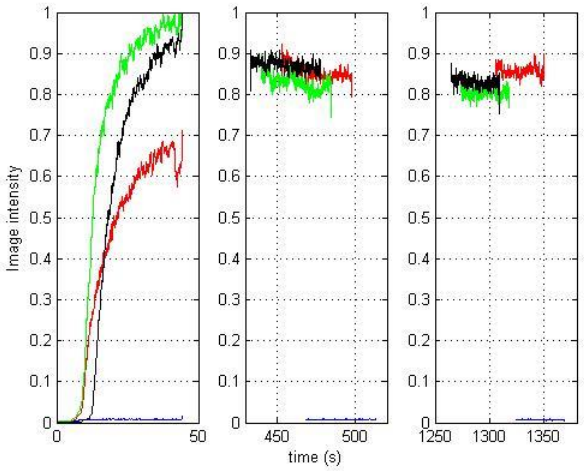

Figure 8. Variation of the image intensity. Blue, Ω=606 rpm, red, Ω=991 rpm, green Ω=1371 rpm and black, Ω=1721 rpm

The images used to compute the number and the mean size of the bubbles have been acquired waiting enough time to ensure that the system is stationary. Four different rotation rates were selected. In each case the procedure was the same. For each rotation rate three instantaneous images are selected. From each of these images, a region of interest (ROI) was selected. The cropped image, corresponding to this ROI, is treated to enhance the resolution facilitating the measurements of individual bubble sizes. Each cropped area yields a set of diameters in terms of pixels, measured in millimeters using a scale. This scale remains the same for all cases. The resulting mean bubble diameter was obtained from the diameter sets measured at the three times mentioned before. Table 3 shows the mean bubble diameter at the four rotation rates. It can be observed that the mean diameter decreases with the velocity. An additional drawback has been found for higher velocities. The system starts to show emulsion behavior from 1371 rpm. Therefore the size of the bubbles is difficult to compute and the experimental value obtained is overestimated as only the bigger bubbles were measured.

Table 3. Mean bubble diameter (reactor without baffle)

Ω (rpm)	$D_m \pm \sigma_m$ (mm)	Number of measurements	D_{MAX} (mm)	D_{MIN} (mm)	σ (mm)
606	0.662±0.020	51	1.026	0.418	0.149
991	0.563±0.013	40	0.7864	0.450	0.084
1371	0.329±0.016	27	0.563	0.215	0.084
1721	0.212±0.024	13	0.298	0.126	0.086

The experimental diameters obtained were compared with the diameters obtained form the correlation proposed by Nagata (Nagata, 1975) for a similar system. Nagata found that the diameter of gas bubbles (d_b) can be expressed as $d_b = K\ \Omega^{-1.2}$, where K is a constant valued. Figure 10 shows de variation of the experimental diameter of gas bubbles with the rotation rate and compares with the diameters obtained with correlation from Nagata considering K=121. The difference between the mean diameter measured and that computed using the correlation proposed by Nagata[18] is within 8 %.

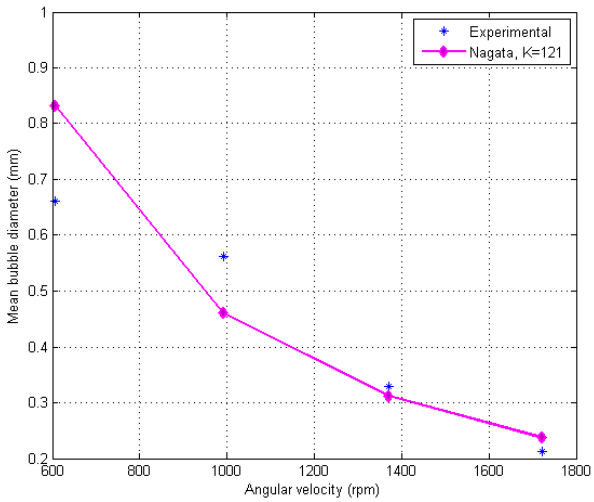

Figure 10. Mean bubble diameter (mm) as function of rotation rate

Using the bubble diameters obtained and the image intensity, the total number of bubbles in the vessel at each rotation rate can be estimated. To do this, first

we define the ideal bubble as the one which has the diameter equal to the mean bubble diameter calculated for each case. To obtain the total number of ideal bubbles for a specific rotation rate a ROI of the entire vessel is selected from the instantaneous images. The image intensity is computed for this ROI and dividing the result by the diameter of the ideal bubble the number of ideal bubbles in the ROI can be obtained. This is repeated for all the acquired images in one experiment to obtain the time evolution of the number of ideal bubbles. The time average provides an estimate of the number of bubbles in one plane. The results obtained for one plane can be extrapolated to the rest of the vessel to obtain the total number of ideal bubbles for each rotation rate. Table 4 shows the results for four rotation rates. It can be observed that the number of bubbles increases substantially for higher velocities.

Table 4. Number of bubbles (reactor without baffle)

Ω (rpm)	Mean number of ideal bubbles per plane	Total number of ideal bubbles into the vessel
606	17	1084
991	2793	209351
1371	7675	984453
1721	19046	3791296

2.3.2. Analysis of the reactor with baffle

The same experiments and analysis were performed for the system with baffle (see Figure 3). Adding this accessory substantially modifies the flow behavior inside the reactor. In this case four rotation rates were analyzed. Figure 11 shows the time evolution of the image intensity for the startup period. The behavior is similar to the unbaffled case although the bubbles seem to need more time to show up for the 1721 rpm than for the 991 and 1371 rpm cases. As it is evident from Figure 11, a interval of 45 s was not enough to reach the stationary state. To determine the time needed to attain the stationary state images at different times where acquired. Figure 12 shows that for time larger that 400 s the system can be considered stationary. In this

case the results are different from the unbaffled case (Figure 8) where for all the velocities the image intensity seemed to reach the same maximum value. In this case the image intensity is a function of the rotation rate and increases with it. One of the reasons for this different behavior could be that for the baffled cause the formation of emulsion which is not observed for any of the rotation rates studied.

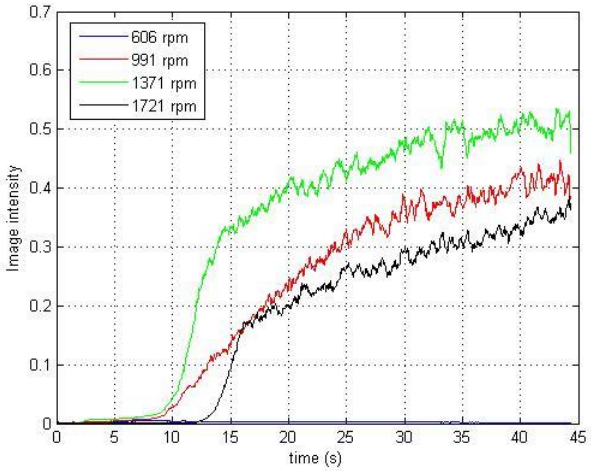

Figure 11. Time evolution of white pixels amount in the selected region for selected rotation velocities

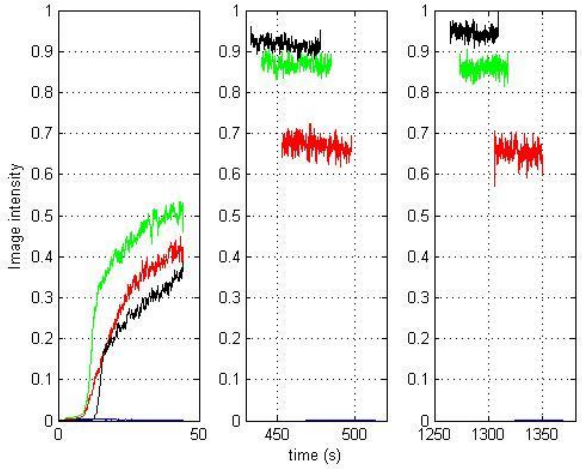

Figure 12. Time evolution of white pixels amount in the selected region for selected rotation velocities in three periods. Blue, Ω=606 rpm, red, Ω=991 rpm, green Ω=1371 rpm and black, Ω=1721 rpm

The same procedure done in the unbaffled case was followed to estimate the number and diameter of the bubbles. The results are summarized in Table 5 (diameters) and Tabel 6 (number of bubbles) for three rotation rates. For Ω=606 rpm the number presented in the system was insufficient to make a representative average (no more than 10 bubbles).

Table 5. Mean bubble diameter for the reactor with baffle

Ω (rpm)	$D_m \pm \sigma_m$ (mm)	Number of measurements	D_{MAX} (mm)	D_{MIN} (mm)	σ (mm)
991	0.551±0.018	55	0.854	0.222	0.136
1371	0.479±0.017	96	1.270	0.159	0.171
1721	0.443±0.021	100	1.200	0.160	0.206

Table 6. Number of bubbles for the reactor with baffle

Ω (rpm)	Mean number of ideal bubbles per plane	Total number of ideal bubbles in the vessel
991	2083	159532
1371	2604	229413
1721	4643	442290

The results of the baffled case were also compared with the correlation of Nagata[18], where the diameter of gas bubbles (d_b) is expressed as $d_b = C\ \Omega^{-1.2}$, considering C=180 (Figure 13).

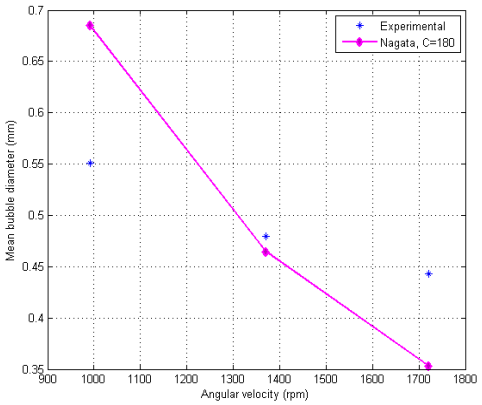

Figure 13. Mean bubble diameter (mm) as function of rotation rate for reactor R2 with baffle

2.4. Three-phase system

The qualitative analysis of the three-phase system (heptane-water-air) was done for two different rotation speeds, 606 rpm and 1371 rpm, and for several percentages in the heptane/water mixture for the reactor R2 with baffle. In this case the system was illuminated with the 300 Watts spotlights and to help visualize Rhodamine B was added to water (0.3 mg / ml). The images were obtained at 50 fps taking two intervals of 66.5 seconds for each rotation rate separated with a period of 540 s. For each series 3324 images were acquired. On the images the water solution with Rhodamine B is the dark fluid and heptane is the colorless fluid as Figure 14 shows. The measurements were carried out at atmospheric pressure (0.1 MPa) and the temperature of the mixture varied from 19 to 25ºC. Several percentages of the mixture water/heptane have been analyzed. In particular the mixtures analyzed were 0/100, 15/85, 50/50, 85/15 and 100/0.

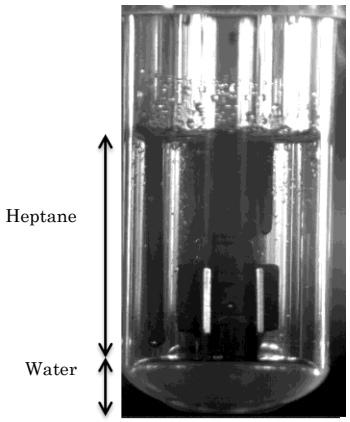

Figure 14: Image of 15/85 water/heptane mix at rest

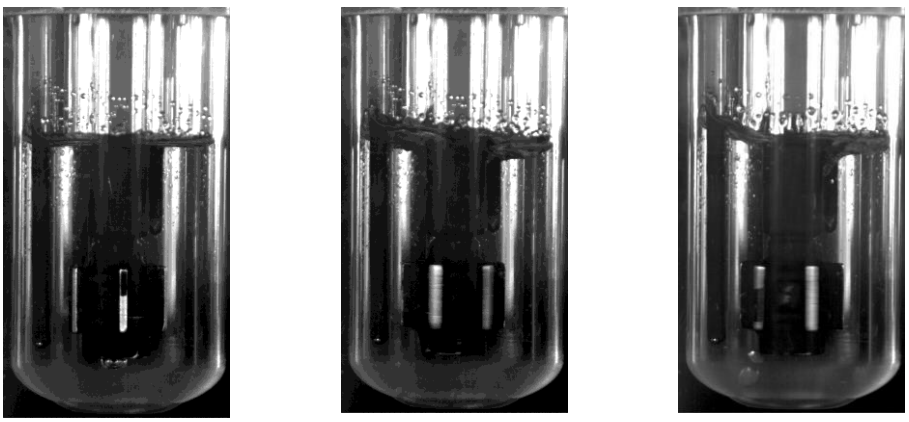

(a) (b) (c)

Figure 15: Acquired images 0/100 water/heptane mixture, Ω=606 rpm, (a) t=0, (b) t=6.6 s, (c) t=606.5 s

Figure 15 shows images of the system working with heptane only for different times (0, 6.6 s and 66.5s) at Ω = 606 rpm. In this case no bubbles appear and only the existence of a small hyperbola shows up at the free surface. Essentially there is no difference between 6.6s and 66.5s. This behavior is basically the same that can be observed when analyzing only water as a fluid at this rotation rate. Adding a 15% of water the behavior of the flow changes substantially. Figure 16 shows results for a mixture 15/85 water/heptane at Ω = 606 rpm. In this case there is no evidence of incorporation of air in the liquid mixture. The "bubbles" that the image shows are water drops inside the heptane. The water is distributed all over the heptane an there is no clear interphase between the two fluids

(a) (b) (c)

Figure 16: Acquired images 15/85 water/heptane mixture, Ω=606 rpm, (a) t=0, (b) t=6.6 s, (c) t=606.5 s

In the case of the 50/50 water/heptane mixture at Ω = 606 rpm (Figure 17) the interphase between water and heptane is maintained even for the larger times. Water droplets are not well defined and the system becomes an emulsion. In this case it is not clear if there is a supply of air into the mixture, although heptane seems to work as a barrier between the emulsion and the air.

(a) (b) (c)

Figure 17: Acquired images 50/50 water/heptane mixture, Ω=606 rpm,
(a) t=0, (b) t=6.6 s, (c) t=606.5 s

The results for the 85/15 water/heptane mixture are shown in Figure 18. In this case an interphase between the fluids and water drops can be observed for shorter times while for longer times the interphase and droplet cannot be distinguished, the mixture is an emulsion. As in the other cases there is no evidence that the air is absorbed into the liquid mixture.

(a) (b) (c)

Figure 18: Acquired images 85/15 water/heptane mixture, Ω=606 rpm,
(a) t=0, (b) t=6.6 s, (c) t=606.5 s

The behavior of the water/heptane mixture for rotation rate of Ω = 1371 rpm has been analyzed for the same times. Figure 19a and 19b show the results for pure the heptane case. Unlike what was obtained for Ω = 606 rpm in here it can be observed that for short times no air bubbles appear in the mixture while for a longer time (606.5 s) the air bubbles are present. When analyzing pure water at this rotation rate the air bubbles also appear for long times (Figure 19c). It can be seen that at the same rotation rate, there is less but bigger air bubbles in the heptane than in the water. The experimental mean diameter of the bubbles in the heptane and in water is summarized en Table 7.

(a) (b) (c)

Figure 19: Acquired images 0/100 water/heptane mixture, Ω=1371 rpm, (a) t=6.6 s anb (b) t=606.5 s, and (c) 100/0 water/heptane mixture at t=606.5 s

Table 7: Mean bubble diameter, reactor with baffle Ω=1371 rpm

Mixture water/heptane	$D_m \pm \sigma_m$ (mm)	Number of measurements	D_{MAX} (mm)	D_{MIN} (mm)	σ (mm)
100/0	0.479±0.017	96	1.270	0.159	0.171
0/100	1.114±0.052	51	1.768	0.442	0.378

The flow dynamics of the 15/85 water/heptane mixture at short times (t=6.6 s) is very similar to that observed for Ω = 606 rpm (Figure 16). For longer times

(t=606.5 s) the number of water drops present in the heptane increases. The behavior shown by the 50/50 water/heptane mixture (Figure 21) and by the 85/15 water/heptane mixture (Figure 22) does not present significant differences to that observed for Ω = 606 rpm. For short times the interphase between two fluids is still visible and an emulsion is present for long times.

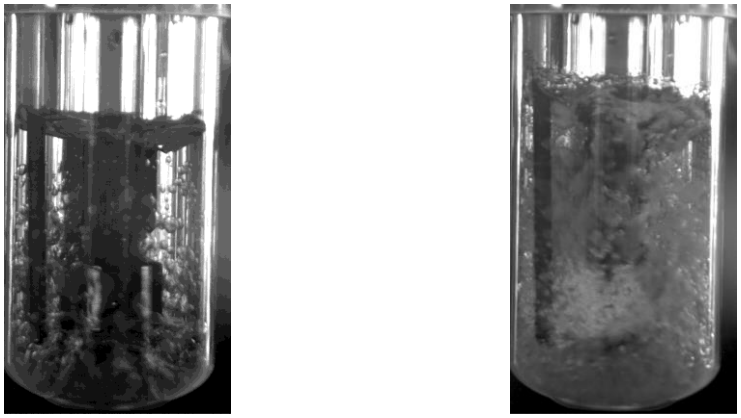

(a) (b)

Figure 20: Acquired images 15/85 water/heptane mixture, Ω=1371 rpm, (a) t=6.6 s anb (b) t=606.5 s

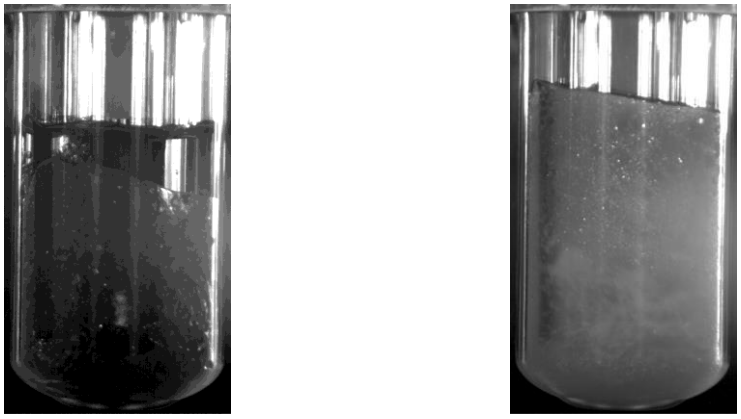

(a) (b)

Figure 21: Acquired images 50/50 water/heptane mixture, Ω=1371 rpm, (a) t=6.6 s anb (b) t=606.5 s

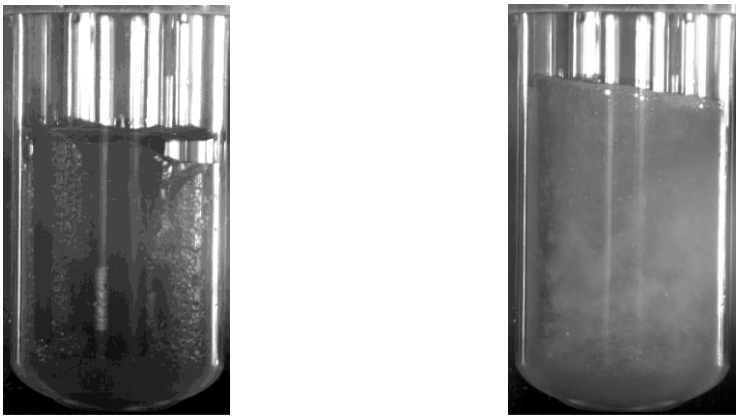

(a) (b)

Figure 22: Acquired images 85/15 water/heptane mixture, Ω=1371 rpm, (a) t=6.6 s anb (b) t=606.5 s

3. Numerical study

The numerical part of the study is presented in this section. First, the physical, mathematical and numerical models are presented. Results are discussed and finally conclusions are outlined.

3.1. Background

Several researchers have carried out numerical simulations of gas-liquid stirred vessels over the years using different numerical techniques. Some authors have performed Large Eddy Simulations (LES) as Ferziger and Peric (2002). In that computational approach, the large scales of the flow are solved, while the smaller scales are modeled. Although not as computationally expensive as performing Direct Numerical Simulations (DNS), where all the flow scales are solved, it is still an expensive method. A key feature in LES is the choice of the SubGrid Scale model (SGS), since the accuracy of the results on the smaller scales will depend on it. Arlov et al.(2008) performed LES to study a gas-liquid Rushton stirred reactor, with an implicit SGS model. To solve the multiphase flow, a combination of Volume of Solid (VOS) and Lagrangian Particle Tracking (LPT) was used in their study (Yeoh and Tu, 2009). Air was entered at the bottom of the reactor and, under the assumption of bubbly flow the bubbles were tracked in the three-dimensional time-dependent flow field generated by LES. Another study using LES is the one by Alcamo et al. (2005), although in that work there was a single-phase flow. The Smagorinsky SGS model (Smagorinsky, 1963) was used for their simulations, performed with the commercial software CFX. As an example of the

computational cost of LES, the authors needed 33 days to solve the flow field for the time corresponding to 22 impeller revolutions at 200 rpm, using a 3 GHz processor.

Given the high computational cost of LES, the Reynolds Averaged Navier-Stokes (RANS) approach (Ferziger and Peric, 2002) has become more popular. In this approach, only the average field is solved and turbulence is modeled. A widely used turbulence model is a two-equation model, the k- ε model (Launder and Spalding, 1972), which uses the kinetic turbulent energy (k) and its dissipation rate (ε) to compute the turbulent viscosity. The works from other authors using RANS reported here all use the k-ε model. Scargiali et al. (2007) simulated a gas-liquid stirred tank using CFX and the Sliding Grid (SG) technique (Perng and Murthy, 1992). In their Eulerian-Eulerian multiphase model (Spalding, 1985), both phases shared the same values of k and ε. The authors found that including lift and virtual mass forces does not change the results. The SG technique was also used by Deen et al. (2002) in their study of an aerated Rushton impeller. The authors report that the drag force is the most important one in these systems, and that the bubble induced turbulence should be taken into account, thus making the effective viscosity the sum of the molecular, turbulent and bubble induced turbulent viscosities. The free surface of a CSTR was studied by Serra et al. (2001). The authors also employed the SG technique, but this time using the Star CD software and the VOF model (Hirt and Nichols, 1981), instead of the Eulerian-Eulerian multiphase model. The range of rotation rate was between 70 and 280 rpm. The authors reported that macromixing is bad in low velocity regions found at the curved bottom, slightly downstream the baffles and near the free surface, although the one at the curved bottom may be destroyed by gas bubbles. Torre et al.(2007) studied the vortex shape in a partially baffled agitated vessel, with a Eulerian-Eulerian multiphase model and using the Multiple Reference Frame (MRF) technique (Luo et al. 1994), where a region of the computational domain, placed around the impeller, rotates with the same velocity that the impeller and the rest of the domain is static. Ranade (1997) studied a stirred vessel using a Rushton turbine. The computational software FLUENT (2009) was used with an

Eulerian-Eulerian multiphase model, and the Snapshot method (Ranade and Dommeti, 1996) was implemented through User Defined Functions (UDF). This method consists in adding a mass source term to the equations solved to model impeller motion. The author reports that there is an accumulation of gas behind the impeller blades, and that the hydrodynamics cannot be determined with a steady state approach.

3.2. Physical model

Figure 23 shows a sketch of the reactor without baffle, while the sketch in Figure 24 corresponds to the reactor with baffle. The shadowed surfaces correspond to solid elements (axis, blades, thermocouple, gas injector and baffle), with the outer wall left transparent in order to allow the inner elements to be displayed. There are six blades disposed equidistantly at 60º one from another. At the initial time there are 66 ml of liquid, with the rest of the non-solid volume being gas. The axis is still at the initial time, and starts rotating accelerating progressively until the desired rotation rate is reached. The dimensions of the vessel and all the inner elements are shown in Table 8. Non-slipping condition is imposed at all the walls, with the difference being that the axis and the blades are rotating, while the thermocouple, the gas injector, the baffle and the outer wall are static.

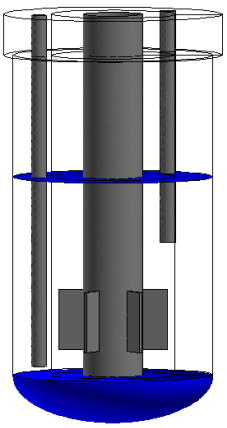

Figure 23. Sketch of the reactor without baffle

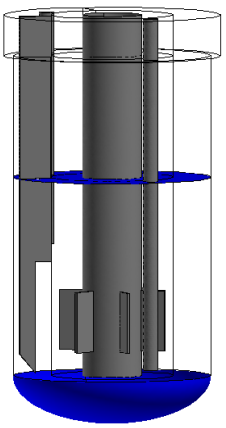

Figure 24. Sketch of the reactor with baffle

The fluids used in the validation part of the study are water and air at room temperature and atmospheric pressure. At those conditions, water density is considered to be 1000 kg/m^3 and its absolute viscosity 10^{-3} Pa·s, while air density is taken as 1.2 kg/m^3 and its absolute viscosity as $1.8 \cdot 10^{-5}$ Pa·s. The rest of the simulations are performed with the actual fluids in the reactor, and their physical properties are evaluated at the operating conditions. The liquid density is 888.6 kg/m^3 and its absolute viscosity $1.5 \cdot 10^{-4}$ Pa·s, which correspond to water and air at 180ºC and 3.1 MPa (NIST Standard Reference Database 23, US Department of Commerce, 2007).

Table 8. Reactor dimensions (mm)

Vessel height	85.80
Vessel diameter	42.20
Axis height	76.10
Axis diameter	12.50
Blades height	12.07
Blades width	5.24
Thermocouple height	74.00
Thermocouple diameter	3.15
Gas injector height	48.80
Gas injector width	3.15

3.3. Mathematical and numerical models

The set of equations that determines the behavior of the flow inside the reactor is shown in this section. Equation 3.1 corresponds to mass conservation, also known as the continuity equation, while momentum conservation is represented by Equation 3.2:

$$\frac{\partial(\rho u_i)}{\partial x} = 0 \qquad \text{Eq. 3.1}$$

$$\rho\bar{u}_j\frac{\partial\bar{u}_i}{\partial x_j}=\frac{\partial}{\partial x_j}\left[-\bar{p}\delta_{ij}+\mu\left(\frac{\partial\bar{u}_i}{\partial x_j}+\frac{\partial\bar{u}_j}{\partial x_i}\right)-\rho\overline{u_i'u_j'}\right] \quad \text{Eq. 3.2}$$

The turbulence model used in this study is the RNG k-epsilon model (FLUENT, 2009), which models the last term of Equation 3.2 according to the Boussinesq hypothesis, shown in Equation 3.3. Equation 3.4 shows the expression for the transport of the turbulent kinetic energy (k), while Equation 3.5 represents the transport of the dissipation of the turbulent kinetic energy (ε).

$$-\rho\overline{u_i'u_j'}=\mu\left(\frac{\partial u_i}{\partial x_j}\right)\frac{2}{3}\left(\rho k+\mu_t\frac{\partial u_k}{\partial x_k}\right)\delta_{ij} \quad \text{Eq. 3.3}$$

$$\frac{\partial}{\partial t}(\rho k)+\frac{\partial}{\partial x_i}(\rho k u_i)=\frac{\partial}{\partial x_j}\left(\alpha_k\mu_{eff}\frac{\partial k}{\partial x_j}\right)+G_k+G_b-\rho\varepsilon \quad \text{Eq. 3.4}$$

$$\frac{\partial}{\partial t}(\rho\varepsilon)+\frac{\partial}{\partial x_i}(\rho\varepsilon u_i)=\frac{\partial}{\partial x_j}\left(\alpha_\varepsilon\mu_{eff}\frac{\partial\varepsilon}{\partial x_j}\right)+C_{1\varepsilon}\frac{\varepsilon}{k}(G_k+C_{3\varepsilon}G_b)-C_{2\varepsilon}\rho\frac{\varepsilon^2}{k}-R_\varepsilon \quad \text{Eq. 3.5}$$

Where,

G_k, turbulent kinetic energy generation due to mean velocity gradients
G_b, turbulent kinetic energy generation due to buoyancy
$C_{1\varepsilon}$, $C_{2\varepsilon}$, $C_{3\varepsilon}$ model constants
α_k, inverse effective Prandtl number for k
α_ϵ, inverse effective Prandtl number for ε

After an initial literature review, several numerical models were tested. As an example, the Sliding Grid (SG) and the Multiple Reference Frame (MRF) approaches were tried (Perng, and Murthy, 1992; Luo et al. 1994). It was found that the SG method was highly unstable, and the required time step to stabilize simulations was too small to obtain results in a reasonable time. On

the contrary, the MRF method was much more stable for the given conditions and representative results could be obtained in reasonable computational times. After this trial-and-error process, the reactor model used in this study followed the MRF approach, using a Eulerian multiphase model where equations are solved for each phase with constant physical properties, since neither chemical reactions nor heat transfer processes are considered at this stage of the project.

In order to carry out the simulations with the axis and the blades rotating, two different systems of reference are used: one rotating with the rotation rate of the axis and another one static. A relative velocity (u_r) is defined in the rotating system as the difference between the absolute velocity and the velocity of the rotational system. The equations of continuity and momentum for this system are shown, respectively, in Equations 3.6 and 3.7:

$$\frac{\partial}{\partial x}(\rho u_{ri}) = 0 \qquad \text{Eq. 3.6}$$

$$\rho \overline{u_{ri}} \frac{\partial \overline{u_i}}{\partial \overline{x_j}} + \rho(w \times u_i) = \frac{\partial}{\partial x_j}\left[-\overline{p}\delta_{ij} + \mu\left(\frac{\partial \overline{u_i}}{\partial x_j} + \frac{\partial \overline{u_j}}{\partial x_i}\right) - \rho \overline{u_i' u_j'} \right] \qquad \text{Eq. 3.7}$$

where the term $w \times u_i$ corresponds to the Coriolis and centripetal accelerations.

The numerical scheme used in the pressure-velocity coupling is a phase coupled SIMPLE, while equations are discretized using second order upwind schemes. The time step for the simulations is 0.001 s, while the grid consists of tetrahedral cells. A detail of the computational mesh is shown in Figure 25.

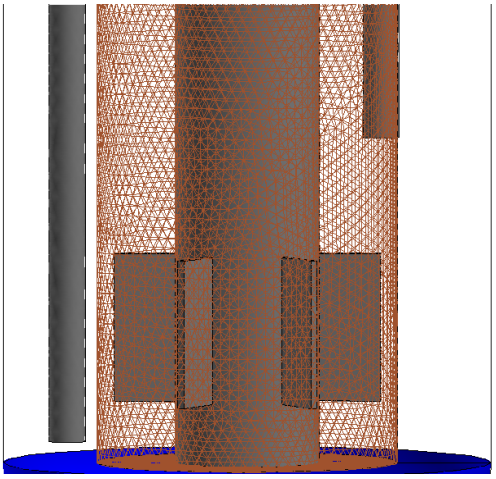

Figure 25. Detail of the computational mesh

3.4. Validation with experimental data

The first step was to perform simulations at a rotation rate of 900 rpm in a water-air system for the unbaffled reactor, in order to validate the numerical model with the experimental data. A mesh independence test was conducted, resulting in a grid of 1,030,845 tetrahedral computational cells fine enough to provide good results. Figure 26 shows the comparison between the numerical results and the experimental data. The lines plotted represent the shape and location of the free surface, taken in the numerical case as an isosurface of liquid volume fraction of 0.9. The horizontal axis corresponds to the reactor radius, while the vertical axis is the height. The blue line corresponds to the numerical results, while the red line corresponds to the experimental visualization. As it can be seen, the results provided by the simulation match the experimental data quite well.

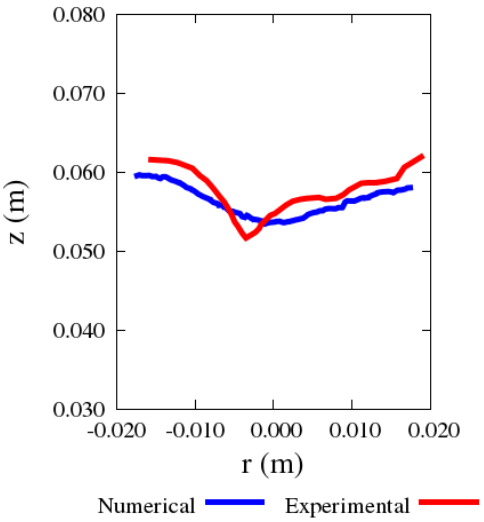

Figure 26. Comparison of the free surface location between the numerical results and the experimental visualization

3.5. Results for the dynamic fields

Once the numerical model was validated, simulations for the actual case were performed for both the baffled and unbaffled case at different rotation rates: 900, 1000, 1100, 1500, 2000 and 2500 rpm.

3.5.1. Unbaffled reactor dynamic field

The results obtained from these simulations show that the flow pattern is dominated by the axis rotation. An increase in rotation rate in the range studied results in the free surface being located at a higher position. This is shown in Figure 27, where an isosurface of liquid volume fraction of 0.9 for the six different rotation rates studied is displayed for the reactor without baffle.

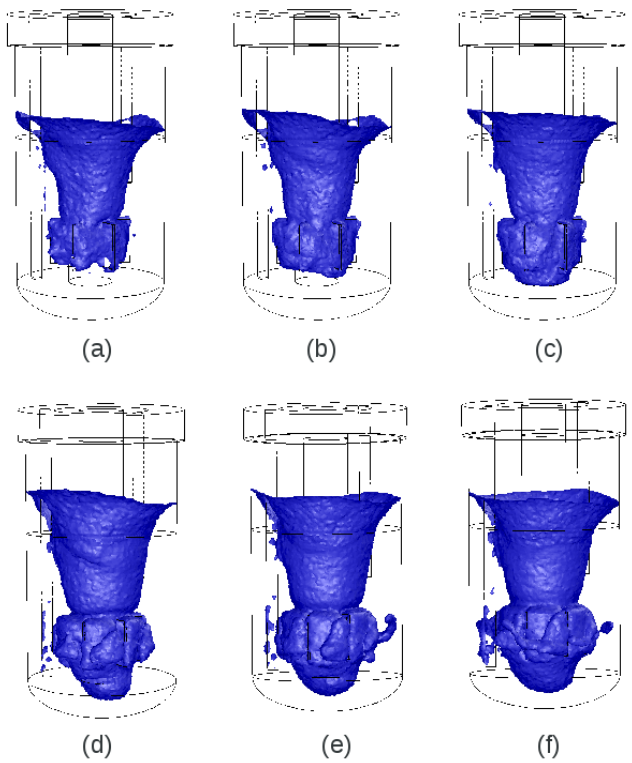

Figure 27. Isosurfaces of liquid volume fraction 0.9 for different rotation rates for the unbaffled reactor: (a) 900, (b) 1000, (c) 1100, (d) 1500, (e) 2000 and (f) 2500 rpm

Figure 28 shows contours of liquid volume fraction at a plane located at 12 mm (towards the reader) from the center of the vessel. The red color corresponds to liquid while the blue color corresponds to gas. The interphase can be clearly distinguished (in green and yellow tonalities) and its shape becomes sharper as the rotation rate increases. It is also worth noting, as Figure 28 shows, that for high rotation rate (1500, 2000 and 2500 rpm) there is a region surrounding the blades where gas is present (green and yellow tonalities) with volume fractions ranging between 0.3 and 0.6. This gas accumulation behind the blades is reported by some other authors (Scargiali et al.,2007; Ranade, 1997). Figure 29 shows a top view of liquid volume fraction contours at a height equivalent to that of the initial liquid height before the impeller starts rotating.

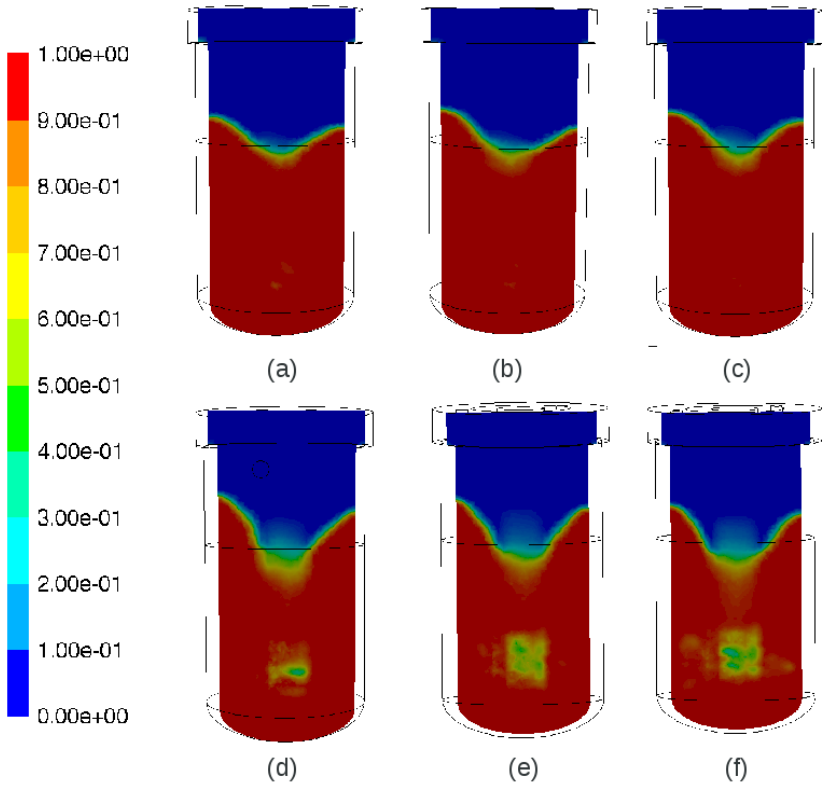

Figure 28. Contours of liquid volume fraction at a plane x=12 mm for different rotation rates for the unbaffled reactor: (a) 900, (b) 1000, (c) 1100, (d) 1500, (e) 2000 and (f) 2500 rpm

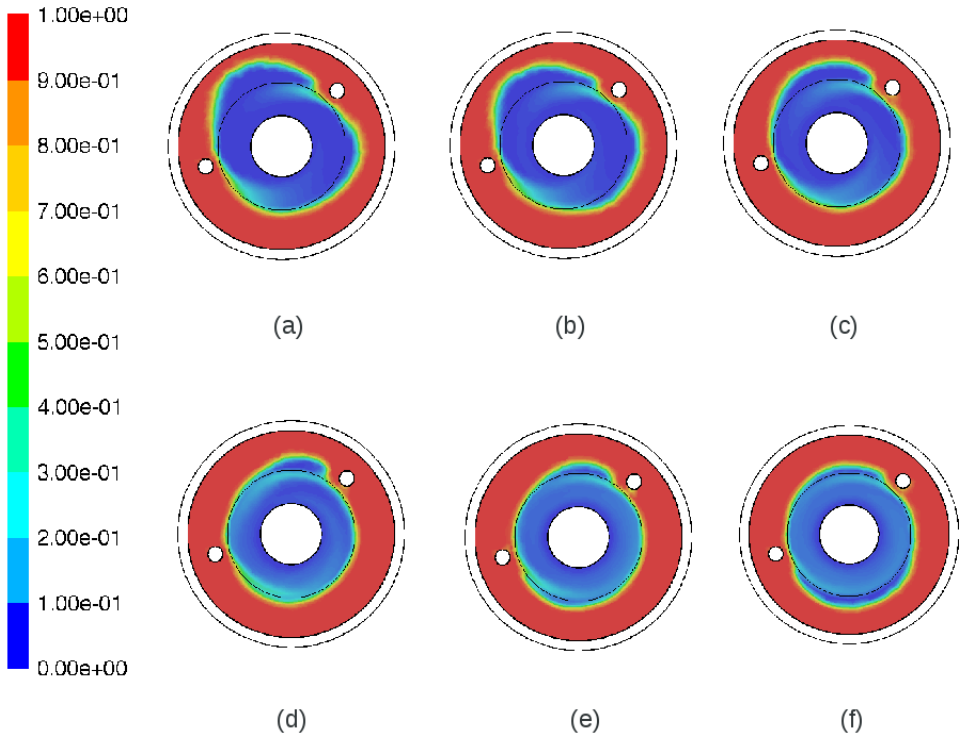

Figure 29. Contours of liquid volume fraction at a plane z=52 mm for different rotation rates for the unbaffled reactor: (a) 900, (b) 1000, (c) 1100, (d) 1500, (e) 2000 and (f) 2500 rpm

Velocity vectors at the same plane of x = 12 mm are shown in Figure 30 for all six rotation rates. The red vectors represent velocities of 0.7 m/s or larger, while blue vectors are close to being static. As expected, the largest velocities are located near the blades, and the larger the rotation rate is the faster the liquid moves. As it can be seen in Figure 30, the region with high velocities is larger at higher rotation rates. Figure 31 shows velocity vectors at a plane located at a z = 52 mm, equivalent to the liquid height at rest.

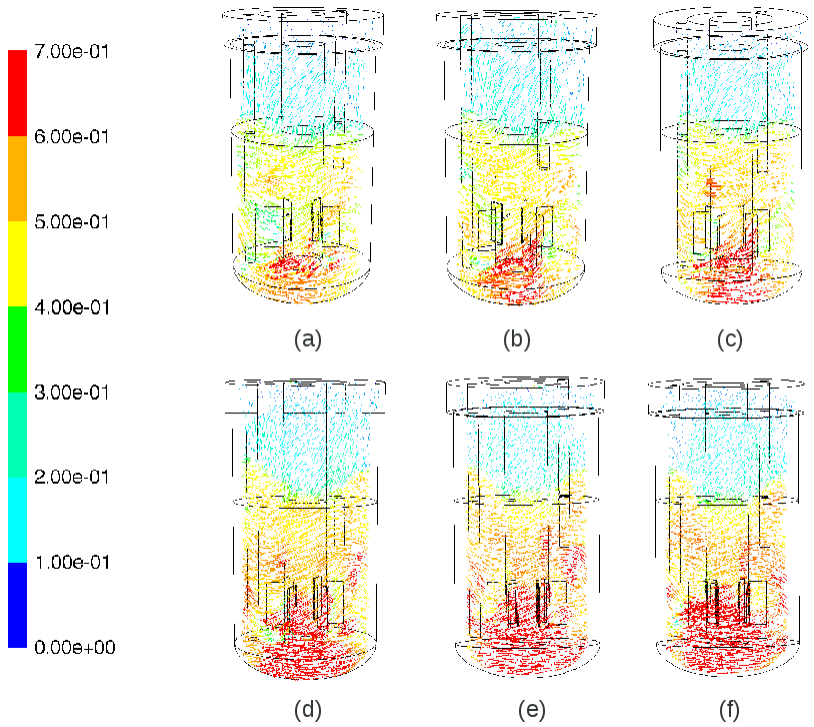

Figure 30. Velocity vectors at a plane x=12 mm for different rotation rates for the unbaffled reactor: (a) 900, (b) 1000, (c) 1100, (d) 1500, (e) 2000 and (f) 2500 rpm.

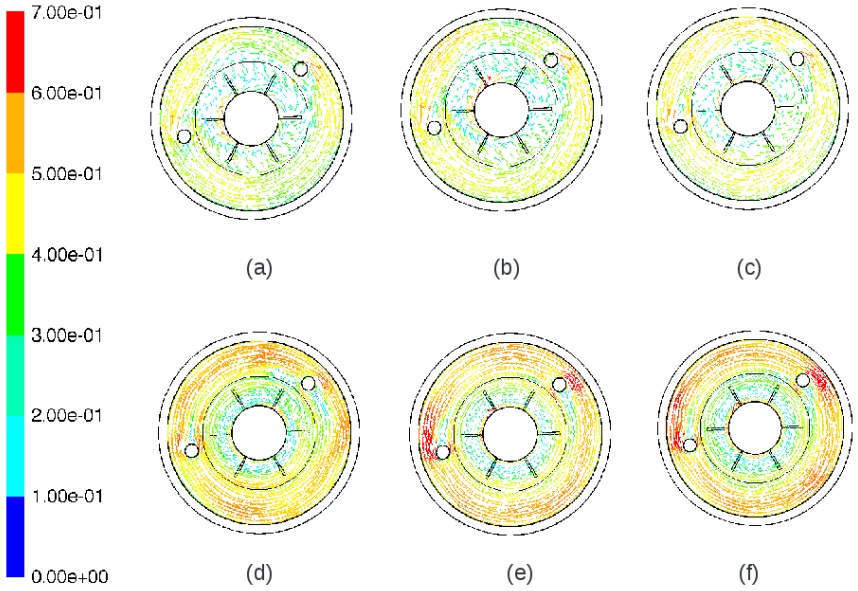

Figure 31. Velocity vectors at a plane z=52 mm for different rotation rates for the unbaffled reactor: (a) 900, (b) 1000, (c) 1100, (d) 1500, (e) 2000 and (f) 2500 rpm

3.5.2. Baffled reactor dynamic field

The simulations for the baffled reactor predict also a flow pattern dominated by rotation, as it happened for the case without baffle. However, the presence of the baffle results in the free surface breaking. Figure 32 shows isosurfaces of liquid volume fraction of 0.9 for different rotation rates, with the vertical red line representing the location of the baffle. As it can be seen in Figure 32, as the rotation rate increases, the free surface is more deformed and the interphase area between the gas and the liquid phases is larger.

Figure 33 shows liquid volume fraction contours in a plane located at x=12 mm. Again, the red color corresponds to liquid while the blue color corresponds to gas. As it can be seen in Figure 33, as the rotation rate increases, the free surface deformation also increases. Another phenomenon which can be seen in Figure 33 is the formation of gas regions surrounding the blades (in yellow and green colors). These regions increase with the rotation rate, but also its gas volume fraction.

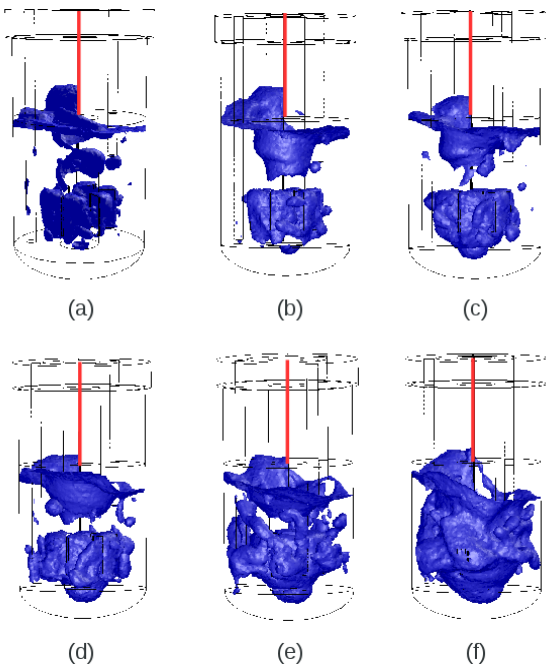

Figure 32. Isosurfaces of liquid volume fraction 0.9 for different rotation rates for the baffled reactor: (a) 900, (b) 1000, (c) 1100, (d) 1500, (e) 2000 and (f) 2500 rpm

Figure 34 shows liquid volume fraction contours in a plane located at z=52 mm. As it can be seen from this top view, the baffle (wider black line) separates the liquid and gas phases, and as the rotation rate increases, more gas is present in this plane, due to the deformation of the free surface.

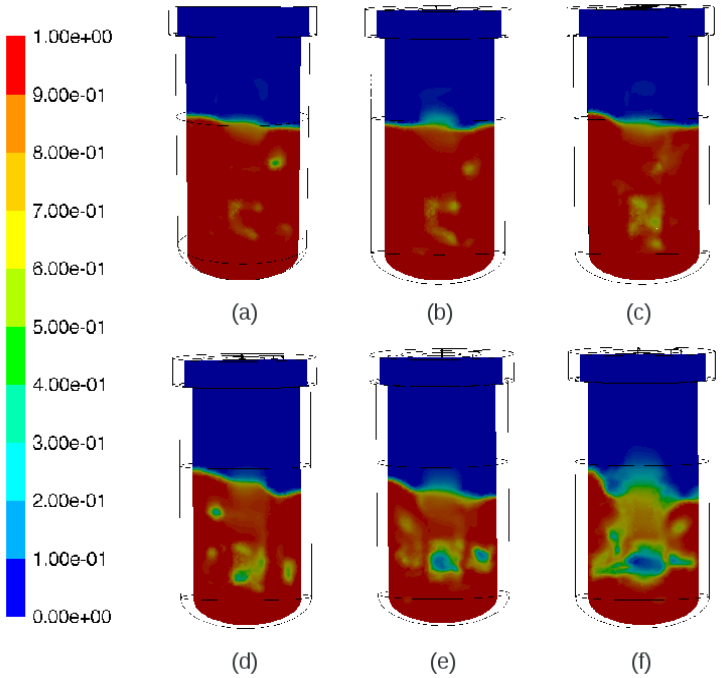

Figure 33. Contours of liquid volume fraction at a plane x=12 mm for different rotation rates for the baffled reactor: (a) 900, (b) 1000, (c) 1100, (d) 1500, (e) 2000 and (f) 2500 rpm

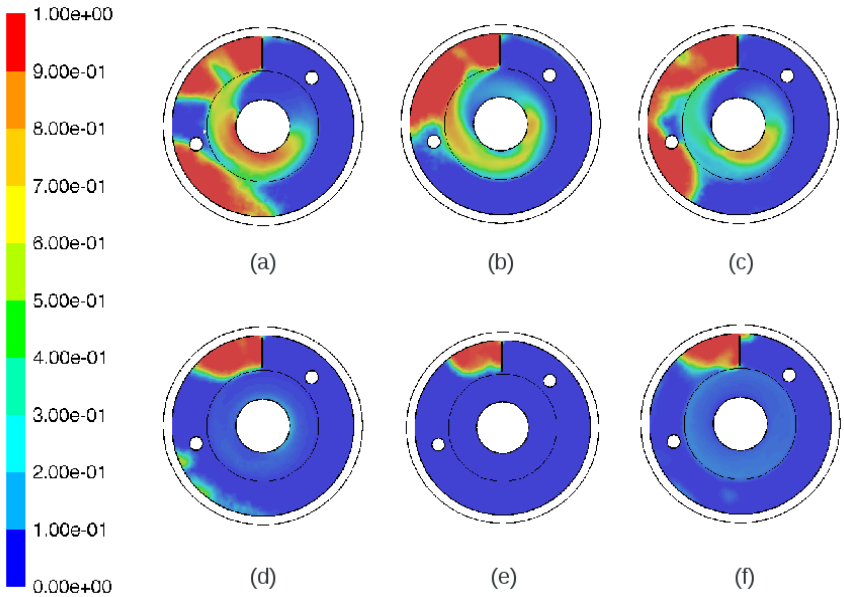

Figure 34. Contours of liquid volume fraction at a plane z=52 mm for different rotation rates for the baffled reactor: (a) 900, (b) 1000, (c) 1100, (d) 1500, (e) 2000 and (f) 2500 rpm

Figure 35 shows velocity vectors in a plane located at x=12 mm. The red color indicates velocities of 0.7 m/s or larger. As expected, vector velocities increase as the rotation rate increases, and the high speed region surrounding the blades grows with larger rotation rates. Figure 36 shows vector velocities in a plane located at z=52 mm. As it can be seen, as the rotation rate increases, the velocities in that plane are smaller. That is due to the fact that, at higher rotation rates, the free surface deformation is larger, and the gas occupies that space.

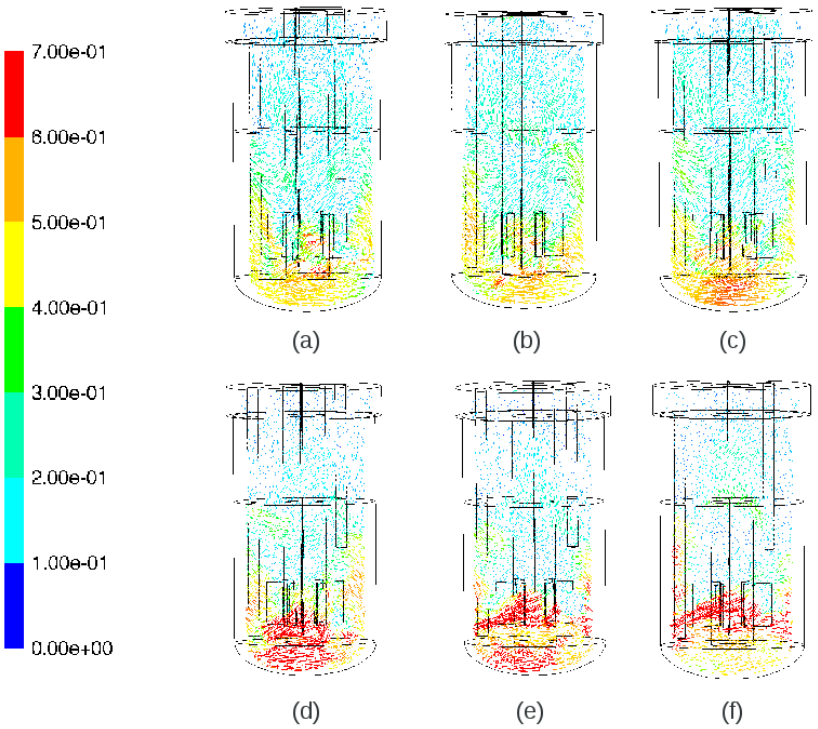

Figure 35. Velocity vectors at a plane x=12 mm for different rotation rates for the baffled reactor: (a) 900, (b) 1000, (c) 1100, (d) 1500, (e) 2000 and (f) 2500 rpm

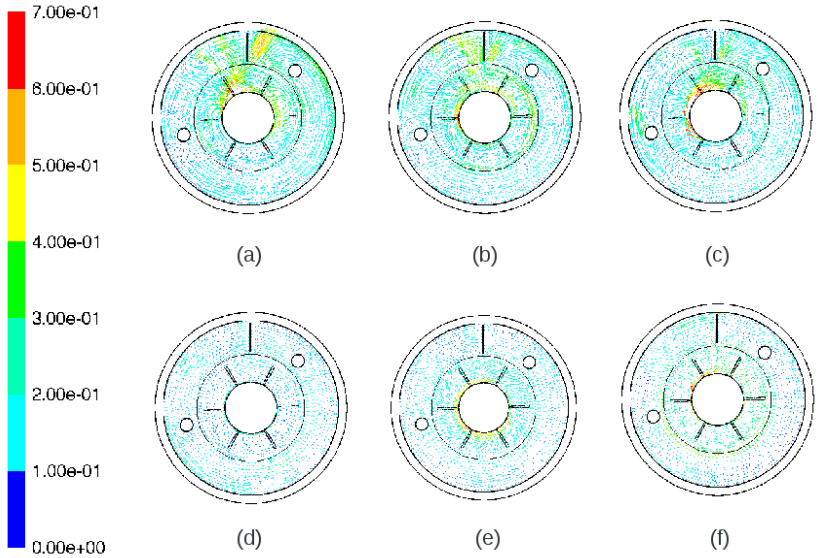

Figure 36. Velocity vectors at a plane z=52 mm for different rotation rates for the baffled reactor: (a) 900, (b) 1000, (c) 1100, (d) 1500, (e) 2000 and (f) 2500 rpm

3.6. Mass transfer

Results for mass transfer between the phases are obtained by coupling the results of the numerical simulations and the experimental results. The amount of bubbles and their sizes are retrieved from the flow visualizations and then, a Lagrangian tracking is performed for the bubbles which are released into the dynamics fields obtained in the simulations. Three different flow regimes are observed in the flow visualizations, depending on rotation rate and the presence of the baffle. In the first regime, no bubbles are formed, so the only mass transfer occurs at the free surface. In the second regime, bubbles form and move into the liquid, leading to mass transfer both in the free surface and in the surface of the bubbles. In the third regime, emulsions are formed. So three different types of correlations are used to compute mass transfer rates: mass transfer at the free surface, mass transfer from the surface of the bubbles to the liquid and mass transfer within emulsions.

The overall mass transfer is defined as

$$m = kA\Delta C \qquad \text{Eq. 3.8}$$

where k is the overall mass transfer coefficient in m/s, A is the surface where mass transfer takes place in m^2 and ΔC is the concentration difference at both sides of the surface in kg/m^3.

3.6.1. Mass transfer at the free surface

The mass transfer coefficient at the free surface is computed following the correlation proposed by Kozinski and King (1966):

$$k_L = 0.25\left(\frac{\varepsilon\mu}{\rho^2}\right)^{\frac{1}{4}}\left(\frac{\mu}{\rho D}\right)^{-\frac{3}{4}} \qquad \text{Eq. 3.9}$$

where k_L is the mass transfer coefficient in cm/min, ε is the rate of energy dissipation per unit volume in $g/cm\ min^3$, μ is the liquid viscosity in g/cm min, ρ is the liquid density in g/cm^3 and D is the diffusivity in cm^2/min. The rate of energy dissipation is obtained from the hydrodynamic simulations. The mass

transfer rate on the free surface is then obtained by multiplying the mass transfer coefficient by the free surface area (also obtained from the simulations).

3.6.2. Mass transfer from the bubbles

The mass transfer coefficient on the surface of the bubbles is related to the Sherwood number (Sh), molecular diffusivity (D) and bubble diameter (d_b) as shown in Equation 3.10:

$$k_b = \frac{ShD}{d_b} \qquad \text{Eq. 3.10}$$

Bubble diameter is obtained from the experimental visualizations, while the Sherwood number is computed using equation 3.11 (Cift et al.,1978):

$$Sh = \frac{2}{\sqrt{\pi}}\left(1 - \frac{2.89}{\mathrm{Re}^{\frac{1}{2}}}\right)^{\frac{1}{2}} Pe^{\frac{1}{2}} \qquad \text{Eq. 3.11}$$

where Re is the particle Reynolds number obtained in the numerical simulations using Lagrangian particle tracking where bubbles are released from the free surface and tracked over time and Pe is the Péclet number:

$$Pe = \mathrm{Re}\,Sc \qquad \text{Eq. 3.12}$$

and the Schmidt number (Sc) is the ratio between kinematic viscosity and diffusivity:

$$Sc = \frac{\upsilon}{D} \qquad \text{Eq. 3.13}$$

The mass transfer rate is then obtained by multiplying the mass transfer coefficient at the surface of the bubble by the bubble surface area and the number of bubbles measured in the experiments.

3.6.3. Mass transfer within emulsions

The mass transfer coefficient within the emulsion is estimated using the following correlation (Boltes et al., 2008):

$$k_L = \frac{1}{30}\sqrt{\frac{D}{\pi}}\left(\frac{V_s \rho_L g \theta}{\mu}\right)^{\frac{1}{4}} \qquad \text{Eq. 3.14}$$

where Vs is the gas slip velocity, g is the gravitational acceleration and θ is the gas volume fraction, estimated from the experimental visualizations. The gas slip velocity is computed using the following equation (Harmathy, 1960):

$$V_s = 1.53\left(\frac{g\Delta\rho\sigma}{\rho_L^2}\right)^{\frac{1}{4}} \qquad \text{Eq. 3.15}$$

where Vs is in cm/s, g in cm/s^2, Δρ is the density difference between the gas and liquid phases in g/cm^3, σ is the surface tension in dyn/cm and ρ_L is the liquid density in g/cm^3. The physical properties are evaluated at T=180ºC and 3.1 MPa and extracted from the NIST Standard Reference Database (US Department of Commerce, 2007).

The mass transfer rate within the emulsion is obtained by multiplying the mass transfer coefficient by the interfacial area between the phases within the emulsion, which is estimated from the experimental visualizations.

3.6.4. Mass transfer rates

Using the equations presented in the three previous sections, the overall mass transfer rates for both hydrogen and carbon monoxide for each case are computed. Table 9 corresponds to the results obtained for the reactor without baffle and Table 10 shows the results for the reactor with baffle. Subscripts b, s and e refer to bubble, free surface and emulsion, respectively. As it can be seen in Table 9, the flow regime changes somewhere between 1000 and 1500 rpm for the unbaffled reactor. Up to 1000 rpm the bubbly flow is observed, but from 1500 rpm onwards it becomes an emulsion.

Table 9. Results for the reactor without baffle

	1000 rpm	*1500 rpm*	*2000 rpm*	*2500 rpm*
Regime	Bubbly flow	Emulsion	Emulsion	Emulsion
Bubble diameter (mm)	0.56	0.28	0.16	0.1
Number of bubbles	$1.20 \cdot 10^{5}$	$2.00 \cdot 10^{6}$	10^{7}	$3.80 \cdot 10^{7}$
Total area of bubbles (m^2)	$1.19 \cdot 10^{-1}$	$4.77 \cdot 10^{-1}$	$8.32 \cdot 10^{-1}$	1.28
Free surface area (m^2)	$4.15 \cdot 10^{-3}$	-	-	-
k_b H_2 (m/s)	$6.37 \cdot 10^{-4}$	-	-	-
k_b CO (m/s)	$4.27 \cdot 10^{-4}$	-	-	-
$k_b A_b$ H_2 (m^3/s)	$7.56 \cdot 10^{-5}$	-	-	-
$k_b A_b$ CO (m^3/s)	$5.08 \cdot 10^{-5}$	-	-	-
k_s H_2 (m/s)	$2.66 \cdot 10^{-4}$	-	-	-
k_s CO (m/s)	$1.46 \cdot 10^{-4}$	-	-	-
$k_s A_{SL}$ H_2 (m^3/s)	$1.10 \cdot 10^{-6}$	-	-	-
$k_s A_{SL}$ CO (m^3/s)	$6.08 \cdot 10^{-7}$	--	-	-
k_e H_2 (m/s)	-	$5.53 \cdot 10^{-5}$	$5.53 \cdot 10^{-5}$	$5.53 \cdot 10^{-5}$
k_e CO (m/s)	-	$3.71 \cdot 10^{-5}$	$3.71 \cdot 10^{-5}$	$3.71 \cdot 10^{-5}$
$k_e A_e$ H_2 (m^3/s)	-	$2.64 \cdot 10^{-5}$	$4.60 \cdot 10^{-5}$	$7.09 \cdot 10^{-5}$
$k_e A_e$ CO (m^3/s)	-	$1.77 \cdot 10^{-5}$	$3.09 \cdot 10^{-5}$	$4.76 \cdot 10^{-5}$
kA H_2 (m^3/s)	$7.67 \cdot 10^{-5}$	$2.64 \cdot 10^{-5}$	$4.60 \cdot 10^{-5}$	$7.09 \cdot 10^{-5}$
kA CO (m^3/s)	$5.14 \cdot 10^{-5}$	$1.77 \cdot 10^{-5}$	$3.09 \cdot 10^{-5}$	$4.76 \cdot 10^{-5}$

For the bubbly flow, the mass transfer from the free surface can be neglected when compared to the mass transfer from the bubbles. The ratio of the mass transfer rates from the bubbles to the mass transfer rate from the free surface is approximately 68 and 83 at 1000 rpm for the hydrogen and carbon monoxide, respectively. However, for the emulsion, the mass transfer coefficient remains unchanged when changing the rotation rate in the range comprised between 1500 and 2500 rpm. The mass transfer coefficient is smaller

for the emulsion than for the bubbly flow. However, the overall mass transfer rate is of the same order of magnitude, because of the larger interphase area within the emulsion. At 2500 rpm, the overall mass transfer within the emulsion is similar to that of the bubbly flow at 1000 rpm, although still lower.

Table 10 shows the results for the baffled reactor. It is worth noting that the presence of the baffle prevents the formation of an emulsion even at high rotation rates. The amount of bubbles increases when increasing rotation rate, while the bubble diameter decreases. Still, the total surface area of bubbles is larger for higher rotation rates. The mass transfer rate from the free surface is also negligible when compared to the one from the bubbles. The ratios for both mass transfer rates for hydrogen are 45, 27, 33 and 52 at 1000, 1500, 2000 and 2500 rpm, respectively. For the carbon monoxide those ratios are 55 at 1000 rpm, 33 at 1500 rpm, 41 at 2000 rpm and 64 at 2500 rpm.

In order to compare all cases, the overall mass transfer rates are plotted in Figures 37 and 38. These overall mass transfer rates are the result of the addition of the mass transfer rates from the bubbles and from the free surface in the bubbly flow regime, and the emulsion when such a regime exists. Figure 37 shows the overall mass transfer rate for the hydrogen. As it can be seen, the case providing a larger overall mass transfer coefficient is the baffled reactor at 2500 rpm, followed by the same system rotating at 2000 rpm and the unbaffled reactor rotating at 1000 rpm, just before the emulsion is formed. Figure 38 shows the overall mass transfer rate for the carbon monoxide.

As it happened with the hydrogen, the case leading to a larger overall mass transfer is the baffled reactor rotating at 2500 rpm. From the data gathered in this study, it can be inferred that for the same rotation rate, the unbaffled reactor provides a larger mass transfer rate as long as the bubbly flow is kept (30% larger). Once the emulsion forms, the mass transfer drops (up 65%). Therefore, up to the critical rotation rate where the emulsion forms (somewhere between 1000 and 1500 rpm), the unbaffled reactor is a better option, while the baffled reactor provides larger mass transfer rates above that critical rotation rate.

Table 10. Results for the reactor with baffle

	1000 rpm	*1500 rpm*	*2000 rpm*	*2500 rpm*
Regime	Bubbly flow	Bubbly flow	Bubbly flow	Bubbly flow
Bubble diameter (mm)	0.55	0.47	0.42	0.38
Number of bubbles	$7.70 \cdot 10^{4}$	$1.55 \cdot 10^{5}$	$3.10 \cdot 10^{5}$	$6.30 \cdot 10^{5}$
Total area of bubbles (m^2)	$7.25 \cdot 10^{-2}$	$1.05 \cdot 10^{-1}$	$1.68 \cdot 10^{-1}$	$2.85 \cdot 10^{-1}$
Free surface area (m^2)	$4.15 \cdot 10^{-3}$	$6.75 \cdot 10^{-3}$	$8.03 \cdot 10^{-3}$	$7.25 \cdot 10^{-3}$
k_b H_2 (m/s)	$7.18 \cdot 10^{-4}$	$5.94 \cdot 10^{-4}$	$6.10 \cdot 10^{-4}$	$6.01 \cdot 10^{-4}$
k_b CO (m/s)	$4.82 \cdot 10^{-4}$	$3.99 \cdot 10^{-4}$	$4.10 \cdot 10^{-4}$	$4.04 \cdot 10^{-4}$
$k_b A_b$ H_2 (m^3/s)	$5.20 \cdot 10^{-5}$	$6.27 \cdot 10^{-5}$	$1.02 \cdot 10^{-4}$	$1.71 \cdot 10^{-4}$
$k_b A_b$ CO (m^3/s)	$3.49 \cdot 10^{-5}$	$4.21 \cdot 10^{-5}$	$6.88 \cdot 10^{-5}$	$1.15 \cdot 10^{-4}$
k_s H_2 (m/s)	$2.75 \cdot 10^{-4}$	$3.43 \cdot 10^{-4}$	$3.83 \cdot 10^{-4}$	$4.52 \cdot 10^{-4}$
k_s CO (m/s)	$1.52 \cdot 10^{-4}$	$1.89 \cdot 10^{-4}$	$2.11 \cdot 10^{-4}$	$2.49 \cdot 10^{-4}$
$k_s A_s$ H_2 (m^3/s)	$1.14 \cdot 10^{-6}$	$2.32 \cdot 10^{-6}$	$3.07 \cdot 10^{-6}$	$3.28 \cdot 10^{-6}$
$k_s A_s$ CO (m^3/s)	$6.29 \cdot 10^{-7}$	$1.27 \cdot 10^{-6}$	$1.69 \cdot 10^{-6}$	$1.81 \cdot 10^{-6}$
kA H_2 (m^3/s)	$5.32 \cdot 10^{-5}$	$6.51 \cdot 10^{-5}$	$1.05 \cdot 10^{-4}$	$1.75 \cdot 10^{-4}$
kA CO (m^3/s)	$3.56 \cdot 10^{-5}$	$4.34 \cdot 10^{-5}$	$7.05 \cdot 10^{-5}$	$1.17 \cdot 10^{-4}$

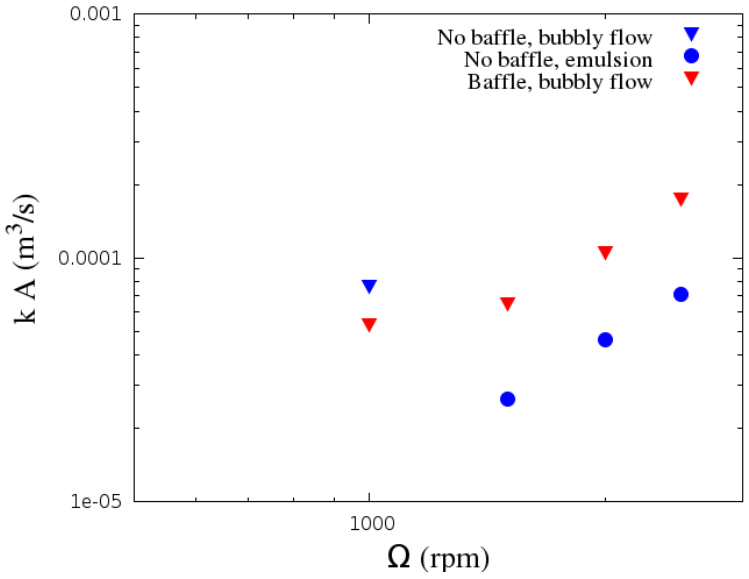

Figure 37. Overall mass transfer rates for the hydrogen

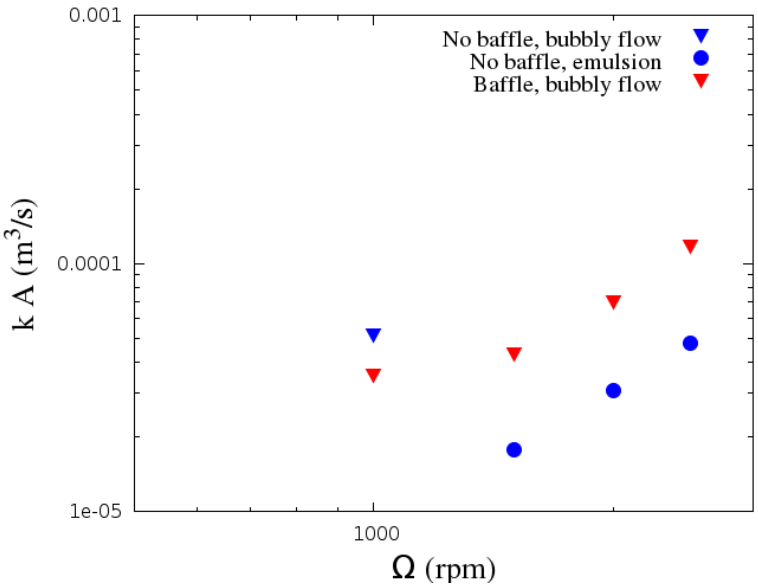

Figure 38. Overall mass transfer rates for the carbon monoxide

4. Conclusions

The flow in the reactor model has been visualized and characterized at rotation rates up to 1721 rpm. The reactor with or without baffle has been considered. It has been determined experimentally that the amount of bubbles inside the reactor increases with the rotation rate (Ω), while the bubble size decreases. Typical bubble diameters range from 0.2 mm to 0.7 mm. The mean measured bubble diameter was compared with that predicted by correlations found in the literature for similar reactors, and the differences are about 8 %.

Experimentally three flow regimes have been observed. At low rotation rates bubbles are not observed and the liquid phase and the gas phase are separated by a well-defined interphase which is deformed vertically by rotation. At larger rotation rates gas bubbles are observed within the liquid phase. An emulsion is formed for rotation rates between 1000 and 1400 rpm for the unbaffled configuration, while bubbly flow is observed for the baffled configuration in the whole range of rotation rates studied (up to 1721 rpm). In general at the same rotation rate the number of bubbles is smaller in the baffled configuration than in the unbaffled configuration.

Numerical simulations with the multiple reference frame technique were conducted. The simulations predict correctly the shape of the interphase observed experimentally. Bubbles with the experimentally measured diameter were tracked numerically to determine the particle Reynolds number. Mass transfer rates of hydrogen and carbon monoxide were estimated with conventional mass transfer correlations for particles using the computed particle Reynolds number.

For the reactor with the baffle the emulsion is not observed in the range of rotation rates considered. In this case predictions indicate that the mass transfer rates of hydrogen (H) and carbon monoxide (CO) from the gas phase to the liquid phase increase with the rotation rate. For example the increase of the rotation rate from 1000 rpm to 2500 rpm increases the mass transfer coefficient of H or CO by a factor of 3.3.

For the unbaffled configuration there is a reduction, of about 65%, of the mass transfer rates from the bubble regime at 1000 rpm to the emulsion at 1400 rpm. The increase of the rotation rate in the emulsion regime produces the augmentation of the mass transfer rate by a factor of 2.7 from 1500 rpm to 2500 rpm.

The comparison of the unbaffled and baffled configurations shows that at 1000 rpm, at which the bubbly regime is observed in both configurations, the mass transfer rate is about 30% larger for the unbaffled configuration. In the range $1500 \leq \Omega \leq 2500$ rpm, the baffled configuration (bubbly flow) shows larger mass transfer rates than the unbaffled configuration (emulsion).

Some experiments were conducted for three phase flows (air-water-heptane) and the flow behavior was analyzed. Different compositions of the liquid mixture and rotation rates were studied. The three-phase system shows different behaviors depending on the composition and rotation rate. At Ω=606 rpm, for the pure fluids (heptane or water) no air bubbles are observed in the liquid phases. At this rotation rate and for a 15/85 water/heptane mixture water drops can be seen within the heptane. A liquid-liquid emulsion is formed for 50/50 and 85/15 water/heptane mixtures. At Ω=1371 rpm and pure composition of the liquid phase air bubbles are observed. The mean diameter of the air bubbles depends on the composition, ranging from 1.114±0.052 mm for pure heptane to 0.479±0.017 mm for pure water. In the case of mixtures it is not clear if air bubbles are distributed within the liquid phases since the visualization cannot differentiate between air bubbles or water drops.

The direct quantitative extrapolation of these conclusions to the real operating conditions of the reactor has to be made with care. It should be noted that the

simulations have been performed with the physical properties of the fluids used in the real operation of the actual reactor but the sizes and amount of bubbles are obtained from experiments performed with air and water. In any case the three flow regimes observed experimentally in the air-water system are likely to exist in the real reactor but probably in different ranges of rotation rates.

5. Future work

The estimation of the mass transfer rates has been carried out using correlations since the experimental setup used did not allowed the direct measurement of the mass transfer rates. An interesting possibility to evaluate the accuracy of the predicted mass transfer rates would be the construction of a new experimental setup equipped with instrumentation able to measure the concentration of a gas component within the liquid phase.

Some preliminary experiments have been carried out for the heptane-water-air system. A deeper and more complete study of the behavior of this system can be of interest to understand the real operation of the reactor.

6. References

Alcamo, R., Micale, G., Grisafi, F., Brucato and A., Ciofalo, M. 2005. Large-eddy simulation of turbulent flow in an unbaffled stirred tank driven by a Rushton turbine. Chemical Engineering Science 60, 2303-2316.

Arlov, D., Revstedt, J. and Fuchs, L. 2008. Numerical simulation of a gas-liquid Rushton stirred reactor – LES and LPT. Computers & Fluids 37, 793-801.

Berje, J., Schedemann, A.., Gmehling J. 2011. Liquid densities of acetone and n-heptane and excess volumes of the binary system in a wide temperature and pressure range. Fluid Phase Equilibria 300, 110–115.

Boltes, K., Caro, A., Leton, P., Rodriguez, A. and Garcia-Calvo, E. 2008. Gas-liquid mass transfer in oil-water emulsions with an airlift bio-reactor. Chemical Engineering and Processing, 47, 2408-2412.

Cift, R., Grace, J.R. and Weber, M.E. 1978. Bubbles, drops and particles. Academic Press, London.

Deen, N.G., Solberg, T. and Hjertager, B.H. 2002. Flow generated by an aerated Rushton impeller: Two-phase PIV experiments and numerical simulations. The Canadian Journal of Chemical Engineering 80, 1-15.

Ferziger, J.H. and Peric, M. 2002. Computational methods for fluid dynamics. 3rd ed. Springer-Verlag, Berlin, Germany.

FLUENT 12.0 Documentation. 2009. ANSYS Inc. Lebanon, NH, USA.

Harmathy, T.Z. 1960. Velocity of large drops and bubbles in media of infinite or restricted extent. AIChE Journal, 6, 2, 281-288.

Hirt, C.W. and Nichols, B.D. 1981. Volume of fluid (VOF) method for the dynamics of free boundaries. Journal of Computational Physics 39, 201-225.

Kozinski, A.A. and King, C.J. 1966. The influence of diffusivity on liquid phase mass transfer to the free interface in a stirred vessel. AIChE Journal 12, 1, 109-116.

Launder, B.E. and Spalding, D.B. 1972. Lectures in mathematical models of turbulence. Academic Press, London, England.

Luo, J.Y., Issa, R.I. and Gosman, A.D. 1994. Prediction of impeller-induced flows in mixing vessels using multiple frames of reference. IchemE Symposium Series 136, 549-556.

Nagata, S. 1975. Mixing. Principles and applications. John Wiley & Sons, New York.

Perng, C.Y. and Murthy, J.Y. 1992. A moving mesh technique for the simulation of flow in mixing tanks. AIChE Annual Meeting, Miami, FL, 109b.

Ranade, V.V. 1997. An efficient computational model for simulating flow in stirred vessels: a case of Rushton turbine. Chemical Engineering Science 52, 4473-4484.

Ranade, V.V. and Dommeti, S. 1996. Computational snapshot of flow generated by axial impellers in baffled stirred vessels. Chemical Engineering Research and Design 74, 476-484.

Scargiali, F., D'Orazio, A., Grisafi, F. and Brucato, A. 2007. Modelling and simulation of gas-liquid hydrodynamics in mechanically stirred tanks. Trans IChemE, Part A, Chemical Engineering Research and Design 85 (A5), 637-646.

Serra, A. Campolo, M. and Soldati, A. 2001. Time-dependent finite-volume simulation of the turbulent flow in a free-surface CSTR. Chemical Engineering Science 56, 2715-2720.

Smagorinsky, J. 1963. General circulation experiments with the primitive equations. Monthly Weather Review 91, 99-165.

Spalding, D.B. 1985. Computer simulation of two-phase flows (R.W. Lewis. Computational techniques in heat transfer). Ed. Pineridge Press, Swansea, UK.

Torré, J.P., Fletcher, D.F., Lasuye, T. and Xuereb, C. 2007. An experimental and computational study of the vortex shape in a partially baffled agitated vessel. Chemical Engineering Science 62, 1915-1926.

Watson, G., Zéberg-Mikkelsen,C.K., Baylaucq, A. and Boned, C. 2006. J. Chem. Eng. Data 51, 112-118.

Yeoh, G.H. and Tu, J. 2009. Computational techniques for multiphase flow. Elsevier.

Zéberg-Mikkelsen,C.K., Watson, G., Baylaucq, A., Galliéro, G. and Boned, C. 2006. Comparative experimental and modeling studies of the viscosity behavior of ethanol +C7 hydrocarbon mixtures versus pressure and temperature. Fluid Phase Equilibria 245, 6–19.